An Investigation into the Effects of Particle Nonsphericity in Cirrus Cloud Radiative Properties

by
John R. Withrow Jr. and Stephen K. Cox

Department of Atmospheric Science
Colorado State University
Fort Collins, Colorado

Funding Agencies:
National Aeronautics and Space Administration Grant NAG-1-1146, S-03
Office of Naval Research Contract No. N00014-91-J-1422, P00004
Department of Energy Contract No. DE-FG02-90ER60970

Colorado State University

Department of Atmospheric Science

Paper No. 557

AN INVESTIGATION INTO THE EFFECTS OF PARTICLE NONSPHERICITY IN CIRRUS CLOUD RADIATIVE PROPERTIES

by: John R. Withrow, Jr. and Stephen K. Cox
Department of Atmospheric Science
Colorado State University
Fort Collins, CO 80523

Research Supported By

National Aeronautics and Space Administration
(Grant NAG-1-1146, S-03)

Office of Naval Research
(Contract No. N00014-91-J-1422, P00004)

Department of Energy
(Contract No. DE-FG02-90ER60970)

May, 1994

Atmospheric Science Paper No. 557

ABSTRACT OF THESIS

AN INVESTIGATION INTO THE EFFECTS OF PARTICLE NONSPHERICITY IN CIRRUS CLOUD RADIATIVE PROPERTIES

The possible effect of tropospheric warming and stratospheric cooling by cirrus clouds arising from their radiative properties has been demonstrated by previous authors. These results, however, have been based upon the assumption that cirrus particles behave radiatively like ice spheres. This study seeks to extend this approximation to circular cylinders and disks. The scattering information for such particles is investigated using two models, one employing the Discrete Dipole Approximation and the other Anomalous Diffraction Theory. The study begins with a general overview of the current state of cirrus research leading to the appropriateness of this study. An exhaustive display of the current theoretical and experimental knowledge of the problem of scattering off of cylindrical particles is then provided. Cylindrical particles with length-to-diameter ratios ranging from .1 to 10 and with effective radius values up to about 6 are then modelled for four refractive indices ranging from nonabsorbing to strongly absorbing. Results are given for the extinction efficiency, Q_{ext}, the single scatter albedo, ω_0, and the asymmetry parameter, g. The results for ω_0 and g are extended to larger sized particles through the fitting of corresponding Mie curves to the cylinder data. Similar extensions for Q_{ext} are performed through comparisons with results from a second model employing Anomalous Diffraction Theory. An analysis of the DDA and ADT results is given, yielding a voluminous supply of information, both quantitative and qualitative. The quantitative information is displayed in a myriad of appendices which are referenced by the chapters. Briefly, the first three appendices show the entirety of the DDA results for Q_{ext}, ω_0, and g, respectivley, information which will be most useful to subsequent studies which have an interest in the scattering results of individual particles.

In addition, the latter three appendices show a series of tabulated results, the curve-fit extension factors which should make the rapid reproduction of cylinder information from currently parameterized information more feasible. Qualitatively the results are analyzed to arrive at some of the mechanisms involved in the scattering from cylindrical particles as well as some initial insights as to the biases introduced in radiative transfer models through the representation of cirrus particles as equivalent volume spheres.

This study should ultimately begin to provide the necessary information for a subsequent two-stream radiative transfer model in which cirrus heating rates and radiative cloud forcings can be calculated to a second approximation from spheres, that of cylinders and disks. Although this study performs an analysis only on individual particles, some educated assertions can now be made in terms of the biases generated by the use of equivalent volume spheres in a modelled cirrus cloud. In general it is found that the equivalent volume sphere approximation should result in an underestimation of absorption as well as an overestimation of the amount of forward scatter for small particles. Also for small particles the infrared optical depth should in most cases be overestimated. Lastly, the use of Anomalous Diffraction Theory in the depiction of cirrus particle radiative properties should in most cases result in a slight underestimation of absorption and optical depth.

ACKNOWLEDGEMENTS

On a professional basis we are greatly indebted to Dr. Piotr Flatau for his remarkable skills and expertise with respect to the Discrete Dipole Approximation and Anomalous Diffraction Theory models which he developed and gladly showed to John Withrow. We would also like to thank Dr. Graeme Stephens and Dr. Chaioyao She for their comments as this M.S. thesis was being prepared. For computer and word processing assistance I (John Withrow) have relied on the expertise of Paul Hein, Chris Cornwall, Brenda Thompson, Melissa Tucker, Dr. Piotr Flatau, Paul Ciesielski, Rick Taft, Bill Thorson, Donna Chester, Scott Denning, and Frank Evans. We should also acknowledge the Scientific Computing Division at the National Center for Atmospheric Research in Boulder, Colorado for the computer usage time which was necessary for the runs of the DDA model. Also, the Academic Computing and Network Services office at Colorado State University should be acknowledged for their assistance as well. We have also relied on the mathematical assistance of Dr. Wayne Schubert, Dr. Kirk Fuller, Dr. Craig F. Bohren, Louie Grasso, Jim Edwards, and Chungu Lu.

On a more personal level within the walls of my own department I (John Withrow) must thank Ran Song, Gordon Beck, Cara-Lyn Lappen, James Harrington, Jane Wilkins, Melissa Tucker, Fredell Boston, Paul Hein, Chris Cornwall, Dave Wood, Dr. John Davis, and Dr. Stephen K. Cox for their encouragement and cunning sense of humor upon which I leaned a great deal in the moments in which humor was difficult for me to find.

Lastly, and perhaps most importantly, on a spiritual basis I (John Withrow) owe much of the stamina and determination that went into this document to the strength I have received from God's grace and patience, which has been shared through my beloved friends at Immanuel Christian Reformed Church in Fort Collins, Colorado, especially from the family of Chrys Remus and her three boys - Chip, Bradley, and Michael. I am also greatly

thankful for the InterVarsity Christian Fellowship group at Colorado State University. The friends that I have been blessed with through these two niches are too important to ever forget and too many to list.

This research was supported by the National Aeronautics and Space Administration under grant NAG-1-1146, S-03, the Office of Naval Research under contract No. N00014-91-J-1422, P00004, and the Department of Energy contract number DE-FG02-90ER60970.

TABLE OF CONTENTS

LIST OF FIGURES

Chapter 1

INTRODUCTION

1.1 Clouds, Climate, and Radiation

It is well-known within the current scientific community involved in the modeling of global climate change that in the study of climate and the earth's radiation budget clouds may represent the greatest source of uncertainty. The problem, outlined in Freeman and Liou (1979) and Liou (1986) is simple in its explanation but highly complex in its solution. Referring to figure 1.1 from Manabe and Wetherald (1967), the presence of a daytime cloud can either have a warming or cooling effect on the surface. This is because the major effects of such clouds can be expressed in terms of two radiative effects on the earth's surface. These are, first, a cooling effect produced by the reflection and scattering of incident solar radiation which would otherwise further illuminate the surface, and, second, a warming effect produced by the trapping of outgoing longwave radiation from the surface and lower atmosphere. The final analysis of the radiative forcing of an arbitrary cloud is, thus, found through a comparison of the relative strengths of these two factors and is usually expressed in terms of a vertical distribution of resultant heating/cooling rates. This analysis, of course, requires a knowledge of the solar and infrared radiative properties not only of the cloud but also of the surrounding atmosphere as well as the surface. Such properties are well-understood for a cloud-free atmosphere and are easily simulated for the surface.

With the above findings in mind it should be noted as a partial aside that there are two cloud types, marine stratocumulus and cirrus clouds, which have recently warranted special attention, the former largely due to the attenuation effect on the solar radiation. Randall et al. (1984) stipulated based on the high solar albedoes of marine stratus and stratocumulus (30 to 40 percent) compared with their oceanic backgrounds (about 10 percent) that such

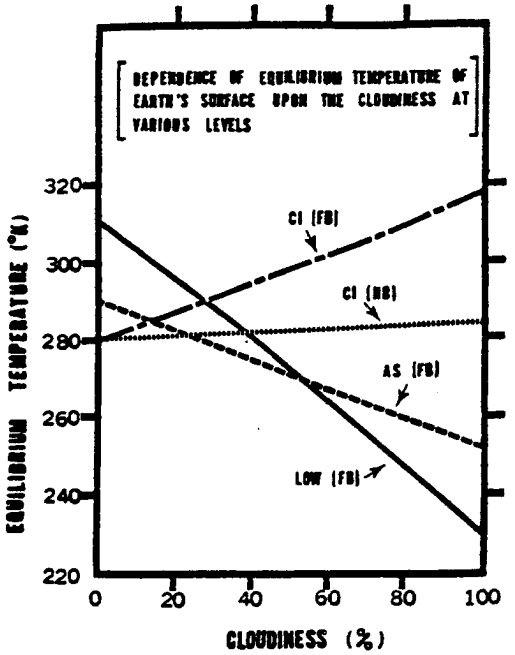

Figure 1.1: . Radiative convective equilibrium temperature at the earth's surface as a function of cloudiness (cirrus, altostratus, low cloud). FB and HB refer to 'full black' and 'half black', respectively (from Manabe and Wetherald (1967)).

clouds could thus play a role in reducing the global incoming solar flux to such an extent that a global increase in their areal coverage of four percent could completely offset the postulated 2-3K increase in surface temperatures associated with a doubling of atmospheric carbon dioxide concentrations.

In addition, knowledge of the longwave properties of the cloud is also required, and it is here that knowledge of the height (and, thus, temperature) of the cloud is also needed. Two clouds with a given longwave emissivity will absorb about the same amount of outgoing longwave radiation, but the higher cloud, due to its lower temperature, will radiate less to space. Less lost means more retained, and it is for this reason that cirrus clouds have achieved their special focus. Manabe and Wetherald (1967) in a classic paper which introduced convective parameterization into atmospheric modeling, revealed in their one-dimensional model that the equilibrium temperature structure of a given atmosphere is highly sensitive not only to the concentrations of its gaseous constituents but also on the location and longwave emissivity of a modeled cloud. Referring once again to figure 1.1, these surface equilibrium temperatures are revealed as a function of percentage cloudiness.

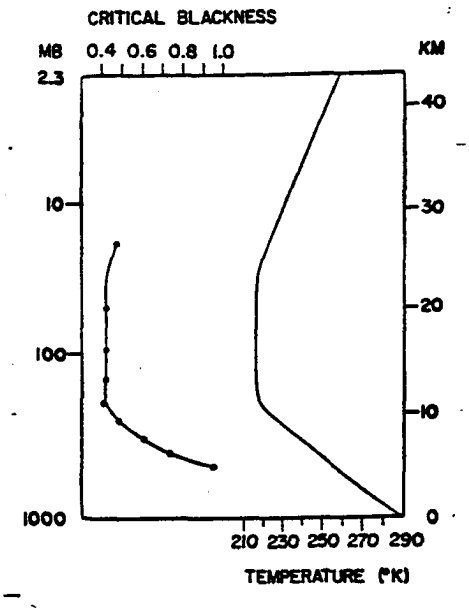

Figure 1.2: . The right hand side of the figure shows the vertical temperature distribution adopted for the computation. On the left, the critical blackness of cirrus for heating the surface is shown (from Manabe and Strickler (1964)).

Here this warming effect of cirrus (CI) can be seen in contrast to a cooling effect for lower clouds. Also the dependence on emissivity is visible in this figure ('half black' vs. 'full black'), and the combined effect from both of these contributing factors was better quantified by Manabe and Strickler (1964), where a height dependent quantity of 'critical blackness', shown in figure 1.2, was introduced, above which a cloud at the given height could produce this warming effect.

Cox (1971) provided the first comparison of the 'critical blackness' quantity with observations (figure 1.3), and from the plots of observed data it has been deduced that cirrus clouds, in particular tropically occurring cirrus around 300-400 mb, could indeed be producing this warming effect. Considering also the fact that cirrus clouds comprise close to 20 percent of the global area coverage (see figure 1.4), the importance of an investigation of cirrus is clearly demonstrated.

Similar results to Manabe and Wetherald (1967) were found by Freeman and Liou (1979). Figures 1.5 through 1.7 show some of their cirrus modeling studies, and here the heating/cooling effects of cirrus clouds are expanded to the full vertical. The results are

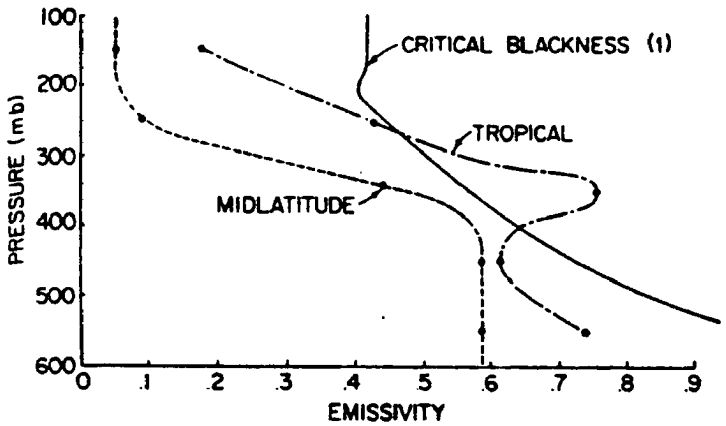

Figure 1.3: . Observed cirrus cloud infrared emissivities plotted with the 'critical blackness' curve from Manabe and Strickler (1964) (figure from Cox (1971)).

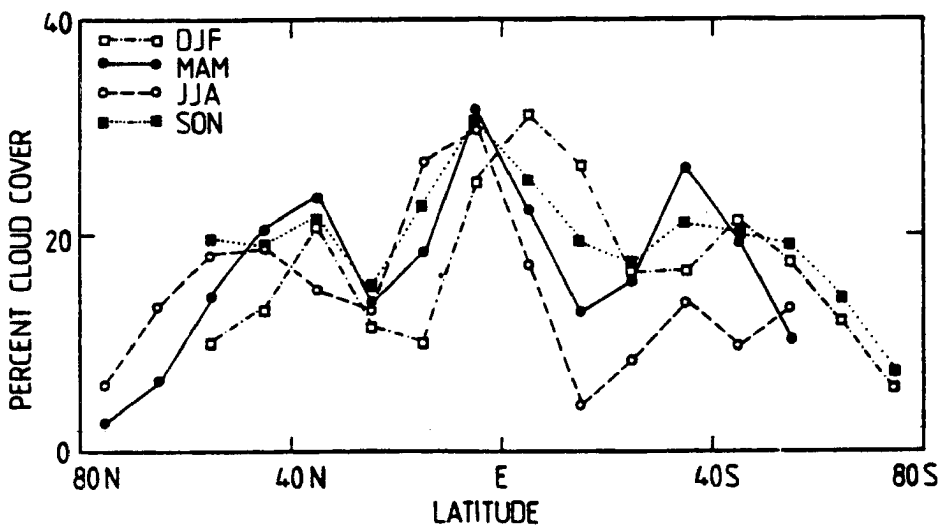

Figure 1.4: . Seasonal zonal average distributions of the occurrence of high clouds (from Barton (1983)).

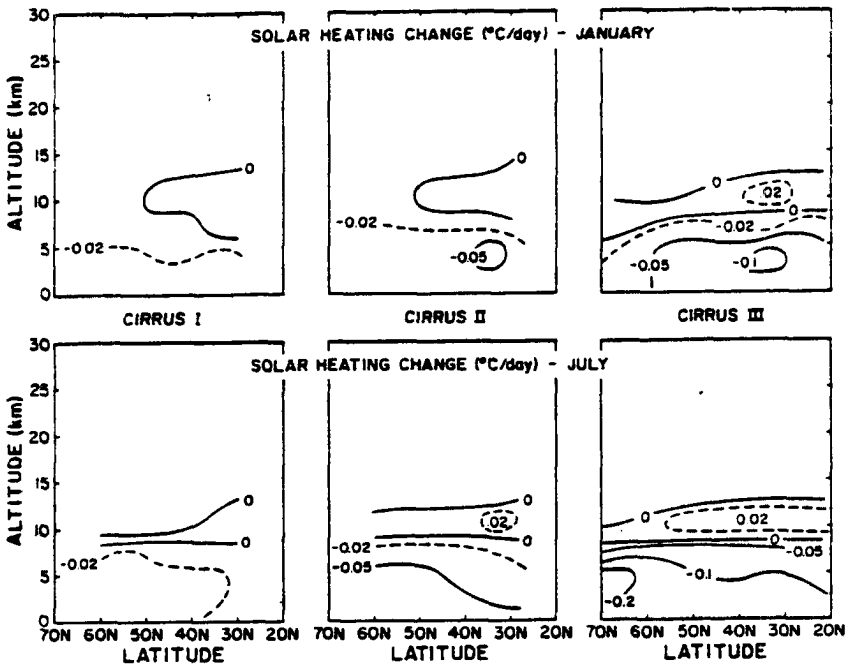

Figure 1.5: . Changes in the solar heating for January and July conditions due to the increased cirrus cloudiness (from Freeman and Liou (1979)).

given for three scenarios, ranging from a 5 percent (CIRRUS I) to a 20 percent increase (CIRRUS III) in subtropical to midlattitude cirrus. Figure 1.5 shows the effects on the solar radiation to be a cooling below the cloud and to a lesser extent a heating above the cloud. This is due to the increased albedo associated with the increase in the cloud amount, resulting in less absorbed below the cloud and more absorbed above. The longwave effects displayed in figure 1.6 reveal the opposite effect, a tropospheric warming due to increases in the downward fluxes as well as an upper tropospheric and stratospheric cooling due to the fact that these locations are now receiving a larger percentage of their longwave emissions from a much colder source. From these two figures it can be seen that the longwave effects are stronger than those of the shortwave, and figure 1.7 confirms this as it shows the net effect to be a warming of the troposphere and a cooling of the tropopause and stratosphere. The authors went on to say that this warming in some cases was only for the troposphere, not the surface; that is, that at the surface the increase in the downward longwave flux had been completely absorbed by the atmosphere to the point of no longer being large enough to overpower the cooling effect produced by the increase in the scattered shortwave from the cloud.

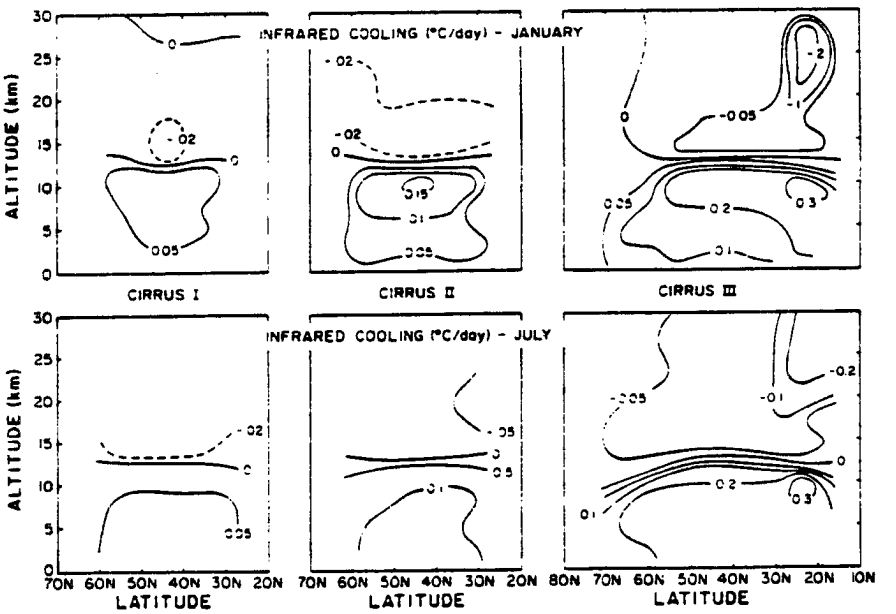

Figure 1.6: . Same as in figure 1.5 but for thermal longwave radiative cooling effects (from Freeman and Liou (1979)).

Stephens and Webster (1981) extended this work back to the arena of atmospheric equilibrium temperatures. In doing so, the large heating rates above the cloud layer seen in figure 1.5 appear to have been more emphatically reiterated in figure 1.8 as inversions above the cloud layers. Employing a Manabe-and-Wetherald-type one dimensional model which now included climatologically-based dynamic transports, effects of surface albedo and cloud ice water path (IWP) were investigated. Some of their results are illustrated in figures 1.9 and 1.10. Figure 1.9 shows changes in equilibrium surface temperatures and reveals this sensitivity to surface albedoes for a variety of latitudes and cloud types.

One interesting finding was a latitude above which all clouds apparently acted to warm the surface. This was reportedly due to the low sun incidence angle which lessened the albedo (cooling) effect of the cloud layers. Another finding was the strong sensitivity to surface albedoes. In particular note that most of the cloud layers for a given latitude had at least a partial region on the surface-albedo-scale in which a warming effect was reached. This prompted the need for the creation of a parameter known as 'critical surface albedo', or a_{sc}, given as a function of latitude as well as cloud type and amount, above which the given cloud layer would produce a surface warming. Thirdly, and most importantly for

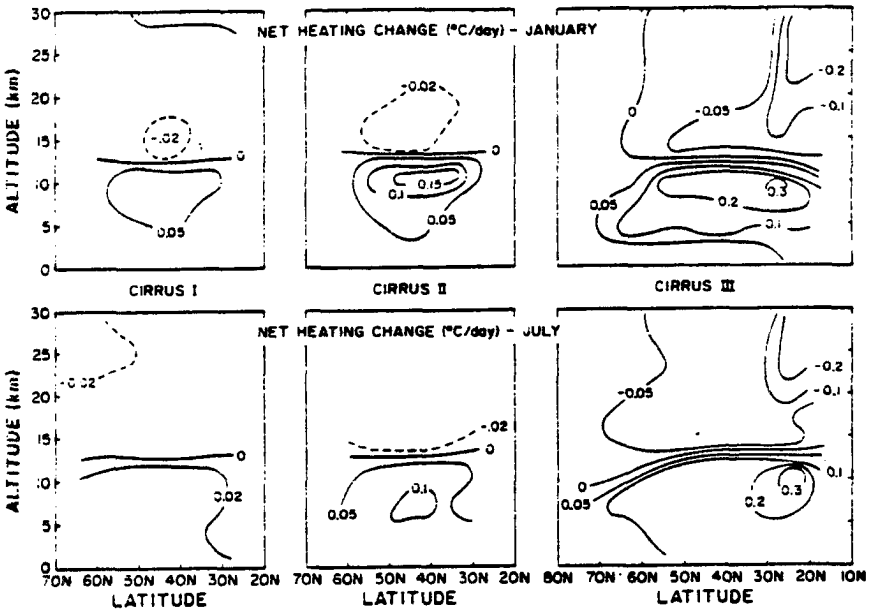

Figure 1.7: . Same as in figure 1.5 but for the net radiative effects (from Freeman and Liou (1979)).

the present study, it was found here that thin high clouds appear to produce the optimum warming as well as having the potential to produce a warming at all latitudes and for all surface albedoes. This is confirmed in figure 1.10. For this an explanation was given that for thin clouds as IWP begins to grow the effective emissivity becomes large before the shortwave albedo, thus resulting in a large difference in these two parameters for thin clouds. (An example is given in Stephens and Webster (1981) in which a cloud having a $20\frac{g}{m^2}$ IWP is estimated at having a shortwave albedo of .36 but a longwave emissivity of .9.) It is only after more extensive increases in the IWP that the albedo effect is able to become the overpowering factor which results in a cooling.

Qualitatively similar results were found by Liou and Gebhart (1982) (see figures 1.11 through 1.13). Here again it can be found that optically thin clouds not only produce the optimum warming but also an unequivocal warming with respect to variations in cloud height, suggesting that if optically thin low and middle clouds had been plotted in figure 1.9 from Stephens and Webster (1981) they might have shown behavior similar to that of thin high clouds.

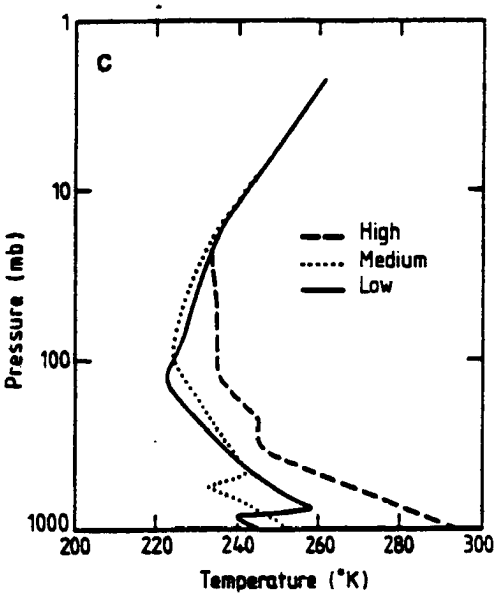

Figure 1.8: . Vertical profiles of equilibrium temperatures for three cloud cases (from Stephens and Webster (1981)).

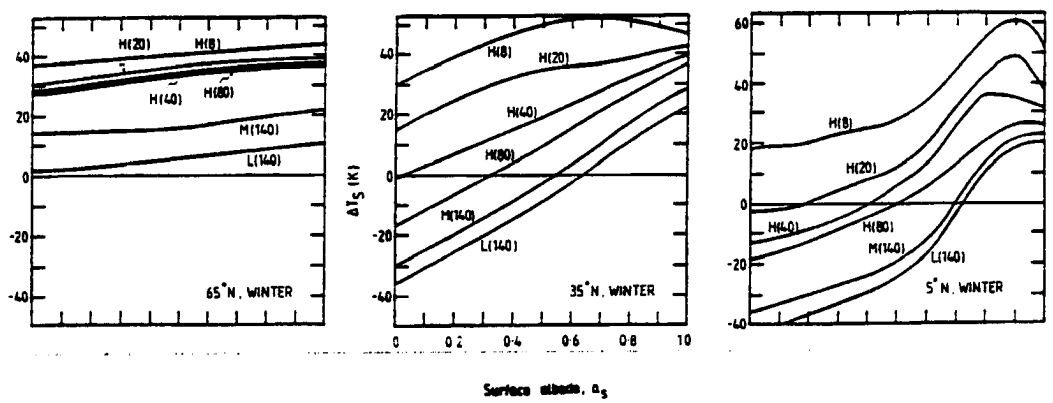

Figure 1.9: . Equilibrium surface temperature differences (ΔT_s) between the clear and cloudy cases for various cloud cases, liquid water paths, and surface albedoes. Results for 5, 35, and 65°N in winter are shown (from Stephens and Webster (1981)).

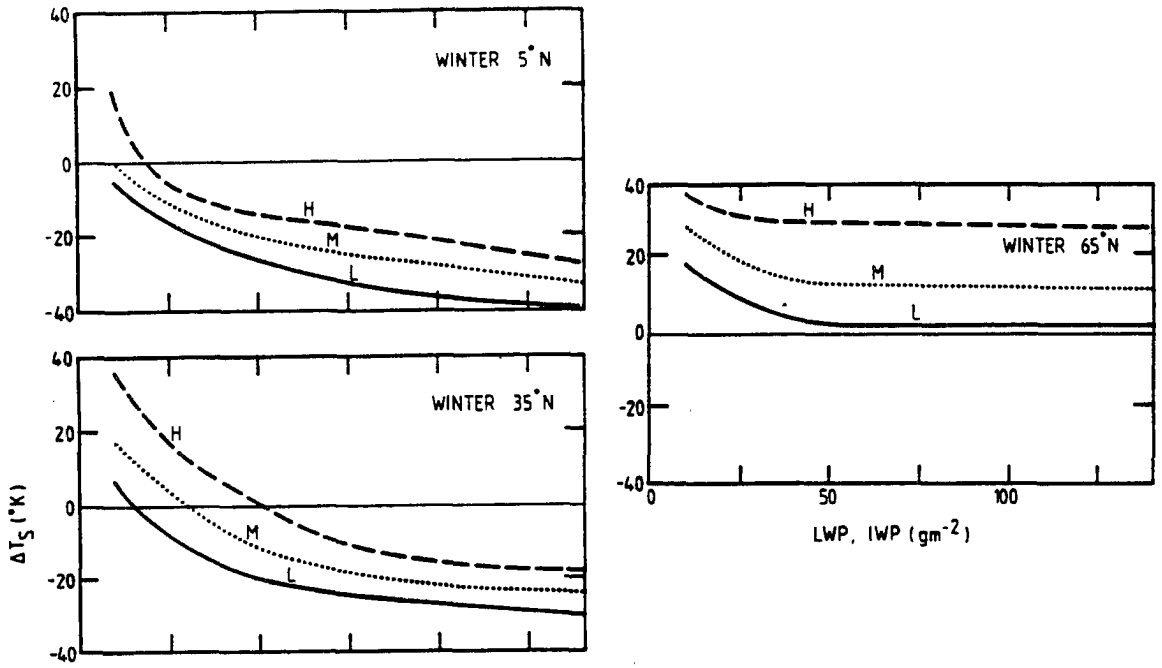

Figure 1.10: . Equilibrium surface temperature differences (ΔT_s) between clear and overcast conditions as a function of water or ice-water path ($\frac{g}{m^2}$) for three cloud layers. Results for 5, 35, and 65°N in winter are shown with a surface albedo of 0.102 (from Stephens and Webster (1981)).

Thus, cirrus clouds, due both to their location and physical makeup, appear in our current understandings to possess the optimum potential for producing this warming effect.

1.2 Cirrus Clouds and their Special Challenges

Cirrus clouds, along with their categorical cousins, cirrocumulus and cirrostratus, are common high level clouds which are reasonably well distributed globally. To the observer they appear thin and fibrous and can take on shapes of anything from thin sheets to cumuliform scales to fibrous strands or hooks. They tend to occur in regions of convective activity or to a lesser extent regions of low-level convergence and tropospheric upward motion. Barton (1983) provided a satellite-based detection of high-level clouds, some of the results of which are presented in figures 1.4 and 1.14. From figure 1.4 the intense convective activity of the ITCZ is visible as well as cloud cover minima at around 30 ° N and S clearly associated with the subtropical ridges. Maxima are seen again at latitudes of about 40 ° associated with midlattitude baroclinic storms. The maximum in the tropics is particularly of interest based on the reported capability of tropical cirrus to produce the tropospheric

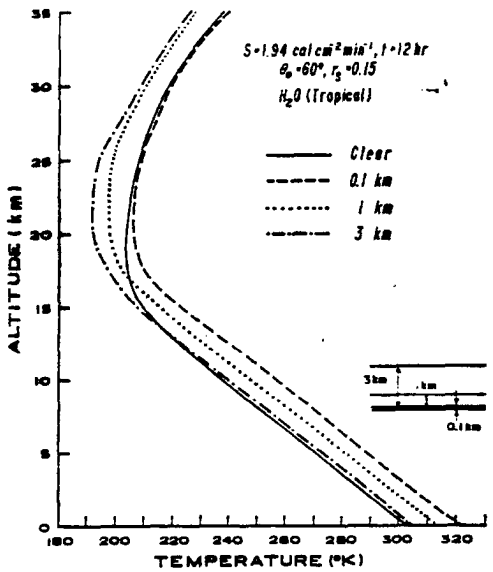

Figure 1.11: . Effects of the cloud thickness (or IWP) on the thermal equilibrium temperature. The cloud base is set at 8 km (from Liou and Gebhart (1982)).

warming. Figure 1.14 reveals that these tropical high clouds are particularly favored in the regions of New Guinea and Southeast Asia. Monsoonal maxima can also be observed in the regions of central South America, West-Central Africa, and parts of China and Southeast Asia. They are particularly uncommon in Central Australia as well as in the Sahara Desert and South Africa. They are definitely a worldwide and seasonwide phenomena employing a widespread degree of opportunity for observation and study.

In addition, there is existing evidence that the amount of cirrus cloudiness may be increasing in certain areas due to added moisture from subsonic commercial jet aircraft contrails. Figure 1.15 from Machta and Carpenter (1971) shows the results of a study in which increases in high cloud cover over Denver, Colorado were compared with increases in jet fuel consumption over time. A correlation was discovered, and although a number of reservations were made concerning the results, especially with respect to the establishment of a causal link, the authors conclude that these findings point to the need for further attention and study of cirrus.

More recently, satellite studies performed by Wylie et al. (1994) have detected a slight upward trend in the global average high cloud cover from June, 1989 to April, 1993. In

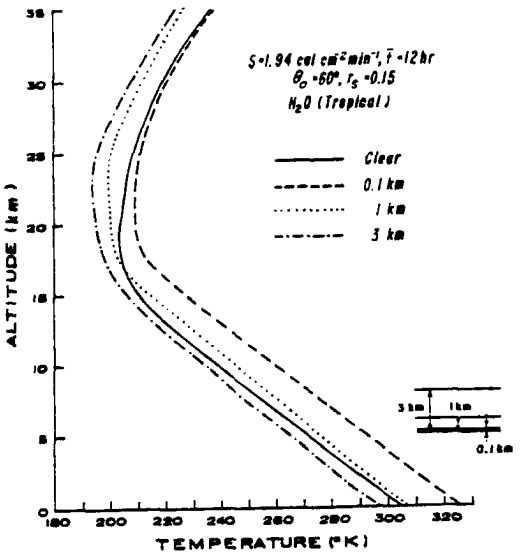

Figure 1.12: . Same as in figure 1.11 but for a cloud base of 5 km (from Liou and Gebhart (1982)).

addition, strong increases in cirrus cloud cover were found from comparing two one-year periods (June, 1990 - May, 1991 and June, 1991 - May, 1992), which suggested a connection to the 1991-92 ENSO event which began in April, 1991 as well as the Mount Pinatubo eruption of June, 1991. Again, the need for further study was indicated.

Towards this end, however, the study of cirrus has raised some unique difficulties. One difficulty is that, as was previously discussed, these clouds are much higher and less optically thick than most other cloud phenomena. This presents some challenges in observation and detection, as cirrus are sometimes even sub-visual, as well as challenges in modeling, since the assumption of complete infrared blackness cannot be assumed for cirrus clouds as it can for most other cloud types, a fact mentioned in the previous section and discussed in Barton (1983).

As has been discussed before, the issue of surface warming or cooling reduces to two factors of shortwave albedo and longwave emissivity, two variables which must be analyzed in tandem and their relative strengths assessed. It is at this point, however, that considerable uncertainties may exist, as the current understanding of the behavior of these two parameters with respect to each other and to IWP is uncertain at best. In Stephens and

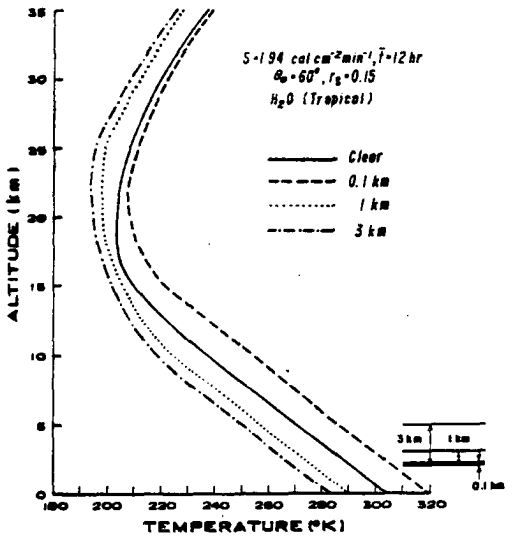

Figure 1.13: . Same as in figure 1.11 but for a cloud base of 2 km (from Liou and Gebhart (1982)).

Webster (1981) the longwave emissivities were calculated based on what is admittedly a somewhat dubious relationship to IWP. In Ou and Liou (1984) a relationship between these two unknowns was postulated in their two dimensional modeling of the global sensitivity to cirrus cloud radiative properties (figure 1.15).

The source of the problem lies in the current knowledge of the scattering properties of the particles that inhabit these clouds, or lack thereof. Stephens (1984a) lists this information as being the primary source of uncertainty associated with the incorporation of clouds into current radiative transfer algorithms of general circulation models. This was supported by the findings of Stephens et al. (1990) which listed the climatic influence of cirrus to be especially sensitive upon one such portion of this information, the asymmetry parameter g. It is this parameter, plus two others, which are used to depict the radiative forcing of clouds in general circulation models. Since these are, thus, a primary focus of this study, it serves us to define and describe these quantities. They are:

1. *The Extinction Efficiency,* Q_{ext}, or sometimes in remote sensing applications referred to as δ. On an individual particle level this quantity is related to a second quantity

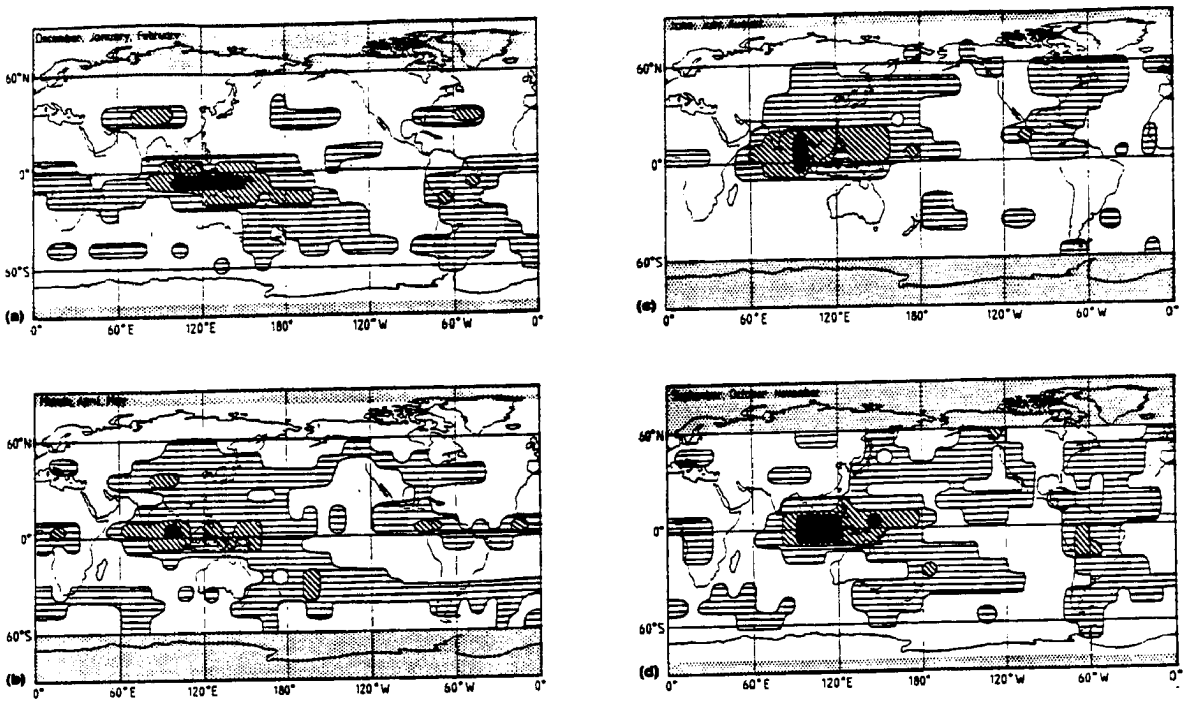

Figure 1.14: . Distribution of high clouds for (a) DJF; (b) MAM; (c) JJA; and (d) SON. Dark areas denote regions of greater than 60 percent cloud cover; diagonal lines, greater than 40 percent; horizontal lines, greater than 20 percent; clear, less than 20 percent; shaded, no observations (from Barton (1983)).

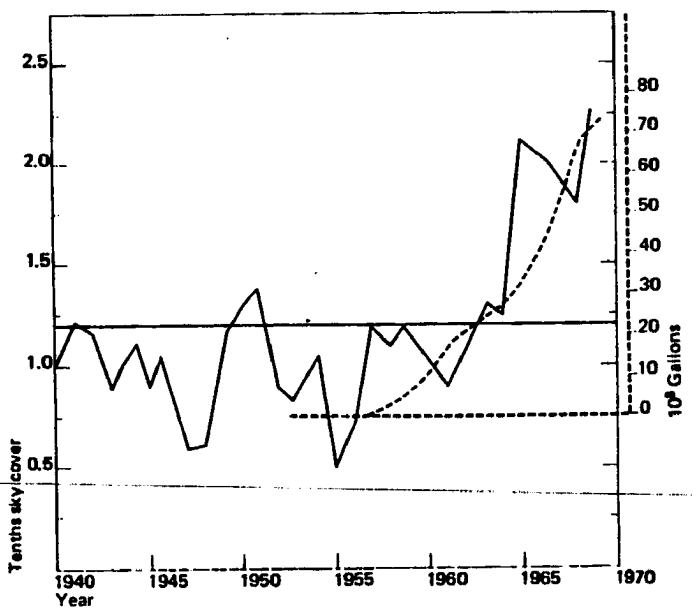

Figure 1.15: . The history of the annual high cloudiness at Denver, Colorado. The dashed line shows the growth in jet fuel consumption by domestic commercial jet aircraft (from Machta and Carpenter (1971)).

which describes the amount of incident radiation which is affected by the particle's presence. This quantity, known as the extinction cross section C_{ext}, expresses this radiation amount in terms of a cross sectional area of the incident beam. The extinction efficiency renormalizes this area, relating it to the geometric cross sectional area of the scattering particle. For spheres this is simply:

$$Q_{ext} = \frac{C_{ext}}{\pi a^2}$$

where a is the radius of the sphere. In atmospheric radiative transfer this quantity is taken from a distribution of particles towards the calculation of a macroscopic version of this quantity known as the optical depth, τ, which can be defined based on the following equation:

$$I_0' = I_0 e^{-\tau}$$

where I_0' and I_0 are, respectively, the intensity of the direct solar beam at a given level and at the top of the atmosphere.

2. *The Single Scatter Albedo, ω_0.* There are two ways in which the radiation incident on a particle can be affected. These are absorption and scattering. Working alongside Q_{ext}, which governs the amount of extinction, ω_0 determines the degree to which either of these processes is contributing to this total. For individual particles it is usually calculated according to the equation:

$$\omega_0 = 1 - \frac{Q_{abs}}{Q_{ext}}$$

where Q_{abs} is defined in a similar fashion to Q_{ext} but for only the amount of radiation which is absorbed by the particle. Thus, a value of 1 indicates that the particle is only scattering radiation, and a value of 0 indicates only absorption. This quantity is, of course, instrumental in atmospheric radiative transfer towards the calculation of absorption and radiative heating rates.

3. *The Asymmetry Parameter, g.* With the amounts of extinction and absorption determined, we need only find a way to describe the scattering. In multi-stream modeling and especially in cases of remote sensing and Monte Carlo modeling this task requires

a somewhat extensive depiction of what is known as the 'phase function', $P(\theta)$, which gives a complete distribution of the scattered energy as a function of the scattering direction. (θ here describes the angle between the incident and scattered beams.) However, in more large scale models this becomes impractical, and, thus, the phase function is parameterized into a single quantity, the asymmetry parameter, which is defined thus:

$$g = \int_0^{\pi} P(\theta) \cos\theta d\theta$$

When g is 1, all of the scattered energy is scattered into the forward hemisphere. When g is -1, all of the scattered radiation is being reflected into the backward hemisphere. When g is zero, the particle is scattering equally in these two hemispheres. Generally for most particles g is between about .6 and .9, indicating a predominance of scattering into the forward scattering hemisphere. In large scale radiative transfer models this quantity, of course, governs the movement within clouds of previously scattered radiation, also known as 'diffuse' radiation. With a negative g for the cloud particle distribution mostly backscattering is occurring, and with a positive g, again the more realistic case, most of the radiation is scattered in the forward direction.

It is these three quantities to which we limit the scope of this research, the pursuit of which for the remainder of this work we will lump together as one term - 'scattering results'.

Looking to the theoretical side for information on these three quantities, previous studies have come across the second unique difficulty associated with cirrus clouds, the shape of the ice particles that inhabit them. Unlike the shapes of water-droplet cloud particles, which are more-or-less spherical, the ice particles in cirrus clouds in their simplest form will most often take the shape of hexagonal plates and columns, and, unlike in the case of spheres and infinitely long cylinders where consummate exact solutions governing their scattering properties exist, the necessary solution of Maxwell's equations on particles of the shapes of those existing in cirrus clouds has not yet been done. Only approximate techniques exist for the solution of the scattering off of such particles.

The governing theory in the case of spheres is formally known as the Lorentz-Mie-Debye theory and is commonly called Mie theory. The similar solution for infinite cylinders

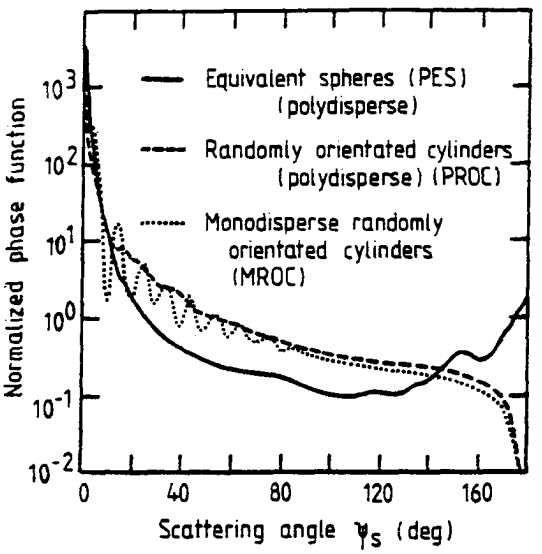

Figure 1.16: . Normalized phase function results for a given size distribution of polydisperse equivalent spheres (PES), a polydisperse size distribution of randomly oriented cylinders (PROC), and a distribution of randomly oriented cylinders of a single size (MROC) (from Stephens (1980)).

will be discussed in chapter 2. For now it is enough for us to refer the reader to figure 1.16, from Stephens (1980), which illustrates differences in the scattering phase functions between distributions of spheres and infinite cylinders, and to simply verbalize its point - the scattering results for a given particle distribution appear to possess at least some dependence upon particle shapes.

1.3 Overview of Scattering Theories

With respect to finding the scattering results for cirrus particles using approximate techniques, it is in a brief discussion of many of the available approximate methods that this section begins its scope. For the sake of employing the best possible tools for this investigation, it is prudent to, first, begin with a 'bird's eye' view of many of the methodologies which may or may not be applicable here. For the sake of discussion these have been divided into four sets, shown in figure 1.17, which are separated according to the ultimate origin of the approximations utilized.

Mie Methods
Equivalent Spheres
Infinite Cylinders

Rayleigh Methods
Rayleigh-Gans
The Discrete Dipole Approximation

Geometric Methods
Geometric Optics
The Airy Approximation
Anomalous Diffraction Theory

Other Methods
Point Matching
Perturbation Methods
Method of Continuous Distribution of Ellipsoids

Figure 1.17: . Diagram of scattering solution methodologies.

The first set has been entitled the Rayleigh Methods. Ultimately involving Rayleigh scattering approximations, these methods employ a 'divide and conquer'-type approach which utilizes a numerical scheme to depict the relevant particle as a summation of particles small enough to be effectively approximated as simple Rayleigh dipole scatterers. As a result, these techniques are by nature more suited to scattering by small particles, since larger particles require an increased number of dipoles. Among these techniques are the Rayleigh-Gans Theory and the Discrete Dipole Approximation (DDA).

The second set, Geometric Methods, has its roots, by contrast, in some of the stipulations associated with geometric optics. By this it is meant that the formulations of ray tracing and Fraunhofer diffraction can be utilized. Ultimately this implies an assumption that the particle is large enough that the aforementioned techniques can be utilized with minimal error. Among these are the Airy Approximation and the Anomalous Diffraction Theory (ADT).

The third set, the Mie Methods, really only has two such elements other than Mie Theory itself, the method of Equivalent Spheres, which is simply the approximation often made in cirrus cloud simulations that the scattering properties of any arbitrary particle can

be approximated by the scattering properties of a sphere of equivalent volume, and what is being called here the method of Infinite Cylinders, which analogously assumes in the case of cylindrical scatterers that the cylinders are acting as infinitely long cylinders.

The fourth and final set is a miscellaneous category, mostly involving various mathematical techniques. Among them are Point Matching and Perturbation Methods, which are well-developed but quite limited in their applicability. In addtion, the Method of a Continuous Distribution of Ellipsoids proceeds under the quite correct assumption that much of the fine structure found in individual particle scatterings is lost, or smoothed out, when a summation over a particle size distribution is performed. Thus, it seeks to find the solution for an arbitrary particle distribution in an equivalent distribution of ellipsoidal particles, of which a relatively quick analytical solution is obtainable. This method, though only in its early stages of development, appears by the author to hold some future promise.

As a result of this introductory analysis, it is observable that a study of optimum applicability and comprehensiveness will invoke the usage of the Discrete Dipole Approximation for the scattering simulations of smaller size parameters and the Anomalous Diffraction Theory for the larger size parameter scattering events. In addition, as an added result, in the size parameter regions where results are obtained for both methods, their results will be compared.

A further comparison with the methods of Equivalent Spheres and Infinite Cylinders is also justified, and in mentioning this the reader is immediately approached with two of the objectives that this study wishes to address. The comparison with infinite cylinders will seek to uncover some of the required length-to-diameter ratios which enable the cylinder to sufficiently behave as an infinite cylinder. Following this same idea, the comparison with equivalent volume spheres will investigate the range of scattering results found with particles having identical volumes and will theorize as to the biases introduced by utilizing equivalent volume spheres when dealing with cylindrical particles.

At this point a self-imposed limitation of this work should be noted; that is, only the scattering effects of circularly-based cylindrical particles will be considered. The added effects associated with changes in the shape of the basal faces as well as the modification of a column to a bullet or a plate into a stellar/dendritic crystal is left to a subsequent

analysis. With this in mind the dimensions of a crystal are reduced to two figures, the volume and the ratio of length-to-diameter, herein defined as the aspect ratio.

1.4 Observed Cirrus Particle Aspect Ratios

As was stated before, the ice particles in cirrus clouds in their simplest form will most often take the shape of hexagonal plates and columns, and although plenty of studies have been performed to observe the general sizes of these crystals, the amount of existing information concerning their aspect ratios is currently somewhat limited, although the recent acquisition of data from the Second FIRE Experiment in 1991 should serve to provide a more accurate source of data on the subject. As of the time of this work the most complete source of aspect ratio information is found in the chart shown in figure 1.18 from Heymsfield (1972). The chart shows information concerning the dimensions of observed cirrus ice crystals as a function of the length of a single dimension. Empirical relationships are given for crystals of various types. Figure 1.19 from Yamashita (1973) shows the mean dimensions of seeded trigonal and hexagonal crystals. Note that the dashed and solid line peaks at -5 and -15°C reveal the existence of hexagonal columns around -5°C and hexagonal plates around -15°C.

The combination of figures 1.18 and 1.19 show the general temperature ranges which may be the most relevant. The Yamashita peak at -5°C confirms the -4 to -6°C temperature range of needles given by Heymsfield. The temperature ranges given for plates, dendrites, and stellars reveal that, although the thinnest platelike crystals occur in the center of the -15°C peak, actual non-dendritic plates only form on the 'wings' of the peak, between -10 and -13°C as well as -17 and -20°C. The top of the chart reveals that columns with aspect ratios close to 1 are found between -8 and -10°C, and that column-like crystals are found between -18 and -20°C, a finding not echoed by the Yamashita curves. Perhaps these columns are found among crystals with non-hexagonal bases. The most relevant temperature ranges are, thus, from -4 to -13°C, where the aspect ratios go from those of long columns to thin plates, as well as from -17 to -20°C, where plates and columns are apparently found in tandem.

CRYSTAL TYPE	WIDTH [mm]	TEMPERATURE RANGE	INVESTIGATOR
BULLET	$0.25L^{.7856}$ [mm] $L \leq 0.3$mm	-18 to -20C	Heymsfield
	$0.185L^{.532}$ [mm] $0.3\text{mm} \leq L$		
COLUMN	$0.5L$ [mm] $L \leq 0.3$mm	-18 to -20C	Heymsfield
	$0.1973L^{0.414}$ [mm] $0.2\text{mm} \leq L$	-18 to -20C -8 to -10C	Heymsfield Auer and Veal (1970)
PLATE	$0.0449D^{.449}$ [mm]	-10 to -13C -17 to -20C	Auer and Veal (1970)
DENDRITE STELLAR	$0.0379D^{.377}$ [mm] $.0398D^{.431}$ [mm]	-13 to -17C	Auer and Veal (1970)
NEEDLE	$0.0746L^{.61078}$ [mm]	-4 to -6C	Auer and Veal (1970)

Figure 1.18: . Relationships between length and width for different crystal forms (from Heymsfield (1972)).

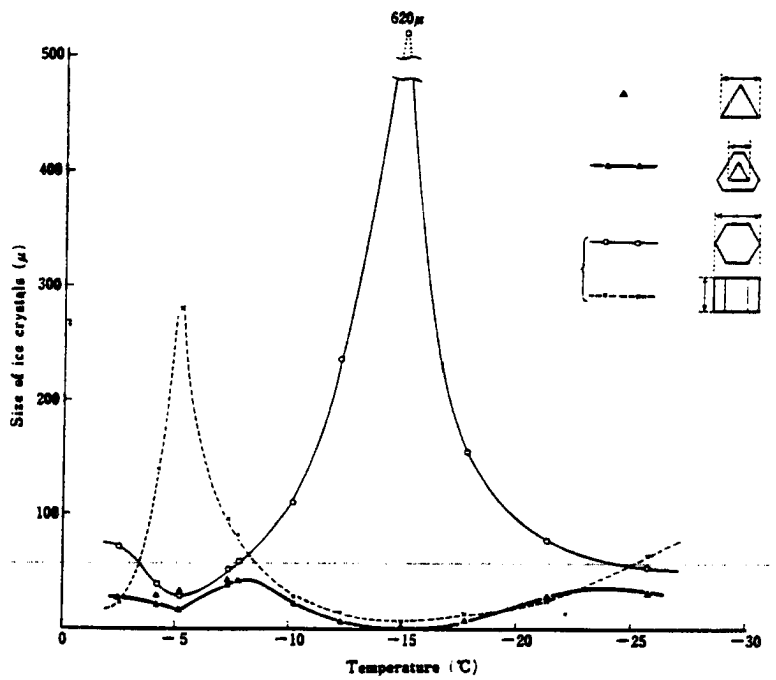

Figure 1.19: . Dimensions of ice crystals obtained by seeding at various temperatures. In particular note the bottom two lines in the key which respectively correspond to the mean sizes of the a and c axes of the hexagonal ice crystals (from Yamashita (1973)).

Figure 1.20: . Slide taken on 26 Nov 1991 flight during FIRE II.

Figure 1.21: . Slide taken on 5 Dec 1991 flight during FIRE II.

Sadly, although at first the information from these sources may at first appear to be helpful, the temperature ranges given here are much warmer than the -30 to $-60°$ C temperatures commonly observed in cirrus clouds. Thus, we are compelled by a lack of additional information into assuming that this wide range of particle aspect ratios also extends to cirrus clouds. This is not unreasonable, since plates and columns have also been observed in cirrus. Although the microphysical FIRE II data has not yet been through rigorous analysis, some example micro-photographs of the data can be shown. An example of columns with rather large aspect ratios can be seen in figures 1.20 and 1.21. The aspect ratios of the particles in figure 1.20 were measured directly on the photographs by the author to be between 2.2 and 6.3, assuming that all the particles measured were columns (i.e., not plates sitting on edge). Similar aspect ratios for figure 1.21 were measured to be between 1.7 and 3.3. An example of a hexagonal plate can also be seen in the upper left portions of figures 1.20 and 1.21. Columns with smaller aspect ratios (near 1) can be visible in figures 1.22 and 1.23. Aspect ratios were measured in figure 1.22 to be between 1.5 and 2.7 and in figure 1.23 to be between 1.1 and 2.7, again, assuming them not to be disks on edge. All in all, a wide range is observed, warranting this study.

1.5 Objectives of this Research

With the above findings in mind it becomes clear that an investigation into the sensitivity of the scattering properties of cirrus cloud particles is both warranted and feasible. As was stated before, this study operates from the assumption that one can arrive closer to the scattering properties of actual cirrus particles by treating them as a simple conglomerate of circular cylinders and disks, the dimensions of which can be varied within set bounds. The dependence of the scattering properties upon changes in the size and aspect ratio will be determined using two models employing the Discrete Dipole Approximation and the Anomalous Diffraction Approximation, respectively. This should begin to provide the necessary information for a subsequent two-stream radiative transfer model in which cirrus heating rates and radiative cloud forcings can be calculated.

Chapter 2 will provide a review of the previous work associated with scattering on cylinders as well as verifications of the accuracies of two models, one from Bohren and

Figure 1.22: . Slide taken on 26 Nov 1991 flight during FIRE II.

Figure 1.23: . Slide taken on 26 Nov 1991 flight during FIRE II.

Huffman (1983) and one from Flatau (personal communication), which give results for infinite cylinders. Chapter 3 will investigate the scattering properties of finite cylinders and disks using a model which employs the DDA. Similarly, chapter 4 will do the same but with a different model, one which employs ADT. Both the DDA and ADT models are those which are developed and discussed in Flatau (1992). Chapter 4 will, in addition, compare the results of both models with each other to examine the instances in which the use of the ADT model is most or least appropriate as well as to gain insight into some of the mechanisms involved in the scattering processes. The result of all these analyses yields not only a large degree of qualitative information discussed in the chapters, but also a voluminous supply of quantitative information which is displayed in a myriad of appendices. Briefly, Appendices A, B, and C show the entirety of the results for Q_{ext}, ω_0, and g, respectively. They will be most valuable to those researchers, most likely from outside the field of atmospheric radiative transfer, who may have a particular interest in the scattering results of individual particles. In addition, Appendices D, E, and F show a series of tabulated results, correction factors which make the rapid calculation of cylinder results from previously existing sources more feasible. It is these correction factors which will prove most useful in an application of these results to the distributions of particles found in the modeling of clouds and climate. Chapter 5 will close with a summary and conclusions.

Finally, before proceeding a few additional definitions and distinctions should be made. When the term 'equivalent sphere' is used in this work, what is meant is an equivalent *volume* sphere, not an equivalent area sphere. It represents a sphere which possess the same volume as the cylinder/disk, and is the only type of equivalent sphere approximation investigated in this study. Secondly, in all of our analyses we refer to the cylinder/disk radius as r_{cyl}, the cylinder/disk axial length as L, and the radius of an equivalent sphere as a_{eff}. Using this terminology, we formally define the aspect ratio, β, as:

$$\beta = \frac{L}{2r_{cyl}}$$

where $\beta < 1$ indicates a disk and $\beta \geq 1$ defines a cylinder. With this in mind, we should also point out that, since cylinders and disks are actually parts of the same β continuum, one which is explored to both extremes by this work, the reader will find the term 'cylinder'

used in this work somewhat loosely, often to describe this entire continuum of cylinders and disks. This should not, however, cause any confusion, since the context of each usage should make it clear as to which definition is appropriate.

Chapter 2

PREVIOUS WORK ON CYLINDER SCATTERING

The problem of electromagnetic scattering on cylindrical particles is a problem which has been pursued mathematically for almost a century. It has been a problem of a multi-faceted nature, which has come from the variety of fields to which applications of such a study are possible. In this section we wish to explore the history of this problem and in the process to give a contemporary 'roll call' of previous findings which hopefully will be as comprehensive as necessary.

This discussion has three obvious delineations; these are:

- Infinite cylinder studies, in which theoretical solutions are given,
- Observational studies on finite cylinders, and
- Theoretical solutions to the finite cylinder problem.

For now, however, we will be forced to postpone the discussion of the last of these three. This will be saved for chapters 3 and 4.

2.1 The Infinite Cylinder Problem

The problem of electromagnetic scattering on an infinitely long cylinder was first solved by Lord Rayleigh (1881 and 1918) . Van de Hulst (1957) also gave a concise description of the solution as well as Bohren and Huffman (1983). Any of these aforementioned papers can be consulted for a version of the derivation; the derivation is presented here in its entirety and using a variety of techniques and notations to give a more intensive and comprehensive description of the solution.

There are generally five steps for determining the scattering properties of an infinite cylinder, or, for that matter, any particle for which exact analytical solutions are possible. These are:

1. *The introduction of the basic equations associated with the scattering wave.* (These are, of course, Maxwell's equations in the case of electromagnetic scattering.) This results in a derivation of a vector and a scalar wave equation.

2. *The application of the scalar wave equation to a chosen coordinate system, and the solution of three separate equations from the wave equation solution.* This coordinate system must be chosen such that the surface of the particle lies on a surface in which one of the independent variables is a constant. Since this severely limits the shapes for which solutions can be derived, this step, in effect, chooses the shape of the particle for which the solutions will be solved. For a Cartesian coordinate system, this is a planar surface of discontinuity; for a spherical coordinate system, this is a sphere; and for a cylindrical coordinate system, this is an infinitely long cylinder. The solution comes from an assumption that mathematically it is separable in the three variables in the coordinate system. This results in three sets of solution functions for each of the independent coordinate system variables. These are then combined together into a complete set of three dimensional harmonics which form a basis for both the depiction of the incident wave and the scattered waves.

3. *The expression of the incident wave in terms of the solution functions.* This is generally the most difficult step.

4. *The imposition of the boundary conditions found at the surface of the particle and, in some cases, at the center of and at far away distances from the particle.*

5. *The expression of the internal and scattered waves through the derivation of appropriate expressions for the coefficients of the solution functions.* These expressions will be functions of the refractive index of the particle relative to the outside medium as well as the particle size relative to the size of the radiation wavelength.

We will now apply this technique to the infinite cylinder.

Step 1. First introducing Maxwell's Equations applied to a vacuum, we have:

$$\nabla \cdot \mathbf{E} = 0 \tag{2.1}$$

$$\nabla \cdot \mathbf{B} = 0 \tag{2.2}$$

$$\nabla \times \mathbf{E} = -\frac{\partial \mathbf{B}}{\partial t} \tag{2.3}$$

$$\nabla \times \mathbf{B} = \frac{1}{c^2}\frac{\partial \mathbf{E}}{\partial t} \tag{2.4}$$

Taking the curl of equation 2.3 and substituting equation 2.4:

$$\nabla \times \nabla \times \mathbf{E} = -\frac{\partial}{\partial t}(\nabla \times \mathbf{B}) = -\frac{1}{c^2}\frac{\partial^2 \mathbf{E}}{\partial t^2}$$

and employing the following vector identity along with equation 2.1:

$$\nabla \times \nabla \times \mathbf{E} = \nabla(\nabla \cdot \mathbf{E}) - \nabla^2 \mathbf{E} = -\nabla^2 \mathbf{E} \tag{2.5}$$

we arrive at what is known as the vector wave equation:

$$\nabla^2 \mathbf{E} - \frac{1}{c^2}\frac{\partial^2 \mathbf{E}}{\partial t^2} = 0 \tag{2.6}$$

which is an equation for a three-dimensional wave propagating at speed c. Similar operations can be done for $\mathbf{B}$. This, of course, reveals that light is a wave-like phenomenon and gives us permission to prescribe a wavelike solution:

$$\mathbf{E} = \mathbf{E}_0 e^{i(\mathbf{k}\cdot\mathbf{r} - \omega t)} \tag{2.7}$$

which, upon substitution to equation 2.6, yields a second version of the vector wave equation, one which we will use:

$$\nabla^2 \mathbf{E} - \frac{1}{c^2}\frac{\partial^2 \mathbf{E}}{\partial t^2} = \nabla^2 \mathbf{E} + k^2 \mathbf{E} = 0 \tag{2.8}$$

where we are considering $\mathbf{r}$ to be in the direction of $\mathbf{k}$ and $k = |\mathbf{k}| = \frac{\omega}{c}$.

We prescribe a set of solutions for $\mathbf{E}$ and $\mathbf{B}$, respectively, based on a given scalar function Ψ, and a vector $\mathbf{c}$ whose properties we will examine later:

$$\mathbf{M} = \nabla \times (\mathbf{c}\Psi) \tag{2.9}$$

$$\mathbf{N} = \frac{\nabla \times \mathbf{M}}{k} \tag{2.10}$$

This prescription is valid in that it satisfies equations 2.1 and 2.2, since:

$$\nabla \cdot (\nabla \times \mathbf{A}) = 0 \tag{2.11}$$

for any vector **A**. In addition,

$$\nabla \times \mathbf{N} = \frac{1}{k}\nabla \times (\nabla \times \mathbf{M}) = \frac{1}{k}\left[\nabla(\nabla \cdot \mathbf{M}) - \nabla^2\mathbf{M}\right] = -\frac{1}{k}\nabla^2\mathbf{M} \sim k\mathbf{M}$$

where equation 2.5 has been used. Thus, the curl of **M** is proportional to **N** and vice-versa, thereby satisfying equations 2.3 and 2.4. Equations 2.9 and 2.10, therefore, are sufficiently of the same form as the electric and magnetic fields in Maxwell's equations. Substituting **M** into equation 2.8 we first note that, for any vector **A**:

$$\begin{aligned}\nabla^2[\nabla \times \mathbf{A}] &= \nabla^2\left[\frac{\partial A_z}{\partial y} - \frac{\partial A_y}{\partial z}\right]\mathbf{i} + \nabla^2\left[\frac{\partial A_x}{\partial z} - \frac{\partial A_z}{\partial x}\right]\mathbf{j} + \nabla^2\left[\frac{\partial A_y}{\partial x} - \frac{\partial A_x}{\partial y}\right]\mathbf{k} \\ &= \begin{vmatrix} \mathbf{i} & \mathbf{j} & \mathbf{k} \\ \frac{\partial}{\partial x} & \frac{\partial}{\partial y} & \frac{\partial}{\partial z} \\ \nabla^2 A_x & \nabla^2 A_y & \nabla^2 A_z \end{vmatrix} = \nabla \times \left(\nabla^2\mathbf{A}\right).\end{aligned} \tag{2.12}$$

Applying this to the vector wave equation we have:

$$\begin{aligned}\nabla^2\mathbf{M} + k^2\mathbf{M} &= \nabla^2[\nabla \times (\mathbf{c}\Psi)] + k^2[\nabla \times (\mathbf{c}\Psi)] \\ &= \nabla \times \left[\nabla^2(\mathbf{c}\Psi)\right] + \nabla \times \left(k^2\mathbf{c}\Psi\right) \\ &= \nabla \times \mathbf{c}\left[\nabla^2\Psi + k^2\Psi\right] + \nabla \times (\Psi\nabla^2\mathbf{c}),\end{aligned} \tag{2.13}$$

and, for reasons which will be discussed in a moment, the object now becomes that of making the second term on the right hand side zero. Since:

$$\nabla \times (\Psi\nabla^2\mathbf{c}) = \nabla\Psi \times \nabla^2\mathbf{c} + \Psi\nabla \times \nabla^2\mathbf{c},$$

if we are to make no limitations on Ψ, this requires that the Laplacian of **c** must be zero:

$$\nabla^2\mathbf{c} = \left\{\nabla^2 c_x, \nabla^2 c_y, \nabla^2 c_z\right\} = \{0, 0, 0\} \tag{2.14}$$

The attraction of making the second term in equation 2.13 zero comes from the expression inside the brackets of the first term. This expression, when set to zero, forms a scalar

version of our vector wave equation, thus simplifying our solution process for the moment into this scalar wave equation.

Thus, the conclusion is that a sufficient condition for the vector wave equation to be satisfied for M:

$$\nabla^2\mathbf{M} + k^2\mathbf{M} = 0 \tag{2.15}$$

is that the following equation, known as the 'scalar wave equation', be satisfied:

$$\nabla^2\Psi + k^2\Psi = 0 \tag{2.16}$$

provided that vector **c** satisfies equation 2.14.

With simplicity in mind, several possible candidate vectors for **c** are available:

$$\mathbf{e}_x \quad \mathbf{e}_y \quad \mathbf{e}_z \quad \mathbf{x} \quad \mathbf{y} \quad \mathbf{z} \quad \mathbf{e}_{r_s} \quad \mathbf{e}_{\theta_s} \quad \mathbf{e}_\phi \quad \mathbf{r}_s \quad \mathbf{r}_c \quad \mathbf{e}_{r_c} \quad \mathbf{e}_{\theta_c}$$

where the s and c subscripts denote spherical and cylindrical coordinate systems, respectively. Using $\mathbf{r}_s$ as an example, we have:

$$\mathbf{r}_s = x\mathbf{e}_x + y\mathbf{e}_y + z\mathbf{e}_z$$

Equation 2.14 is clearly satisfied here:

$$\frac{\partial^2}{\partial x^2}(x) = 0 \quad \frac{\partial^2}{\partial y^2}(y) = 0 \quad \frac{\partial^2}{\partial z^2}(z) = 0$$

In the same way **x**, **y**, and **z** have zero Laplacians. The corresponding unit vector of $\mathbf{r}_s$, however, does not satisfy equation 2.14:

$$\mathbf{e}_{r_s} = \frac{x}{\sqrt{x^2+y^2+z^2}}\mathbf{e}_x + \frac{y}{\sqrt{x^2+y^2+z^2}}\mathbf{e}_y + \frac{z}{\sqrt{x^2+y^2+z^2}}\mathbf{e}_z$$

for the obvious reason of the denominator radicals. In the same way, $\mathbf{e}_{\theta_s}$, $\mathbf{e}_\phi$, $\mathbf{e}_{r_c}$, and $\mathbf{e}_{\theta_c}$ will not work either. The vectors $\mathbf{e}_x$, $\mathbf{e}_y$, and $\mathbf{e}_z$ are, of course, constants, easily satisfying equation 2.14. We are, thus, left with:

$$\mathbf{x} \quad \mathbf{y} \quad \mathbf{z} \quad \mathbf{e}_x \quad \mathbf{e}_y \quad \mathbf{e}_z \quad \mathbf{r}_s \quad \mathbf{r}_c \tag{2.17}$$

We have, therefore, listed eight vectors which will work. Only one of them, $\mathbf{r}_s$, is applicable to a spherical coordinate system, and it is the vector which has always been used for the

application to spherical scatterers. This is, of course, known as Lorentz-Mie-Debye theory, or simply Mie Theory. Note, however, that there are six somewhat redundant vectors - $\mathbf{x}$, $\mathbf{y}$, $\mathbf{z}$, $\mathbf{e}_x$, $\mathbf{e}_y$, and $\mathbf{e}_z$ - which are applicable to the study of an infinite planar surface of discontinuity, and three - $\mathbf{r}_c$, $\mathbf{z}$, and $\mathbf{e}_z$ - which are applicable to the infinite cylinder.

In review, we have introduced the scalar wave equation by demonstrating its applicability to the case of electromagnetic scattering. Note that we have not yet limited ourselves to a particular coordinate system; although equations 2.12 and 2.14 are deduced in Cartesian terms, they are, of course, valid regardless of the system.

Perhaps the largest degree of creativity which is found in an historical examination of this step is in the form of notation. Rayleigh (1881), for example, presents Maxwell's equations in the following form:

$$u = p + \frac{df}{dt}$$

$$4\pi f = KP$$

$$p = CP$$

$$P = -\frac{dF}{dt} - \frac{d\Psi}{dx}$$

$$a = \frac{dH}{dy} - \frac{dG}{dz}$$

$$a = \mu\alpha$$

$$4\pi u = \frac{d\gamma}{dy} - \frac{d\beta}{dz}$$

These are component forms of the vector wave equations which appeared in Maxwell's *Treatise on Electricity and Magnetism* (1873) as follows:

$$\mathcal{C} = \mathcal{R} + \frac{d\mathcal{D}}{dt}$$

$$\mathcal{D} = \frac{1}{4\pi} K\mathcal{E}$$

$$\mathcal{R} = C\mathcal{E}$$

$$\mathcal{E} = V.\mathcal{G}\mathcal{B} - \frac{d\mathcal{U}}{dt} - \nabla\Psi$$

$$\mathcal{B} = V.\nabla\mathcal{U}$$

$$\mathcal{B} = \mu\mathcal{H}$$

$$4\pi\mathcal{C} = V.\nabla\mathcal{H}$$

Translating each of these individually across a century of notational change, we have:

$$\mathcal{C} = \mathbf{J} + \epsilon_0\frac{\partial \mathbf{E}}{\partial t} \tag{2.18}$$

$$\mathbf{P} = \chi_e\mathbf{E} \tag{2.19}$$

$$\mathbf{J} = \sigma\mathbf{E}$$

$$\mathbf{E} = \mathbf{v} \times \mathbf{B} - \frac{\partial \mathcal{U}}{\partial t} - \nabla\phi \tag{2.20}$$

$$\mathbf{B} = \nabla \times \mathcal{U} \tag{2.21}$$

$$\mathbf{H} = \mu\mathbf{B} \tag{2.22}$$

$$\mu_0\mathcal{C} = \nabla \times \mathbf{B} \tag{2.23}$$

where $\mathbf{v}$, $\mathbf{J}$, $\mathbf{P}$, $\mathbf{H}$, ϕ ,ϵ_0 ,χ_e ,σ, μ_0, and μ represent velocity, current density, electric polarization, magnetization, electric potential, permittivity of free space, electric susceptibility, electrical conductivity, and magnetic permeabilities of free space and of a given medium, respectively. The variables $\mathcal{C}$ and $\mathcal{U}$ go by the respective nineteenth century names of 'total current' and 'electrokinetic momentum', the latter term describing the 'momentum' of an electrical current, thereby providing a mechanical explanation for the finite amount of time required for the current in a circuit to 'accelerate' to its stable value once an electromotive force is applied. Taking the curl of equation 2.20 applied to a vacuum, we have:

$$\nabla \times \mathbf{E} = -\frac{\partial}{\partial t}(\nabla \times \mathcal{U})$$

where the first term on the right hand side governing motionally generated electro-motive force becomes inapplicable, and the third term is zero, since $\nabla \times \nabla\phi = 0$ for any scalar function ϕ. Substituting equation 2.21 into the right hand side, this becomes:

$$\nabla \times \mathbf{E} = -\frac{d\mathbf{B}}{dt}$$

thus yielding equation 2.3. Combining equations 2.18 and 2.23 and applying the result to a vacuum, we have equation 2.4:

$$\nabla \times \mathbf{B} = \mu_0 \epsilon_0 \frac{\partial \mathbf{E}}{\partial t} = \frac{1}{c^2} \frac{\partial \mathbf{E}}{\partial t}$$

where we have also been able to pinpoint the speed of electromagnetic radiation, $c = \frac{1}{\sqrt{\mu_0 \epsilon_0}}$. Further, as is demonstrated in van de Hulst (1957), the two remaining Maxwell equations can be derived by first assuming a wavelike solution:

$$\nabla \times \mathbf{E} = -i\omega \mathbf{B}$$

$$\nabla \times \mathbf{B} = \frac{i\omega}{c^2} \mathbf{E}$$

and taking the divergence of both sides. We then have from equation 2.11:

$$-i\omega(\nabla \cdot \mathbf{B}) = \nabla \cdot (\nabla \times \mathbf{E}) = 0 \quad \Rightarrow \quad \nabla \cdot \mathbf{B} = 0$$

$$\frac{i\omega}{c^2}(\nabla \cdot \mathbf{E}) = \nabla \cdot (\nabla \times \mathbf{B}) = 0 \quad \Rightarrow \quad \nabla \cdot \mathbf{E} = 0$$

Rayleigh then derived the scalar wave equation by applying his component form of Maxwell's equations to a simple case of a plane wave obliquely incident on a planar surface. Each individual component was found to obey the scalar wave equation.

Step 2. As was stated before, we will choose the cylindrical coordinate system for the application and solution of the scalar wave equation. In cylindrical coordinates the gradient, divergence, and curl operators take on the following forms:

$$\nabla a = \frac{\partial a}{\partial r}\mathbf{e}_r + \frac{1}{r}\frac{\partial a}{\partial \theta}\mathbf{e}_\theta + \frac{\partial a}{\partial z}\mathbf{e}_z \tag{2.24}$$

$$\nabla \cdot \mathbf{A} = \frac{1}{r}\frac{\partial}{\partial r}(rA_1) + \frac{1}{r}\frac{\partial}{\partial \theta}(A_2) + \frac{1}{r}\frac{\partial}{\partial z}(rA_3) \tag{2.25}$$

$$\nabla \times \mathbf{A} = \frac{1}{r}\left[\frac{\partial}{\partial \theta}(A_3) - \frac{\partial}{\partial z}(rA_2)\right]\mathbf{e}_r + \left[\frac{\partial}{\partial z}(A_1) - \frac{\partial}{\partial r}(A_3)\right]\mathbf{e}_\theta + \frac{1}{r}\left[\frac{\partial}{\partial r}(rA_2) - \frac{\partial}{\partial \theta}(A_1)\right]\mathbf{e}_z \tag{2.26}$$

and, thus, applying this to equation 2.16, the scalar wave equation becomes:

$$\frac{1}{r}\frac{\partial}{\partial r}\left(r\frac{\partial \Psi}{\partial r}\right) + \frac{1}{r^2}\frac{\partial^2 \Psi}{\partial \theta^2} + \frac{\partial^2 \Psi}{\partial z^2} + k^2 \Psi = 0 \tag{2.27}$$

To solve this, we assume that the solution is separable in r,θ, and z:

$$\Psi(r,\theta,z) = R(r)\Theta(\theta)Z(z)$$

Substituting this solution into equation 2.27 and dividing by Ψ we get:

$$\frac{1}{rR}\frac{\partial}{\partial r}\left(r\frac{\partial R}{\partial r}\right) + \frac{1}{r^2\Theta}\frac{\partial^2\Theta}{\partial\theta^2} + \frac{1}{Z}\frac{\partial^2 Z}{\partial z^2} + k^2 = 0 \tag{2.28}$$

we can first separate out the z dependence:

$$\frac{1}{Z}\frac{\partial^2 Z}{\partial z^2} = \mathcal{Z}$$

$$Z = e^{ihz}$$

$$\frac{1}{Z}\frac{\partial^2 Z}{\partial z^2} = \mathcal{Z} = -h^2$$

substituting this $-h^2$ back into equation 2.28 this becomes:

$$\frac{1}{Rr}\frac{\partial}{\partial r}\left(r\frac{\partial R}{\partial r}\right) + \frac{1}{r^2\Theta}\frac{\partial^2\Theta}{\partial\theta^2} + (k^2 - h^2) = 0$$

Multiplying by r^2 and separating out the θ dependence we have:

$$\frac{1}{\Theta}\frac{\partial^2\Theta}{\partial\theta^2} = r^2(h^2 - k^2) - \mathcal{R}$$

$$\Theta = e^{in\theta}$$

$$\frac{1}{\Theta}\frac{\partial^2\Theta}{\partial\theta^2} = -n^2 = r^2(h^2 - k^2) - \mathcal{R}$$

and, thus,

$$\mathcal{R} = r^2(h^2 - k^2) + n^2 = n^2 - \rho^2$$

where $\rho = r\sqrt{k^2 - h^2}$. Substituting into equation 2.28 this becomes:

$$\frac{r}{R}\frac{\partial}{\partial r}\left(r\frac{\partial R}{\partial r}\right) = n^2 - \rho^2$$

or,

$$\rho\frac{\partial}{\partial\rho}\left(\rho\frac{\partial R}{\partial\rho}\right) + (\rho^2 - n^2)R = 0 \tag{2.29}$$

Equation 2.29 is known as Bessel's equation, and the linearly independent solutions to it are the Bessel functions of the first and second kind, J_n and Y_n, where n is an integer.

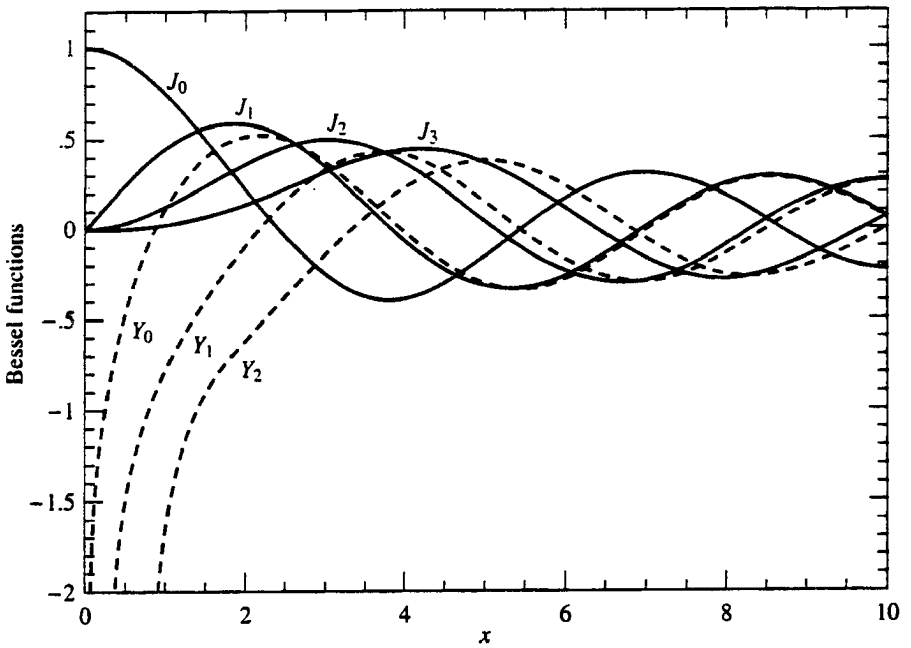

Figure 2.1: . Bessel functions of the first kind, J_n, and second kind, Y_n (from Press et al. (1992).)

These functions are illustrated in figure 2.1, immediately revealing that the Y_n solutions, since they are unbounded at the origin, are not physically useful here. We will, thus, from here on restrain ourselves almost exclusively to the J_n solutions.

One such property of these functions which can be demostrated is orthogonality, which is given from Schubert (personal communication). Assuming two solutions to equation 2.29 exist, J_n and $J_{n'}$, then we can write:

$$\frac{d}{\rho d\rho}\left(\rho\frac{dJ_{n'}}{d\rho}\right)+\left(1-\frac{n'^2}{\rho^2}\right)J_{n'}=0$$

$$\frac{d}{\rho d\rho}\left(\rho\frac{dJ_{n}}{d\rho}\right)+\left(1-\frac{n^2}{\rho^2}\right)J_{n}=0$$

or,

$$-J_n\frac{d}{\rho d\rho}\left(\rho\frac{dJ_{n'}}{d\rho}\right)-\left(1-\frac{n'^2}{\rho^2}\right)J_nJ_{n'}=0$$

$$J_{n'}\frac{d}{\rho d\rho}\left(\rho\frac{dJ_{n}}{d\rho}\right)+\left(1-\frac{n^2}{\rho^2}\right)J_nJ_{n'}=0$$

where total differentials are permissible, since J_n is independent of all variables except ρ. Adding these two equations together and integrating, this becomes,

$$\int_0^\infty\left[J_{n'}\frac{d}{\rho d\rho}\left(\rho\frac{dJ_n}{d\rho}\right)-J_n\frac{d}{\rho d\rho}\left(\rho\frac{dJ_{n'}}{d\rho}\right)\right]\rho d\rho+\left(n'^2-n^2\right)\int_0^\infty J_nJ_{n'}\frac{d\rho}{\rho}=0$$

Since the first term is actually,

$$\int_0^\infty \left[J_{n'} \frac{d}{d\rho}\left(\rho \frac{dJ_n}{d\rho}\right) - J_n \frac{d}{d\rho}\left(\rho \frac{dJ_{n'}}{d\rho}\right)\right] d\rho$$

$$= \int_0^\infty \left[\frac{d}{d\rho}\left(\rho J_{n'} \frac{dJ_n}{d\rho}\right) - \rho \frac{dJ_n}{d\rho}\frac{dJ_{n'}}{d\rho} - \frac{d}{d\rho}\left(\rho J_n \frac{dJ_{n'}}{d\rho}\right) + \rho \frac{dJ_n}{d\rho}\frac{dJ_{n'}}{d\rho}\right] d\rho$$

$$= \int_0^\infty \left[\frac{d}{d\rho}\left(\rho J_{n'} \frac{dJ_n}{d\rho}\right) - \frac{d}{d\rho}\left(\rho J_n \frac{dJ_{n'}}{d\rho}\right)\right] d\rho$$

$$= \rho J_{n'} \frac{dJ_n}{d\rho}\bigg|_0^\infty - \rho J_n \frac{dJ_{n'}}{d\rho}\bigg|_0^\infty$$

and both of these terms are zero, since J_n and its derivatives are finite at the origin, and:

$$\lim_{\rho \to \infty} J_n(\rho) = \lim_{\rho \to \infty} \frac{dJ_n}{d\rho} = 0 \quad \forall \quad n$$

We are then left with,

$$\left(n'^2 - n^2\right) \int_0^\infty J_n J_{n'} \frac{d\rho}{\rho} = 0 \tag{2.30}$$

and so, if $|n| \neq |n'|$, then the following orthogonality relation is true:

$$\int_0^\infty J_n J_{n'} \frac{d\rho}{\rho} = 0 \tag{2.31}$$

In addition, it is important to point out the following two Bessel function identities:

$$Z_n'(\rho) = -Z_{n+1}(\rho) + \frac{n}{\rho} Z_n(\rho) \quad \forall \quad \rho, n \tag{2.32}$$

$$Z_{n-1}(\rho) - Z_{n+1}(\rho) = 2Z_n'(\rho) \quad \forall \quad \rho, n \tag{2.33}$$

where Z_n is used to indicate that these identities apply to both functions, J_n and Y_n. We will make use of these identities later.

Thus, with these Bessel functions as well as the functions which govern the Θ and Z dependencies, we arrive at the following solution:

$$\Psi_n = J_n(\rho) e^{in\theta} e^{ihz} \quad (n = 0, 1, 2, ...)$$

There are three independent variables associated with this solution. These are, first, n, which covers the θ dependence; the wavenumber, k, which is implicit in ρ and covers the radial dependence; and the separation constant, h, which covers the z dependence. The separation constant h will be determined once the incident field is known, and we will find

that it possesses a dependence on k, which is intuitively reasonable since oscillations in the r and z directions should bear some relationship to each other based on the direction of the incident radiation. Thus, we find two truly independent variables, n and k. Only n, however, is shown as a subscript to Ψ since only n is discretized. We see also here and from equation 2.30 that negative values of n should not be used, since [1]:

$$J_{-n}(\rho) = (-1)^n J_n(\rho)$$

and, thus, no orthogonality of any form similar to that discussed in this chapter could exist between Bessel functions of order n and $-n$. In addition, the following is also true and will be used later[2]:

$$J_n(-\rho) = (-1)^n J_n(\rho) \tag{2.34}$$

With this solution of the scalar wave equation at our disposal we now turn to the problem of finding solutions to the vector wave equation by applying equations 2.9 and 2.10. In doing so we are reminded of the fact that we still need to find the best choice for a pilot vector. From the following choices:

$$\mathbf{r}_c \quad \mathbf{e}_z \quad \mathbf{z}$$

the vector $\mathbf{e}_z$ will be chosen (and is chosen by previous authors), since it produces results which are the least complex mathematically. From equations 2.9 and 2.10 as well as equation 2.26 this becomes:

$$\begin{aligned}\mathbf{M}_n &= \nabla \times (\mathbf{e}_z \Psi) = \frac{1}{r}\frac{\partial \Psi}{\partial \theta}\mathbf{e}_r - \frac{\partial \Psi}{\partial r}\mathbf{e}_\theta = \frac{in}{r}\Psi \mathbf{e}_r - \frac{\partial \Psi}{\partial r}\mathbf{e}_\theta \\ &= \frac{in}{r}J_n(\rho)\, e^{i(n\theta+hz)}\mathbf{e}_r - \sqrt{k^2-h^2}\,J_n'(\rho)\, e^{i(n\theta+hz)}\mathbf{e}_\theta \qquad (2.35)\end{aligned}$$

$$\mathbf{N}_n = \frac{1}{k}\nabla \times \mathbf{M}_n = \frac{1}{kr}\left[-\frac{\partial}{\partial z}\left(-r\frac{\partial \Psi}{\partial r}\right)\right]\mathbf{e}_r - \frac{nh}{kr}\Psi \mathbf{e}_\theta + \frac{1}{kr}\left[\frac{\partial}{\partial r}\left(-r\frac{\partial \Psi}{\partial r}\right) + \frac{n^2}{r}\Psi\right]\mathbf{e}_z$$

---

[1] This is taken from equation 9.1.5 on page 358 of Abramowitz and Stegun (1972)

[2] This is deducible from equation 9.1.10 on page 360 of Abramowitz and Stegun (1972).

Notice that, using equation 2.29:

$$\mathbf{N}_n \cdot \mathbf{e}_z = \frac{1}{kr}\left[-\frac{\partial}{\partial r}\left(r\frac{\partial \Psi}{\partial r}\right) + \frac{n^2}{r}\Psi\right]$$

$$= \frac{e^{i(n\theta+hz)}}{kr}\left\{\sqrt{k^2-h^2}\left[-\frac{\partial}{\partial \rho}\left(\rho\frac{\partial J_n}{\partial \rho}\right)\right] + \frac{n^2\sqrt{k^2-h^2}}{\rho}J_n\right\}$$

$$= \frac{e^{i(n\theta+hz)}}{kr}\left\{\sqrt{k^2-h^2}\left[\frac{(\rho^2-n^2)}{\rho}J_n\right] + \frac{n^2\sqrt{k^2-h^2}}{\rho}J_n\right\}$$

$$= \frac{e^{i(n\theta+hz)}}{kr}\left[\rho\sqrt{k^2-h^2}J_n\right]$$

$$= \frac{k^2-h^2}{k}\Psi$$

Thus,

$$\mathbf{N}_n = \frac{1}{k}\nabla \times \mathbf{M}_n = \frac{ih}{k}\frac{\partial \Psi}{\partial r}\mathbf{e}_r - \frac{nh}{kr}\Psi\mathbf{e}_\theta + \frac{k^2-h^2}{k}\Psi\mathbf{e}_z$$

$$= \frac{ih}{k}\sqrt{k^2-h^2}J_n'(\rho)\,e^{i(n\theta+hz)}\mathbf{e}_r - \frac{nh}{kr}J_n(\rho)\,e^{i(n\theta+hz)}\mathbf{e}_\theta + \frac{k^2-h^2}{k}J_n(\rho)\,e^{i(n\theta+hz)}\mathbf{e}_z \quad (2.36)$$

$\mathbf{M}_n$ and $\mathbf{N}_n$ form an infinite series of cylindrical vector harmonics for the expression of the electric and magnetic fields which are incident upon and scattered by the cylinder. We can then show that these harmonics are orthogonal in the following ways:

$$\int_0^\infty \int_0^{2\pi} \int_{-\frac{\pi}{h}}^{\frac{\pi}{h}} \mathbf{M}_n^* \cdot \mathbf{M}_{n'} dz d\theta \rho d\rho = 0 \quad (n \neq n') \quad (2.37)$$

$$\int_0^\infty \int_0^{2\pi} \int_{-\frac{\pi}{h}}^{\frac{\pi}{h}} \mathbf{N}_n^* \cdot \mathbf{N}_{n'} dz d\theta \rho d\rho = 0 \quad (n \neq n') \quad (2.38)$$

$$\int_0^\infty \int_0^{2\pi} \int_{-\frac{\pi}{h}}^{\frac{\pi}{h}} \mathbf{M}_n^* \cdot \mathbf{N}_{n'} dz d\theta \rho d\rho = 0 \quad (n \neq n') \quad (2.39)$$

$$\int_0^\infty \int_0^{2\pi} \int_{-\frac{\pi}{h}}^{\frac{\pi}{h}} \mathbf{M}_n^* \cdot \mathbf{N}_{n'} dz d\theta \rho d\rho = 0 \quad (n = n') \quad (2.40)$$

where an asterisk (*) denotes the complex conjugate, and the integration with respect to '$\rho d\rho$' is necessary for an integration over volume (see figure 2.2). Also, the limits on the z integral are permissible for a description of the entire volume, since the functions $\mathbf{M}_n$ and $\mathbf{N}_n$ are periodic over z and do not die out as $z \to \infty$, and, thus, an integral over $(-\infty, \infty)$ would not yield a finite result. With the current limits the integrals give a result 'per oscillation' in the z axis.

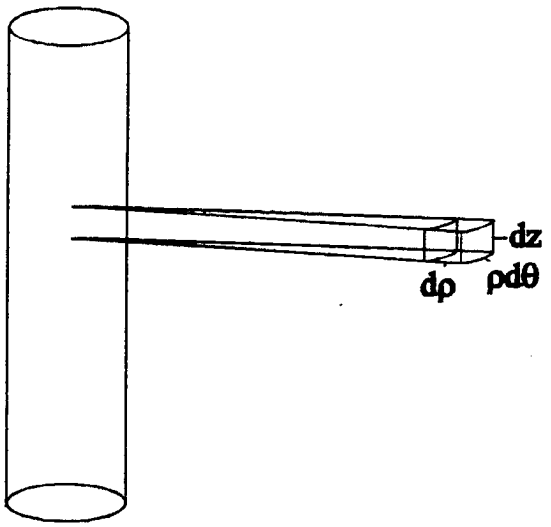

Figure 2.2: . Physical explanation for the integration limits.

Since the integration limits remain the same throughout this derivation, they will often be omitted from subsequent such integrals. Illustrating equation 2.37,

$$\iiint \mathbf{M}_n^* \cdot \mathbf{M}_{n'} dz d\theta \rho d\rho =$$

$$\iiint \frac{nn'}{r^2} J_n(\rho) J_{n'}(\rho) e^{-in\theta} e^{in'\theta} + (k^2 - h^2) J_n'(\rho) J_{n'}'(\rho) e^{-in\theta} e^{in'\theta} d\theta \rho d\rho$$

$$= \frac{2\pi}{h} \int_\theta e^{-in\theta} e^{in'\theta} d\theta \int_\rho \frac{nn'}{r^2} J_n(\rho) J_{n'}(\rho) + (k^2 - h^2) J_n'(\rho) J_{n'}'(\rho) \rho d\rho$$

where for the z dependence the terms e^{ihz} and e^{-ihz} cancel in both terms. Here we see that the orthogonality is clearly visible in the θ dependence, since:

$$\int_0^{2\pi} e^{-in\theta} e^{in'\theta} d\theta = \int_0^{2\pi} e^{i(n'-n)\theta} d\theta = \frac{1}{i(n'-n)} e^{i(n'-n)\theta} \Big|_0^{2\pi}$$

$$= \frac{1}{i(n'-n)} \{\cos[2\pi(n'-n)] + i \sin[2\pi(n'-n)] - \cos(0) - i \sin(0)\}$$

$$= \frac{1}{i(n'-n)} \{1 + 0 - 1 - 0\} = 0$$

In the same way, equation 2.38 is found to be clearly true in the θ dependence. Equations 2.39 and 2.40 are illustrated thus:

$$\iiint \mathbf{M}_n^* \cdot \mathbf{N}_{n'} dz d\theta \rho d\rho = \frac{2\pi}{h} \cdot \frac{1}{k} \iint \frac{nh\sqrt{k^2 - h^2}}{r} J_n(\rho) J_{n'}'(\rho) e^{-in\theta} e^{in'\theta}$$

$$+\frac{n'h\sqrt{k^2-h^2}}{r}J'_n(\rho)J_{n'}(\rho)e^{-in\theta}e^{in'\theta}d\theta\rho d\rho$$

$$=\frac{2\pi}{h}\cdot\frac{1}{k}\int_\theta e^{-in\theta}e^{in'\theta}d\theta\int_\rho\frac{nh\sqrt{k^2-h^2}}{r}J_n(\rho)J'_{n'}(\rho)+\frac{n'h\sqrt{k^2-h^2}}{r}J'_n(\rho)J_{n'}(\rho)\rho d\rho$$

Orthogonality is again shown in the θ dependence for $n \neq n'$, so equation 2.39 is satisfied. For the case of $n = n'$ (equation 2.40) each of the two terms in the ρ dependence identically becomes:

$$\int_0^\infty\frac{nh\sqrt{k^2-h^2}}{r}J_nJ'_n\rho d\rho=\int_0^\infty nh\left(k^2-h^2\right)J_nJ'_nd\rho$$

Using equation 2.32 this becomes:

$$\int_0^\infty nh\left(k^2-h^2\right)J_n\left(\frac{n}{\rho}J_n-J_{n+1}\right)d\rho$$

$$\int_0^\infty n^2h\left(k^2-h^2\right)J_nJ_n\frac{d\rho}{\rho}-\int_0^\infty nh\left(k^2-h^2\right)J_nJ_{n+1}d\rho$$

At this point we make use of the following two identities from Prudnikov et al. (1988): [3]

$$\int_0^\rho J_n^2(\rho)\frac{d\rho}{\rho}=\frac{1}{2n}\left[1+J_0^2(\rho)+J_n^2(\rho)-2\sum_{k=0}^{n}J_k^2(\rho)\right]$$

$$\int_0^\rho J_n(\rho)J_{n+1}(\rho)d\rho=\frac{1}{2}-\frac{1}{2}J_0^2(\rho)-\sum_{k=1}^{n}J_k^2(\rho)$$

Taking the limit as $\rho\to\infty$ of both of these identities, we have:

$$\int_0^\infty J_n^2(\rho)\frac{d\rho}{\rho}=\frac{1}{2n} \tag{2.41}$$

$$\int_0^\infty J_n(\rho)J_{n+1}(\rho)d\rho=\frac{1}{2} \tag{2.42}$$

since all Bessel functions approach zero at this limit. Returning to the orthogonality derivation, the two integrals become:

$$n^2h\left(k^2-h^2\right)\left(\frac{1}{2n}\right)-nh\left(k^2-h^2\right)\left(\frac{1}{2}\right)=0$$

---

[3] These are taken from equations 17 and 8 on page 41 of volume 2. Technically the first of these identities is only true when $n \geq 1$ and 'blows up' when $n = 0$. It can be shown, however, that this is due simply to the fact that $\frac{1}{2n}$ 'blows up' as $n \to 0$ and not to any fundamental change in the properties of the Bessel functions as $n \to 0$; that is, n times the integral should yield a finite result. (This is evident from equation 9.1.64 on page 362 of Abramowitz and Stegun (1972), which shows derivatives of J_n with respect to order being representable in a way which requires no restrictions on the interval of n.) This is significant, since this integral, when it appears later in the chapter, will always be multiplied by n^2. Thus, this restriction of $n \neq 0$ is not necessary.

and both of the terms describing the ρ dependence of the last orthogonality integral drop out. Thus, the orthogonality relations 2.37 through 2.40 are all proven.

At this point it is also most convenient to provide the solutions to two other integrals which will appear later. The first is:

$$\int_0^\infty J_n^2(\rho)\,\rho d\rho$$

For this derivation we make use of the following identity again from Prudnikov et al. (1988)[4]:

$$\int_0^\infty J_n^2 \rho d\rho = \left[\frac{\rho^2}{2}\left(J_n^2 - J_{n-1}J_{n+1}\right)\right]\Bigg|_0^\infty$$

and we must once again credit this derivation to Schubert (personal communication). Evaluating the integral according to this identity, we have:

$$\left[\frac{\rho^2}{2}\left(J_n^2 - J_{n-1}J_{n+1}\right)\right]\Bigg|_0^\infty = \lim_{\rho\to\infty}\left[\frac{\rho^2}{2}\left(J_n^2 - J_{n-1}J_{n+1}\right)\right] - 0$$

and the crux of the question immediately becomes apparent; we need to know if ρJ_n is bounded as $\rho \to \infty$.

Since we are dealing with large values of ρ, we can use the following asymptotic form of J_n, taken from Abramowitz and Stegun (1972)[5]:

$$\lim_{\rho\to\infty} J_n(\rho) = \sqrt{\frac{2}{\pi\rho}}\cos\left(\rho - \frac{n\pi}{2} - \frac{\pi}{4}\right)$$

and, thus,

$$\lim_{\rho\to\infty}\left[\frac{\rho^2}{2}\left(J_n^2 - J_{n-1}J_{n+1}\right)\right] =$$

$$\frac{\rho^2}{2}\cdot\frac{2}{\pi\rho}\left\{\cos^2\left(\rho - \frac{n\pi}{2} - \frac{\pi}{4}\right) - \cos\left[\rho - \frac{(n-1)\pi}{2} - \frac{\pi}{4}\right]\cos\left[\rho - \frac{(n+1)\pi}{2} - \frac{\pi}{4}\right]\right\}$$

Since,

$$\cos(A \pm B) = \cos A \cos B \mp \sin A \sin B$$

---

[4]This is taken from equation 12 on page 41 of volume 2.

[5]This is from equation 9.2.1 on page 364.

the products in the latter term become,

$$\cos\left[\rho - \frac{(n-1)\pi}{2} - \frac{\pi}{4}\right] = \cos\left(\rho - \frac{n\pi}{2} - \frac{\pi}{4}\right)\cos\left(\frac{\pi}{2}\right) + \sin\left(\rho - \frac{n\pi}{2} - \frac{\pi}{4}\right)\sin\left(\frac{\pi}{2}\right)$$
$$= \sin\left(\rho - \frac{n\pi}{2} - \frac{\pi}{4}\right)$$
$$\cos\left[\rho - \frac{(n+1)\pi}{2} - \frac{\pi}{4}\right] = \cos\left(\rho - \frac{n\pi}{2} - \frac{\pi}{4}\right)\cos\left(\frac{\pi}{2}\right) - \sin\left(\rho - \frac{n\pi}{2} - \frac{\pi}{4}\right)\sin\left(\frac{\pi}{2}\right)$$
$$= -\sin\left(\rho - \frac{n\pi}{2} - \frac{\pi}{4}\right)$$

and so the quantity $\frac{\rho^2}{2}\left(J_n^2 - J_{n-1}J_{n+1}\right)$ becomes

$$\frac{\rho^2}{2}\cdot\frac{2}{\pi\rho}\left[\cos^2\left(\rho - \frac{n\pi}{2} - \frac{\pi}{4}\right) + \sin^2\left(\rho - \frac{n\pi}{2} - \frac{\pi}{4}\right)\right] = \frac{\rho^2}{2}\cdot\frac{2}{\pi\rho} = \frac{\rho}{\pi}$$

Thus,

$$\int_0^\infty J_n^2\rho d\rho = \lim_{\rho\to\infty}\left[\frac{\rho^2}{2}\left(J_n^2 - J_{n-1}J_{n+1}\right)\right] = \lim_{\rho\to\infty}\left(\frac{\rho}{\pi}\right) = \infty$$

This is a result which warrants some discussion, this being an integral which plays a part in our solution for the A_n and B_n coefficients. Although this may at first appear to present an insurmountable and physically confusing 'dead end' to our solution for these coefficients, it is important to note that the problems will still be solvable if we represent this quantity by, say, ϵ:

$$\int_0^\infty J_n^2\rho d\rho = \epsilon \tag{2.43}$$

and set it aside as a simple constant, albeit an infinite one. The reader will find that as we proceed, this constant can be factored out and cancelled between the numerators and denominators of equations 2.53 and 2.54, leaving behind finite solutions.

The other integral of importance is the following:

$$\int_0^\infty J_n'^2\rho d\rho$$

Using equation 2.32, this becomes:

$$\int_0^\infty \left(\frac{n}{\rho}J_n - J_{n+1}\right)\left(\frac{n}{\rho}J_n - J_{n+1}\right)\rho d\rho$$
$$= \int_0^\infty n^2 J_n^2\frac{d\rho}{\rho} - \int_0^\infty 2nJ_nJ_{n+1}d\rho + \int_0^\infty J_{n+1}^2\rho d\rho$$

Using the solutions from the previous integrals, this becomes:

$$= n^2\left(\frac{1}{2n}\right) - 2n\left(\frac{1}{2}\right) + \epsilon = \frac{n}{2} - n + \epsilon = \epsilon - \frac{n}{2}$$

and, thus:

$$\int_0^\infty J_n'^2 \rho d\rho = \epsilon - \frac{n}{2} \tag{2.44}$$

Equations 2.32, 2.33, 2.34, 2.41, 2.42, 2.43, and 2.44 are all to be used later in the chapter.

Lord Rayleigh (1881 and 1918) made the same general approach as is illustrated in this step, but utilized different solution functions of the scalar wave equation:

$$\psi_n(kr) = (-1)^n \frac{d^n}{d(kr)^n}[\psi_0(kr)]$$

where,

$$\psi_0(kr) = Af(0) + Bf'(0)$$

and $f(0) = J_0(kr)$. Thus, from the previous equation as well as equation 2.32 these functions become:

$$\psi_0(kr) = AJ_0(kr) + BJ_0'(kr) = AJ_0(kr) - BJ_1(kr)$$

$$\psi_1(kr) = -\frac{d}{d(kr)}[AJ_0(kr) - BJ_1(kr)] = AJ_1(kr) + \frac{B}{kr}J_1(kr) - BJ_2(kr)$$

$$= \left(A + \frac{B}{kr}\right)J_1(kr) - BJ_2(kr)$$

$$\psi_2(kr) = -\frac{d}{d(kr)}\left[\left(A + \frac{B}{kr}\right)J_1(kr) - BJ_2(kr)\right]$$

$$= -\frac{B}{(kr)^2}J_1(kr) + \left(A + \frac{B}{kr}\right)J_1'(kr) - BJ_2'(kr)$$

$$= -\frac{B}{(kr)^2}J_1(kr) + \frac{1}{kr}\left(A + \frac{B}{kr}\right)J_1(kr) - \left(A + \frac{B}{kr}\right)J_2(kr) - \frac{2B}{kr}J_2(kr) + BJ_3(kr)$$

$$= \frac{A}{kr}J_1(kr) - \left(A + \frac{3B}{kr}\right)J_2(kr) + BJ_3(kr)$$

and so on. These were first defined in his book on sound (1878), and they are obviously analogous to the Bessel functions that we use, both in their form and in their usage. Rayleigh combined these functions into a general solution in which the divergent wave is expressed by an infinite series of these functions multiplied by $\cos n\theta$, again illustrating the analogy to our functions.

Thus, with our version of the solution functions, $\mathbf{M}_n$ and $\mathbf{N}_n$, at hand, we are ready to proceed onward to the next step.

Step 3. As was stated before, this step is often the most complex, especially in the case of spheres. The expression of a planar incident wave in terms of spherical harmonics is described by Bohren and Huffman (1983) as much like 'trying to fit a square peg into a round hole'. In the end for spheres it requires an infinite series of such harmonics, which will also be the case here.

In our derivation for cylinders we will make use of the following identity, which was apparently well-known even as far back as Rayleigh's derivation:

$$J_n(\rho) = \frac{i^{-n}}{2\pi}\int_0^{2\pi} e^{i(n\theta+\rho\cos\theta)}d\theta \tag{2.45}$$

$$e^{i\rho\cos\theta} = \sum_{n=-\infty}^{\infty}(-i)^n J_n(\rho)e^{in\theta} \tag{2.46}$$

The identity is expressed in two inverse forms, since both appear in the literature. Taking the derivative of equation 2.45, we have:

$$J_n'(\rho) = \frac{i^{1-n}}{2\pi}\int_0^{2\pi} e^{i(n\theta+\rho\cos\theta)}\cos\theta d\theta \tag{2.47}$$

Notice further that, if we apply equation 2.45 to the case of $(n-1)$ and $(n+1)$, subtracting them we arrive at

$$\begin{aligned} 2\pi i^{n-1}J_{n-1}(\rho) - 2\pi i^{n+1}J_{n+1}(\rho) &= \int_0^{2\pi} e^{i(n\theta+\rho\cos\theta)}(e^{-i\theta}-e^{i\theta})d\theta \\ &= -2i\int_0^{2\pi} e^{i(n\theta+\rho\cos\theta)}\sin\theta d\theta \end{aligned} \tag{2.48}$$

If we combine equations 2.32 and 2.33, we can arrive at the following identity for all Bessel functions:

$$Z_{n-1} + Z_{n+1} = \frac{2n}{\rho}Z_n$$

which is used thus:

$$2\pi i^{n-1}J_{n-1} + 2\pi i^{n-1}J_{n+1} = 2\pi i^{n-1}\frac{2n}{\rho}J_n$$

and modified slightly:

$$2\pi i^{n-1}J_{n-1} - 2\pi i^{n+1}J_{n+1} = -2i\pi i^n\frac{2n}{\rho}J_n \tag{2.49}$$

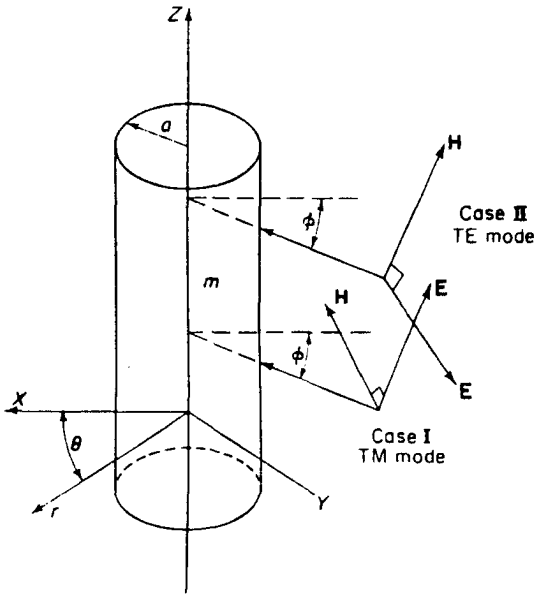

Figure 2.3: . Diagram of the incident wave relative to the cylinder, showing the two polarization cases (from Kerker (1969); ϕ will be $(90-\alpha)$ in this chapter.)

Combining equations 2.48 and 2.49, another expression for J_n is found:

$$J_n(\rho) = \frac{i^{-n}\rho}{2\pi n}\int_0^{2\pi} e^{i(n\theta+\rho\cos\theta)}\sin\theta d\theta \tag{2.50}$$

Thus, equations 2.45, 2.47, and 2.50 must be added to our impressive repertiore of Bessel function knowledge for the task ahead.

A moment's consideration reveals that an arbitrary incident plane wave can be represented by its angle of incidence relative to the cylinder, represented in this chapter by α, and its polarization, measured relative to the cylinder axis. For the latter, all possibilities will be adequately described in terms of two cases. The first is where the **E** vector is parallel to the plane created by **k** and $\mathbf{e}_z$, and the second is when **E** is perpendicular to that plane (see figure 2.3). These are, respectively, referred to as the TM and TE modes in much of the literature (e.g., Kerker (1969) and Pozar (1990)).

Taking a partial step outside of cylindrical coordinates for a moment and taking the x-axis as being parallel to the **k**-$\mathbf{e}_z$ plane and, of course, perpendicular to $\mathbf{e}_z$, we can express the incident waves in both cases. A quick glance at figure 2.4 shows that in the case of

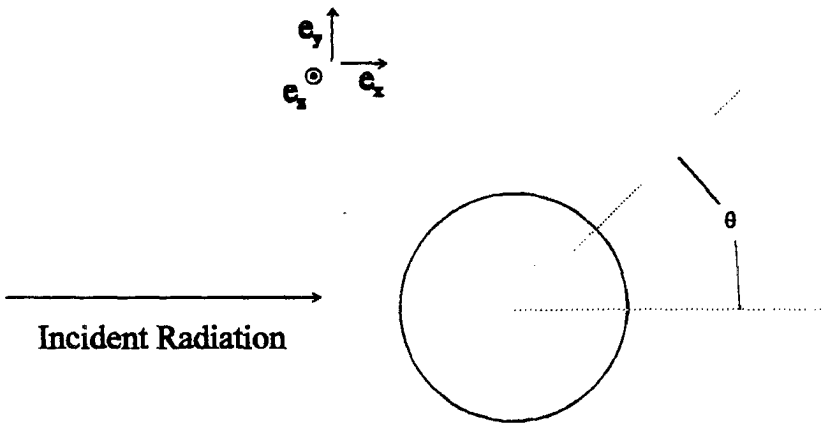

Figure 2.4: . Diagram of the case of perpendicular incidence, shown with the axis of the cylinder coming out of the page.

perpendicular incidence these equations should be:

$$\mathbf{E}_{i1} = E_0 \mathbf{e}_z e^{ik(r\cos\theta)}$$

$$\mathbf{E}_{i2} = E_0 \mathbf{e}_y e^{ik(r\cos\theta)}$$

where any time dependence can be neglected for reasons which will be discussed in a moment. When we expand beyond perpendicular incidence these become:

$$\mathbf{E}_{i1} = E_0 \left(\sin\alpha \mathbf{e}_z + \cos\alpha \mathbf{e}_x\right) e^{ik(r\sin\alpha\cos\theta + z\cos\alpha)} \tag{2.51}$$

$$\mathbf{E}_{i2} = E_0 \mathbf{e}_y e^{ik(r\sin\alpha\cos\theta + z\cos\alpha)} \tag{2.52}$$

where it now becomes apparent that in equations 2.35 and 2.36 h is now prescribed with the following consequences:

$$h = k\cos\alpha$$

$$\sqrt{k^2 - h^2} = k\sin\alpha \quad \rho = kr\sin\alpha$$

We now have the rather involved task of expressing equations 2.51 and 2.52 in terms of the harmonic functions; i.e., finding the coefficients A_n and B_n in the following formulae:

$$\mathbf{E}_i = \sum_{n=0}^{\infty} \left[A_n \mathbf{M}_n + B_n \mathbf{N}_n\right]$$

$$\mathbf{B}_i = \sum_{n=0}^{\infty} [B_n \mathbf{M}_n + A_n \mathbf{N}_n]$$

where the analogous relationships of $\mathbf{M}_n$ to $\mathbf{N}_n$ and $\mathbf{E}$ to $\mathbf{B}$ have been exploited. Here it becomes apparent as to why the time dependence has been ignored. Including it would simply place an $e^{i\omega t}$ factor into $\mathbf{E}_i$, $\mathbf{B}_i$, $\mathbf{M}_n$, and $\mathbf{N}_n$. Thus, due to the form of the above equations we can simply cancel this from both sides and not worry about it. If we next take the complex conjugate of both sides,

$$\mathbf{E}_i^* = \sum_{n=0}^{\infty} [A_n \mathbf{M}_n^* + B_n \mathbf{N}_n^*]$$

$$\mathbf{B}_i^* = \sum_{n=0}^{\infty} [B_n \mathbf{M}_n^* + A_n \mathbf{N}_n^*]$$

and take the inner product of the first equation above with $\mathbf{M}_N$, we have, upon integrating:

$$\iiint \mathbf{E}_{i1}^* \cdot \mathbf{M}_N d\theta \rho d\rho dz = \sum_{n=0}^{\infty} \iiint A_n \mathbf{M}_n^* \cdot \mathbf{M}_N d\theta \rho d\rho dz \quad (n \neq N)$$

$$+ \iiint A_N \mathbf{M}_N^* \cdot \mathbf{M}_N d\theta \rho d\rho dz + \sum_{n=0}^{\infty} \iiint B_n \mathbf{N}_n^* \cdot \mathbf{M}_N d\theta \rho d\rho dz$$

If we make use of the orthogonality properties of $\mathbf{M}_n$ and $\mathbf{N}_n$, on the right hand side only the second term remains:

$$\iiint \mathbf{E}_{i1}^* \cdot \mathbf{M}_N d\theta \rho d\rho dz = A_N \iiint \mathbf{M}_N^* \cdot \mathbf{M}_N d\theta \rho d\rho dz$$

and it becomes clear that the solutions for A_n and B_n can be achieved through the following:

$$A_{n1} = \frac{\iiint \mathbf{E}_{i1}^* \cdot \mathbf{M}_n d\theta \rho d\rho dz}{\iiint \mathbf{M}_n^* \cdot \mathbf{M}_n d\theta \rho d\rho dz} \tag{2.53}$$

$$B_{n1} = \frac{\iiint \mathbf{E}_{i1}^* \cdot \mathbf{N}_n d\theta \rho d\rho dz}{\iiint \mathbf{N}_n^* \cdot \mathbf{N}_n d\theta \rho d\rho dz} \tag{2.54}$$

Considering the numerator of A_n first,

$$\iiint \mathbf{E}_{i1}^* \cdot \mathbf{M}_n d\theta \rho d\rho dz$$

we have,

$$E_0 \iiint \left\{ [\sin\alpha \mathbf{e}_z + \cos\alpha \mathbf{e}_x] \, e^{-ik(r\sin\alpha\cos\theta + z\cos\alpha)} \right\} \cdot$$

$$\left\{ \frac{in}{r} J_n(\rho) \mathbf{e}_r - k \sin\alpha J_n'(\rho) \mathbf{e}_\theta \right\} e^{i(n\theta + hz)} d\theta \rho d\rho dz$$

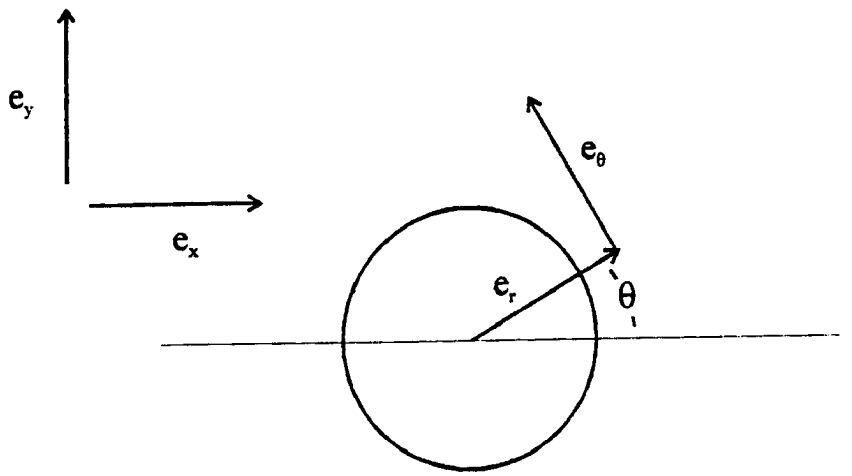

Figure 2.5: . Geometry associated with the two coordinate systems in use.

where it is also understood, according to figure 2.5, that:

$$\mathbf{e}_r = \mathbf{e}_x \cos\theta + \mathbf{e}_y \sin\theta$$

$$\mathbf{e}_\theta = -\mathbf{e}_x \sin\theta + \mathbf{e}_y \cos\theta$$

so that,

$$\mathbf{e}_r \cos\theta - \mathbf{e}_\theta \sin\theta = \mathbf{e}_x$$

and, thus, the integral becomes:

$$E_0 \cos\alpha \iiint e^{-ik(r\sin\alpha\cos\theta + z\cos\alpha)} e^{i(n\theta+hz)} \left[\cos\theta \frac{in}{r} J_n(\rho) + k\sin\alpha\sin\theta J_n'(\rho)\right] d\theta\rho d\rho dz$$

Considering the first term,

$$\left(\frac{2\pi}{h}\right) in\cos\alpha E_0 \iint e^{i(n\theta - kr\sin\alpha\cos\theta)} \cos\theta \frac{J_n(\rho)}{r} d\theta\rho d\rho$$

$$= \left(\frac{2\pi}{h}\right) in\cos\alpha E_0 \int_\rho \frac{J_n(\rho)}{r} \int_\theta e^{i(n\theta - \rho\cos\theta)} \cos\theta d\theta\rho d\rho$$

Using equation 2.47 this becomes:

$$\left(\frac{2\pi}{h}\right) 2\pi i^n k E_0 \sin\alpha\cos\alpha \int_\rho \frac{n}{\rho} J_n(\rho) J_n'(-\rho)\rho d\rho$$

$$= \left(\frac{2\pi}{h}\right) 2\pi (-1)^n i^n k E_0 \sin\alpha \cos\alpha \int_\rho \frac{n}{\rho} J_n(\rho) J_n'(\rho) \rho d\rho \tag{2.55}$$

where equation 2.34 has been used.[6] Similarly for the other term we have,

$$\left(\frac{2\pi}{h}\right) k E_0 \sin\alpha \cos\alpha \iint e^{i(n\theta - \rho\cos\theta)} J_n' \sin\theta d\theta \rho d\rho$$

$$= \left(\frac{2\pi}{h}\right) k E_0 \sin\alpha \cos\alpha \int_\rho \rho J_n'(\rho) \int_\theta e^{i(n\theta - \rho\cos\theta)} \sin\theta d\theta d\rho$$

$$= \left(\frac{2\pi}{h}\right) 2\pi (-1)^n i^n k E_0 \sin\alpha \cos\alpha \int_\rho \frac{n}{\rho} J_n'(\rho) J_n(\rho) \rho d\rho$$

where we have used equations 2.32, 2.34, and 2.50. These two terms both involve the following integral:

$$\int_\rho \frac{n}{\rho} J_n J_n' \rho d\rho = n \int_\rho J_n J_n' d\rho$$

According to equation 2.33 this becomes:

$$\frac{n}{2} \int_\rho J_n (J_{n-1} - J_{n+1}) d\rho$$

$$= \frac{n}{2} \left[\int_\rho J_{n-1} J_n d\rho - \int_\rho J_n J_{n+1} d\rho \right]$$

and from equation 2.42 we find that each of these integrals has the same value:

$$\frac{n}{2} \left[\frac{1}{2} - \frac{1}{2} \right] = 0$$

Thus, we have a total numerator of zero. Since the denominator is clearly not zero:

$$\iiint \mathbf{M}_n^* \cdot \mathbf{M}_n d\theta \rho d\rho dz = \iiint \left[\frac{n^2}{r^2} J_n J_n + k^2 \sin^2\alpha J_n' J_n' \right] d\theta \rho d\rho dz$$

$$= (2\pi) \left(\frac{2\pi}{h}\right) \left[n^2 k^2 \sin^2\alpha \left(\frac{1}{2n}\right) + k^2 \sin^2\alpha \left(\epsilon - \frac{n}{2}\right) \right] = \frac{4\pi^2 k^2 \epsilon}{h} \sin^2\alpha$$

where equations 2.41 and 2.44 have been used, the quotient is defined (when $\alpha \neq 0$), and all A_{n1}'s will be zero.

For B_{n1}, again considering the numerator first, we have:

$$\iiint \mathbf{E}_{i1}^* \cdot \mathbf{N}_n d\theta \rho d\rho dz =$$

---

[6] Equation 2.34 should also apply to $J_n'(\rho)$. This is deducible from an inspection of equation 2.33.

$$E_0 \iiint \left\{ \left[\sin\alpha \mathbf{e}_z + \cos\alpha \mathbf{e}_x \right] e^{-ik(r\sin\alpha\cos\theta + z\cos\alpha)} \right\} \cdot$$

$$\left\{ ik\sin\alpha\cos\alpha J_n'(\rho)\mathbf{e}_r - \frac{n\cos\alpha}{r} J_n(\rho)\mathbf{e}_\theta + k\sin^2\alpha J_n(\rho)\mathbf{e}_z \right\} e^{i(n\theta + k\cos\alpha z)} d\theta\rho d\rho dz$$

$$= E_0 \iiint \left[e^{i(n\theta - \rho\cos\theta)} \right] \cdot$$

$$\left\{ ik\sin\alpha\cos^2\alpha\cos\theta J_n'(\rho) - \left[\frac{n}{r}\cos^2\alpha\sin\theta - k\sin^3\alpha \right] J_n(\rho) \right\} d\theta\rho d\rho dz$$

and, considering only the first term as before, this becomes:

$$\left(\frac{2\pi}{h}\right) ikE_0 \sin\alpha\cos^2\alpha \iint e^{i(n\theta - \rho\cos\theta)} \cos\theta J_n'(\rho)\, d\theta\rho d\rho$$

$$= \left(\frac{2\pi}{h}\right) 2\pi (-1)^n i^n kE_0 \sin\alpha\cos^2\alpha \int J_n'(\rho) J_n'(\rho)\rho d\rho$$

$$= \left(\frac{2\pi}{h}\right) 2\pi (-i)^n kE_0 \sin\alpha\cos^2\alpha \left(\epsilon - \frac{n}{2}\right)$$

where equation 2.47 has been used. Considering the second term in the same way:

$$\left(\frac{2\pi}{h}\right) nE_0 k\sin\alpha\cos^2\alpha \iint \frac{J_n}{\rho} e^{i(n\theta - \rho\cos\theta)} \sin\theta d\theta\rho d\rho$$

$$= \left(\frac{2\pi}{h}\right) 2\pi n^2 (-1)^n i^n kE_0 \sin\alpha\cos^2\alpha \int \frac{J_n J_n}{\rho^2}\rho d\rho$$

$$= \left(\frac{2\pi}{h}\right) 2\pi n^2 (-i)^n kE_0 \sin\alpha\cos^2\alpha \left(\frac{1}{2n}\right)$$

$$= \left(\frac{2\pi}{h}\right) \pi n (-i)^n kE_0 \sin\alpha\cos^2\alpha$$

where equations 2.41 and 2.50 have been used, we arrive at a result which cancels with the $-\frac{n}{2}$ portion of the result for the first term. Lastly, term 3 becomes:

$$\left(\frac{2\pi}{h}\right) E_0 k\sin^3\alpha \iint e^{i(n\theta - \rho\cos\theta)} J_n d\theta\rho d\rho = \left(\frac{2\pi}{h}\right) 2\pi (-1)^n i^n E_0 k\sin^3\alpha \int J_n J_n \rho d\rho$$

$$= \left(\frac{2\pi}{h}\right) 2\pi (-i)^n kE_0\epsilon \sin^3\alpha$$

Thus, the complete expression for the numerator becomes:

$$\left(\frac{2\pi}{h}\right) 2\pi (-i)^n kE_0\epsilon \sin\alpha \left(\cos^2\alpha + \sin^2\alpha\right) = 2\pi (-i)^n kE_0\epsilon \sin\alpha$$

For the denominator we have:

$$\iiint \mathbf{N}_n^* \cdot \mathbf{N}_n d\theta \rho d\rho dz =$$

$$\frac{2\pi}{h} \iint \left(k^2 \sin^2\alpha \cos^2\alpha J_n' J_n' + \frac{n^2 \cos^2\alpha}{r^2} J_n J_n + k^2 \sin^4\alpha J_n J_n \right) e^{in\theta} e^{-in\theta} d\theta \rho d\rho$$

$$= \left(\frac{2\pi}{h}\right) 2\pi \int \left(k^2 \sin^2\alpha \cos^2\alpha J_n' J_n' + n^2 k^2 \sin^2\alpha \cos^2\alpha \frac{J_n J_n}{\rho^2} + k^2 \sin^4\alpha J_n J_n \right) \rho d\rho$$

$$= \left(\frac{2\pi}{h}\right) 2\pi \left[k^2 \sin^2\alpha \cos^2\alpha \left(\epsilon - \frac{n}{2}\right) + n^2 k^2 \sin^2\alpha \cos^2\alpha \left(\frac{1}{2n}\right) + k^2 \sin^4\alpha \epsilon \right]$$

$$= \left(\frac{2\pi}{h}\right) 2\pi k^2 \sin^2\alpha \epsilon$$

where we have considered, again, only the ρ and θ dependence. Putting it all together, we make note of the fact that the ϵ's cancel as promised:

$$B_{n1} = \frac{\left(\frac{2\pi}{h}\right) 2\pi (-i)^n E_0 k \epsilon \sin\alpha}{\left(\frac{2\pi}{h}\right) 2\pi k^2 \epsilon \sin^2\alpha} = \frac{(-i)^n E_0}{k \sin\alpha}$$

leaving us with, for case 1:

$$A_{n1} = 0 \quad B_{n1} = \frac{(-i)^n E_0}{k \sin\alpha} = E_n$$

and for case 2, since for this the functions of $\mathbf{E}_i$ and $\mathbf{B}_i$ are merely reversed, so too are the coefficients merely reversed for this case:

$$A_{n2} = \frac{(-i)^n E_0}{k \sin\alpha} = E_n \quad B_{n2} = 0$$

Therefore, the incident fields can be expanded to the following:

$$\mathbf{E}_{i1} = \sum_{n=0}^{\infty} E_n \mathbf{N}_n \qquad \mathbf{B}_{i1} = \frac{-ik}{\omega\mu} \sum_{n=0}^{\infty} E_n \mathbf{M}_n$$

$$\mathbf{E}_{i2} = \sum_{n=0}^{\infty} E_n \mathbf{M}_n \qquad \mathbf{B}_{i2} = \frac{-ik}{\omega\mu} \sum_{n=0}^{\infty} E_n \mathbf{N}_n$$

Van de Hulst (1957) uses the same general approach, but makes use of two solutions of the scalar wave equation in order to arrive at a solution.

Step 4. This is the most straightforward step. In it there are three general conditions that must be met:

- Finiteness at the origin (for obvious physical reasons).

- Satisfaction of boundary conditions on the particle surface
- Well-behaved nature of the functions at large distances from the particle

The three common solutions to Bessel's equation are:

$$J_n \quad Y_n \quad H_n$$

As was stated before, finiteness at the origin requires that J_n be the generating function inside the particle, and outside the particle both of the functions are well-behaved. The use, thus, of the Hankel function:

$$H_n = J_n - iY_n$$

for the scattering in the outside regime is legal. Also, since h must be given by the same formula inside and outside the particle, inside the particle the radical $\sqrt{k^2 - h^2}$ becomes:

$$\sqrt{m^2k^2 - h^2} = k\sqrt{m^2 - \cos^2\alpha}$$

making,

$$\rho_I = kr\sqrt{m^2 - \cos^2\alpha}$$

where a subscript of I signifies that it applies to the region inside the particle. In addition, for any particle scattering problem the following boundary conditions must be satisfied on the particle surface:

$$[\mathbf{E}_2(\mathbf{x}) - \mathbf{E}_1(\mathbf{x})] \times \mathbf{n} = 0$$

$$[\mathbf{B}_2(\mathbf{x}) - \mathbf{B}_1(\mathbf{x})] \times \mathbf{n} = 0$$

where $\mathbf{x}$ describes a point on the surface of a particle, on which $\mathbf{n}$ is a normal to the surface, and the subscripts 1 and 2 describe total fields inside and outside the particle, respectively. This effectively states that the tangential components of $\mathbf{E}$ and $\mathbf{B}$ must be continuous on the particle surface. For our purposes this translates, at $r = a$, to:

$$E_{iz} + E_{sz} = E_{Iz} \qquad E_{i\theta} + E_{s\theta} = E_{I\theta} \tag{2.56}$$

$$B_{i\theta} + B_{s\theta} = B_{I\theta} \qquad B_{iz} + B_{sz} = B_{Iz} \tag{2.57}$$

where again it should be pointed out that here and from now on the subscripts of i, I, and s denote the incident, internal, and scattered, fields, respectively. Note that for Case 1:

$$E_{i\theta} = B_{iz} = 0$$

and for Case 2:

$$E_{iz} = B_{i\theta} = 0$$

although for the final step ahead this does not significantly simplify the problem and is taken here to be superfluous.

Step 5. Finally, the task remains of using the boundary conditions to solve for the internal and scattered fields:

$$\mathbf{E}_I = \sum_{n=0}^{\infty} E_{nI}\left[g_n \mathbf{M}_n^{(1)} + f_n \mathbf{N}_n^{(1)}\right] \qquad \mathbf{B}_I = \frac{-ik_I}{\omega\mu_I}\sum_{n=0}^{\infty} E_{nI}\left[f_n \mathbf{M}_n^{(1)} + g_n \mathbf{N}_n^{(1)}\right]$$

$$\mathbf{E}_s = -\sum_{n=0}^{\infty} E_n\left[ia_n \mathbf{M}_n^{(3)} + b_n \mathbf{N}_n^{(3)}\right] \qquad \mathbf{B}_s = \frac{ik}{\omega\mu}\sum_{n=0}^{\infty} E_n\left[b_n \mathbf{M}_n^{(3)} + ia_n \mathbf{N}_n^{(3)}\right]$$

where a superscript of 1, 2, or 3, above a spherical harmonic respectively denotes the use of J_n, Y_n, or H_n in its generation.

We have four equations (2.56 and 2.57) for the four unknowns a_n, b_n, f_n, and g_n. The first equation is:

$$E_{iz} + E_{sz} = E_{Iz}$$

This can be expanded accordingly:

$$\mathbf{E}_{i1}\cdot\mathbf{e}_z + \mathbf{E}_s\cdot\mathbf{e}_z = \mathbf{E}_I\cdot\mathbf{e}_z$$

$$\left(\sum_{n=0}^{\infty} E_n \mathbf{N}_n^{(1)}\right)\cdot\mathbf{e}_z + \left[-\sum_{n=0}^{\infty} E_n\left(ia_n \mathbf{M}_n^{(3)} + b_n \mathbf{N}_n^{(3)}\right)\right]\cdot\mathbf{e}_z = \left[\sum_{n=0}^{\infty} E_{nI}\left(g_n \mathbf{M}_n^{(1)} + f_n \mathbf{N}_n^{(1)}\right)\right]\cdot\mathbf{e}_z$$

where:

$$E_{nI} = \frac{(-i)^n E_0}{k_I \sin\alpha} = \frac{(-i)^n E_0}{mk\sin\alpha} = \frac{E_n}{m}$$

Fortunately, we can make use of the orthogonality properties of $\mathbf{M}_n$ and $\mathbf{N}_n$ so that values of n can be evaluated individually:

$$\left(E_n \mathbf{N}_n^{(1)}\right)\cdot\mathbf{e}_z + \left[-E_n\left(ia_n \mathbf{M}_n^{(3)} + b_n \mathbf{N}_n^{(3)}\right)\right]\cdot\mathbf{e}_z = \left[\frac{E_n}{m}\left(g_n \mathbf{M}_n^{(1)} + f_n \mathbf{N}_n^{(1)}\right)\right]\cdot\mathbf{e}_z$$

Recalling equations 2.35 and 2.36, we find that there is an $e^{i(n\theta+hz)}$ term in each of the components of **M** and **N**. This is a portion of these components which need not be included when making the substitutions here, since it will only create a common factor. The substitution without this common factor yields:

$$\frac{k^2-h^2}{k}J_n(\xi)-b_n\frac{k^2-h^2}{k}H_n(\xi)=\frac{1}{m}f_n\frac{k_I^2-h^2}{k_I}J_n(\eta)$$

where the E_n's have been cancelled and ξ and η respectively represent ρ and ρ_I evaluated at $r=a$:

$$\xi=ka\sin\alpha \qquad \eta=ka\sqrt{m^2-\cos^2\alpha}$$

Multiplying by ka^2 and simplifying, this becomes:

$$k^2a^2\sin^2\alpha J_n(\xi)-b_nk^2a^2\sin^2\alpha H_n(\xi)=f_n\frac{1}{m^2}k^2a^2\left(m^2-\cos^2\alpha\right)J_n(\eta)$$

$$\xi^2J_n(\xi)-b_n\xi^2H_n(\xi)=f_n\frac{\eta^2}{m^2}J_n(\eta) \tag{2.58}$$

Performing the same for the second equation:

$$E_{i\theta}+E_{s\theta}=E_{I\theta}$$

we have:

$$-E_n\frac{nh}{ka}J_n(\xi)-E_n\left[ia_n\left(-\sqrt{k^2-h^2}H_n'(\xi)\right)+b_n\left(-\frac{nh}{ka}H_n(\xi)\right)\right]=$$
$$\frac{E_n}{m}\left[g_n\left(-\sqrt{m^2k^2-h^2}J_n'(\eta)\right)+f_n\left(-\frac{nh}{mka}J_n(\eta)\right)\right]$$

Multiplying by ma this simplifies to:

$$-mn\cos\alpha J_n(\xi)+ia_nmka\sin\alpha H_n'(\xi)+b_nmn\cos\alpha H_n(\xi)$$
$$=-g_nka\sqrt{m^2-\cos^2\alpha}J_n'(\eta)-f_n\frac{n\cos\alpha}{m}J_n(\eta)$$

$$-mn\cos\alpha J_n(\xi)+ia_nm\xi H_n'(\xi)+b_nmn\cos\alpha H_n(\xi)=-g_n\eta J_n'(\eta)-f_n\frac{n\cos\alpha}{m}J_n(\eta) \tag{2.59}$$

The third equation,

$$B_{i\theta}+B_{s\theta}=B_{I\theta}$$

yields:

$$\frac{-ik}{\omega\mu}E_n\left(-\sqrt{k^2-h^2}J_n'(\xi)\right)+\frac{ik}{\omega\mu}E_n\left[b_n\left(-\sqrt{k^2-h^2}H_n'(\xi)\right)+ia_n\left(-\frac{nh}{ka}H_n(\xi)\right)\right]=$$

$$\frac{-imk}{\omega\mu}\frac{E_n}{m}\left[f_n\left(-\sqrt{m^2k^2-h^2}J_n'(\eta)\right)+g_n\left(-\frac{nh}{mka}J_n(\eta)\right)\right]$$

where we have assumed that $\mu_I=\mu$. Multiplying by a, this simplifies to:

$$\xi J_n'(\xi)-b_n\xi H_n'(\xi)-ia_nn\cos\alpha H_n(\xi)=f_n\eta J_n'(\eta)+g_n\frac{n\cos\alpha}{m}J_n(\eta) \tag{2.60}$$

and, lastly, the fourth equation,

$$B_{iz}+B_{sz}=B_{Iz}$$

yields:

$$\frac{ik}{\omega\mu}E_n\left(ia_n\frac{k^2-h^2}{k}H_n(\xi)\right)=\frac{-imk}{\omega\mu}\frac{E_n}{m}\left(g_n\frac{m^2k^2-h^2}{mk}J_n(\eta)\right)$$

$$ia_nmk^2a^2\sin^2\alpha H_n(\xi)=-g_nk^2a^2\left(m^2-\cos^2\alpha\right)J_n(\eta)$$

$$ia_nm\xi^2H_n(\xi)=-g_n\eta^2J_n(\eta) \tag{2.61}$$

Note that equations 2.58 and 2.61 provide direct substitutionary relationships between the coefficients f_n and b_n, and g_n and a_n, respectively. Using these in equation 2.59:

$$-mn\cos\alpha J_n(\xi)+ia_nm\xi H_n'(\xi)+b_nmn\cos\alpha H_n(\xi)=-\left[\frac{-ia_nm\xi^2H_n(\xi)}{\eta^2J_n(\eta)}\right]\eta J_n'(\eta)-$$

$$\left[\frac{m^2\xi^2J_n(\xi)-b_nm^2\xi^2H_n(\xi)}{\eta^2J_n(\eta)}\right]\frac{n\cos\alpha}{m}J_n(\eta)$$

$$-n\cos\alpha\eta J_n(\eta)J_n(\xi)+ia_n\eta\xi J_n(\eta)H_n'(\xi)+b_nn\cos\alpha\eta J_n(\eta)H_n(\xi)=ia_n\xi^2J_n'(\eta)H_n(\xi)$$

$$-n\cos\alpha\frac{\xi^2}{\eta}J_n(\eta)J_n(\xi)+b_nn\cos\alpha\frac{\xi^2}{\eta}J_n(\eta)H_n(\xi)$$

$$ia_n\left[\eta\xi J_n(\eta)H_n'(\xi)-\xi^2J_n'(\eta)H_n(\xi)\right]+n\cos\alpha\frac{\xi^2}{\eta}J_n(\eta)J_n(\xi)-n\cos\alpha\eta J_n(\eta)J_n(\xi)=$$

$$b_n\left[n\cos\alpha\frac{\xi^2}{\eta}J_n(\eta)H_n(\xi)-n\cos\alpha\eta J_n(\eta)H_n(\xi)\right] \tag{2.62}$$

and equation 2.60:

$$\xi J_n'(\xi) - b_n \xi H_n'(\xi) - i a_n n \cos\alpha H_n(\xi) = \left[\frac{m^2\xi^2 J_n(\xi) - b_n m^2 \xi^2 H_n(\xi)}{\eta^2 J_n(\eta)}\right] \eta J_n'(\eta) +$$

$$\left[\frac{-i a_n m \xi^2 H_n(\xi)}{\eta^2 J_n(\eta)}\right] \frac{n\cos\alpha}{m} J_n(\eta)$$

$$\eta\xi J_n(\eta) J_n'(\xi) - b_n \eta\xi J_n(\eta) H_n'(\xi) - i a_n n \cos\alpha \eta J_n(\eta) H_n(\xi) = m^2\xi^2 J_n'(\eta) J_n(\xi) -$$

$$b_n m^2 \xi^2 J_n'(\eta) H_n(\xi) - i a_n n \cos\alpha \frac{\xi^2}{\eta} J_n(\eta) H_n(\xi)$$

$$i a_n \left[n\cos\alpha \frac{\xi^2}{\eta} J_n(\eta) H_n(\xi) - n\cos\alpha \eta J_n(\eta) H_n(\xi)\right] =$$

$$m^2\xi^2 J_n'(\eta) J_n(\xi) - \eta\xi J_n(\eta) J_n'(\xi) + b_n \left[\eta\xi J_n(\eta) H_n'(\xi) - m^2\xi^2 J_n'(\eta) H_n(\xi)\right] \qquad (2.63)$$

We now have two equations, 2.62 and 2.63, which can be respectively simplified to the following:

$$a_n W_n + C_n = b_n D_n \qquad i a_n D_n = B_n - b_n V_n$$

where,

$$B_n = \xi\left[m^2\xi J_n'(\eta) J_n(\xi) - \eta J_n(\eta) J_n'(\xi)\right]$$

$$C_n = n\cos\alpha\eta J_n(\eta) J_n(\xi)\left(\frac{\xi^2}{\eta^2} - 1\right)$$

$$D_n = n\cos\alpha\eta J_n(\eta) H_n(\xi)\left(\frac{\xi^2}{\eta^2} - 1\right)$$

$$V_n = \xi\left[m^2\xi J_n'(\eta) H_n(\xi) - \eta J_n(\eta) H_n'(\xi)\right]$$

$$W_n = i\xi\left[\eta J_n(\eta) H_n'(\xi) - \xi J_n'(\eta) H_n(\xi)\right]$$

Combining these two equations for a_n and b_n we arrive at[7]

$$a_{n1} = \frac{B_n D_n - C_n V_n}{W_n V_n + i D_n^2} \qquad b_{n1} = \frac{W_n B_n + i D_n C_n}{W_n V_n + i D_n^2}$$

---

[7]This solution possesses an as-of-yet unexplained difference from that given in Bohren and Huffman (1983). The solution for a_{n1} differs by a factor of -1, and the solutions for a_{n2} and b_{n2} both differ by factors of i.

and the coefficients for case 2 are found in the same way:

$$a_{n2} = \frac{C_n D_n + i A_n V_n}{W_n V_n + i D_n^2} \qquad b_{n2} = \frac{C_n W_n + A_n D_n}{W_n V_n + i D_n^2}$$

where in addition to the previous simplifying variables a new one is defined:

$$A_n = i\xi \left[\xi J_n'(\eta) J_n(\xi) - \eta J_n(\eta) J_n'(\xi)\right]$$

These solutions were also arrived at by Kerker (1969) as well as Farone and Querfield (1966) but were placed in a determinant form:

$$a_{n1} = \frac{\Lambda_1}{\Delta}$$

$$b_{n1} = \frac{\Upsilon_1}{\Delta}$$

$$a_{n2} = \frac{\Lambda_2}{\Delta}$$

$$b_{n2} = \frac{\Upsilon_2}{\Delta}$$

where,

$$\Lambda_1 = \begin{vmatrix} -\frac{ink\cos\alpha}{\alpha} J_n(\rho) & -\frac{ink\cos\alpha}{m\alpha} J_n(\eta) & -\frac{ink\cos\alpha}{\alpha} H_n(\rho) & -k\sqrt{m^2-\cos^2\alpha}\, J_n'(\eta) \\ -k\sin^2\alpha J_n(\rho) & -\frac{k\left(m^2-\cos^2\alpha\right)}{m} J_n(\eta) & -k\sin^2\alpha H_n(\rho) & 0 \\ -k\sin\alpha J_n'(\rho) & -mk\sqrt{m^2-\cos^2\alpha}\, J_n'(\eta) & -k\sin\alpha H_n'(\rho) & \frac{ink\cos\alpha}{\alpha} J_n(\eta) \\ 0 & 0 & 0 & -k^2\left(m^2-\cos^2\alpha\right) J_n(\eta) \end{vmatrix}$$

$$\Upsilon_1 = \begin{vmatrix} k\sin\alpha H_n'(\rho) & -\frac{ink\cos\alpha}{m\alpha} J_n(\eta) & -\frac{ink\cos\alpha}{\alpha} J_n(\rho) & -k\sqrt{m^2-\cos^2\alpha}\, J_n'(\eta) \\ 0 & -\frac{k\left(m^2-\cos^2\alpha\right)}{m} J_n(\eta) & -k\sin^2\alpha J_n(\rho) & 0 \\ -\frac{ink\cos\alpha}{\alpha} H_n(\rho) & -mk\sqrt{m^2-\cos^2\alpha}\, J_n'(\eta) & -k\sin\alpha J_n'(\rho) & \frac{ink\cos\alpha}{\alpha} J_n(\eta) \\ k^2\sin^2\alpha H_n(\rho) & 0 & 0 & -k^2\left(m^2-\cos^2\alpha\right) J_n(\eta) \end{vmatrix}$$

$$\Lambda_2 = \begin{vmatrix} -k\sin\alpha J_n'(\rho) & -\frac{ink\cos\alpha}{m\alpha} J_n(\eta) & \frac{ink\cos\alpha}{\alpha} H_n(\rho) & -k\sqrt{m^2-\cos^2\alpha}\, J_n'(\eta) \\ 0 & -\frac{k\left(m^2-\cos^2\alpha\right)}{m} J_n(\eta) & k\sin^2\alpha H_n(\rho) & 0 \\ \frac{ink\cos\alpha}{\alpha} J_n(\rho) & -mk\sqrt{m^2-\cos^2\alpha}\, J_n'(\eta) & k\sin\alpha H_n'(\rho) & \frac{ink\cos\alpha}{\alpha} J_n(\eta) \\ -k^2\sin^2\alpha J_n(\rho) & 0 & 0 & -k^2\left(m^2-\cos^2\alpha\right) J_n(\eta) \end{vmatrix}$$

$$\Upsilon_2 =$$

$$\begin{vmatrix} -k\sin\alpha H_n'(\rho) & -\frac{ink\cos\alpha}{m\alpha}J_n(\eta) & -k\sin\alpha J_n'(\rho) & -k\sqrt{m^2-\cos^2\alpha}J_n'(\eta) \\ 0 & -\frac{k\left(m^2-\cos^2\alpha\right)}{m}J_n(\eta) & 0 & 0 \\ \frac{ink\cos\alpha}{\alpha}H_n(\rho) & -mk\sqrt{m^2-\cos^2\alpha}J_n'(\eta) & \frac{ink\cos\alpha}{\alpha}J_n(\rho) & \frac{ink\cos\alpha}{\alpha}J_n(\eta) \\ -k^2\sin^2\alpha H_n(\rho) & 0 & -k^2\sin^2\alpha J_n(\rho) & -k^2\left(m^2-\cos^2\alpha\right)J_n(\eta) \end{vmatrix}$$

$$\Delta =$$

$$\begin{vmatrix} k\sin\alpha H_n'(\rho) & -\frac{ink\cos\alpha}{m\alpha}J_n(\eta) & -\frac{ink\cos\alpha}{\alpha}H_n(\rho) & -k\sqrt{m^2-\cos^2\alpha}J_n'(\eta) \\ 0 & -\frac{k\left(m^2-\cos^2\alpha\right)}{m}J_n(\eta) & -k\sin^2\alpha H_n(\rho) & 0 \\ -\frac{ink\cos\alpha}{\alpha}H_n(\rho) & -mk\sqrt{m^2-\cos^2\alpha}J_n'(\eta) & -k\sin\alpha H_n'(\rho) & \frac{ink\cos\alpha}{\alpha}J_n(\eta) \\ k^2\sin^2\alpha H_n(\rho) & 0 & 0 & -k^2\left(m^2-\cos^2\alpha\right)J_n(\eta) \end{vmatrix}$$

and the determinants have been modified slightly to account for our different definition of α. As is mentioned earlier, Lord Rayleigh (1881) expressed the divergent scattering wave in terms of the following scalar series:

$$B_0\psi_0 + B_1\psi_1\cos\theta + B_2\psi_2\cos 2\theta + \cdots$$

where the coefficients B_n are determined thus:

$$B_n = \frac{2i^n\left[mkaJ_n(ka)J_n'(mka) - kaJ_n(mka)J_n'(ka)\right]}{ka\frac{d\psi_n}{d(ka)}J_n(mka) - mka\psi_n\frac{d}{d(mka)}\left[J_n(mka)\right]}$$

Although this is not obvious from the solutions, the usage of the Bessel functions along with their derivatives, as well as the general form of the solutions for B_n seems to indicate that this solution is mathematically similar to our mainstream solution.

This concludes the derivation.

Figure 2.6 shows two sets of extinction profiles which have been calculated not only to illustrate these results, but also to provide a test of two simple models which calculate the extinction of an infinite cylinder. Both cases are for perpendicular incidence, and the comparison is between the model whose code is printed in Bohren and Huffman (1983), which can only calculate results for perpendicular incidence, and another model, acquired from Flatau (personal communication), which can make such calculations for any arbitrary incidence. The attraction of the model from Bohren and Huffman (1983) is understandable, since at $\alpha = \frac{\pi}{2}$ the solution becomes much less complex:

$$\xi = ka \qquad \eta = mka$$

$$A_n = ik^2a^2\left[J_n'(mka)J_n(ka) - mJ_n(mka)J_n'(ka)\right]$$

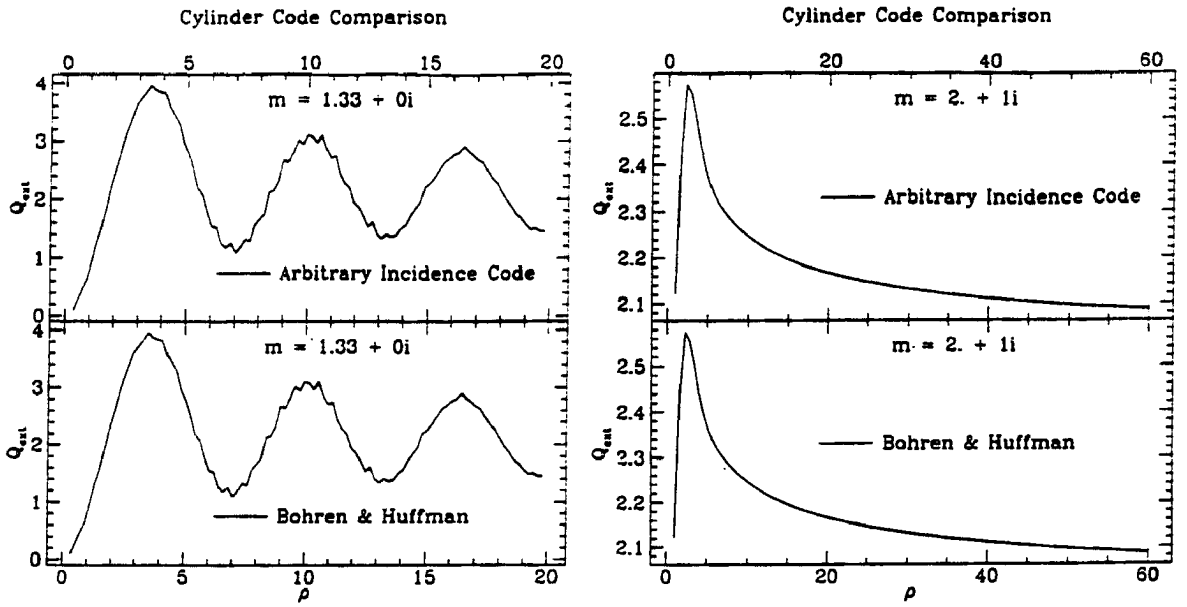

Figure 2.6: . Q_{ext} profiles from two separate infinite cylinder programs set for the perpendicular incidence case.

$$B_n = mk^2a^2\left[mJ_n'(mka)J_n(ka) - J_n(mka)J_n'(ka)\right]$$

$$C_n = 0 \qquad D_n = 0$$

$$V_n = mk^2a^2\left[mJ_n'(mka)H_n(ka) - J_n(mka)H_n'(ka)\right]$$

$$W_n = ik^2a^2\left[mJ_n(mka)H_n'(ka) - J_n'(mka)H_n(ka)\right]$$

$$a_{n1} = 0$$

$$b_{n1} = \frac{B_n}{V_n} = \frac{mJ_n'(mka)J_n(ka) - J_n(mka)J_n'(ka)}{mJ_n'(mka)H_n(ka) - J_n(mka)H_n'(ka)}$$

Since both models are applied in each case to an identical refractive index, they should yield identical results. The plots do indeed show such results.

A further application to concentrically inhomogeneous cylinders is given by Farone and Querfield (1966), and the solutions given utilize the determinant form mentioned earlier, but require much larger determinants.

As is discussed in Wait (1955), a situation arises when the cylinder becomes very thin which is analogous to the transition from Mie scattering to Rayleigh scattering when a

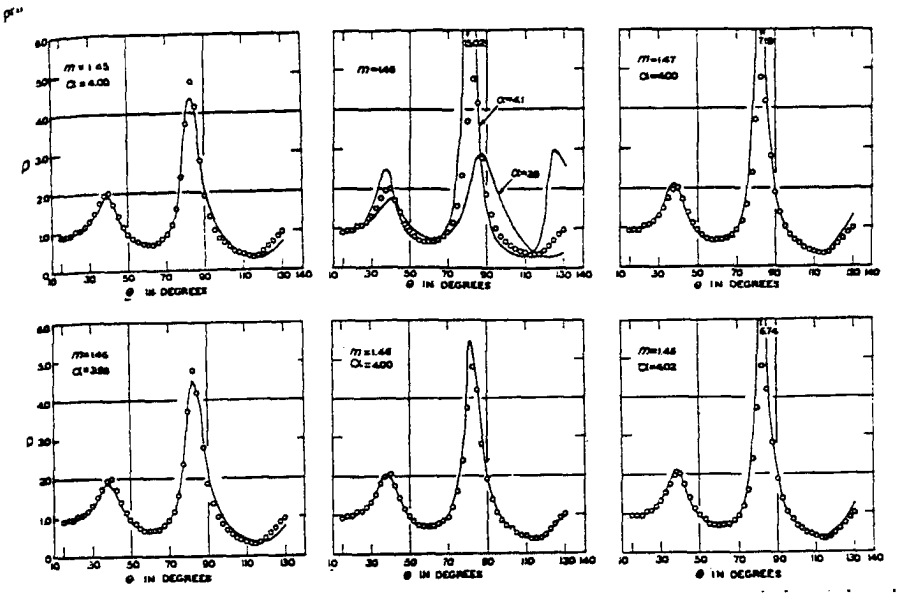

Figure 2.7: . Polarization ratios for silica fibers given as functions of scattering angle. Here $\lambda = 546\mu$m, and the same experimental results (circles) are presented in each plot along with theoretical results for a series of fibers of varying refractive index m and cylinder radius (For this figure $\alpha = \frac{2\pi r_{cyl}}{\lambda}$). As is evident from the plots, this technique enables the radius and refractive index of the fiber to be remotely sensed with great accuracy. (from Farone and Kerker (1966).)

spherical scatterer becomes very small, thus reaching a point where only the first coefficient of the harmonic series is non-negligible. In this case, a_0, $a_{\pm 1}$, and $b_{\pm 1}$ remain as non-negligible, thus simplifying the solution considerably.

2.2 Finite Cylinder Observations

There are generally two classes of studies which span the experimental domain on this subject. The first involves the study of thin fibers, and the second involves observations on actual cylinders, usually a microwave study making use of cylinders on the order of 10 cm in size. The cylinders are usually composed of a solidified mixture of two substances mixed together in varying degrees so that the dielectric properties of the cylinders can be easily varied.

We begin with the study of thin fibers, since we just so recently mentioned them in our section on theory. Farone and Kerker (1966) began this investigation with the case of

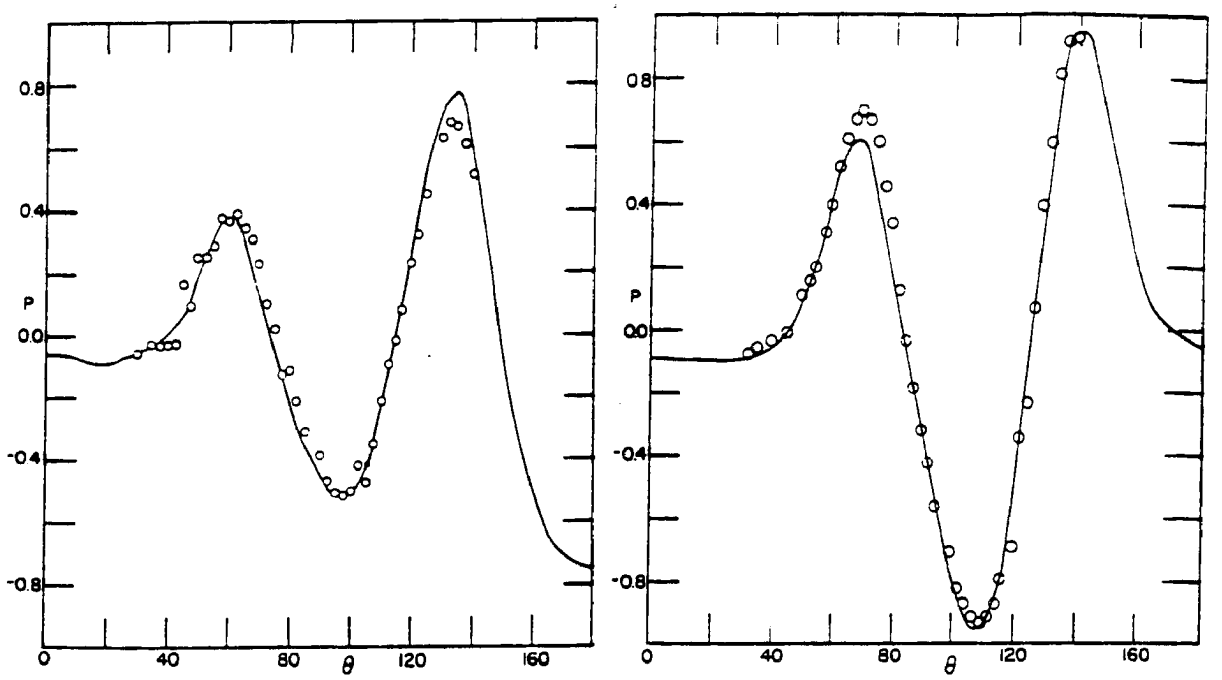

Figure 2.8: . Experimental scattering results from Cooke and Kerker (1969) done on thin Pyrex fibers. The results are for polarization, and show comparisons of experimental data (circles) with theory (solid curves) as a function of scattering angle. Results are for $\lambda = .546\mu m$. The left plot shows the case of $\beta = 2.99$ and $\alpha = 90$, and the right plot a case of $\beta = 2.94$ and $\alpha = 60$ (from Farone and Kerker (1966)).

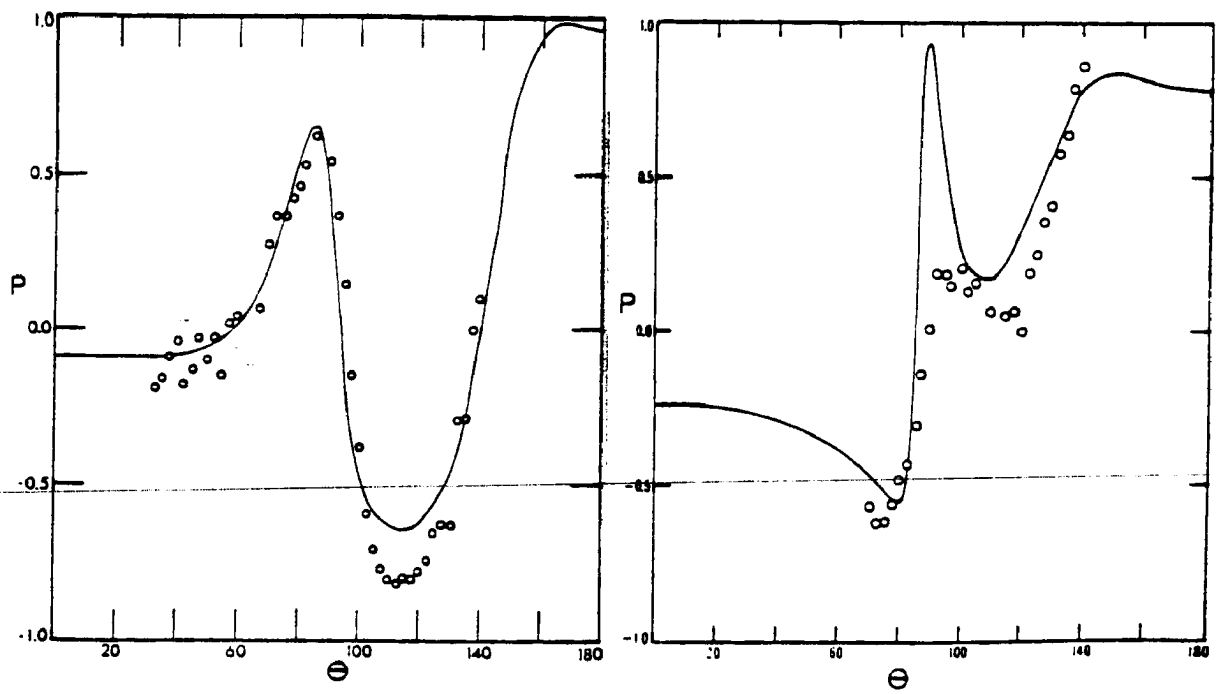

Figure 2.9: . Same as figure 2.8 but for $\beta = 2.76$ and $\theta = 45$ (left) and $\beta = 2.78$ and $\alpha = 30$ (right). (From Farone and Kerker (1966)).

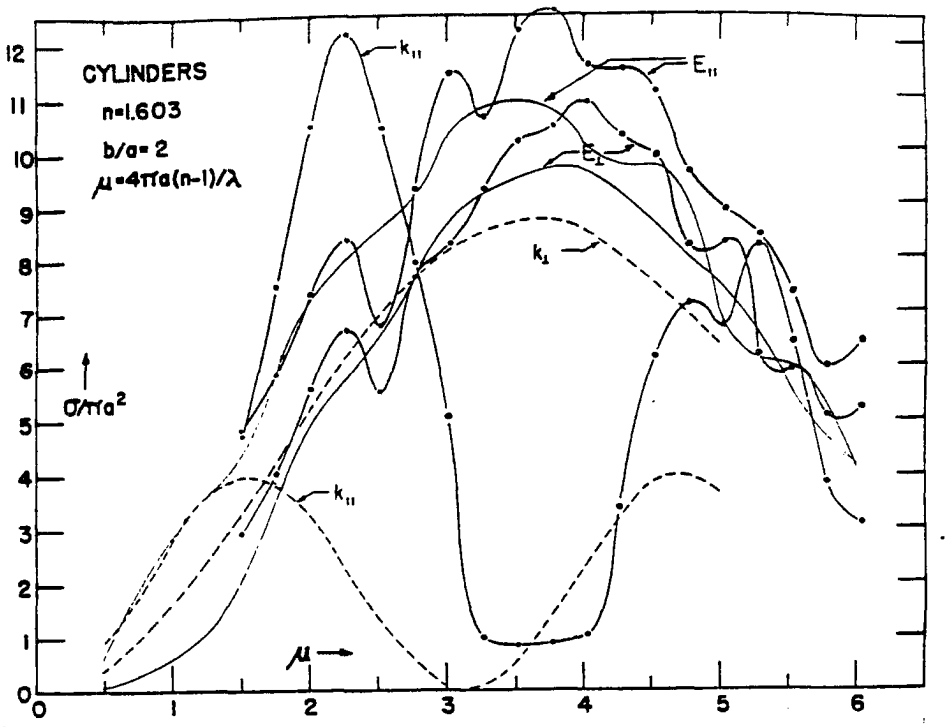

Figure 2.10: . Q_{ext} profiles taken from experimental results (heavy solid curves and dotted curves) as well as theoretical results which assume that the cylinders are infinite (solid fine curves) taken as a function of cylinder radius. Here $m = 1.603$ and $\beta = 2$. Within each set of curves $k_\perp$, $k_{||}$, $E_\perp$, and $E_{||}$ denote the direction of the propagation vector and the electric vector of the incident beam relative to the axis of the cylinder (from Greenberg et al. (1961)).

perpendicular incidence. Using Pyrex and silica fibers of varying thicknesses, the results, shown in figure 2.7, compared well with theory, even providing a methodology of 'remotely sensing' the fiber radius to within an accuracy of one percent. Cooke and Kerker (1969) extended this to oblique incidence and examined the depolarization at various scattering angles. As can be seen by figures 2.8 and 2.9, the results again compared well with theory, especially at angles close to perpendicular incidence. Apparently at oblique angles longer fiber lengths are required for the cylinder to act as an infinite cylinder.

Greenberg et al. (1961) began the work in our second category, the results of whom are presented in figures 2.10 through 2.12. Although there was a different refractive index used here than in this present study, there are certain relevant qualitative observations which can be gathered. From figure 2.10 it is apparent that for perpendicular incidence at this aspect ratio, infinite cylinder values of extinction provide a good approximation to the extinction of these cylinders. From figure 2.11 it is visible that the extinction per unit

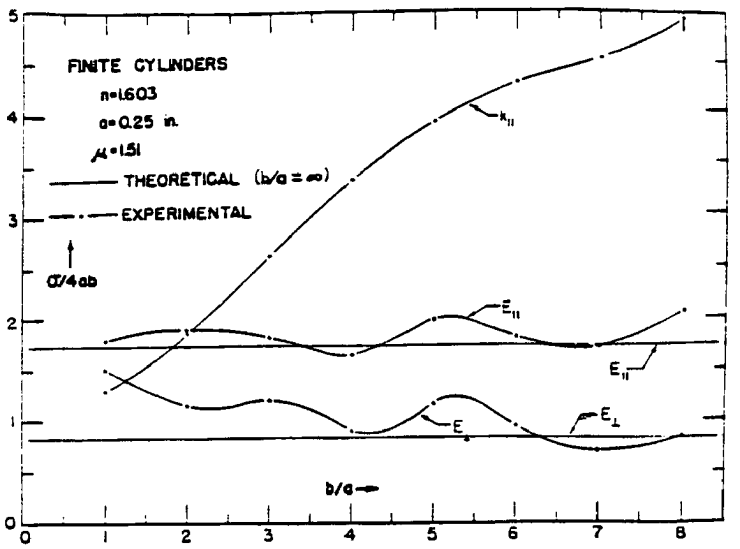

Figure 2.11: . Experimentally derived values of extinction per unit length for finite cylinders as a function of aspect ratio and compared with theoretical values for infinite cylinders. Here $m = 1.603$, $\lambda = 1.254$ inches, and $r_{cyl} = .25$ inches. The results are taken for two polarizations and with the same labels as in figure 2.10 (from Greenberg et al. (1961)).

length of a finite cylinder as it is elongated to an infinite cylinder can go through a series of maxima and minima, oscillating about the infinite cylinder value. We will also witness both of these effects in chapter 3. Thirdly, in figure 2.12, there is an effect, for the case of parallel incidence, in which the extinction exhibits a very strong maximum. It is postulated by the previous authors that this effect is due to the cylinder acting as a waveguide. We will address this issue in our results more intensively in chapters 3 and 4. Figures 2.13 and 2.14 are from Allan and McCormick (1980), who performed calculations of phase functions as well as polarization information. It is clear from this figure the degree to which the angular structure becomes more complex as the radius of the cylinder increases.

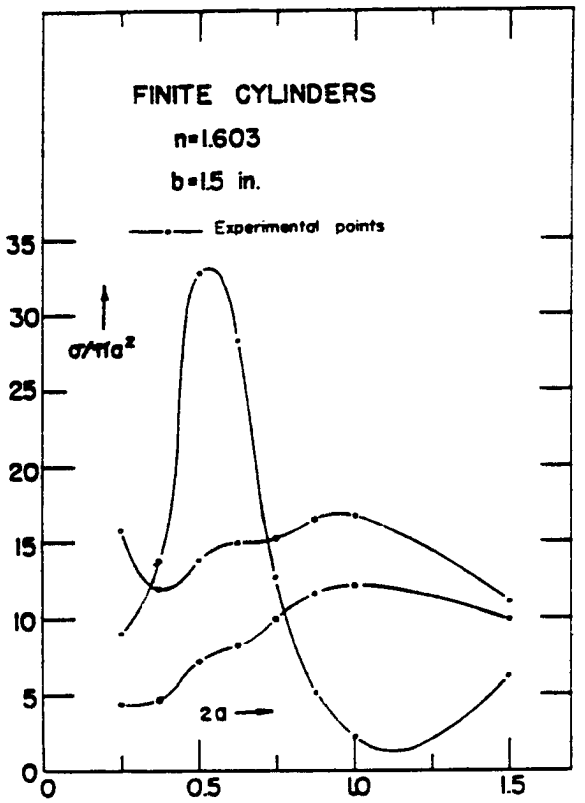

Figure 2.12: . Experimentally derived values of extinction per unit cross sectional area when viewed in the axial direction, given as a function of cylinder radius. Here m and λ are the same as in figure 2.11, and the cylinder length is held constant at 1.5 inches (from Greenberg et al. (1961)).

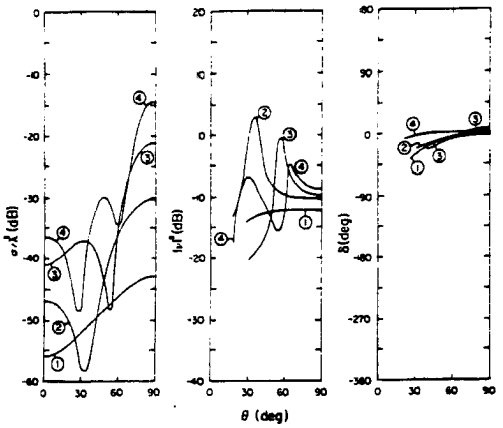

SAMPLE NUMBER	①	②	③	④
ka	0.1143	0.1904	0.2666	0.3428
c/a	10.00	9.99	9.99	10.00
Re(ϵ)	3.13	3.13	3.15	3.14

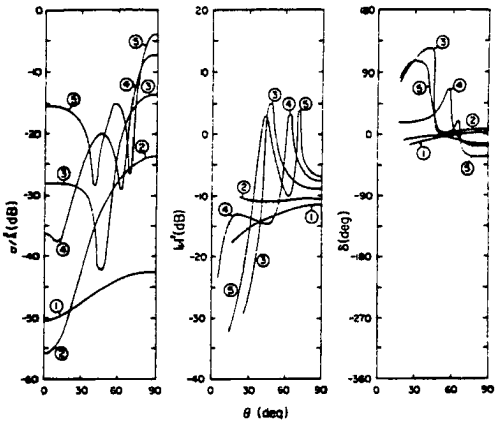

SAMPLE NUMBER	①	②	③	④	⑤
ka	0.152	0.305	0.458	0.610	0.762
c/a	5.00	5.01	5.00	4.99	5.00
Re(ϵ)	3.15	3.13	3.14	3.16	3.14

Figure 2.13: . Experimentally derived extinction efficiencies and degrees of polarization taken as functions of incidence angle for cylinders and disks of various sizes relative to the wavelength ($ka = kr_{cyl}$) as well as aspect ratios ($\frac{c}{a} = \beta$), and refractive indices ($Re(\epsilon)$ is the real part of the dielectric constant and is related to the refractive index by the equation $Re(m) = \sqrt{\frac{\epsilon}{\epsilon_0}}$, assuming the substance to be nonferromagnetic (from Allan and McCormick (1980)).

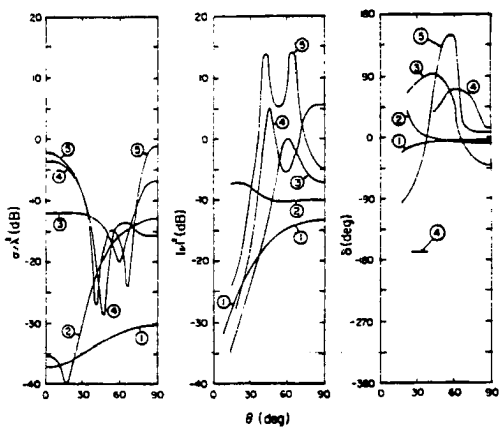

SAMPLE NUMBER	①	②	③	④	⑤
ka	0.305	0.609	0.914	1.219	1.523
c/a	2.500	2.503	2.498	2.499	2.495
Re(ϵ)	3.16	3.14	3.14	3.12	3.13

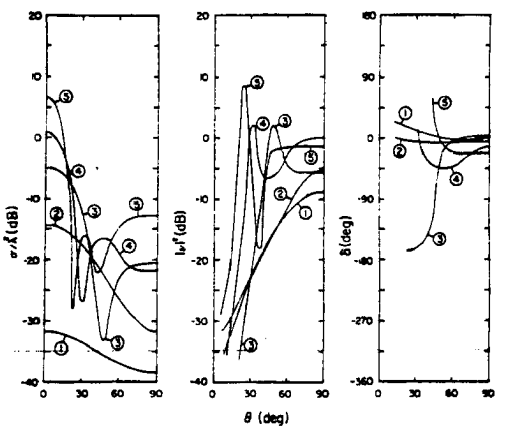

SAMPLE NUMBER	①	②	③	④	⑤
ka	0.762	1.523	2.283	3.042	3.792
c/a	0.1060	0.1000	0.1008	0.1009	0.1020
Re(ϵ)	3.12	3.11	3.13	3.10	3.16

Figure 2.14: . Same as figure 2.13. Note that the rightmost plot deals with disks instead of cylinders (from Allan and McCormick (1980)).

Chapter 3

RESULTS FROM THE DISCRETE DIPOLE APPROXIMATION

With most of the theoretical bones in place we now begin the process of putting onto them some appropriate new meat, beginning with the results gained through our usage of the Discrete Dipole Approximation. Since its theoretical development and previous usage has not yet been explained, we begin this chapter with such a review, thus providing a partial discussion of the third category of previous cylinder scattering work, listed in the previous chapter. We then give an explanation of our procedures used with this model and then proceed with the results themselves, which are divided into their three forms, known from chapter 1 as the extinction efficiency, Q_{ext}, the single scatter albedo, ω_0, and the asymmetry parameter, g. We conclude with a summary discussion of the observations where we also apply the results to larger particles.

3.1 Explanation, History, and Previous Cylinder Studies

The Discrete Dipole Approximation originates from the intuitively sensible notion that the scattering effects of a given particle are equal to a summation of the scattering effects of the constituent subparticles which together make up the particle. This idea can be traced even as far back as Lord Rayleigh (1881) :

'..we see that, under the circumstances in question, each element of a homogeneous obstacle acts independently as a centre of disturbance, and that the aggregate effect in any direction depends upon the phases of the elementary secondary disturbances as affected by the situation of the element along the paths of the primary and secondary light.'

The size, shape, and number of these constituent subparticles, or 'elements', is arbitrary, resulting from arbitrary divisions made of the particle.

DDA is not the only technique which has utilized this idea. The application of Mie theory to the solution for coated spheres (that is, inhomogeneous spheres whose refractive index is only a function of radius) utilizes this notion, as do all problems in radiative transfer partcile scattering which make use of boundary conditions. In the same way, Fuller (1988 and 1991) has extended Mie Theory to a series of solutions for two or more conglomerate spheres.

In the case of DDA, instead of using spheres, we make use of a simpler particle, the dipole, whose relatively simplistic scattering solution is exploited to make this technique as computationally efficient as possible. All that is required to depict the scattering solution of a dipole is a simple dielectric polarization response vector. The drawback, however, is that a diplole, by definition, is an infinitessimally small particle, an approximate form of the scattering solution of a finite particle which is asymptotically approached as the particle becomes very small. The problem, then, with the usage of dipoles is obvious; an infinite number of such particles is required to consummately depict a finite particle. The question one arrives at is analogous to the use of a finite grid or a finite number of wavenumbers in a synoptic weather forecasting model or GCM. The question is to the degree to which nature can be 'cheated' – the degree to which a macroscopic particle, exactly represented by an infinite number of dipoles, can be adequately represented by a large, but finite number of dipoles, the number of which we will hereafter refer to as N.

As it turns out, this threshold in which results become adequate is reasonably well-understood, and a general rule of thumb given by Flatau (personal communication) is given as follows:

Quantity for which Accuracy is Desired	$Re\{m\} \cdot kd$
Q_{ext}	.8
g	.5

where $k = \frac{2\pi}{\lambda}$ and d is the relative spacing of the dipoles, assuming them to be arranged in a cubical lattice. According to Flatau (1992), phase functions can also be depicted well, but only with a much higher constraint, where $Re\{m\}kd \sim .1$ and less.

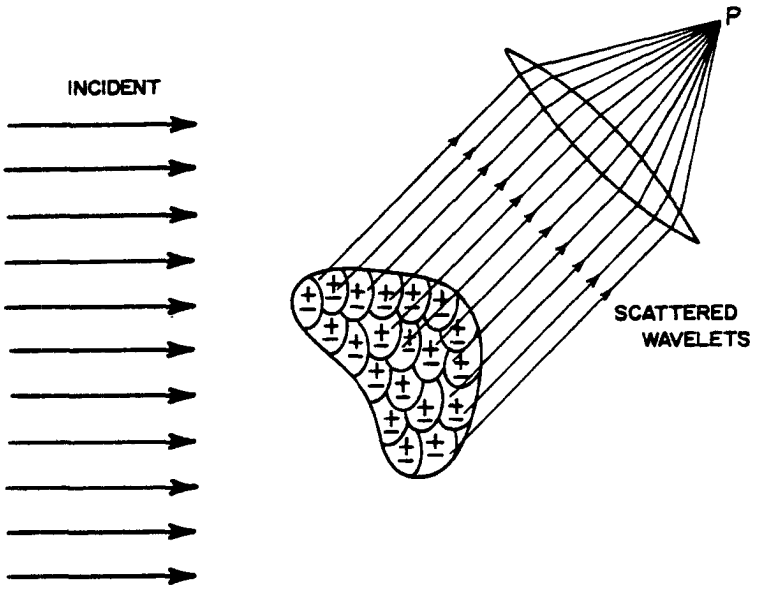

Figure 3.1: . Schematic drawing of particle subdivision and its use in particle scattering. The field at point P is the resultant of the scattering fields emitted by each of the subparticles (from Bohren and Huffman (1983)).

The basic idea is illustrated in figure 3.1, from Bohren and Huffman (1983), in which the scattering effects of each dipole are summed up to give a combined response. Although this provides a good introduction to the theory, this alone is not DDA, but another faster and less useful application known as Rayleigh-Gans theory. The additional step required for DDA is to make the dipole polarization responses not only a function of the incident wave, but also of the scattering responses of the dipoles themselves - to consider not only the interactions of the dipoles with the incident wave, but also the mutual interactions that the dipoles communicate to each other. This effect becomes increasingly important as the particle increases in size or when its refractive index increases beyond being close to 1. Mathematically, this involves the solution of the following matrix equation:

$$\mathbf{E}_{inc} = \mathbf{AP} \tag{3.1}$$

where $\mathbf{E}_{inc}$ is a $3N$-long vector describing the incident field at the location of each dipole. $\mathbf{A}$, sometimes, known as the 'DDA Matrix' is a $3N \times 3N$ matrix governing the interactions between dipoles. $\mathbf{P}$ is a $3N$-long vector which gives a stable, self-consistent set of solutions

for the polarization responses of the dipoles. The solution is, thus, found by first solving for $\mathbf{P}$ by inverting $\mathbf{A}$:

$$\mathbf{P} = \mathbf{A}^{-1}\mathbf{E}_{inc}$$

and then using $\mathbf{P}$ to solve for the scattering properties according to the following equations given in Draine (1988):

$$C_{ext} = \frac{4\pi k}{|\mathbf{E}_{inc}|^2}\sum_{j=1}^{N} Im\left\{\mathbf{E}^*_{inc,j}\cdot\mathbf{P}_j\right\}$$

$$C_{abs} = \frac{4\pi k}{|\mathbf{E}_{inc}|^2}\sum_{j=1}^{N}\left[Im\left(\mathbf{P}_j\cdot\frac{1}{\alpha_j}\mathbf{P}_j\right) - \frac{2}{3}k^3\mathbf{P}_j\cdot\mathbf{P}_j^*\right]$$

$$C_{sca} = \frac{k^4}{|\mathbf{E}_{inc}|^2}\int\left|\sum_{j=1}^{N}\left[\mathbf{P}_j - \hat{\mathbf{n}}(\hat{\mathbf{n}}\cdot\mathbf{P}_j)e^{-ik\hat{\mathbf{n}}\cdot\mathbf{r}_j}\right]\right|^2 d\Omega$$

$$g \equiv \langle\cos\theta\rangle = \frac{k^3}{C_{sca}\,|\mathbf{E}_{inc}|^2}\int\left|\sum_{j=1}^{N}\left[\mathbf{P}_j - \hat{\mathbf{n}}(\hat{\mathbf{n}}\cdot\mathbf{P}_j)e^{-ik\hat{\mathbf{n}}\cdot\mathbf{r}_j}\right]\right|^2 \hat{\mathbf{n}}\cdot\mathbf{k}d\Omega$$

where C_{ext}, C_{sca}, and C_{abs} are the extinction, scattering, and absorption cross sections, respectively. The dipole polarizability is denoted by α_j. The unit vector pointing in a given scattering direction is denoted by $\hat{\mathbf{n}}$, which has an angle relative to the incident beam of θ ($\mathbf{k}\cdot\hat{\mathbf{n}} = k\cos\theta$). As in the previous chapter, an asterisk denotes the complex conjugate. Also, the amplitude and phase of the incident wave at the location of an individual dipole is denoted by $\mathbf{E}_{inc,j}$, and the latter two expressions show integrals over the entire scattering solid angle, Ω.

Of course, the more difficult of these two tasks is the solution of equation 3.1, which involves the inversion of a very large matrix. We, thus, turn our attention more intensely to a further understanding of this DDA matrix in the hope of achieving a shortcut in arriving at its inversion.

Another way of conceiving the inversion of equation 3.1 is the following, also from Draine (1988):

$$\mathbf{P}_j = \alpha_j\left(\mathbf{E}_{inc,j} - \sum_{j\neq k}\mathbf{A}_{jk}\mathbf{P}_k\right) \tag{3.2}$$

where the individual dipole responses, $\mathbf{P}_j$, are clearly divided between their contributions from the incident field:

$$\mathbf{P}_{j,inc} = \alpha_j\mathbf{E}_{inc,j} \tag{3.3}$$

and their contributions from each other:

$$\mathbf{P}_{j,dip} = -\alpha_j \sum_{j \neq k} \mathbf{A}_{jk}\mathbf{P}_k$$

$$= -\alpha_j \sum_{j \neq k} \frac{e^{ikr_{jk}}}{r_{jk}^3} \left\{ k^2 \mathbf{r}_{jk} \times (\mathbf{r}_{jk} \times \mathbf{P}_k) + \frac{1 - ikr_{jk}}{r_{jk}^2} \left[r_{jk}^2 \mathbf{P}_k - 3\mathbf{r}_{jk} (\mathbf{r}_{jk} \cdot \mathbf{P}_k) \right] \right\} \qquad (3.4)$$

where $\mathbf{r}_{jk}$ and its magnitude r_{jk} describe the vector spanning the difference in positions of the dipoles j and k. The polarizability, α_j, is again according to Draine (1988), arrived at only after some nontrivial consideration. The Clausius-Mossoti relation, which provides this relationship between macroscopic optical properties and infinitesimal dipole properties:

$$\alpha_j^0 = \frac{3}{4\pi n} \frac{\epsilon - 1}{\epsilon + 2}$$

where n is the number density of dipoles, only works exactly in cases of constant applied fields. The adjustment to periodic fields, also described in Draine (1988) as well as in Jackson (1975) is as follows:

$$\alpha_j = \frac{\alpha_j^0}{1 - \frac{2i}{3N} (k a_{eq})^3 \frac{\epsilon - 1}{\epsilon + 2}}$$

where we have ruled out the presence of optical anisotropies for simplicity. Referring again to equations 3.1 and 3.2, it becomes clear that, since:

$$\mathbf{E}_{inc,j} = \sum_{j \neq k} \mathbf{A}_{jk}\mathbf{P}_k + \frac{1}{\alpha_j}\mathbf{P}_j = \sum \mathbf{A}_{jk}\mathbf{P}_k$$

then,

$$\mathbf{A}_{jj} = \frac{1}{\alpha_j} \quad \forall \quad j = 1...N$$

and, thus, it is understood that the diagonal elements of $\mathbf{A}$ are trivial. Another property is that $\mathbf{A}$ exhibits the following symmetry:

$$\mathbf{A}_{jk} = \mathbf{A}_{kj} \qquad (3.5)$$

which can be immediately seen from equation 3.4 since:

$$r_{jk} = r_{kj} \quad \mathbf{r}_{jk} = -\mathbf{r}_{kj}$$

and since the operations:

$$\mathbf{r} \times (\mathbf{r} \times \mathbf{P}) \qquad \mathbf{r}(\mathbf{r} \cdot \mathbf{P})$$

both remain the same when $\mathbf{r} = -\mathbf{r}$:

$$\mathbf{A} \times (\mathbf{A} \times \mathbf{B}) = (-\mathbf{A}) \times [(-\mathbf{A}) \times \mathbf{B}] \qquad \mathbf{A}(\mathbf{A} \cdot \mathbf{B}) = (-\mathbf{A})[(-\mathbf{A}) \cdot \mathbf{B}]$$

The symmetry in equation 3.5 is shown and can be exploited to reduce the storage requirements of the matrix. In addition, it has been shown by Flatau et al. (1989) that in the case of rectangular particles the matrix **A** also has a Block-Toeplitz structure, which serves to lessen further the memory requirements as well as the solution time.

In most cases, however, the conjugate-gradient technique is the most feasible and efficient solution technique. This technique generates a sequence of vectors $\mathbf{P}_j^k$ (k referring here to the iteration number) which converge exactly to the actual solution in N iterations and in most cases far less than N iterations. What is most powerful about this technique is that it by-passes the prohibitively time consuming task of inverting the matrix **A** and in its solution only requires the following matrix-vector products:

$$\mathbf{A} \cdot \mathbf{P}_j^k$$

$$\mathbf{A}^\dagger \cdot \mathbf{P}_j^k$$

where $\mathbf{A}^\dagger$ is the Hermitian conjugate of **A**, also known as the transpose of the complex conjugate:

$$\mathbf{A}_{ij}^\dagger = \mathbf{A}_{ji}^*$$

Recalling once again equations 3.4 and 3.5 we are reminded that **A** is a matrix which depends only on the value of the vector $\mathbf{r}_{ij}$. Thus, the value of $\mathbf{A}_{ij}$ depends only on the difference in its indices, and the above products can be written in the following form:

$$\mathbf{Y}_i = \sum_j \mathbf{A}_{ij} \cdot \mathbf{P}_j^k = \sum_j \mathbf{A}'_{i-j} \cdot \mathbf{P}_j^k \tag{3.6}$$

$$\mathbf{Y}'_i = \sum_j \mathbf{A}_{ij}^\dagger \cdot \mathbf{P}_j^k = \sum_j \mathbf{A}_{i-j}^{\dagger\prime} \cdot \mathbf{P}_j^k \tag{3.7}$$

where $\mathbf{A}'_{i-j}$ and $\mathbf{A}_{i-j}^{\dagger\prime}$ are vector forms of the matrices **A** and $\mathbf{A}^\dagger$:

$$\mathbf{A}'_{i-j} = \mathbf{A}_{ij} \quad \mathbf{A}_{i-j}^{\dagger\prime} = \mathbf{A}_{ij}^\dagger \qquad (j \neq k)$$

With this in mind, the convolution of any functions $f(x)$ and $g(x)$ is defined as follows:

$$f * g = \int_{-\infty}^{\infty} f(u)g(x-u)du$$

and, thus, since $\mathbf{A}'$ and $\mathbf{A}^{\dagger\prime}$ display the properties seen in equations 3.6 and 3.7, $\mathbf{A}'$ and $\mathbf{A}^{\dagger\prime}$ have the same form in these equations as g in the above equation, revealing equations 3.6 and 3.7 to be convolutions. An important theorem, often referred to as the 'convolution theorem', states that the Fourier transform of the convolution of $f(x)$ and $g(x)$ is equal to the product of the Fourier transforms of $f(x)$ and $g(x)$:

$$\widehat{f * g} = \hat{f} \cdot \hat{g}$$

where $\hat{f}$ denotes the fourier transform of the function f.

For our purposes this means that equations 3.6 and 3.7 can be solved through Fourier transforms:

$$\hat{\mathbf{Y}}_n = \hat{\mathbf{A}}'_n \cdot \hat{\mathbf{P}}_n$$

$$\hat{\mathbf{Y}}'_n = \hat{\mathbf{A}}^{\dagger\prime}_n \cdot \hat{\mathbf{P}}_n$$

where n represents a quantity in frequency space. $\mathbf{Y}_i$ and $\mathbf{Y}'_i$ are then constructed from their respective Fourier components, $\hat{\mathbf{Y}}_n$ and $\hat{\mathbf{Y}}'_n$. Thus, the specific form of the conjugate-gradient solution technique makes the use of Fourier transforms possible, which further increases the solution efficiency. This is the present 'state-of-the-art' of the model which is utilized in this chapter.

The model in an earlier form was first utilized by Purcell and Pennypacker (1973) towards the solution for rectangular grains. The use of the conjugate-gradient technique was first introduced by Draine (1988) as he provided solutions for interstellar hexagonal graphite cylinders and disks. Some of his results are presented in figure 3.2. The plots are comparisons of an observed extinction peak to the calculated extinction profiles of randomly oriented graphite cylinders of various sizes and aspect ratios ($\beta = \frac{a}{b}$). The best fit was found for cylinders in which $a_{eff} = 100$ angstroms and $\beta = .645$ as well as when $a_{eff} = 200$ angstroms and $\beta = 1.47$.

The work on rectangular solids was echoed somewhat by Flatau et al. (1989) as they introduced the Block-Toeplitz structure of the matrix A. Evans and Vivekanandan (1990)

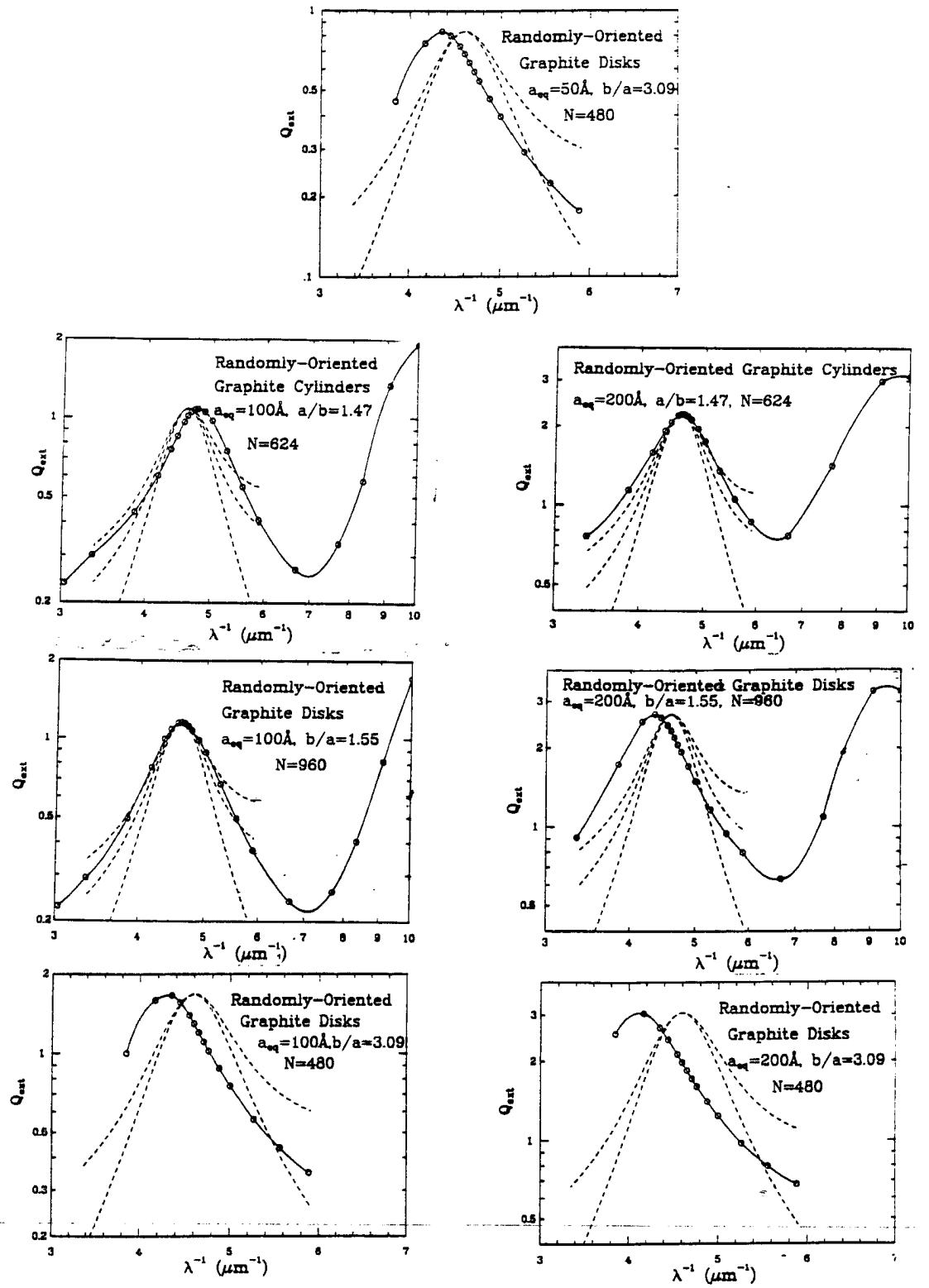

Figure 3.2: . Extinction efficiency results for hexagonal graphite cylinders and disks compared with an observed interstellar absorption peak (from Draine (1988)).

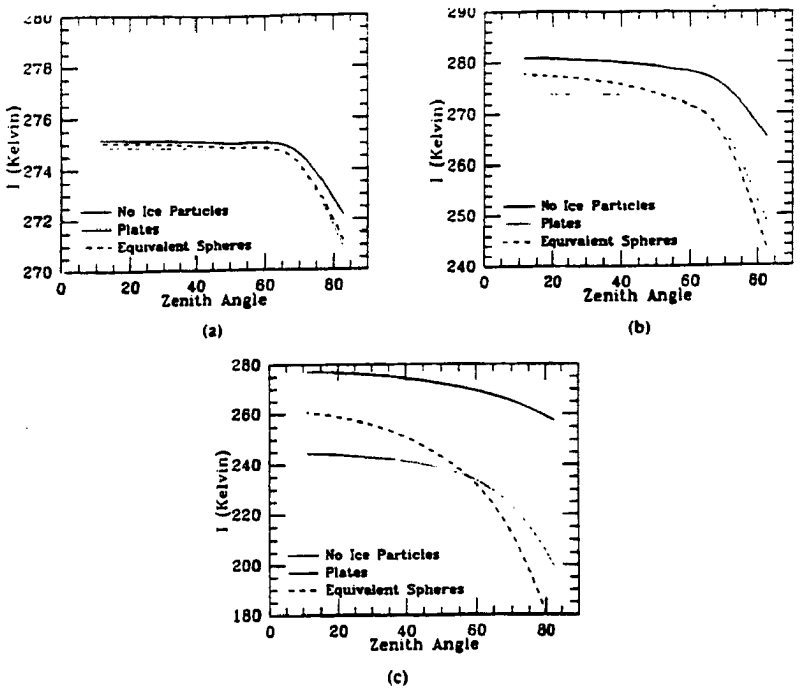

Figure 3.3: . Upwelling brightness temperature I as a function of zenith angle for a layer of solid plates, equivalent volume spheres, and the absence of an ice layer. The results are for three microwave frequencies - 37 GHz (a), 85 GHz (b), and 157 GHz (c) (from Evans and Vivekanandan (1990)).

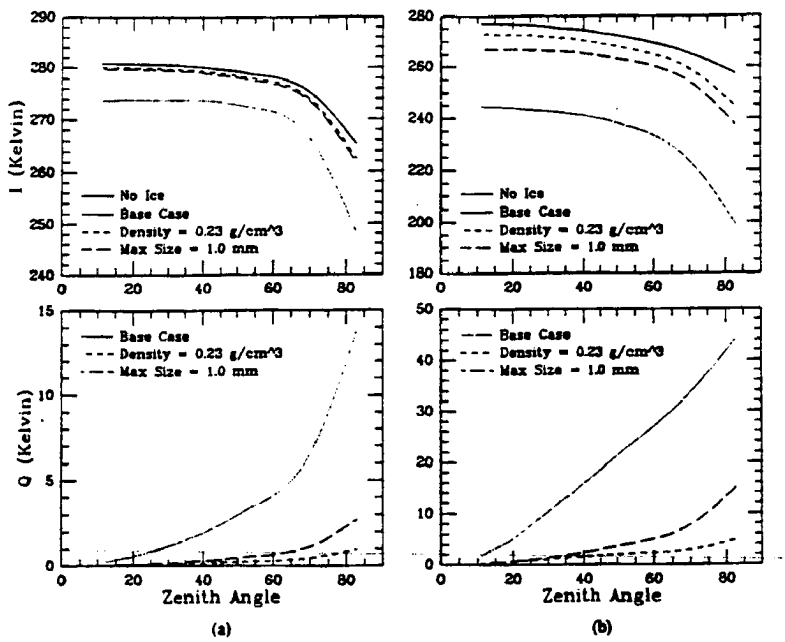

Figure 3.4: . Upwelling brightness temperature I and polarized brightness temperature Q as functions of zenith angle. The results are for 85 GHz (a) and 157 GHz (b), and they compare plates having bulk densities of .92 g/cm^3 and maximum sizes of 2 mm with plates having bulk densities of .23 g/cm^3 as well as with plates having maximum sizes of 1 mm. (from Evans and Vivekanandan (1990)).

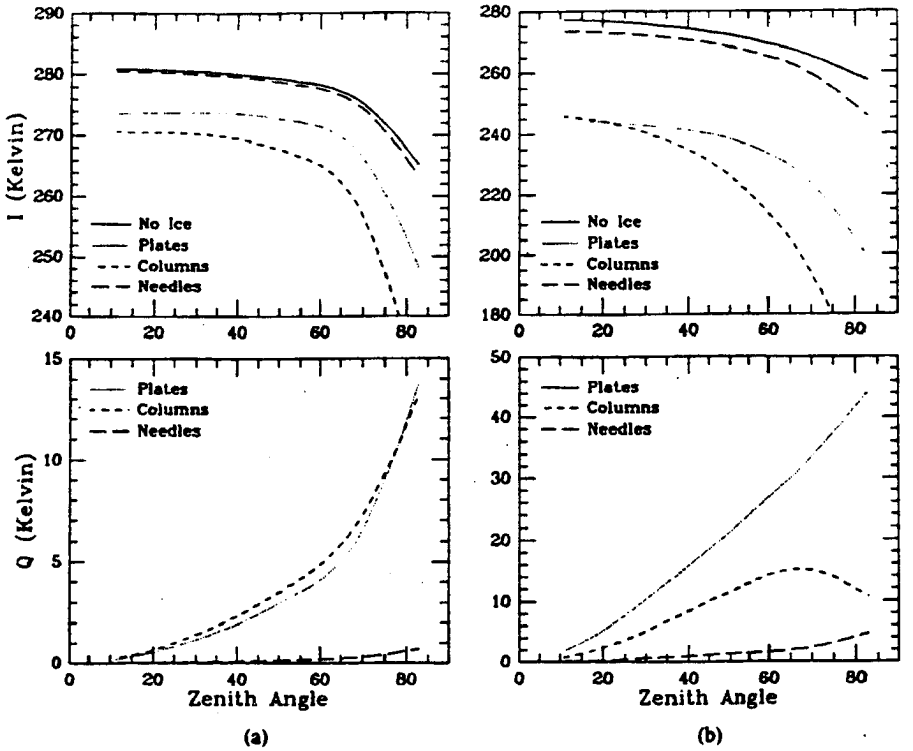

Figure 3.5: . Same as in figure 3.4 except that plates, columns, needles, are compared along with the absence of an ice layer. (from Evans and Vivekanandan (1990)).

applied DDA to hexagonal cylinders for three microwave frequencies. Figures 3.3 through 3.5 are from the latter study and show upwelling brightness temperatures for the Stokes parameter I (total unpolarized intensity) as well as Q (polarized intensity) in figures 3.4 and 3.5, all shown as functions of zenith angle, measured at the top of the atmosphere. Figure 3.3 compares results for ice spheres, plates, and the absence of an ice layer for three microwave frequencies. The results show the strongest sensitivities to the presence of ice at the highest frequencies in addition to showing that the equivalent spheres technique is a poor approximation for plates. In particular the third plot implies an overestimation of the asymmetry parameter by the equivalent spheres technique, thus overestimating the forward scatter. Figure 3.4 shows the same intensities as well as degrees of polarization for plates (Base Case) compared with plates having smaller bulk densities and plates which are smaller in diameter. The plot reveals a strong sensitivity to maximum particle size as well as to decreases in the bulk density of the particle which may arise from small bubbles or porous surfaces. Thirdly, in figure 3.5 they compared plates, columns, and needles individually. Each case was run with an ice mass of .1 g/m^3 and with a maximum particle size of 2 mm. The results show a comparatively small effect from needles as compared with plates and

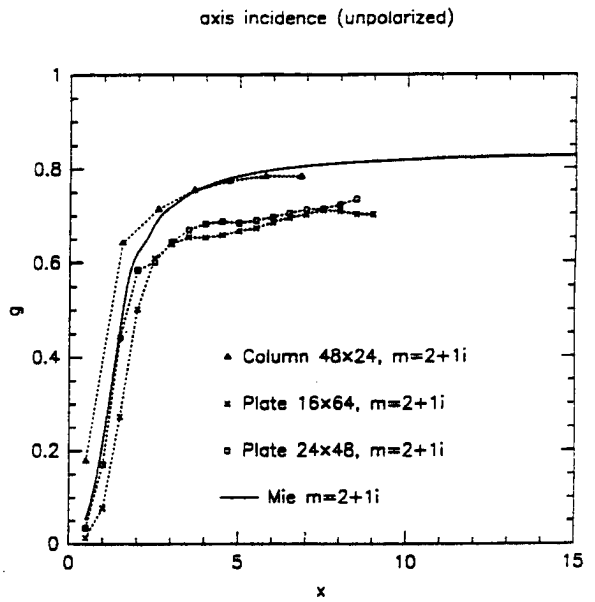

Figure 3.6: . Asymmetry parameter calculations for cylinders with dipole dimensions of 48 × 24 ($\beta = 2$), 16 × 64 (disk in which $\beta = .25$), and 24 × 48 (disk in which $\beta = .5$). Here $m = 2 + 1i$ (from Flatau (1992)).

columns which the authors attribute to the smaller sizes of needles, showing a third element of sensitivity, particle volume. At their maximum sizes, columns possess twice the volume of plates and twenty times the volume of needles.

Dungey and Bohren (1991) applied DDA to spheroids and ellipsoids. The FFT technique for enhancing the conjugate-gradient solution technique was first introduced by Goodman et al. (1991) as they tested it on spheres. Lastly, Flatau (1992) demonstrates the development of the current model as well as a series of calculations on a myriad of example particles, some of which were hexagonal plates and columns. Figures 3.6 through 3.8 show plots of g as functions of a_{eff} for cylinders and disks with β values of 2, .25, and .5. Figure 3.6 confirms the suspicion discussed in response to figure 3.3, that the use of equivalent spheres causes an overestimation of g for the case of cylindrical particles in a size range which we will later define as large particles, but the nonabsorbing cases shown in figures 3.7 and 3.8 show more of an underestimation. This implies that the overestimation of g suggested by figure 3.3 may be largely due to contributions from within absorption bands, where the real and imaginary parts of m fluctuate greatly.

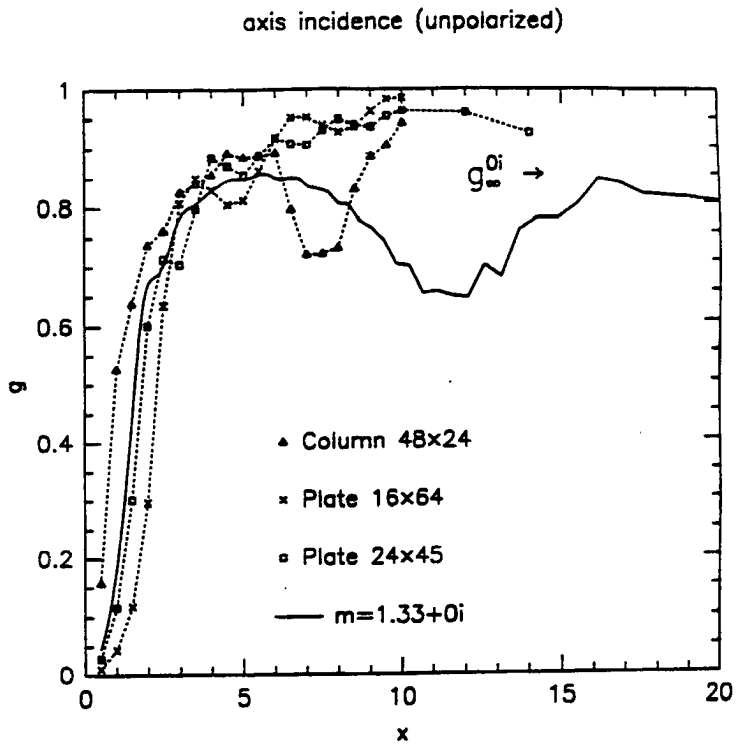

Figure 3.7: . Same as in figure 3.6 but with $m = 1.33 + 0i$ (from Flatau (1992)).

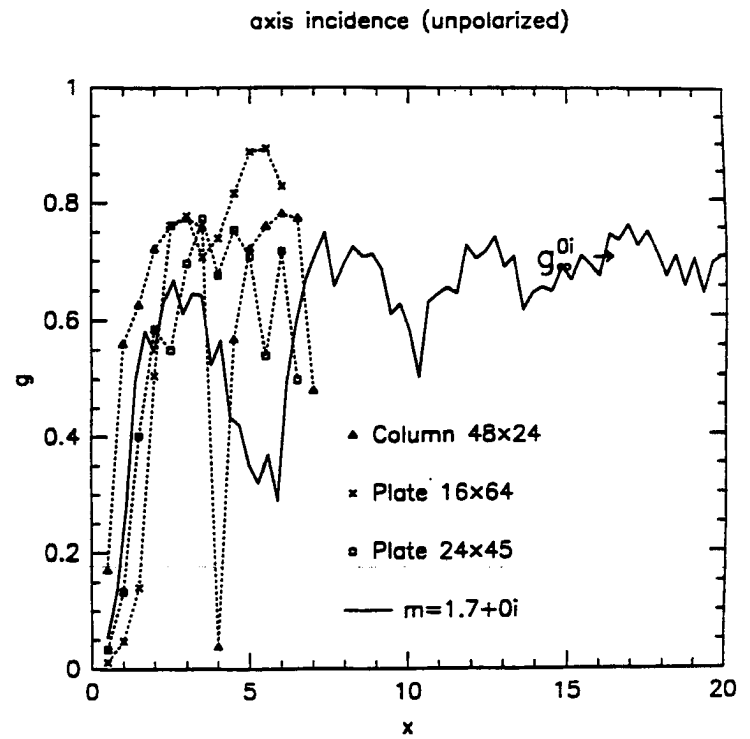

Figure 3.8: . Same as in figure 3.6 but with $m = 1.7 + 0i$ (from Flatau (1992)).

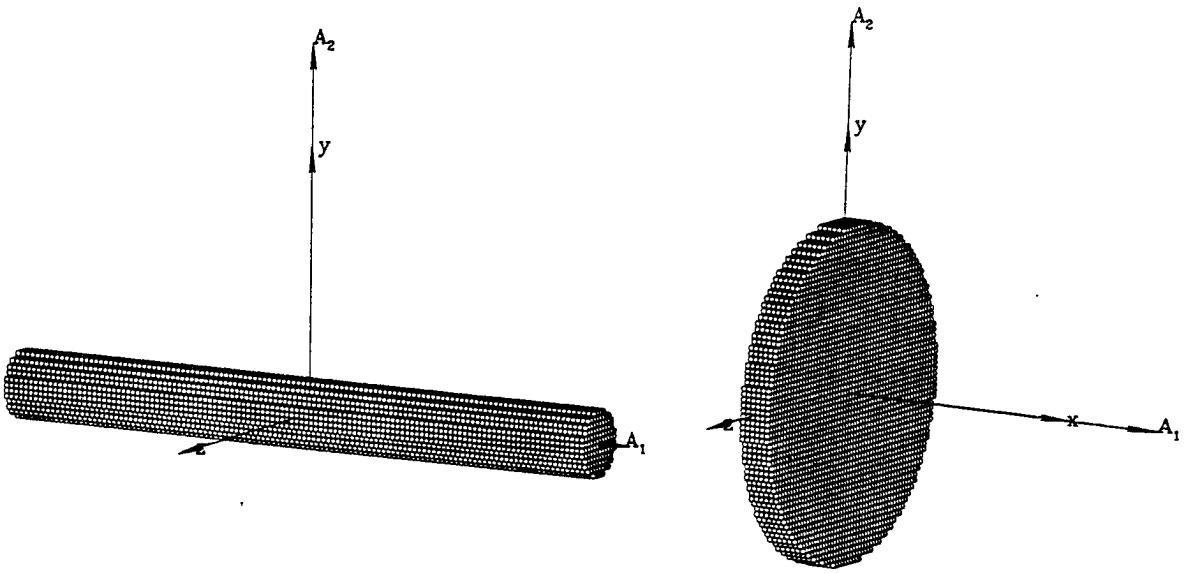

Figure 3.9: . Dipole constructions for a pseudo-cylinder of aspect ratio 10, and a pseudo-disk of aspect ratio .1.

3.2 The Model and Its Present Usage

The specific DDA model which was used in this study was developed by B. Draine and P. Flatau, and a complete discussion of its development can be found in Flatau (1992). The model was applied for the purpose of studying the behavior of circular cylinders of various sizes, aspect ratios, refractive indices, and incidence angles. Figure 3.9 shows the dipole construction for the two aspect ratio extremes in the current study. There were a total of 21 values of aspect ratio chosen between (and including) .1 and 10, the former representing a considerably thin disk and the latter a long cylinder. The wavelength, λ, for this entire study was kept constant at a value of 2π, which does not mean that this was a monochromatic study since the refractive index was varied and, thus, the wavelength only had a meaning relative to the given size of the cylinder. With this relative size of the wavelength in place at a constant value, the cylinder radius, r_{cyl}, was given 21 values ranging between (and including) .2 and 10. Thus, with an actual 'real world' wavelength of, say, 6.28 microns, this corresponds to particles with radii of up to 10 microns, a level which appears to be uselessly small until one increases the wavelength into more of the

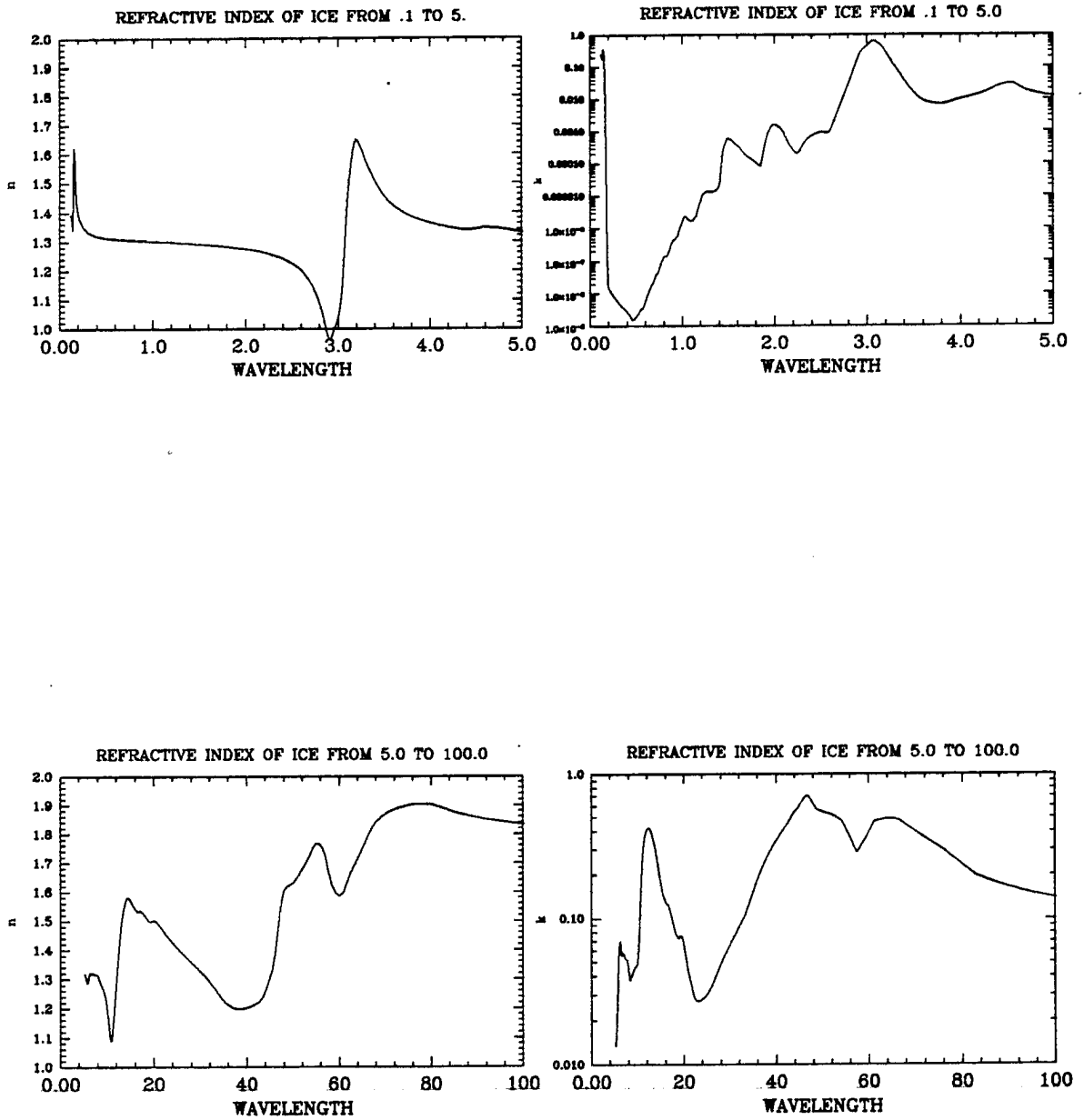

Figure 3.10: . The real and imaginary parts of the refractive index for solar and infrared wavelengths for ice at 250K, plotted against the wavelength in microns. Here $m = n + ik$.

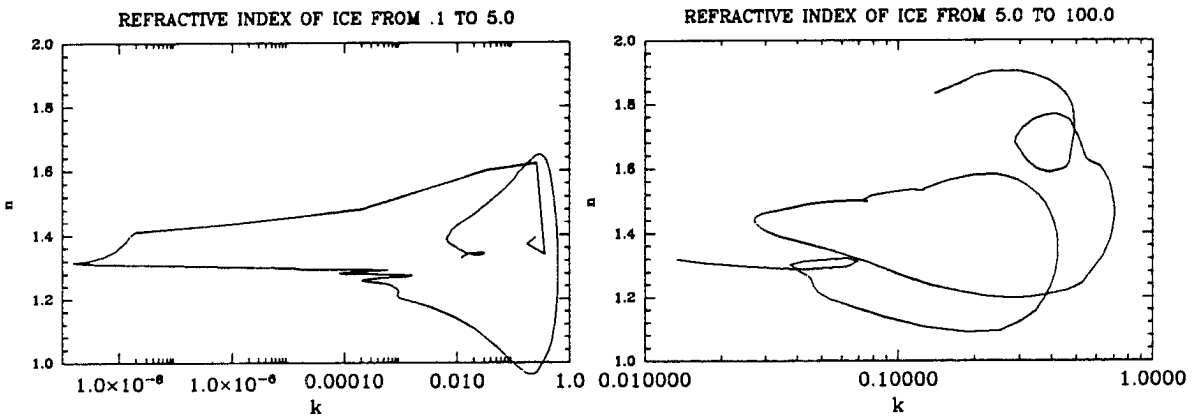

Figure 3.11: . Same as in figure 3.10 but for the real and imaginary parts of the refractive index plotted against each other.

thermal infrared region, where these sizes can reach 30 to 40 microns. For this reason, these results are not specifically applicable to any solar radiation study of cirrus clouds. For the examination of cirrus clouds in the infrared, however, it becomes a study of some of its smaller particles, a topic of some contention in the current studies of cirrus.

The choosing of the refractive indices and the incidence angles was not as trivial, and what follows about them applies not only to the DDA results presented in this chapter, but also to the Anomalous Diffraction Theory results in chapter 4.

Figure 3.10 shows a series of plots giving the real and imaginary parts of the refractive index of ice at different spectral intervals. In addition, figure 3.11 shows a series of similar plots specifically relating the real and imaginary portions of the refractive index again within different spectral intervals. These results are presented over both solar and infrared wavelengths only because the upcoming ADT results will be over some of the necessarily larger size parameters associated with the scattering of solar wavelengths on cirrus cloud

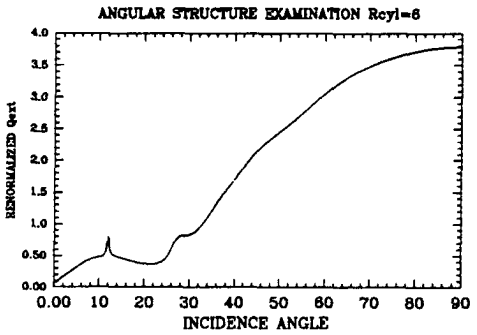

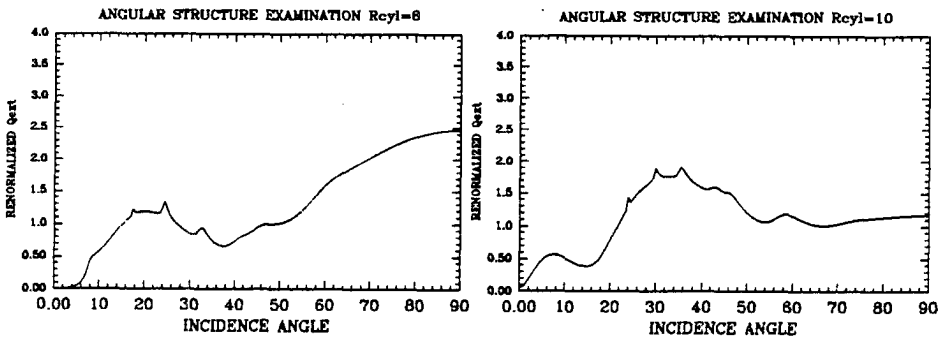

Figure 3.12: . Extinction results for infinite cylinders plotted as a function of incidence angle for three different values of r_{cyl}. Here $m = 1.33 + .000003i$, and the extinction is renormalized according to equation 3.8.

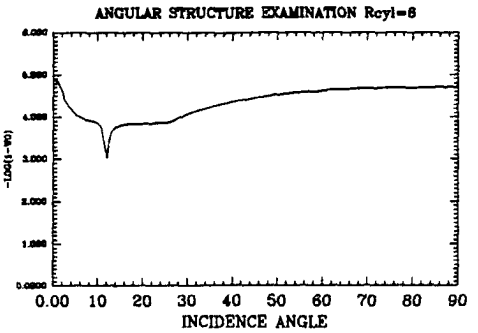

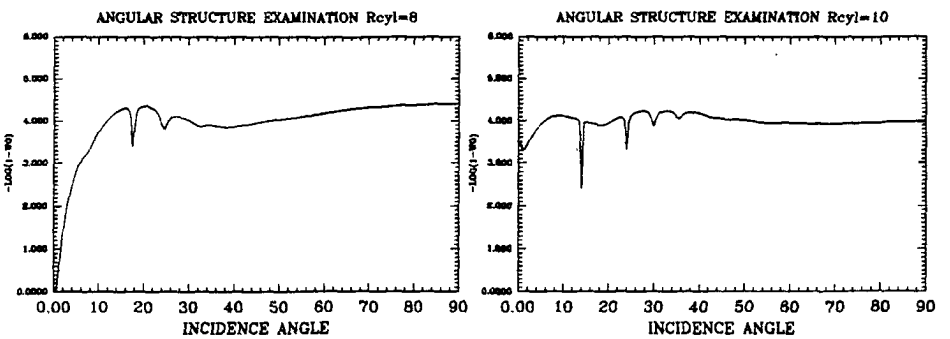

Figure 3.13: . Same as in figure 3.12 but for the single scatter albedo, displayed on an axis of the quantity $-\log_{10}(1-\omega_0)$. On this scale a value of 1, for example, corresponds to an ω_0 value of .9. Similarly, a value of 2 on this axis corresponds to an ω_0 value of .99, and so on. Thus, an increase in this y-axis quantity corresponds to an increase in ω_0 and a decrease in absorption.

Priority	Ref. Index	Usage	d
1	1.32+0i	Visible	.35
2	1.3+3E-6i	Visible	.35
3	1.32+.05i	Infrared	.35
4	1.3+.2i	Infrared	.35
5	1.2+.05i	Infrared	.40
6	1.45+.05i	Infrared	.30
7	1.52+.2i	Infrared	.30
8	1.12+.2i	Infrared	.40
9	1.28+4.6E-4i	Visible	.35

Table 3.1: . Chosen refractive indices for this study given in order of their respective priorities. The last two columns show the primary usage of the refractive index as well as a maximum allowable value of the interdipole spacing, given in relative units when $\lambda = 2\pi$.

particles. For consistency we have made the refractive index and incidence angle inputs for these two models as identical as possible.

Table 3.1 shows the location of the nine refractive indices chosen for this study, along with a priority listing of them, as well as their primary spectral usage and a maximum value that the inter-dipole spacing, d, can attain if we are to keep $Re\{m\}kd < .5$ and $k = \frac{2\pi}{\lambda} = 1$. The DDA model has been applied to the first four of these refractive indices, two of which are only applicable in the visible. This is not a mistake, as it not only makes good pure scientific sense to examine a nonabsorbing and weakly absorbing case, but it also serves to provide a good set of comparisons with the ADT results. More on this later. The two infrared refractive indices are both strongly absorbing.

At this point it should be mentioned that a full realization of results from all nine wavelengths would be too voluminous for a standard-sized research venture of the type we are pursuing. Thus, since the first four wavelengths are all that are investigated here, and that there is no known credible way of extending our current results to any of the other five, any subsequent atmospheric study which makes use of our data exclusively will have to basically assume that in the instances in which the real part of m departs significantly from 1.3, the relatively high degree of absorption in these spectral intervals makes this departure of little importance. Under this premise we proceed for now with the hope that this research will not only possess value in and of itself, but will also provide a framework which will direct the course of subsequent study.

Ref. Index	r_{cyl}	Result	Angles
1.33+0i	5	Q_{ext}	5
	6	Q_{ext}	3
	7	Q_{ext}	7
	8	Q_{ext}	11
	9	Q_{ext}	9
	10	Q_{ext}	7
1.33+0.00001i	5	Q_{ext}	5
	6	Q_{ext}	3
	7	Q_{ext}	7
	8	Q_{ext}	11
	9	Q_{ext}	9
	10	Q_{ext}	7
	5	ω_0	3
	6	ω_0	3
	7	ω_0	3
	8	ω_0	15
	9	ω_0	3
	10	ω_0	3
1.33+0.1i	5	Q_{ext}	5
	6	Q_{ext}	5
	7	Q_{ext}	7
	8	Q_{ext}	7
	9	Q_{ext}	7
	10	Q_{ext}	7
	5	ω_0	5
	6	ω_0	7
	7	ω_0	7
	8	ω_0	7
	9	ω_0	7
	10	ω_0	7

Table 3.2: . Number of incidence angles required for a cosine quadrature to provide an accurate depiction (to within 4 percent error) of the orientational averages of the given quantities for the respective values of the refractive index and r_{cyl}.

θ	Angle
θ_1	0.00000
	19.18814
	27.26604
θ_2	33.55731
	38.94244
	43.76174
θ_3	48.18969
	52.33011
	56.25101
θ_4	60.00000
	63.61220
	67.11462
θ_5	70.52878
	73.87238
	77.16041
θ_6	80.40593
	83.62063
	86.81526
θ_7	90.00000

Table 3.3: . Relevant incidence angles.

In choosing the incidence angles, the DDA model employs a cosine quadrature, choosing the angles so that they are equally spaced in $\cos\theta$ [1], which, in the case of calculating averages for random orientation, enables the quadrature weights to be of an equal value for all of the angles except the boundaries, which for our purposes are, of course, 0 and 90°. The problem reduces to merely the number of angles to be used, the object being to have an angular coverage which is representative enough that the resulting orientational averages are reasonably accurate.

The choosing of this number is a clear example of one having to 'leap before he looks'. There is, of course, no way of completely knowing whether the angular coverage in the forthcoming results is representative enough that the resulting orientational averages will be reliable. This problem can, however, be examined with infinite cylinders. Figures 3.12 and

[1] From now on we change our variable describing the angle of incidence from α to θ, and it is defined in the same way - relative to the cylinder axis. We are no longer in danger of confusing this with the angle around the cylinder axis, defined as θ in the previous chapter.

$\beta_1 = .1$	$\beta_8 = .333333$	$\beta_{15} = 4$
$\beta_2 = .111111$	$\beta_9 = .5$	$\beta_{16} = 5$
$\beta_3 = .125$	$\beta_{10} = .666667$	$\beta_{17} = 6$
$\beta_4 = .142857$	$\beta_{11} = 1$	$\beta_{18} = 7$
$\beta_5 = .166667$	$\beta_{12} = 1.5$	$\beta_{19} = 8$
$\beta_6 = .2$	$\beta_{13} = 2$	$\beta_{20} = 9$
$\beta_7 = .25$	$\beta_{14} = 3$	$\beta_{21} = 10$

Table 3.4: . Aspect ratio values utilized in the present study.

3.13 show the dependence of Q_{ext1}[2] and ω_0 upon the angle of incidence for infinite cylinders of varying size and refractive index. The resolution used here was half a degree, which was apparently adequate to depict the vast majority of the angular structure. Calculations of the orientational averages were then performed, as the number of incidence angles (and, thus, quadrature points) was varied between 3 and 25. These were then compared with the 'exact' orientational averages calculated according to the half-degree resolution. These resulted in a series of percent error calculations for each value of the number of angles. The number of incidence angles in each case required to arrive at an error of less than 4 percent is displayed in Table 3.2.

As can be seen, seven incidence angles provide adequate coverage in the vast majority of all cases, but in a few cases a number as high as 15 is sometimes required. A quick inspection of figures 3.12 and 3.13 reveals that this increase is due to a rather sudden increase in the complexity of the structure at angles relatively close to 0°, as well as an absorption resonance at $r_{cyl} = 8$ for incidence angles close to 0°. Since the horizontal fall orientations of cirrus cylinders create a preference towards the 90° region of the results, this effect should not be as important in cirrus optics as it is appears here. We have chosen seven incidence angles for our present DDA study. They appear in table 3.3 along with twelve intermediate angles.

Lastly, table 3.4 lists the 21 different values of aspect ratio used throughout the present study.

---

[2]This is a different normalization of extinction efficiency which will be defined later in this chapter.

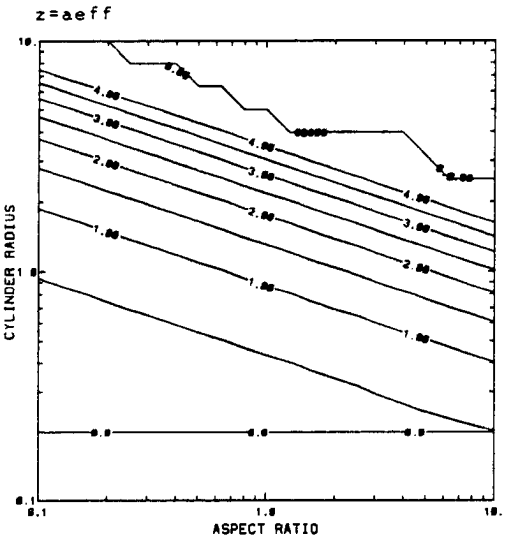

Figure 3.14: . Lines of constant a_{eff}. The contour interval is .5.

3.3 Results of the Extinction Efficiency

Before proceeding, a few definitions and distinctions must be given. The first involves the normalization of the extinction efficiency for nonspherical particles. Usually, Q_{ext} is normalized according to the following equation:

$$Q_{ext} = \frac{C_{ext}}{\pi a_{eff}^2}$$

where C_{ext} is the extinction cross section and a_{eff} is the (effective) radius of the particle. This method is in some cases inappropriate for nonspherical particles and in the case of an infinite cylinder becomes inapplicable. For the infinite cylinder case, as defined in Bohren and Huffman (1983), the normalization becomes:

$$Q_{ext1} = \frac{C_{ext}}{2r_{cyl}L} \tag{3.8}$$

where r_{cyl} is the cylinder radius and L is the cylinder length. Of course, this represents a normalization with respect to actual cross sectional area (in the case of perpendicular incidence) instead of an 'effective' cross sectional area.

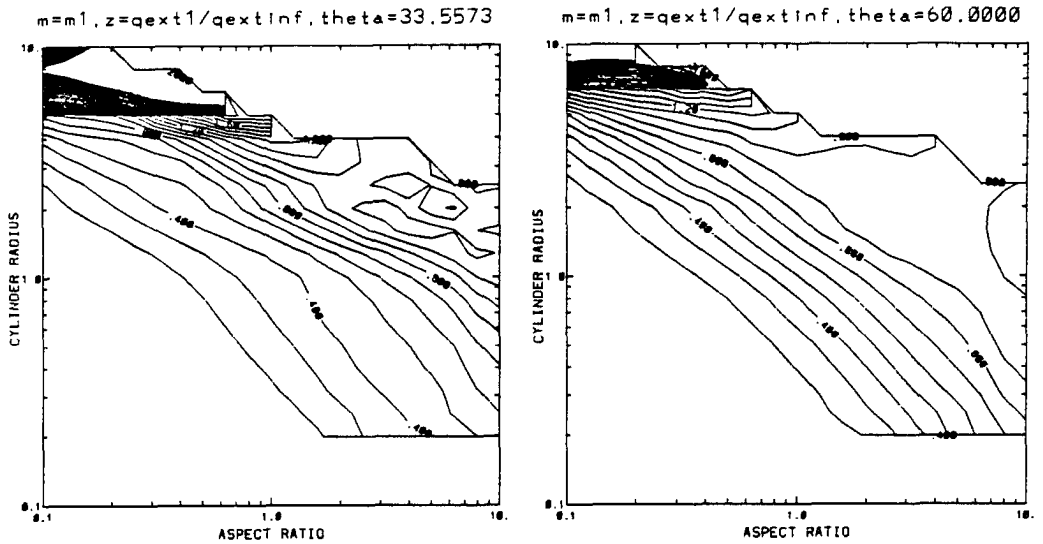

Figure 3.15: . Ratios of Q_{ext1} values to Q_{ext1} values of corresponding infinite cylinders of the same radii. Here $m_1 = 1.32 + 0i$ for both plots, $\theta = 33.5573$ (left) and $\theta = 60$ (right). The contour interval is .1, and the contours extend from .2 to 3.0, although the data appears to reach beyond these extremes. (The plateaus in the upper left corners are most likely fictitious.)

All of the graphs shown in this analysis (as well as in the upcoming single scatter albedo and asymmetry parameter analyses) are contour plots in which results are expressed in terms of cylinder radius and aspect ratio, β, where:

$$\beta = \frac{L}{2r_{cyl}}$$

By this definition it is easily shown that:

$$(Volume) = \frac{4}{3}\pi a_{eff}^3 = \pi r_{cyl}^2 L = 2\pi r_{cyl}^3 \beta$$

$$\frac{2}{3}a_{eff}^3 = r_{cyl}^3 \beta \tag{3.9}$$

$$r_{cyl} = \sqrt[3]{\frac{2}{3\beta}}a_{eff} \quad \Longrightarrow \log(r_{cyl}) = -\frac{1}{3}\log(\beta) + \frac{1}{3}\log\left(\frac{2}{3}\right) + \log(a_{eff})$$

and, since both of the axes are logarithmic, lines of constant a_{eff} on a plot of r_{cyl} vs. β will be linear with a slope of $-\frac{1}{3}$ (see figure 3.14). Also, the top and bottom contours in figure

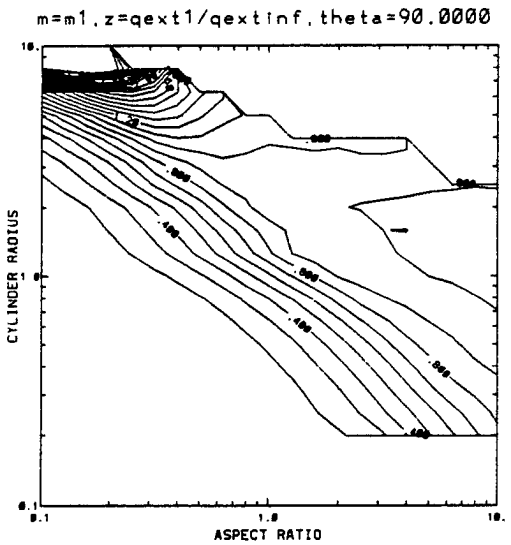

Figure 3.16: . Same as in figure 3.15, but for $\theta = 90$.

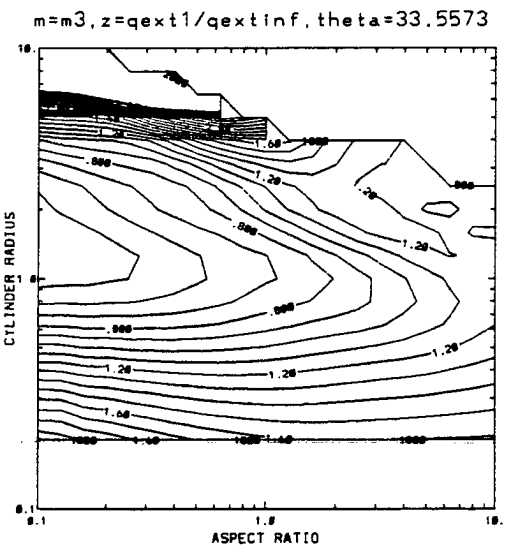

Figure 3.17: . Same as in figure 3.15, but for $m_3 = 1.32 + .05i$.

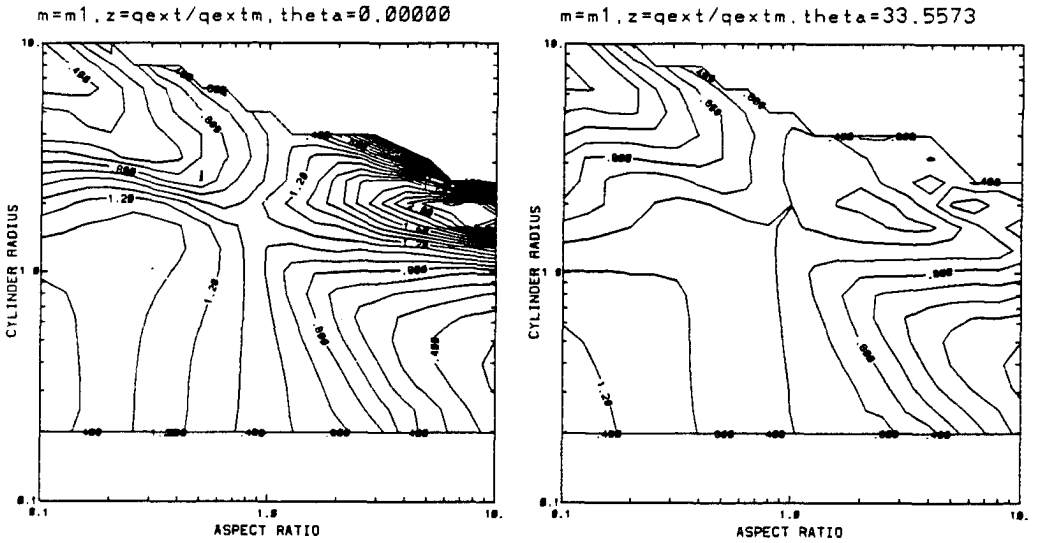

Figure 3.18: . Ratios of Q_{ext} values to those of equivalent spheres. Here $m_1 = 1.32 + 0i$, the contour interval is .1, and $\theta = 0$ (left) and $\theta = 33.5573$ (right).

3.14 reveal the region of the available data. They appear in all such plots in this chapter as well as those in chapter 4.

Lastly, we should point out that a complete display of the results is extensive enough that we have saved such a full display for Appendix A. Similarly, the full extent of the single scatter albedo and asymmetry parameter results are given respectfully in Appendices B and C. With this in mind, the results displayed here are only done so to provide good examples of the kinds of phenomena that are visible in all of the results.

It is most appropriate to begin the analysis with a look at the Q_{ext1} values. With the aforementioned renormalization we will be able to address the degree to which finite cylinders are behaving like infinite cylinders. Figures 3.15 through 3.17 display ratios of extinction efficiency for finite cylinders and infinite cylinders of the same radius. (Thus, a value of 1 for this plotted quantity reveals a cylinder acting precisely like an infinite cylinder of the same radius.) In figure 3.16 $m_1 = 1.32 + 0i$ and $\theta = 90$, so this is a case of perpendicular incidence. Note first that a 'plateau' of near infinite cylinder behavior is visible in this figure in a region where r_{cyl} is between about .4 and 3 and where β is between

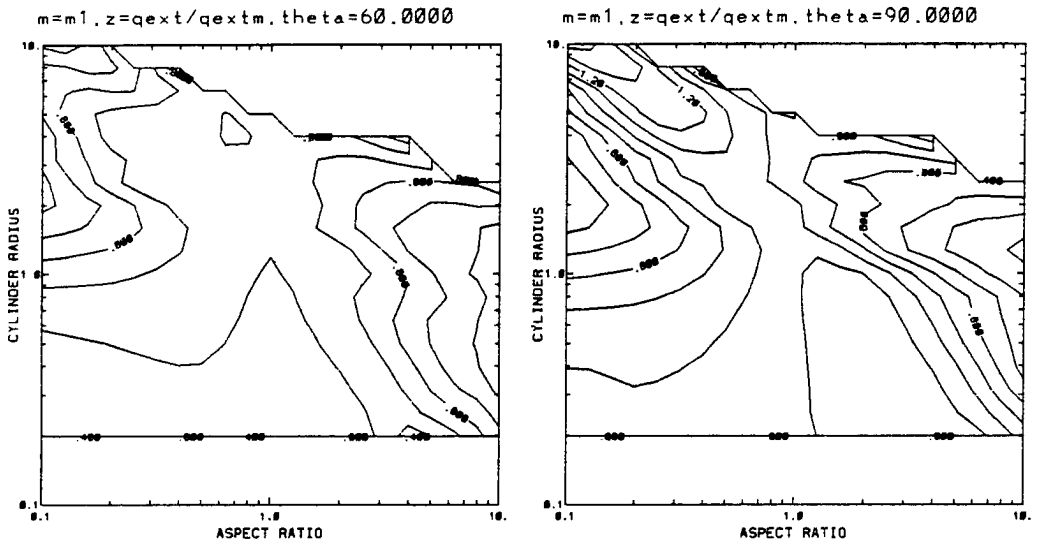

Figure 3.19: . Same as in figure 3.18, but for $\theta = 60$ (left) and $\theta = 90$ (right).

about .6 and 10, revealing that in some cases, especially at this incidence angle, the behavior of finite cylinders can approach that of their infinite counterparts very quickly, sometimes with aspect ratios as low as one or less (by near we mean to within 10%). The region of this approach shows a strong but apparently monotonic dependence on r_{cyl}, appearing at lower values of β as r_{cyl} increases. This confirms the phenomena shown in figure 2.9, that for thin fibers, ironically, very large aspect ratios sometimes may be necessary for infinite cylinder behavior to be approached by a finite cylinder. Both plots in figure 3.15 reveal that there is also a dependence upon incidence angle, with the oblique incidence case showing a slightly more complex approach to infinitum. At $\theta = 33.5573$, resonance peaks are present near $r_{cyl} = 2$, revealing perhaps even a Struve-function-type approach to infinitum instead of a purely monotonic approach. This confirms the phenomena illustrated in figure 2.11. The peak found in the region of $r_{cyl} = 10$ is very strong and becomes increasingly stronger as θ gets closer to 0 (left hand plot of figure 3.15). More on this in a moment. Extending this to a case of strong absorption ($m_3 = 1.32 + .05i$), the same basic structure as in the left hand plot of figure 3.15 is observed in figure 3.17, where it becomes apparent that the

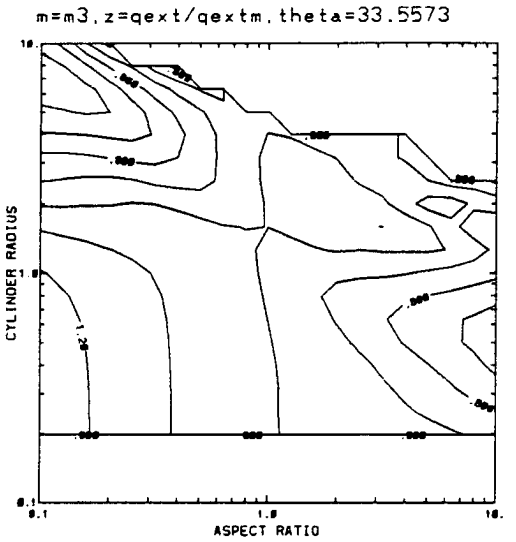

Figure 3.20: . Same as the right hand plot in figure 3.18, but for $m_3 = 1.32 + .05i$.

approach to infinitum and its dependence upon r_{cyl} is in fact not monotonic in regions below $r_{cyl} = 1.0$. To some extent this will remain unexplained, but a quick and somewhat premature glance at the right plot of figure 3.18 reveals that around $\beta \sim 1$ a region of mostly 'Mie-like' behavior exists (the contours remain close to 1). Recalling equation 3.9 and taking the derivative of both sides,

$$\frac{2}{3} 3a_{eff}^2 da_{eff} = 3r_{cyl}^2 \beta dr_{cyl} + r_{cyl}^3 d\beta$$

we find that for $r_{cyl} < 1$ and $\beta \sim 1$ the first term on the right hand side is the stronger of the two. Thus, we find that this Mie-like behavior translates to a high sensitivity to r_{cyl} and a relatively low sensitivity to cylinder length, perhaps playing a part in this change in the direction of the contours.

Figures 3.18 through 3.20 show ratios of traditionally normalized Q_{ext} values to those of equivalent spheres. Here in the same region around $r_{cyl} = 10$ efficiencies which are much less than that of spheres are observed. A quick glance at figure 3.14 reveals that the $r_{cyl} = 10$ resonances displayed in figures 3.15 through 3.17 occur in a region in which a_{eff} is close to 4, where the Mie extinction profiles reach a maximum. Apparently the strong resonances

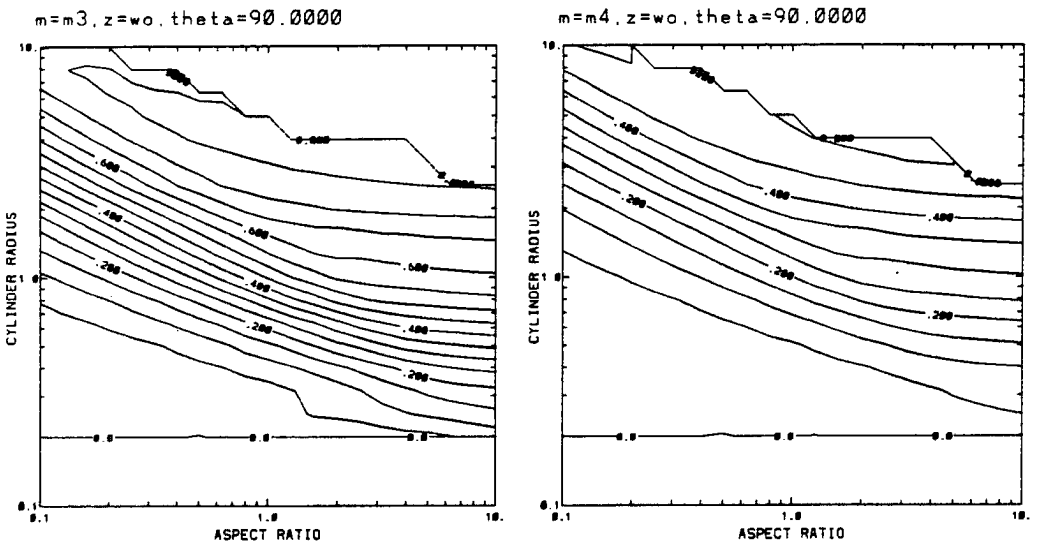

Figure 3.21: . Single scatter albedo results for $m_3 = 1.32 + .05i$ (left) and $m_4 = 1.3 + .2i$ (right). Here $\theta = 90$, and the contour interval is .05.

in figures 3.15 through 3.17 are due to the disks behaving to some extent as Mie particles, behavior which translates into a large amount of extinction per unit length in the case of thin disks. In contrast, however, the peaks near $r_{cyl} = 2$ in the left hand plot of figure 3.15 are reiterated here in the right hand plot of figure 3.18, revealing that neither spherical nor infinite cylinder theory can explain their existence. They are, thus, most likely resonances associated with characteristic distances in the particle or the particle even acting perhaps as a waveguide, two effects which will be investigated further in chapter 4.

What is most observable is a large degree of remarkable agreement between finite cylinders and spheres for a large range of cylinder radii, incidence angles, refractive indices, and in some cases aspect ratios. As would be expected, the region of agreement is centered around $\beta = 1$ and also exists in a slightly larger region in cases of strong absorption.

3.4 Results of the Single Scatter Albedo

As was previously mentioned, there are two cases to consider, a weakly absorbing case and two strongly absorbing cases, and for the sake of simplicity we first consider the two

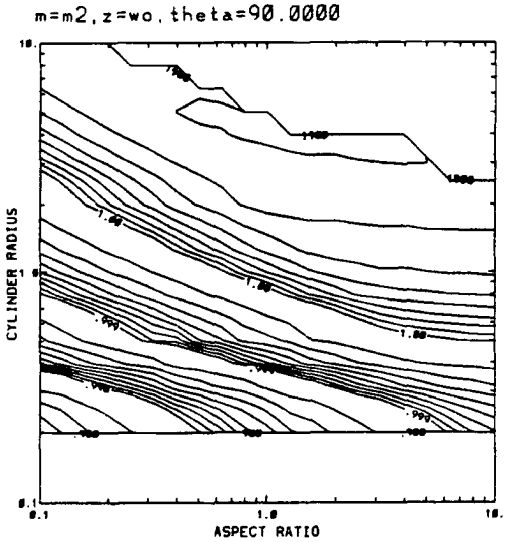

Figure 3.22: . Same as in figure 3.21, but for $m_2 = 1.32 + .000003i$. The reader is referred to the text for an explanation of the contours.

strongly absorbing cases (m_3 and m_4). Figure 3.21 shows the case of prependicular incidence for each of these refractive indices. Only these two figures are required here for our entire DDA analysis of ω_0, since the results show a very weak dependence on incidence angle. The contours show an almost exclusive dependence on effective radius in all regions except where β becomes large, in which case the dependence 'flattens out' in an approach to an infinite cylinder value.

The weak dependence on incidence angle in the case of strong absorption is surprisingly repeated in the case of weak absorption. Figure 3.22 shows results for the same incidence angle at weak absorption. The figure requires some explanation. The contours contain values of .90, .91, .92, ..., .98, .99, .991, .992, .993, ..., .998, .999, .9991, .9992, and so on. The unusual contouring system is necessary since at this level of absorption changes in ω_0 from .9 to .99 to .999 can be quite significant when employed in a cloud model involving many scatterings. Also, the '1.00' contour level is actually at a value of .9999; the contour labeling system is limited to three significant figures. The results show the same general properties as in the case of strong absorption.

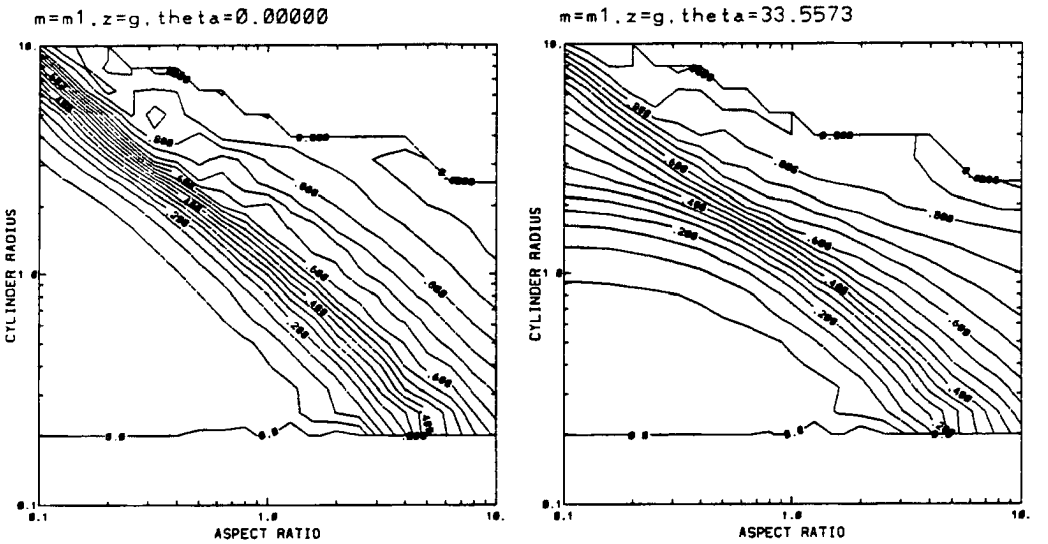

Figure 3.23: . Asymmetry parameter results for $m_1 = 1.32 + 0i$ and $\theta = 0$ (left) and $\theta = 33.5573$ (right). The contour interval is .05

3.5 Results of the Asymmetry Parameter

Figures 3.23 and 3.24 show values of the asymmetry parameter g at four incidence angles. We begin our discussion with a look at the two extremes in the θ direction. The left hand plot of figure 3.23 and the right hand plot of figure 3.24 illustrate two scenarios between which intermediate values of θ show a steady transition.

The first scenario, shown in the left hand plot of figure 3.23, shows a sharp increase in the asymmetry parameter in a direction which makes the contour lines slope too sharply downward to suggest a dependence on effective radius (see figure 3.14). Figure 3.25, however, shows lines of constant cylinder lengths, expressed in terms of wavelengths internal to the cylinder at the current refractive index. Note that the slopes of these contours are quite similar, suggesting a strong dependence on cylinder length, which makes good intuitive sense, since at this angle the characteristic distances and resonances therefrom are regulated by changes in the cylinder length alone. This will be explored more fully later with our ADT results, which depend exclusively on integrated phase differences.

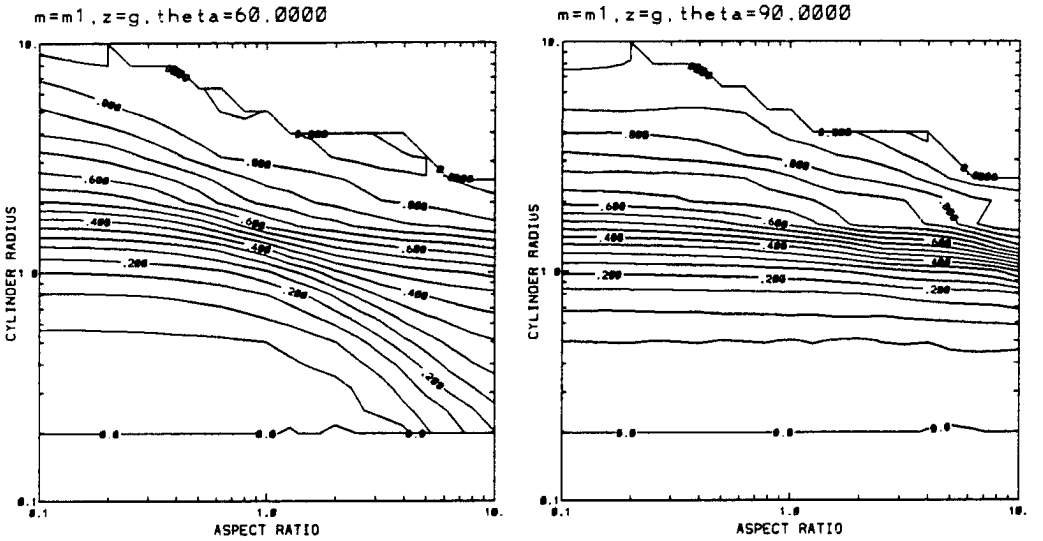

Figure 3.24: . Same as in figure 3.23 but for $\theta = 60$ (left) and $\theta = 90$ (right).

As θ is increased the results slowly shift from this regime to the one illustrated in the right hand plot of figure 3.24. Here the major dependence turns to r_{cyl} and off of the cylinder length, which, again, makes good intuitive sense. There is, however, a slight dependence on cylinder length, one which gives an increase in g (i.e., more scatter in the forward direction) with an increase in length, apparently revealing that edge effects play a role even at this incidence angle. Actually, however, this dependence does not really take hold until β starts to increase past 1. At values less than this, there is relatively little dependence on length, apparently revealing that at this incidence angle, values of g approach very quickly an asymptotic value, one which is associated with the disk being of a single dipole thickness, which usually was the case in the dipole construction of the disks which had aspect ratios close to .1.

Figures 3.26 and 3.27 show the same results as in figures 3.23 and 3.24 except that now $\frac{g}{g_{mie}}$ is being plotted. Much of the results are immediately explainable, based upon our previous findings. Referring to the slope of the lines in the left hand plot of figure 3.23, the sharp increase with aspect ratio should create g values much higher than their

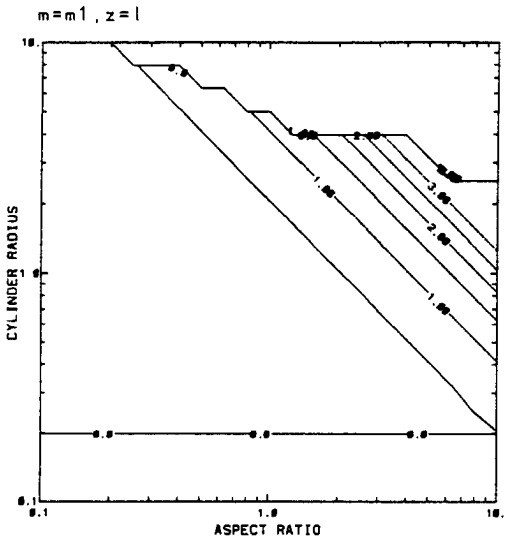

Figure 3.25: . Lines of constant cylinder lengths, expressed in terms of wavelengths internal to the cylinder at the refractive index $m_1 = 1.32 + 0i$. The contour interval is .5.

equivalent sphere counterparts in the case of small cylinders (lower right portion of each plot). Similarly, at this incidence angle the opposite effect should be seen for small and large disks. A look at both plots in figures 3.26 reveals this to be true. In the same way, the near horizontal contours of the right hand plot of figure 3.24 produce the opposite effect on the right hand side of figure 3.27. In general for aspect ratios close to 1 the use of equivalent spheres results in little or no bias. For the more atmospherically common cases of disks at $\theta = 0$ and cylinders at $\theta = 90$ this translates to overestimations of g.

Above these peaks and valleys there is a considerably large region (where $a_{eff} > 3$) in which Mie theory provides a good approximation (within 10% error). This, of course, shows that as cylinders, disks, and spheres all become relatively large ($a_{eff} > 3$ or so), they approach approximately the same value of g. With this in mind we define 'small' particles as those in which $a_{eff} < 3$, 'intermediate' sized particles as those in which $3 < a_{eff} < 6$, and 'large' particles as those in which $a_{eff} > 6$.

As θ is varied between 0 and 90, there is a point at which the slope of the contours most closely approximates the lines of constant effective radius shown in figure 3.14. For all

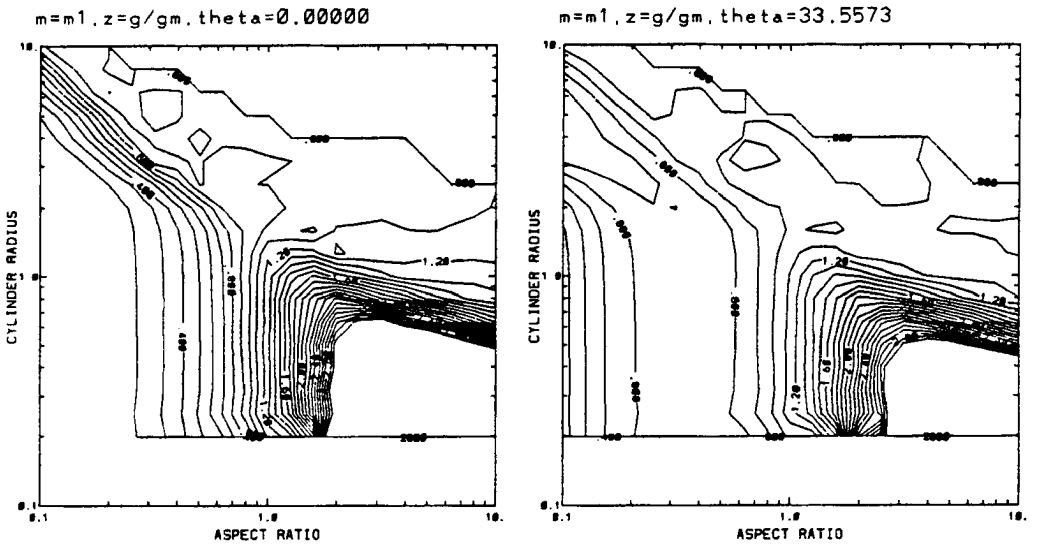

Figure 3.26: . Ratios of the asymmetry parameter calculations to those of equivalent spheres. Here $m_1 = 1.32 + 0i$ and $\theta = 0$ (left) and $\theta = 33.5573$ (right). The contour interval is .1, and the contours extend from .2 to 3.0, although the data appears to reach beyond these extremes. (The plateaus in the lower left and right corners are most likely fictitious.)

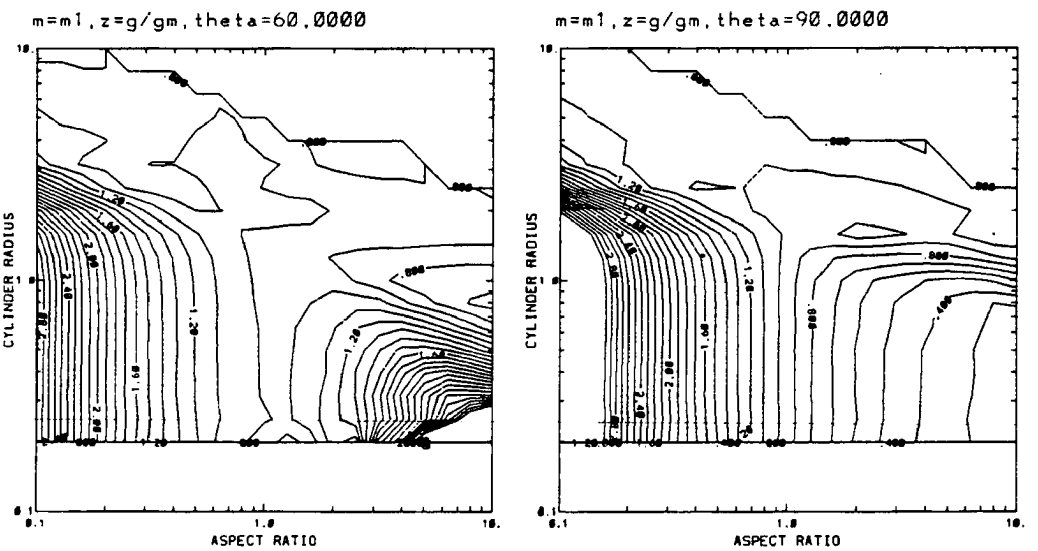

Figure 3.27: . Same as in figure 3.26, but for $\theta = 60$ (left) and $\theta = 90$ (right).

values of m this occurs at about $\theta = 48.1897$ (i.e., somewhere between 33.5573 and 60.0000), and it should be also noted that at this incidence angle the area of agreement with spheres maximizes in size, taking effect now when $a_{eff} > 2$ or so.

These results, like those of the single scatter albedo, also appear to show little or no dependence on the addition of absorption. Their dependence upon the real part of m, however, will have to be addressed in a later study.

3.6 Overall Discussion and Extension to Large Particles

In this section, we have the following objectives:

- To begin shedding light on the biases introduced through the use of equivalent spheres in the case of cylinders and disks
- In the cases where it is applicable, to provide empirically-based equations for the quantities which appear to be representable through simplistic means

In the case of extinction efficiencies, the results are complex enough that only the first of these objectives is feasible; such an analysis of this quantity will be postponed until chapter 4 where we will compare the results with similar results from the ADT model. For now, from an overall analysis of the previous Q_{ext} figures, it can be said that in general the method of equivalent spheres provides an overestimation of the extinction of finite cylinders and disks. The main exceptions are as follows:

- Cases at or near parallel incidence, where equivalent spheres underestimates the extinction for small disks ($r_{cyl} < 2$) and large cylinders ($r_{cyl} > 1.5$). All sizes here refer to r_{cyl}.
- Cases at or near perpendicular incidence, where equivalent spheres underestimates the extinction for large disks ($r_{cyl} > 3$) and, in weakly absorbing cases, for some small cylinders ($1 < r_{cyl} < 2$) and disks ($r_{cyl} < 2$).
- Cases in which β is close to 1, where equivalent spheres provides a relatively good approximation in all cases but weak absorption, where it, again, underestimates the extinction for small cylinders ($r_{cyl} < 2$).

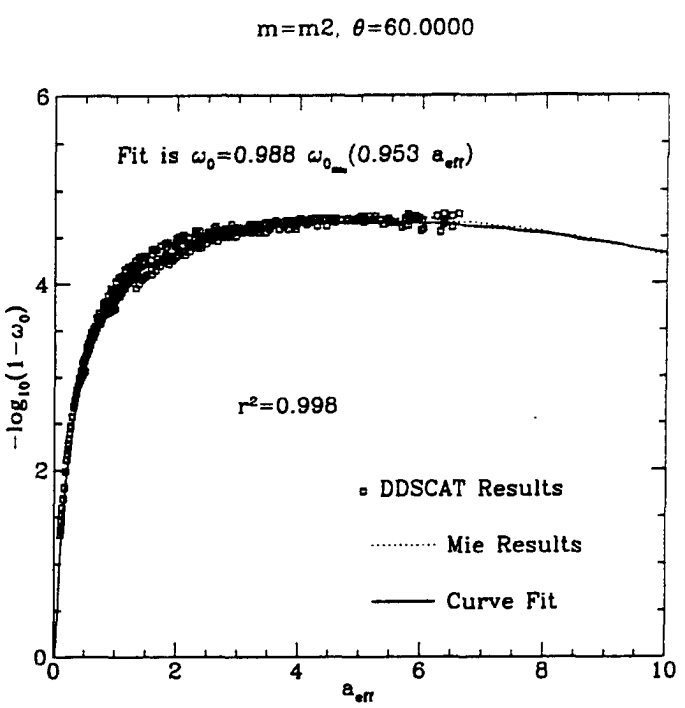

Figure 3.28: . Scatter plot of ω_0 results for the case of weak absorption ($m_2 = 1.32+.000003i$ and $\theta = 60$), plotted as a function of a_{eff}. Shown are the cylinder results for all sizes and aspect ratios (points), the corresponding results for equivalent spheres (dotted curve) and an empirical fit of the Mie curve to the cylinder data (solid curve). The results are plotted along with an r^2 value for the curve fit. Here the term 'DDSCAT' refers to the DDA model.

Since these aforementioned cases in which the extinction is underestimated by spheres are of relative rarity, it can be said with some confidence that *the use of equivalent spheres in the place of a distribution of cylinders and disks of the relative sizes and refractive indices discussed here should in most cases result in an overestimation of extinction.*

Both of the objectives stated in the beginning of this section appear to be appropriate for the cases of ω_0 and g, since the form of their results appeared to be less complex when plotted in terms of a_{eff} or ρ. Thus, for the case of ω_0 figure 3.28 shows a scatter plot of the cylinder results for all values of r_{cyl} and β for a given refractive index and incidence angle plotted as a function of a_{eff}. The points are plotted along with the corresponding Mie results as well as a fit of the Mie curve to the cylinder results according to the following equation:

$$\omega_{0_{cyl}} = b\omega_{0_{Mie}}(aa_{eff}) \tag{3.10}$$

where the coefficients a and b serve to stretch the curve in two different dimensions. The resulting curve is plotted along with its coefficients as well as an r^2 value for the curve fit.

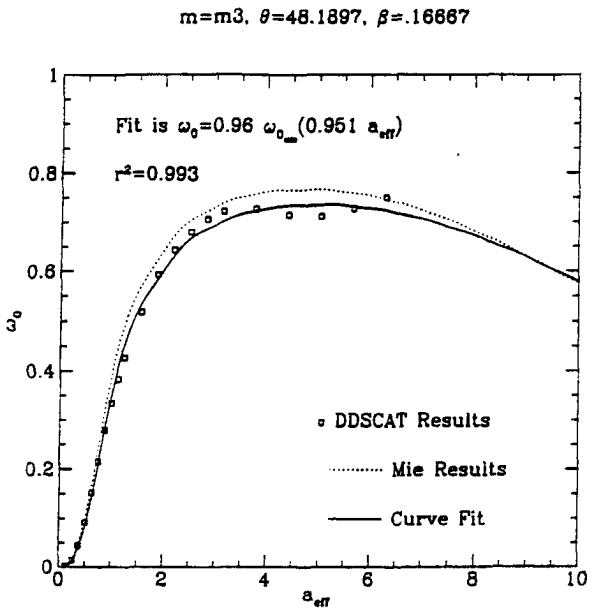

Figure 3.29: . Curve fit results of ω_0 for the m_3, θ_3, β_5 case. Here the term 'DDSCAT' refers to the DDA model.

Since some of these results appear to be definitive enough, especially for the cases of weak absorption, such curve fits were performed for each incidence angle for the case of weak absorption and for each case of incidence angle and aspect ratio for the strongly absorbing cases, where the results were more complex. The results are displayed in various tables in Appendix D.

From these tables it is apparent that in most cases of weak absorption ω_0 is overestimated by spheres by about 5% when measured on a $-\log_{10}(1-\omega_0)$ scale. This extends to a slight underestimation of absorption. The exception to this is in the vicinity of parallel incidence, where the overestimation gets as high as 12%, a systematic phase shift becomes more apparent, and the results take on a greater dependence on aspect ratio, as evidenced by the slightly lower r^2 value.

For strong absorption a summary of the b portions of the appendix tables are listed for m_3 and m_4 in tables 3.5 and 3.6. The values, moving downward within each column, are for aspect ratios of .1, 1, and 10, respectively. It is shown in these figures that for aspect ratios close to 1 there is remarkably good agreement. In most cases, however, a departure from this aspect ratio in either direction makes the use of correction factors necessary. In most cases

b						
1	2	3	4	5	6	7
0.85	0.88	0.92	0.96	0.96	0.94	0.93
1.00	0.99	0.99	1.00	1.00	1.00	1.00
0.93	1.03	0.98	0.94	0.91	0.90	0.89

Table 3.5: . Summary and qualitative description of the b results for the ω_0 curve fittings in the m_3 case. The numerical values of the coefficients are listed for each of the seven θ values and for three cases of aspect ratio - successively from top to bottom, β_1, β_{11}, and β_{21}.

b						
1	2	3	4	5	6	7
0.73	0.79	0.88	0.98	1.00	0.96	0.94
1.01	0.98	0.98	0.99	0.99	1.00	1.00
0.99	1.11	0.98	0.90	0.86	0.83	0.83

Table 3.6: . Same as in previous table but for m_4.

these correction factors reveal, again, an overestimation of ω_0 and, thus, an underestimation of absorption. In some cases this overestimation can be by a factor as high as 10 to 15%, as in the case of thin disks at $\theta = 0$. The only exceptions to this are in the midstream cases of θ around 50 or 60°, where aspect ratio departures from 1 offer a relatively minor effect, and the $\theta = 33.5573$ case for long cylinders, where a slight underestimation of ω_0 is noticed.

Thus, it appears that *the use of equivalent spheres in the place of a distribution of cylinders and disks of the refractive indices discussed here should in most cases for small and large particles result in an overestimation of* ω_0 *and a consequential underestimation of absorption.*

Lastly, the r^2 values should also be discussed, since they in effect describe the appropriateness of this analysis, the 'fittability' of cylinder results to spherical results. What they describe more than anything is the strengths of secondary resonances which were not found in the spherical results and were persistent in all cylindrical cases in which aspect ratios were not equal to 1. An example of these secondary resonances is given in figure 3.29. The resonances reversed themselves when β went from < 1 to > 1, revealing a strong dependence on aspect ratio, and as aspect ratios were pushed farther away from 1, these

b						
1	2	3	4	5	6	7
1.07(4)	1.10(5)	1.09	0.99	1.03	1.06	1.07
1.02	1.00	0.99	1.00	1.01	1.01	1.01
1.09	1.03	1.08	1.04	0.98	1.04(20)	1.07(20)
1.06(4)	1.09(5)	1.08	0.98	1.02	1.05	1.06
1.02	0.99	1.00	1.00	1.01	1.01	1.01
1.08	1.02	1.07	1.03	0.97	1.03	1.06
1.00(5)	1.03(9)	1.02(8)	1.03	1.01	1.02(6)	1.02(8)
1.02	0.99	0.99	1.00	1.01	1.01	1.01
1.03(14)	1.03	1.03(16)	1.02(17)	1.01(15)	1.02(19)	N/A
1.02(5)	1.03(6)	1.04(7)	0.98	0.99	1.01	1.01
1.01	1.00	1.00	1.01	1.01	1.00	1.00
1.01	1.03(19)	1.03(17)	1.02	1.01(15)	1.02(18)	1.04(13)

Table 3.7: . Tables of the b coefficient derived for the fitting of cylindrical g data to corresponding Mie curves. The data is listed for m_1, m_2, m_3, and m_4, respectively. Each portion of the table lists the b values for the seven values of θ and for three β values - β_1, β_{11}, and β_{21}. The numbers in parentheses denote cases in which reliable b information was not available for this value of θ and β. The number denotes the source used, which was the closest β value which contained reliable information. For the 'N/A' case no information was available.

resonances became steadily stronger, hitting a steady maximum in all cases except those of θ_1 and θ_2, where these resonances actually became steadily weaker after a maximum (minimum of r^2) at around β_7 and β_{15}.

The reader will recall that the results for g are similar in form to those of ω_0, except that here there is a 'rotation' from a dependence on cylinder length to a dependence on r_{cyl}. For these results a similar curve fit was attempted through the addition of a third variable, ζ, which was used in the following way:

$$g_{cyl} = b g_{Mie}\left[a\left(r_{cyl}\cos\zeta + L\sin\zeta\right)\right]$$

As it turned out, a reliable convergence was achieved for each case of incidence angle and refractive index, but upon plotting the results the data showed enough of a scatter that it was decided that the results should be expressed in the same form as those of the strongly absorbing cases of the ω_0 results. These are displayed in Appendix E, along with a disclaimer which points out that these results apply only to large particles ($a_{eff} > 6$).

For our analysis of g we employ numerical charts similar to those found in the ω_0 analysis. The charts, shown in table 3.7, reveal that in all cases, with the possible exception of parallel incidence, there appears to be little or no bias introduced into the large particle g data by the use of Mie results if the aspect ratios are near 1. As we depart from 1 in either direction the data becomes more spotty, but in general if the incidence angle is near $\theta_4 = 48.1897$, there is still little or no bias introduced. This leaves four cases - thin disks and long cylinders near parallel and perpendicular incidence - in which biases are introduced.

In each of these cases the biases are positive, showing an underestimation of g by Mie theory, and the biases become weaker with increases in absorption, and for strong absorption are virtually nonexistent. In the cases of little or no absorption, where they are, thus, most visible, the biases reach a level of $6 - 10\%$ for the near parallel incidence cases on thin disks and long cylinders and a level of $5 - 7\%$ for the near perpendicular incidence cases on thin disks and long cylinders. These positive biases of g indicate that in each of these four cases a relatively large amount of forward scatter is occurring, when compared with spheres. Figures 3.7 and 3.8 from Flatau (1992) show a confirmation of this underestimation, but figure 3.6 suggests that as $Im\{m\}$ becomes exceedingly large, this changes to an overestimation. The dependence on $Re\{m\}$ is yet to be examined, although the similarity in the results shown in figures 3.7 and 3.8 suggests that this sensitivity may be weak. Thus, it can be said again with some confidence that *the use of equivalent spheres in the place of a distribution of cylinders and disks of the refractive indices discussed here for small particles should in most cases result in an overestimation of the amount of forward scatter, but for large particles underestimations can abound.*

All of the results presented in this chapter will be itemized in chapter 5.

Chapter 4

RESULTS FROM THE ANOMALOUS DIFFRACTION APPROXIMATION

Results from the Discrete Dipole Approximation have yielded results which are valuable and plentiful, but even with its current state of efficient storage and quick solution techniques it is still an approximation which is largely inapplicable for larger particles. To supplement the data from the previous chapter, we look towards the other end of the scattering approximation continuum, from the realm of dipoles to the realm of geometric optics, where the Anomalous Diffraction Approximation, also referred to as Anomalous Diffraction Theory or ADT, will provide us with results for such larger particles.

The structure of this chapter bears some similarity to that of the previous chapter; we begin with a look at its formulation and previous history, providing the second half of the discussion of the third topic mentioned at the start of chapter 2. We then approach a necessary departure from the previous chapter where the results were presented in their raw form. Here we will display our ADT results only in the form of comparisons with the DDA and infinite cylinder results in an effort to arrive at a set of ADT correction factors for the use on cylinders. We conclude by presenting these correction factors with a summary discussion.

4.1 Explanation and History

ADT was first introduced by van de Hulst (1957) as an approximation for large spheres, and since its introduction its form has changed very little.

Referring to figure 4.1, ADT begins with measuring a phase lag between a ray which passes through the particle and a ray which merely passes by the particle. This phase lag can be expressed as follows:

$$\phi = kd(m-1)$$

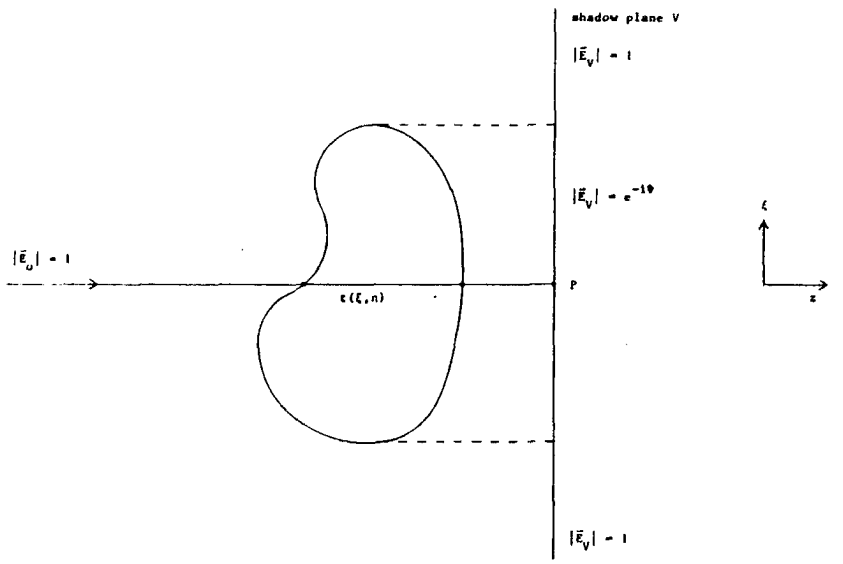

Figure 4.1: . Illustration of phase lag used in the ADT integral (from Mahood (1987)).

where $k = \frac{2\pi}{\lambda}$ as before, and d is the distance within the particle that the ray traverses, assuming that the ray undergoes no deflection from its original direction. Using this simplistic view, the scattered field in the forward direction becomes:

$$S(0) = \frac{k^2}{4\pi} \int_A 1 - e^{-i\phi} dA \tag{4.1}$$

where the integral represents a summation over the entire geometric shadow of the particle. The extinction cross section can then be calculated from the optical theorem:

$$C_{ext} = \frac{4\pi}{k^2} Re\{S(0)\} = Re\{\int_A 1 - e^{-i\phi} dA\} \tag{4.2}$$

Dividing this by the projected area of the scatterer gives the extinction efficiency:

$$Q_{ext} = \frac{Re\left\{\int_A 1 - e^{-i\phi} dA\right\}}{\int_A dA}$$

Similarly, the absorption efficiency is found to be:

$$Q_{abs} = \frac{Re\left\{\int_A 1 - e^{-\phi} dA\right\}}{\int_A dA}$$

and, thus, the single scatter albedo is simply:

$$\omega_0 = 1 - \frac{Q_{abs}}{Q_{ext}} = 1 - \frac{Re\left\{\int_A 1 - e^{-\phi} dA\right\}}{Re\{\int_A 1 - e^{-i\phi} dA\}}$$

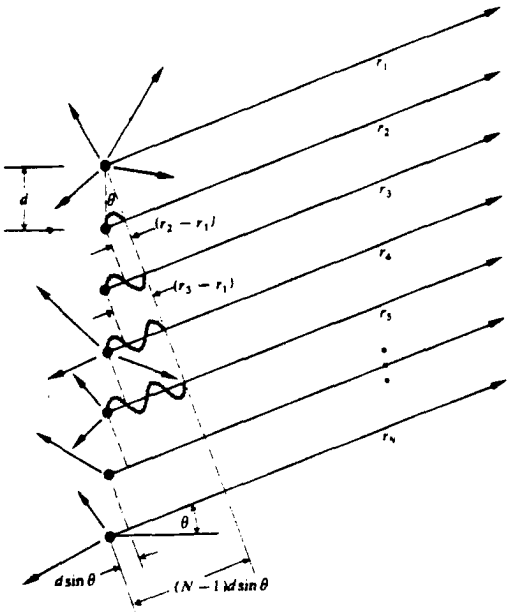

Figure 4.2: . Simplistic diffraction event produced by a linear array of point oscillators (from Hecht (1987)).

There are basically two approximations made with this approach:

$$x \gg 1 \qquad |m-1| \ll 1$$

the first signifying that we are in the regime of geometric optics, which makes the previous ray tracing technique permissible, and the second indicating that very little reflection occurs and that all of the scattered energy will be at or near the forward direction. For this reason, this method is sometimes referred to as the 'soft particle approximation'.

In the grand scheme of understanding, the technique is an extension of what is known in optics as Fraunhofer diffraction. That is, the technique assumes that the particle merely acts as a diffraction facilitator, like a slit in a diffraction grating. This problem in physics is presented in Hecht (1987) and is herein summarized.

Referring to figure 4.2, the most simplistic example of a diffraction event involves a linear array of identical coherent point oscillators, which are all in phase with each other. For now we assume that the radiation of all such oscillations is collimated into a single direction - to a distant arbitrary point P. At this point the entirety of the array emits an

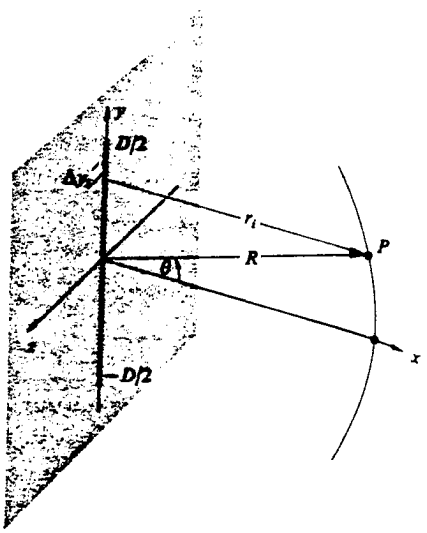

Figure 4.3: . Same as figure 4.2, but for a large number of oscillators approaching a differential representation of a macroscopic long slit (from Hecht (1987)).

electric field which is depicted by:

$$E = E_0 e^{i(kr_1-\omega t)} + E_0 e^{i(kr_2-\omega t)} + \cdots + E_0 e^{i(kr_N-\omega t)}$$

$$= E_0 e^{i(kr_1-\omega t)} \left[1 + e^{ik(r_2-r_1)} + e^{ik(r_3-r_1)} + \cdots + e^{ik(r_N-r_1)}\right]$$

where for simplicity we have considered only one polarization. In this way the field is a summation of the emitted fields from each point arriving at P. Extending this to three dimensions as well as a large number of points, we arrive at the situation presented in figure 4.3, which brings us close to a differential representation of a realistic long slit having a width much smaller than λ. In this three-dimensional case it should first be pointed out that, according to Babinet's Principle, the diffraction field produced by an arbitrary opening is identical to that produced by a perfectly opaque obstruction of the same size and shape (figure 4.4). Thus, the problem of finding the diffraction pattern of an obstruction and an opening is one and the same, and, thus, although the diffraction problems which will be discussed in this chapter will involve sources of oscillation, they can also be thought of as diffraction problems caused by obstructions or particles of the same size and shape.

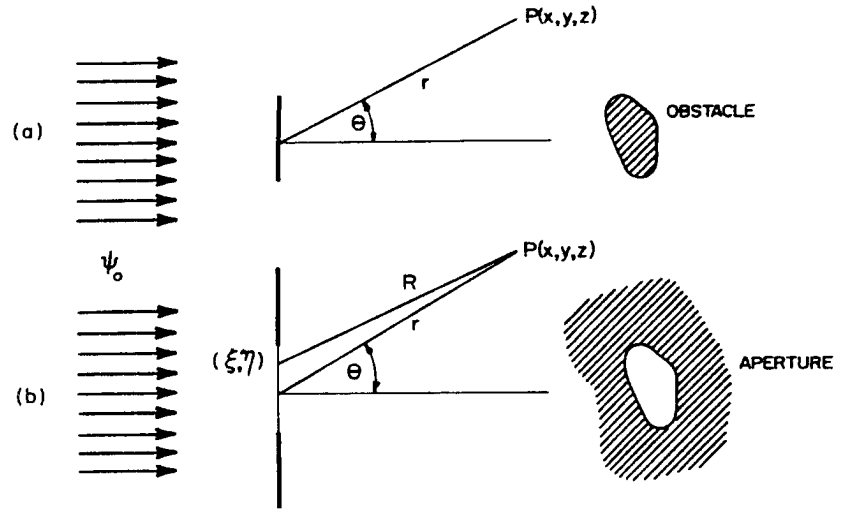

Figure 4.4: . Babinet's Principle (from Bohren and Huffman (1983)).

In this case each point now radiates a spherical wavelet, which can be written as:

$$E = \left(\frac{\mathcal{E}_0}{r}\right) \sin(\omega t - kr)$$

Here the expression shows the inverse-r amplitude relationship of a spherical wave, and the quantity $\mathcal{E}_0$ is known as the source strength, or the strength of an individual oscillator. As we approach a realistic long slit we increase the number of oscillators N, but the individual oscillator strengths $\mathcal{E}_0$ become weaker. A small but finite portion of this array, Δy_i, will contain $\frac{\Delta y_i}{D} N$ sources, where D is the length of the array. Assuming the segment Δy_i to be small enough that the relative phase differences of oscillators within the segment can be ignored, the contribution of this individual element to the field at P is:

$$E_i = \left(\frac{\mathcal{E}_0 N \frac{\Delta y_i}{D}}{r_i}\right) \sin(\omega t - k r_i)$$

Extending this to a realistic continuous slit requires letting N approach infinity and, thus, $\mathcal{E}_0$ approach zero. We are, therefore, compelled to define a source strength per unit length:

$$\mathcal{E}_L = \frac{1}{D} \lim_{\substack{N \to \infty \\ \mathcal{E}_0 \to 0}} (\mathcal{E}_0 N)$$

which makes the expression for the total field at P to be:

$$E = \sum_{i=1}^{M} \frac{\mathcal{E}_L}{r_i} \sin(\omega t - kr_i)\,\Delta y_i$$

or, in a differential form,

$$E = \mathcal{E}_L \int_{-\frac{D}{2}}^{+\frac{D}{2}} \frac{\sin(\omega t - kr)}{r} dy \tag{4.3}$$

In this form each differential element, dE, takes on the following form:

$$dE = \frac{\mathcal{E}_L}{r} \sin(\omega t - kr)\, dy \tag{4.4}$$

and it is in the treatment of the variables r and y that the differences between the two different kinds of diffraction, known as Fresnel and Fraunhofer diffraction, become apparent.

An illuminated hand that is placed close to a projection screen casts a shadow which bears a resemblance to a hand but with bright and dark bands closely following the outer edges of the shadow. Light illuminating through a small keyhole creates a series of bright spots or bands on a far wall. Both of these effects are due to diffraction, but only one is due to Fraunhofer diffraction. As the screen in the first example is moved farther away from the hand the image of the hand begins to disappear, transformed into a simple series of bright and dark spots or bands. We have moved from Fresnel to Fraunhofer diffraction.

Fraunhofer (also known as 'far-field') diffraction, is an approximation which can be made to the more general Fresnel equations when the light source and the projection screen are moved to a large distance from the diffracting opening or obstacle. As it turns out, this has manifestations with the variables r and y, which simplify the equations considerably, taking out much of the dependence of the diffraction pattern on the shape of the opening or obstacle.

Upon inspection of equation 4.4, one first notices that the variable r takes on a role of affecting both the amplitude and the phase of dE. If it is assumed that $r \gg D$, then the variations of r within the extent of $\pm\frac{D}{2}$ should not present any significant effects to the amplitude. Here, thus, it can be replaced in this case with R. In addition, if we apply the

law of cosines to figure 4.3, we arrive at:[1]

$$r^2 = R^2 + y^2 - 2Ry\cos\left(\frac{\pi}{2} - \theta\right)$$

or

$$r = \sqrt{R^2 + y^2 - 2Ry\sin\theta}$$

Applying this to a Maclaurin series,[2]

$$f(x) = f(0) + xf'(0) + \frac{x^2}{2!}f''(0) + \frac{x^3}{3!}f'''(0) + \cdots + \frac{x^{n-1}}{(n-1)!}f^{(n-1)}(0) + \frac{x^n}{n!}f^{(n)}(\theta x), 0 < \theta < 1.$$

where for our purposes,

$$x = y \qquad f(x) = r(y) \qquad f(0) = r(0) = R$$

this results in,

$$r = R - y\sin\theta + \frac{y^2}{2R}\cos^2\theta + \cdots$$

The third (and all subsequent terms) can be ignored as long as its contribution to the phase is small even when $y = \pm\frac{D}{2}$. Note that if this is done, then:

$$r = R - y\sin\theta$$

What we have effectively done is to assume that the waves are no longer curved, but planar by the time they reach the projection screen, which is intuitively sensible in the case of R being large. This is known as the Fraunhofer condition, and its substitution into equation 4.3 results in:

$$E = \frac{\mathcal{E}_L}{R}\int_{-\frac{D}{2}}^{+\frac{D}{2}} \sin\left[\omega t - k\left(R - y\sin\theta\right)\right] dy$$

Evaluating the integral, we arrive at the following:

$$E = \frac{\mathcal{E}_L D}{R}\frac{\sin\left(\frac{kD}{2}\sin\theta\right)}{\frac{kD}{2}\sin\theta}\sin\left(\omega t - kR\right)$$

---

[1] Here the angle θ is not to be confused with incidence angle, but is for the moment defined according to figure 4.3.

[2] This is taken from page A-85 of Weast et al. (1986).

where it is now apparent that the diffraction pattern takes the form of a sinh curve, which is responsible for creating the spots or bands commonly found in Fraunhofer diffraction. This sinh curve has as its central amplitude the magnitude:

$$\frac{\mathcal{E}_L D}{R}$$

which is located in the direct forward direction. Since we are only considering extinction and absorption efficiencies, which, according to the optical theorem, are fully revealed when considering only the forward direction, the entirety of the requested information is found in the above magnitude. Thus, the solution for $S(0)$ and the other quantities reduces to an integral of the total source strength over the entire opening or obstruction.

To extend this to particles of arbitrary opaqueness (i.e., arbitrary refractive indices and geometric thickness) requires the lifting of the approximation that the strength of each source be equal. Thus, our previous solution now involves an integral of these source strengths over the geometric cross section of the particle:

$$\int_A \mathcal{E}_0 dA = \int_A 1 - e^{i\phi} dA$$

This is the connection to ADT. The model is an extension of Fraunhofer diffraction with some additional assistance from simple geometric optics to make it applicable to an arbitrary particle. In addition, Ackerman and Stephens (1987) succeeded in upgrading ADT to a form which included refraction effects, but most studies have used the more simple form of ADT described here.

This method would most likely be of use only as an academic exercise were it not for the fact that, perhaps out of a strange gesture of mercy from Mother Nature, it works far better than one would expect after examining the simplicity of its formulation! Van de Hulst (1957) applied it to spheres and found that with an appropriate correction factor the method was quite accurate even in cases where m was close to 2. As a result of its simplicity and proven applicability to spheres, it has been used extensively in scattering literature on a variety of particle shapes to an extent which Flatau (1992) suggests may have even been haphazard. A full review of the use of this approximation is beyond the

scope of this work and has already been well-documented by Mahood (1987). A review of its usage on cylinders will be given later.

ADT is an approximation. Unlike the DDA and infinite cylinder codes, its formulation is based on an idea which only partially describes the scattering effects of a given situation. This may be considered to be a mere 'thorn-in-the-side', but it can also be advantageous to the observer interested in the processes involved in a scattering event. That is, when both ADT and another more consummate solution code are applied to the same scattering event, insight is gained into the individual scattering processes involved through an inspection of ADT's performance. This is particularly true now, since unlike in the previous chapter, we are not comparing spheres with cylinders, each in their own full complexity of scattering. Here we are comparing cases of identical particles, but with two different solutions, one simple and well-understood and the other complete.

ADT assumes that the particle acts as a simple diffraction facilitator. In doing so it treats very well the translucence of the particle. It also, however, assumes that there are no effects due to reflection or refraction. It is for this reason that edge effects are also poorly depicted. In addition, ADT's Fraunhofer diffraction parentage, if one chose to do so, could be applied towards the solution of phase functions, but these results would be most unreliable. Since reflection and refraction are both ignored, the phase functions would exhibit no backscatter effects and no refractive effects which are based on the shape of the particle, such as the phase function elements which manifest themselves in the cirrostratus halo. As to be expected, what ADT would perhaps display the least well would be the near-isotropic scattering effects produced by dipoles and particles with some degree of conductivity.

This lack of reliable phase function results makes ADT inapplicable for the simulation of many atmospheric scattering effects such as the 'glory', and it excludes its usage in any remote sensing capacity, asymmetry parameter calculations, or Monte Carlo modeling or n-stream modeling, if additional scattering information is not provided from elsewhere.

However, this is not the case for our purposes of solving for Q_{ext} and ω_0, and within this context, our aforementioned effects, some of which are derived from the previous chapter, can be listed as follows:

1. *Mie-like behavior.* As was stated before, van de Hulst (1957) was the first to provide solutions for spheres. He found that with a simple correction factor ADT worked quite well. Most recently, Ackerman and Stephens (1987) applied two corrections for reflection and refraction which improved the results further. In the realm of non-spherical particles this concept deals with the model's ability to react according to changes in the a_{eff} of the particle. We have seen from chapter 3 that such changes are in some cases of almost exclusive importance, especially for the ω_0 results as well as for the Q_{ext} results in which β is close to 1. This implies that in such cases shape considerations, along with their respective reflection and refraction effects, are negligible, leaving only bulk volume (a_{eff}) as a controlling factor. For this reason, ADT should be able to simulate this phenomena well for the aforementioned cases in which it is of greatest importance.

2. *Cylindrical behavior.* The reader will recall that this effect describes the situations where the scattering particle is behaving much like an infinite cylinder of the same radius. Since ADT assumes no refraction, edge effects are not considered, and, thus, at perpendicular incidence ADT should not be able to distinguish a finite cylinder from an infinite cylinder. Similarly, at oblique incidences using similar arguments ADT should not handle the approach of a finite cylinder to an infinite cylinder very well.

3. *Characteristic distances.* This addresses the postulation that resonances may be caused by the particle attaining certain geometric dimensions which would interact with the radiation wavelength in a way which maximizes extinction. To examine this idea in its simplest form, consider the case of parallel incidence on a cylinder with a nonabsorbing refractive index. Here ADT's calculations can be easily simulated on paper, since at this incidence the particle has a constant thickness at each point within its geometric shadow. Assuming that the cylinder is of a greater refractive index than the surrounding medium, internal reflection considerations suggest that resonances with the radiation wavelength should occur when

$$L = \frac{n\lambda}{4m} \qquad n = 1, 2, 3, \ldots \tag{4.5}$$

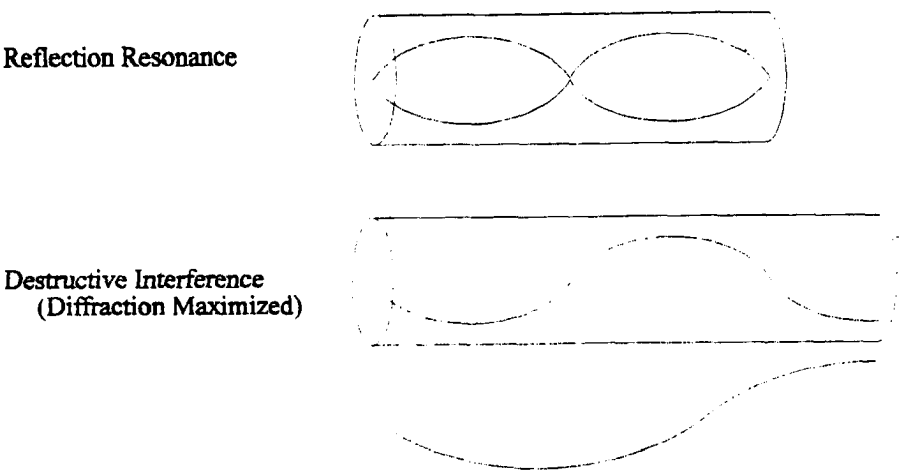

Figure 4.5: . Plausible extinction resonances according to two scenarios.

(Again, recall, m is real.) This corresponds to ϕ values of:

$$\phi = kL(m-1) = \frac{nk(m-1)\lambda}{4m} = \frac{n\pi}{2}\frac{m-1}{m} \qquad (k=1, \lambda = 2\pi)$$

(see figure 4.5). Intuition says that these should be accompanied by maxima in extinction. This, however, is not something which ADT should predict very well, as is evidenced by the fact that the quantity $S(0)$ doesn't do anything special here:

$$S(0) = \int_A 1 - e^{-i\phi} dA = (1 - e^{-i\frac{n\pi}{2}\frac{m-1}{m}})\pi r_{cyl}^2 \sim (1 - e^{i(.23\frac{n\pi}{2})})\pi r_{cyl}^2$$

where we have used a value of 1.3 for m. Thus, C_{ext} from the optical theorem does not produce a resonance[3]. To examine where ADT does predict this resonance as occurring, we set $\cos\phi = 0$ so that the real part of the expression for $S(0)$ will be maximized (see equation 4.1). We, thus, arrive at a different series of characteristic

[3] Babinet's principle can be used here to aid in one's understanding. Think of the particle now as an opening which can create a diffraction pattern identical to that created by the particle. $S(0)$ being set to zero is equivalent to the light being turned off. $S(0)$ at a maximum sets the diffraction pattern and, thus, the extinction at a maximum.

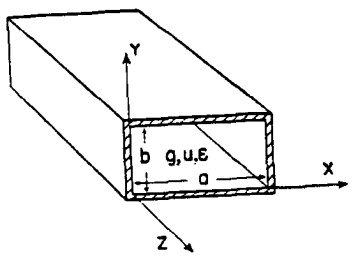

Figure 4.6: . Rectangular waveguide (from Southworth (1961)).

phase shifts in which extinction should be maximized:

$$\phi = \frac{\pi}{2}, \frac{3\pi}{2}, \frac{5\pi}{2}, \ldots$$

These correspond to the following lengths:

$$L = \frac{n\lambda}{4(m-1)} \qquad n = 1, 3, 5, \ldots \tag{4.6}$$

which are illustrated in the second half of figure 4.5. The difference is that the first of these is a reflection effect, while the second is a diffraction effect, and ADT's performance in the case of parallel incidence on a finite nonabsorbing cylinder should give some insight into which is most important.

4. *Waveguide behavior.* This is a special effect which may occur in the case of long cylinders at incidences which are close to parallel. Qualitatively the effect is similar to that of the total internal reflection effects that are utilized in such applications as fiber optics. The wave is, in a manner of speaking, deflected from its original course and detoured into the direction of the cylinder axis, exiting out the far end of the cylinder in this axial direction. The formulations involved in fundamental waveguide

physics are well understood, and are utilized for the transmission of electromagnetic radiation. The simplest waveguide example is in the form illustrated in figure 4.6, where a cavity is enclosed by a conducting pipe having a rectangular cross-section. If we initiate an electromagnetic wave of a singular polarization in the y-direction:

$$\mathbf{E} = E_y \quad E_x = E_z = 0$$

then, recalling Maxwell's equations:

$$\nabla \times \mathbf{E} = -\frac{\partial \mathbf{B}}{\partial t} = -i\omega \mathbf{B} \qquad \nabla \times \mathbf{B} = \mu \left(\mathbf{J} + \epsilon \frac{\partial \mathbf{E}}{\partial t} \right) = \mu (\sigma + i\omega\epsilon) \mathbf{E}$$

which in component form become, for our purposes:

$$-\frac{\partial E_y}{\partial z} = -i\omega B_x$$

$$\frac{\partial E_y}{\partial x} = -i\omega B_z$$

$$\frac{\partial B_x}{\partial z} - \frac{\partial B_z}{\partial x} = \mu (\sigma + i\omega\epsilon) E_y$$

$$\frac{\partial B_x}{\partial y} = 0 \qquad B_y = 0 \qquad \frac{\partial B_z}{\partial y} = 0$$

We can combine the top three equations to arrive at a propagation equation for the E-field:

$$\frac{\partial^2 E_y}{\partial x^2} + \frac{\partial^2 E_y}{\partial z^2} = \kappa^2 E_y \tag{4.7}$$

where a new propagation constant:

$$\kappa = \sqrt{i\omega\mu (\sigma + i\omega\epsilon)}$$

is defined. If it is also assumed that E_y is separable in x and z:

$$E_y (x, z) = \hat{E}_y (x) e^{-\Gamma z}$$

then equation 4.7 becomes:

$$\frac{d^2 \hat{E}_y}{dx^2} = \left(\kappa^2 - \Gamma^2 \right) \hat{E}_y = \chi^2 \hat{E}_y$$

and its general solution is:

$$\hat{E}_y = A \sin \chi x + B \cos \chi x$$

Since the tube is a conductor, the values of E_y at $x = 0$ and $x = a$ must be zero. Thus, $B = 0$, and:

$$\chi = \frac{m\pi}{a} \qquad m = 1, 2, 3, \ldots \tag{4.8}$$

Thus, the final solution becomes:

$$E_y = E \sin\left(\frac{m\pi}{a}x\right) e^{-\Gamma z} \qquad B_x = -\frac{\Gamma}{i\omega}E_y \qquad B_z = -\frac{m\pi}{i\omega a}E \cos\left(\frac{m\pi}{a}x\right) e^{-\Gamma z}$$

Thus, the solution is found through solving Maxwell's equations inside the waveguide and applying appropriate boundary conditions. This methodology is appropriate not only for rectangular waveguides, but also for circular ones. When completed, it results in a series of resonant modes. To the reader that has successfully suffered through chapter 2 this all should sound familiar. The only difference here between this solution and that of solving for the scattering off of an infinite cylinder is that here we are dealing with an outer boundary which is a conductor instead of a mere discontinuity in the refractive index, and so the boundary conditions which lead to the modes which are described in equation 4.8 are not as obviously appropriate. If, however, the reader recalls that similar boundary conditions must be made on the cylinder surface in order to provide the solutions given in chapter 2, then if these boundary conditions are set to zero, we have recreated the same condition! In effect what we have done is to turn off the incident radiation on every part of the cylinder except its near end (assuming here that we are dealing with a very long but finite cylinder). We have set up the appropriate conditions to enable the cylinder to act as a waveguide. Thus, the solution on an infinite cylinder creates at near parallel incidences the conditions necessary for waveguide behavior. A quick glance at figure 4.7, which shows infinite cylinder solution results for a series of incidence angles and cylinder radii (on these graphs 90° is equivalent to our parallel incidence), reveals that such an effect may occur even before incidences become parallel. Thus, such boundary condition restraints may only need to be approximately true for this waveguide effect to occur. Unfortunately the infinite cylinder solutions do not yield results at parallel incidence, but although there is some remaining question as to whether or not the large foreground peak in

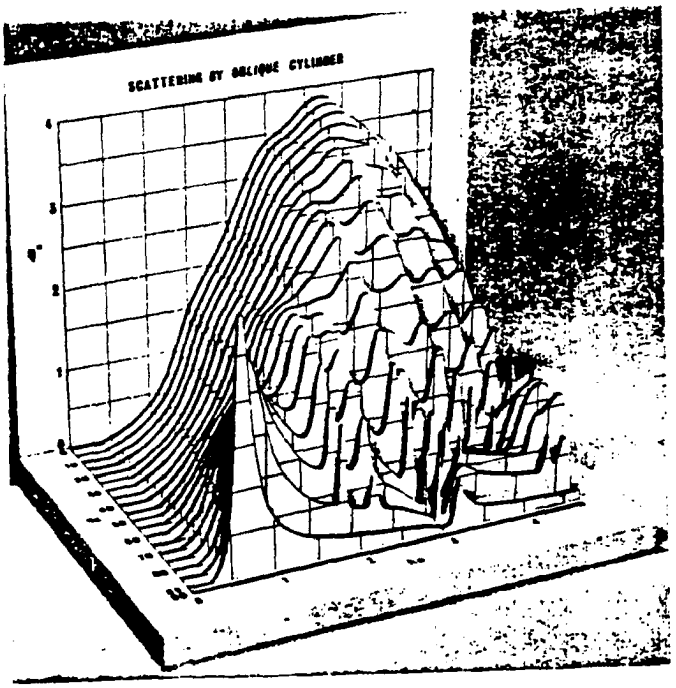

Figure 4.7: . Infinite cylinder results showing probable waveguide behavior (from Lind and Greenberg (1966)).

figure 4.7 is due to a waveguide effect, it is in the opinion of the principle author that there is sufficient evidence to confidently label it as such. It is a peak which should appear in all long cylinders and should not be depicted well by the ADT model, since it relies upon an effect which can be described as similar to an internal reflection effect. This may be of some consequence, since, as the reader will recall from chapter 3, it does appear to occur in the DDA results, especially at near parallel incidence. Also, in particular at this parallel incidence, there may be some confusion between this effect and the previous one. If there is an observed extinction peak at this incidence, which is the cause? The difference is that in the case of waveguide behavior the extinction should exhibit a dependence on r_{cyl} (see figure 2.12), something which is not possible in the case of characteristic distances and something which the ADT model should not be able to simulate. Also, the waveguide effect should be more prominent for longer cylinders, leaving shorter cylinders for the previously mentioned study of characteristic distances.

Thus, with a breadth of theory under our belts, we approach the ADT model and its results with our eyes open.

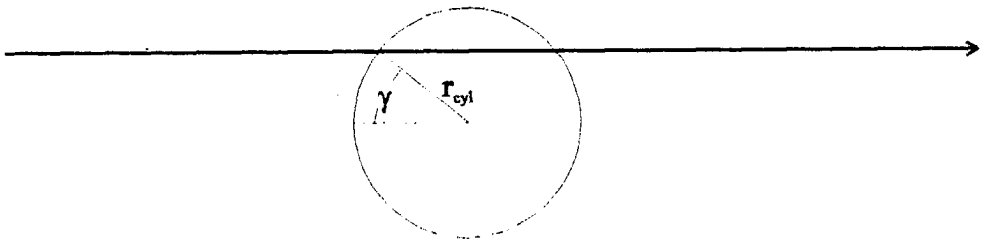

Figure 4.8: . Infinite cylinder cross section showing arbitrary incident beam.

4.2 Applications to Cylinders

Although the specific ADT model used here, which, like the DDA model of chapter 3, was also developed and described by Flatau (1992), utilizes a technique to numerically perform the integration shown in equation 4.1, this is not always necessary. Cross and Latimer (1970) as well as Stephens (1984b) showed that for infinite cylinders this integral can be reduced to an analytical form. Since Mahood (1987) found numerous errors in the formulation by Stephens (1984b), the derivation from Cross and Latimer (1970) will be shown in detail along with an attempt to produce a similar derivation for finite cylinders.

Referring to figure 4.8, which shows the cross section of an infinite cylinder in which the z-axis is coming out of the page, note that in the case of perpendicular incidence the path length traversed within the cylinder by the arbitrary ray is:

$$2r_{cyl}\cos\gamma$$

where the angle γ is defined in the figure. Extending this to oblique incidence this becomes:

$$2r_{cyl}\cos\gamma\csc\theta$$

Thus, the phase delay ϕ becomes:

$$\phi = 2kr_{cyl}(m-1)\cos\gamma\csc\theta = 2kr_{cyl}(m-1)\frac{\cos\gamma}{\sin\theta} = 2kr_{cyl}\frac{\cos\gamma}{\sin\theta}(n-1-in')$$

If we define:

$$\tan\beta = \frac{n'}{n-1}$$

where the angle β is used here to be consistent with the literature and should not be confused with aspect ratio, then the equation for ϕ becomes:

$$\phi = 2kr_{cyl}\frac{\cos\gamma}{\sin\theta}(n-1)(1-i\tan\beta)$$

and equation 4.2 becomes:

$$C_{ext} = Re\left\{\int_A 1 - e^{-i2kr_{cyl}\frac{\cos\gamma}{\sin\theta}(n-1)(1-i\tan\beta)}dA\right\}$$

or,

$$C_{ext} = Re\left\{2\int_0^{\frac{\pi}{2}}\left[1 - e^{-i2kr_{cyl}\frac{\cos\gamma}{\sin\theta}(n-1)(1-i\tan\beta)}\right]\cos\gamma d\gamma\right\}$$

where we have adjusted the integral to be over a unit length of the cylinder. Setting,

$$\rho = \frac{2kr_{cyl}(n-1)}{\sin\theta} \qquad \rho' = \frac{2r_{cyl}k(n-1)}{\sin\theta}(1-i\tan\beta) = \rho(1-i\tan\beta)$$

this becomes

$$C_{ext} = Re\left\{2\int_0^{\frac{\pi}{2}}\left(1 - e^{-i\rho'\cos\gamma}\right)\cos\gamma d\gamma\right\} \tag{4.9}$$

$$= 2Re\left\{\int_0^{\frac{\pi}{2}}\left[1-\cos(\rho'\cos\gamma)\right]\cos\gamma d\gamma + 2i\int_0^{\frac{\pi}{2}}\sin(\rho'\cos\gamma)\cos\gamma d\gamma\right\}$$

Taking the first integral,

$$\int_0^{\frac{\pi}{2}}\left[1-\cos(\rho'\cos\gamma)\right]\cos\gamma d\gamma = \sin\gamma\Big|_0^{\frac{\pi}{2}} - \int_0^{\frac{\pi}{2}}\cos(\rho'\cos\gamma)\cos\gamma d\gamma$$

and integrating by parts, we arrive at:

$$= 1 - \int_0^{\frac{\pi}{2}}\cos(\rho'\cos\gamma)\cos\gamma d\gamma = 1 - \left[\sin\gamma\cos(\rho'\cos\gamma)\Big|_0^{\frac{\pi}{2}} - \rho'\int_0^{\frac{\pi}{2}}\sin^2\gamma\sin(\rho'\cos\gamma)\,d\gamma\right]$$

$$= 1 - \left[1 - \rho'\int_0^{\frac{\pi}{2}}\sin^2\gamma\sin(\rho'\cos\gamma)\,d\gamma\right] = \rho'\int_0^{\frac{\pi}{2}}\sin^2\gamma\sin(\rho'\cos\gamma)\,d\gamma$$

Similarly with the second integral, this becomes:

$$\int_0^{\frac{\pi}{2}} \sin(\rho' \cos\gamma) \cos\gamma d\gamma = \sin(\rho' \cos\gamma) \sin\gamma \Big|_0^{\frac{\pi}{2}} + \rho' \int_0^{\frac{\pi}{2}} \sin^2\gamma \cos(\rho' \cos\gamma)\, d\gamma$$

$$= \rho' \int_0^{\frac{\pi}{2}} \sin^2\gamma \cos(\rho' \cos\gamma)\, d\gamma$$

Thus, we have:

$$C_{ext} = Re\left\{2\rho' \int_0^{\frac{\pi}{2}} \sin^2\gamma \sin(\rho' \cos\gamma)\, d\gamma + 2i\rho' \int_0^{\frac{\pi}{2}} \sin^2\gamma \cos(\rho' \cos\gamma)\, d\gamma\right\}$$

According to Abramowitz and Stegun (1972), using his notation[4],

$$H_\nu(z) = \frac{2\left(\frac{1}{2}z\right)^\nu}{\sqrt{\pi}\Gamma\left(\nu + \frac{1}{2}\right)} \int_0^{\frac{\pi}{2}} \sin(z\cos\theta) \sin^{2\nu}\theta d\theta$$

and[5]

$$J_\nu(z) = \frac{\left(\frac{1}{2}z\right)^\nu}{\sqrt{\pi}\Gamma\left(\nu + \frac{1}{2}\right)} \int_0^{\pi} \cos(z\cos\theta) \sin^{2\nu}\theta d\theta$$

which makes the following true:

$$J_\nu(z) = \frac{2\left(\frac{1}{2}z\right)^\nu}{\sqrt{\pi}\Gamma\left(\nu + \frac{1}{2}\right)} \int_0^{\frac{\pi}{2}} \cos(z\cos\theta) \sin^{2\nu}\theta d\theta$$

since the function $\cos(z\cos\theta)\sin^{2\nu}\theta$ is even about $\frac{\pi}{2}$ (see figure 4.9), and:

$$\Gamma\left(n + \frac{1}{2}\right) = \frac{1 \cdot 3 \cdot 5 \cdot 7 \cdot \cdots \cdot (2n-1)}{2^n}\sqrt{\pi}$$

H_ν, J_ν, and Γ are the Struve functions, the Bessell functions of the first kind, and the Gamma function, respectively. Thus, the solution becomes

$$C_{ext} = Re\left\{2\rho' \frac{\sqrt{\pi}\Gamma\left(\frac{3}{2}\right)}{2\left(\frac{1}{2}\rho'\right)} H_1(\rho') + 2i\rho' \frac{\sqrt{\pi}\Gamma\left(\frac{3}{2}\right)}{2\left(\frac{1}{2}\rho'\right)} J_1(\rho')\right\} = Re\left\{\pi H_1(\rho') + i\pi J_1(\rho')\right\}$$

where ρ' is complex. Similarly, for the absorption efficiency:

$$C_{abs} = Re\left\{2\int_0^{\frac{\pi}{2}} \left(1 - e^{-\rho' \cos\gamma}\right) \cos\gamma d\gamma\right\}$$

---

[4]This is taken from equation 12.1.7 on page 496.

[5]This is taken from equation 9.1.20 on page 360.

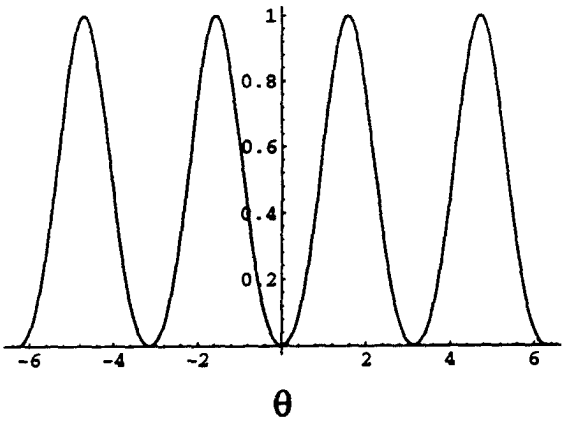

Figure 4.9: . The function $cos(zcos\theta)sin^2\theta$, shown plotted with z set to 1.

one arrives at the following result:

$$C_{abs} = Re\left\{\frac{\pi}{2}\left[I_1(\rho') - L_1(\rho')\right]\right\}$$

where I_1 and L_1 are the first-order modified Bessell and modified Struve functions, respectively. In the case of a nonabsorbing cylinder, Q_{abs} is, of course, zero, and $\rho' = \rho$. Thus, the above equation simplifies to:

$$C_{ext} = \pi Re\left\{H_1(\rho) + iJ_1(\rho)\right\} = \pi H_1(\rho) \tag{4.10}$$

and, since ρ, unlike ρ', is real, this case is more simple for the sake of comparison with the actual ADT model results. Figure 4.10 compares the ADT model with the results obtained from equation 4.10 for the case of $m_1 = 1.32 + 0i$ and $\theta = 90$. The results appear to be virtually identical. Thus, from a case in which the ADT model results can be reproduced by analytical means, it is found that the model appears to be yielding correct results.

For the sake of finite cylinders the formulation increases in its complexity, although at first glance it may not appear to be so. One can first note, again, that at perpendicular incidence the problem, when solved for Q_{ext} renormalized according to chapter 3, the solution is identical to that of an infinite cylinder. In effect, since the ADT model assumes no deflection of the incident rays, the model cannot here tell the difference between a finite and an infinite cylinder, since at this incidence the model cannot 'see' the cylinder edges. This raises the question of whether this is also true for oblique cases.

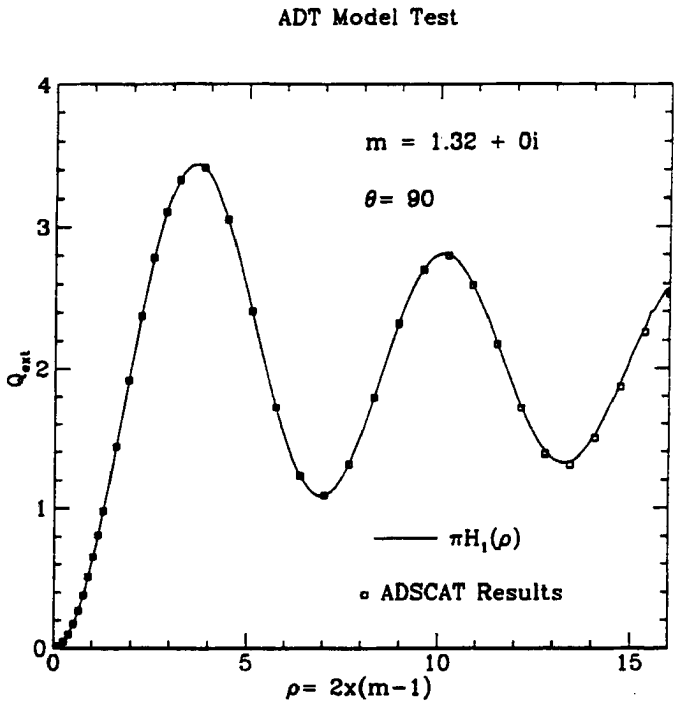

Figure 4.10: . Tests of the ADT model.

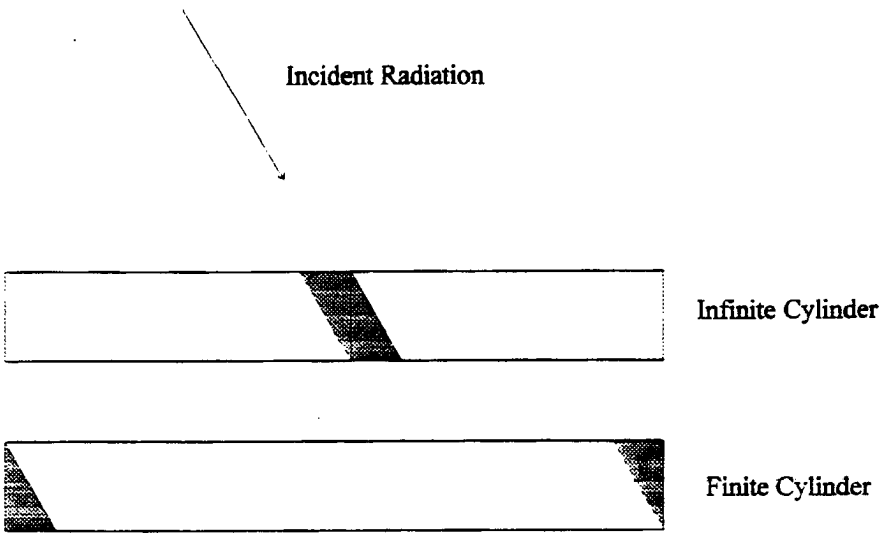

Figure 4.11: . Rectangular cylinders at the same oblique incidence. (Shaded regions are of identical size.)

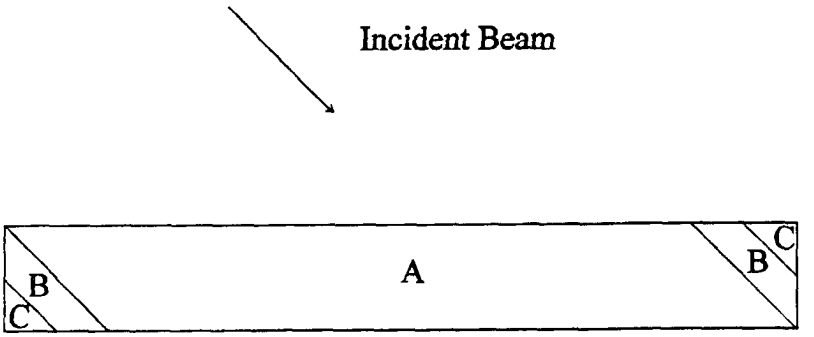

Figure 4.12: . Finite cylinder with divisions relevant to the evaluation of the ADT integral.

The answer to this question is, 'No.' Referring to figure 4.11, which shows a simpler case of a cubical cylinder laying on its side amidst incident radiation which is within the plane of the paper, we can see that, since the ADT model is based solely on phase shifts, it may at first appear that the two illustrated scenarios would yield identical results, but this is not so. In the illustrated case their phase shifts would identically add, but the exponentials of such phase shifts would not (see equation 4.1). Thus, we are presented with a more complex case.

To explore for a moment this case, the reader is referred to figure 4.12, which shows a division of the particle into five parts which can be grouped into three types. Type A is the simplest type, occurring in regions of the particle which in this approximation effectively act as infinite cylinders. Thus, their integral formulations are identical to those derived previously. Types B and C describe regions of the particle whose path lengths are controlled by two surfaces. Together the total extinction of the particle can be found through the following:

$$\int_A 1 - e^{i\phi} dA + 2\int_B 1 - e^{i\phi} dA + 2\int_C 1 - e^{i\phi} dA \tag{4.11}$$

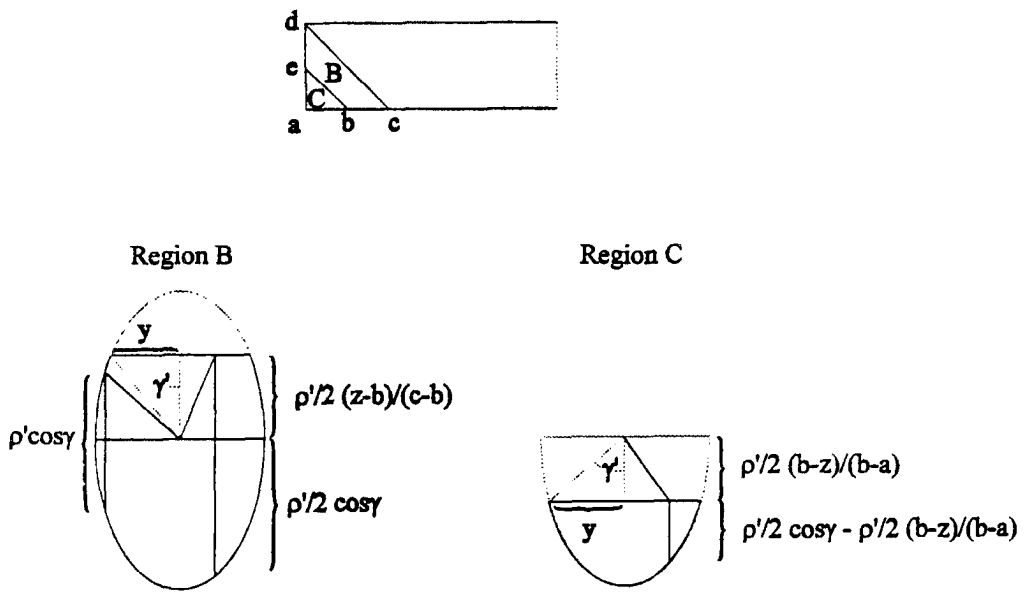

Figure 4.13: . Region types B and C from figure 4.12 shown in front and side views, respectively.

Beginning with region type A, a quick look at figure 4.12 should again convince the reader that here the above integral yields results identical to an infinite cylinder at this incidence angle:

$$\int_A 1 - e^{i\phi} dA = 2 \int_0^{L \sin\theta - 2r_{cyl} \cot\theta} \int_0^{\frac{\pi}{2}} \left(1 - e^{i\rho' \cos\gamma}\right) \cos\gamma \; d\gamma \; dz \qquad (L \sin\theta \geq 2r_{cyl} \cot\theta)$$

where $\rho' = 2kr_{cyl} \csc\theta \, (m-1)$, and the integration limits for z have changed.

Region types B and C require some discussion, and for this the reader is referred to figure 4.13 which shows both regions from a side view and then from a view in which the plane of the incident radiation is within the paper. Note that from this latter perspective it is visible that the regions possess elliptical boundaries which are truncated off at a point controlled by the location of this plane in the z direction. For region type B this means in terms of the γ integral that there is an interval in which the path lengths are identical to those of an infinite cylinder:

$$2 \int_{\gamma'}^{\frac{\pi}{2}} (1 - e^{i\rho' \cos\gamma}) \cos\gamma d\gamma$$

where γ' is defined by the figure. For $\gamma < \gamma'$ the path length becomes half of what is listed in the previous equation plus a fixed distance:

$$2\int_0^{\gamma'}\left[1-e^{i\left(\frac{\rho'}{2}\cos\gamma+\frac{\rho'}{2}\frac{z-b}{c-b}\right)}\right]\cos\gamma d\gamma$$

Thus, for region B we arrive at:

$$2\int_0^{\gamma'}\left[1-e^{i\left(\frac{\rho'}{2}\cos\gamma+\frac{\rho'}{2}\frac{z-b}{c-b}\right)}\right]\cos\gamma d\gamma+2\int_{\gamma'}^{\frac{\pi}{2}}(1-e^{i\rho'\cos\gamma})\cos\gamma d\gamma$$

where we are for now only considering the γ dependence. For region C we have a similar result:

$$2\int_0^{\gamma'}\left[1-e^{i\left(\frac{\rho'}{2}\cos\gamma-\frac{\rho'}{2}\frac{b-z}{b-a}\right)}\right]\cos\gamma d\gamma$$

and we are left with the task of further defining γ', a, b, and c.

Since we are dealing with an elliptical boundary, we can write, according to the drawing of region B:

$$\frac{y^2}{r_{cyl}^2}+\frac{\left(\frac{\rho'}{2}\frac{z-b}{c-b}\right)^2}{r_{cyl}^2\csc^2\theta}=1$$

which leads to:

$$y=\sqrt{r_{cyl}^2-\sin^2\theta\left(\frac{\rho'}{2}\frac{z-b}{c-b}\right)^2}$$

Thus:

$$\gamma'=\arctan\frac{y}{\left(\frac{\rho'}{2}\frac{b-z}{b-a}\right)^2}=\arctan\frac{\sqrt{r_{cyl}^2-\sin^2\theta\left(\frac{\rho'}{2}\frac{z-b}{c-b}\right)^2}}{\left(\frac{\rho'}{2}\frac{b-z}{b-a}\right)^2}$$

Distances *ab* and *bc* are identical, since triangles *abe* and *acd* are similar and distances *ae* and *cd* are identical. Thus, using the geometry of figure 4.13:

$$\tan\theta=\frac{r_{cyl}}{b-a}\qquad\Rightarrow\qquad b-a=c-b=\frac{r_{cyl}}{\tan\theta}\qquad c-a=\frac{2r_{cyl}}{\tan\theta}$$

Setting $a=0$ the expression for γ' becomes:

$$\gamma'=\arctan\frac{\sqrt{4r_{cyl}^4-\rho'^2\sin^2\theta\left(r_{cyl}-z\tan\theta\right)^2}}{\rho'\left(r_{cyl}-z\tan\theta\right)}$$

Thus, the total integral set becomes:

$$2\int_0^{L\sin\theta-2r_{cyl}\cot\theta}\int_0^{\frac{\pi}{2}}\left(1-e^{i\rho'\cos\gamma}\right)\cos\gamma d\gamma dz$$

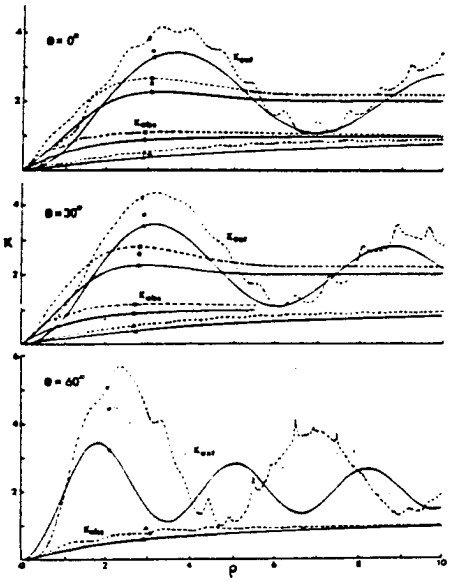

Figure 4.14: . ADT infinte cylinder results (from Cross and Latimer (1970) - Here 0° corresponds to our $\theta = 90.$).

$$+8\int_0^{\frac{r_{cyl}}{\tan\theta}}\int_0^{\arctan\frac{\sqrt{4r_{cyl}^4-\rho'^2\sin^2\theta\left(r_{cyl}-z\tan\theta\right)^2}}{\rho'\left(r_{cyl}-z\tan\theta\right)}}\left[1-e^{i\left(\frac{\rho'}{2}\cos\gamma+\frac{\rho'}{2}\frac{\tan\theta}{r_{cyl}}z\right)}\right]\cos\gamma d\gamma dz$$

$$+4\int_0^{\frac{r_{cyl}}{\tan\theta}}\int_{\arctan\frac{\sqrt{4r_{cyl}^4-\rho'^2\sin^2\theta\left(r_{cyl}-z\tan\theta\right)^2}}{\rho'\left(r_{cyl}-z\tan\theta\right)}}^{\frac{\pi}{2}}\left(1-e^{i\rho'\cos\gamma}\right)\cos\gamma d\gamma dz$$

where the integral for region C has been combined with the first integral of region B. In particular because of the unusual integration limits, the latter two integrals are at least at the time of this paper unsolvable by any analytical means known to the authors. Thus, the use of the ADT model is necessary to numerically evaluate equations 4.1 and 4.2.

4.3 Results and Analysis

In this section we compare the ADT results for Q_{ext} and ω_0 with similar results for the DDA and infinite cylinder codes. In doing so we begin with the Q_{ext} results and again the previous studies by Cross and Latimer (1970) and Stephens (1984b). Figure 4.14 shows the results of the ADT model applied to very long cylinders compared with results from infinite cylinder codes. The results initially are for normal incidence. Note that for this incidence

the ADT results perform well, but as we shift to oblique incidence, the ADT results become increasingly skewed away from the infinite cylinder results.

What is causing this? As was stated before, there are two possible answers for this case – reflection and refraction. A clue as to which is given in the fact that most of the difference appears to be a simple multiplicative factor in the abscissa. ADT assumes that the entirety of the Q_{ext} results is based on the path lengths traversed by rays through the particle, and an inspection of the top plot in figure 4.14 strongly suggests that this describes much of the scattering effects of a long cylinder. Thus, it is plausible to suggest that the deviations shown in the bottom two plots of figure 4.14 are due simply to changes in the path lengths of rays beyond merely multiplying by $\csc\theta$. Referring to figure 4.15, it is easily shown that refraction causes a decrease in this path length, while reflection results in an increase in path lengths. A close inspection of the bottom plot of figure 4.14 shows that, relative to the ADT curve, the consummate infinite cylinder solution shows at a given point signs of behaving like an ADT cylinder with a smaller radius - i.e., a cylinder with a shorter path length. Thus, it appears that the effect which ADT is not picking up is one which is causing a decrease in path lengths. Thus, the diagnosis for this effect is refraction.

For the sake of providing a more quantitative analysis for this effect on infinite and finite cylinders a series of constants have been derived to relate the results to each other:

$$Q_{ext,DDA} = bQ_{ext,ADT}(a\rho) \tag{4.12}$$

where

$$\rho = 2kr_{cyl}(n-1) \qquad k = \frac{2\pi}{\lambda} = 1$$

and the remainder of the comparison results for this section will take the form of the preceeding comparison for infinite cylinders, but will be applied to a series of aspect ratios.

The results of this investigation are shown in a series of tables given in Appendix F. Although they are not shown in the chapter, the reader should refer to them periodically, since their results are analyzed here in the chapter. Towards this end, the reader should also now read the introduction to this appendix to attain an understanding of the markings and comments which accompany the numerical data in the tables.

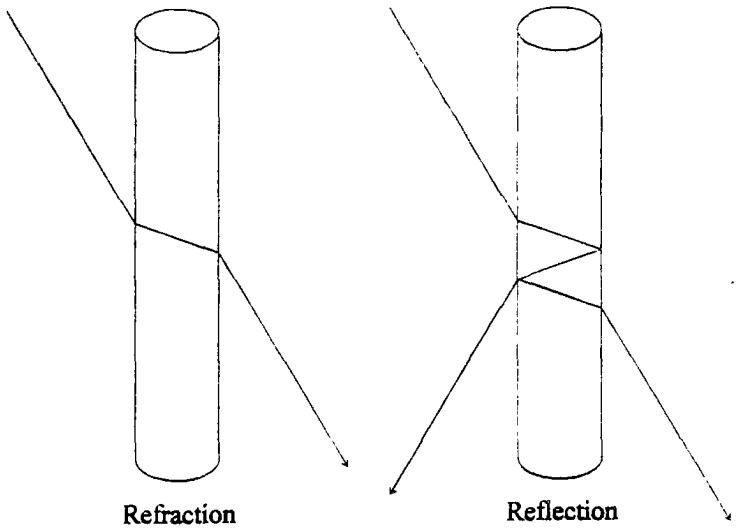

Figure 4.15: . Reflection and refraction in an infinite cylinder, illustrating the change in in-particle path lengths associated with each effect.

Since the results presented in Stephens (1984b) as well as Cross and Latimer (1970) are for a refractive index which is close to $m_1 = 1.32 + 0i$, the reader is referred to tables F1 through F4 for this discussion, which will begin with a general discussion and will then proceed to an examination of the individual effects listed earlier in this chapter.

After a short glance over the tables, one first notices certain patterns in the numerical data. These are displayed in table 4.1.

In general for extensions to larger particles, ADT gives an underestimation of extinction, except for the following:

1. cylinders at or near perpendicular incidence, which are well-represented by ADT

2. disks at parallel or oblique incidence, where ADT represents the results well and for some oblique incidences can even provide overestimations of extinction

In a further analysis of these results, note first that a and b appear to act inversely of each other. Generally, when one is low, the other is high, and vice-versa. To examine this more fully, we first approach this from a more basic standpoint:

Table 4.1: . Qualitative summary of tables F1 through F4. β increases as one moves down each column. (Note: the asterisked cases from Appendix F are here given indicators of $a = 1$ and $b = 1$.)

θ_1		θ_2		θ_3		θ_4		θ_5		θ_6		θ_7	
a	b	a	b	a	b	a	b	a	b	a	b	a	b
1	1	high	low	1	1	1	1	high	low	low	high	low	high
1	1	1	1	1	1	1	1	high	1	low	high	low	high
low	high	low	high	low	high	low	high	low	high	low	high	low	high
low	high	low	high	low	high	low	high	low	high	low	high	1	1
low	high	low	high	low	high	low	high	1	1	1	1	1	1

When b is high, it means that somehow the extinction of the particle is becoming excessive; that is, more than what would be expected from the formulations of ADT. To use some explanations from geometric optics, whose applicability in some situations here granted may be somewhat questionable, it can be said that a high value of b indicates that radiation is being deflected by refraction and reflection effects. Similarly, a small value of b indicates that somehow less energy is being deflected from the forward direction, which, in the geometric optics world, appears to be almost impossible. With this in mind, intuition says that, for exinction amounts, ADT should provide a kind of minimum value, since it neglects the effects of two extinction-hungry processes. In addition, as was discussed before, high or low values of a respectively imply that increases or decreases in the path lengths traveled within the particle are occurring.

With these concepts in mind, a number of hypothetical scenarios can be introduced. Beginning first with reflection, it is possible that some internal reflections may be occuring, which, according to figure 4.16, should cause a high value of b.

In the case of refraction we become compelled to separate this effect into two types. The first, which we term as 'base refraction', refers to the refraction of energy incident on the curved cylindrical surface. This is the kind of refraction that is observed in infinite cylinders of oblique incidence (figure 4.15). In this case the result is a low value of a.

The second type of refraction is termed here as 'side refraction', or 'edge effects'. This deals with the energy which is incident on the ends of the cylinder or disk. Illustrated in

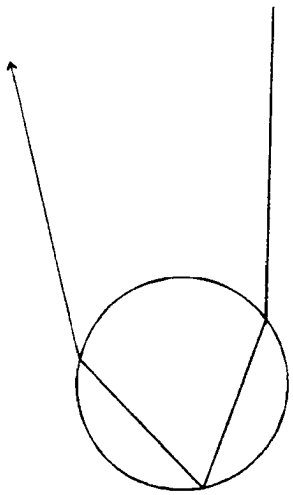

Figure 4.16: . Internal reflection effects.

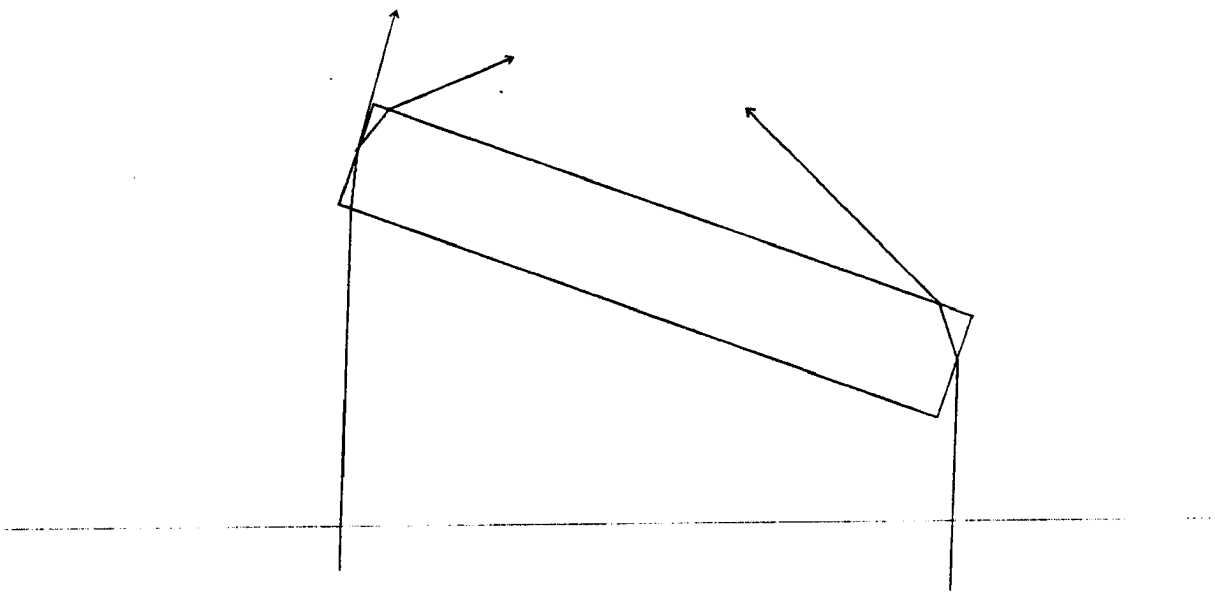

Figure 4.17: . Edge effects.

No.	Effect	a	b
1	Internal Reflections	↑	↑
2	Base Refraction	↓	↑
3	Edge Effects - Oblique	↑	↑
4	Edge Effects - Perpendicular Disk	↓	↑
5	Geometric Optics Departure		↓

Table 4.2: . Hypothesized scattering effects.

figure 4.17, this effect is especially applicable at oblique incidences and would in most cases result in an increase in the amount of side scattering and, thus, an increase in b. For the cylinder shown in figure 4.17 this effect results in an increase in the path length, and, thus, an increase in a. For disks at perpendicular incidence, however, the same effect reduces the path length resulting in a decrease in a. Lastly, we also include the previously mentioned case of a departure from geometric optics.

It should be conceded here that these five scenarios are purely hypothetical and pitifully undeveloped. However, this analysis can avoid much impending embarassment if it is understood that it is only to be taken as purely introductory and speculative.

These effects are summarized in table 4.2. The inverse behavior of a and b suggests that effects 2 and 4 are probably the most important, and upon an inspection of table 4.1, we find a great deal of support for both of these scenarios. An edge effect scenario is required, however, for the explanation of the β dependence of the results given for the long cylinders at θ_5 and θ_6. If we postulate that the effects of scenario 4 on a are very small compared to its effects on b, and then that scenario 3 is weak for these incidences, then an explanation is available for the $a = 1, b = 1$ cases when the cylinder is long and only scenario 3 is working, and the $a < 1, b > 1$ cases in which effects 3 and 4 are working in tandem to make b large and to a lesser extent a small. All that is still needed is an explanation of the results found for disks for θ_3, θ_4, and θ_5. For this we must search for a possible scenario which would increase a and decrease b, and, as was stated before, making b small requires that we invoke effect 5 as being important. What this means is that somehow the thinness of the disks in question causes a departure from geometric optics which results in the particles being less 'opaque' than what would be expected from geometric optics; that is, it forms less of a

scattering barrier to the incident radiation. Thus, the best theoretical explanation derived from ADT's performance on nonabsorbing finite cylinders is as follows:

Reflection and refraction effects take a minor role in the case of long cylinders at incidence angles which are perpendicular or near to perpendicular. As the cylinders are shortened into disks or the incidences become oblique, however, that starts to change. In the case of disks at perpendicular incidence extinction takes on a value greater than what would be expected by ADT due to edge effects which decrease path lengths traversed within the particle. In the case of cylinders at oblique incidences extinction is again increased and path lengths shortened but due to base refraction effects, which become excessively strong as θ approaches 0. In addition, edge effects appear to be at work in at least the θ_5 and θ_6 cases. For disks at some incidence angles in the vicinity of 60° and lower, effects which decrease extinction start to become important again, effects which cannot be adequately described by geometric optics. The predominance of refractive effects which shorten path lengths may provide some explanation for the single scatter albedo results from chapter 3, which found that, relative to spheres, the shape of a cylinder or disk had the effect of directing the incident radiation out of the particle's clutch and making a less efficient absorptive use of the particle's volume. Also, there is additional confirmation from the asymmetry parameter results for large particles, which suggest a relatively high amount of forward scatter in cylinders compared with spheres, since refraction and edge effects tend to scatter more towards this direction while reflection effects tend to result in backscatter.

Proceeding onto the more specific analyses:

1. *Mie-like behavior.* This deals with the ADT model's ability to give similar results in cases in which the DDA model results appear to agree with spherical results or appear to have an almost exclusive dependence on a_{eff}. This is done mostly as an exercise to confirm that the ADT model's ability to simulate spheres can be extended to cylinders in the cases where the cylinders are exhibiting behavior which approximates spheres. In the case of extinction efficiency this occurs when β is close to 1. Examining the tabular results, we find that the ADT model does not perfectly simulate the DDA results, but they are, however, off by a similar degree of error. Examining the $\beta = 1$

(tabular, β_{11}) case for each incidence angle, we find that in most cases a is close to .9, and b is close to 1.3. We may speculate that this result is analogous to the general correction factors which are required for ADT's application to spheres.

2. *Cylindrical behavior.* It is already well-known that ADT works well for long cylinders at perpendicular incidence, and that this agreement diminishes as incidence angles become oblique. It has been also shown that the theoretical makeup of ADT makes it unsuitable for discerning differences between finite and infinite cylinders, especially for incidences close to perpendicular. All that is required here is a simple confirmation of these facts, and just as was predicted we find good performance of ADT for long cylinders at and near perpendicular incidence as well as diminished agreement as θ and/or β decreases.

3. *Characteristic distances.* For this analysis the reader is referred to the θ_1 portion of table 4.1. This shows a summary of the ADT results applied to a nonabsorbing cylinder at parallel incidence. Note that in most cases of thin to moderate disks the DDA results show good agreement with ADT, revealing diffraction effects to be of a greater importance in the creation of extinction peaks than reflection effects. Here we see a confirmation of why ADT is all-in-all doing fairly well; reflection effects are weak in comparison to those of diffraction.

4. *Waveguide phenomena.* The only phenomena discovered in chapter 3 which resembled a waveguide effect was a sharp peak in the $\frac{Q_{ext}}{Q_{ext_{Mie}}}$ results which was found in the left hand plot of figure 3.18 and to a lesser extent the peaks found in the same region in the left hand plot in figure 3.15 and in the right hand plot of figure 3.18, a region which is of a larger aspect ratio than that which was examined in the discussion on 'characteristic distances' a moment ago. Considering that the contours in figure 3.18 show this peak having a definite dependence on r_{cyl}, and that the ADT results show a poor representation of particles at this aspect ratio and incidence, it appears reasonable to associate waveguide behavior with this peak as well as by association those in the other previously mentioned figures, but with less certainty.

For the ω_0 results it should be pointed out that a full analysis of the ADT/DDA comparisons would be unnecessary. The reader will recall that we already possess a series of correction factors to describe the ω_0 results. They relate the DDA results to that of equivalent spheres. Thus, such an exhaustive display of the results here would be superfluous. However, a few qualitative statements are in order. Plots similar to those found in Appendix F were made comparing ADT and DDA data for ω_0 as a function of a_{eff}. The results were not surprising, and were similar in form regardless of the degree of absorption. In most cases the shapes of the curves were quite similar, and so, although in most cases the results were not in agreement, the agreement would in most cases be easily resolvable with the use of correction factors similar to those found in our Q_{ext} analysis. In most cases it is found that ADT overestimates ω_0, which should result in a macroscale underestimation in absorption.

The best agreement was found for thin disks at parallel incidence, although it should be pointed out that the DDA ω_0 results for most disks contained secondary peaks which did not appear in the ADT results, indicating these peaks to not be diffractive in nature. The worst agreement, as one might expect, came from long cylinders at parallel incidence and thin disks at perpendicular incidence, two cases in which it would be more difficult to adjust the ADT results to reality.

As in chapter 3, all of the findings presented in this chapter will be itemized in chapter 5.

Chapter 5

CONCLUSIONS AND FINAL THOUGHTS

5.1 Conclusions

We have begun a new process of examining this issue of particle nonsphericity in cirrus clouds more systematically. To do this we have covered a wide range of topics. It is, thus, most appropriate to now list the conclusions which can be drawn from each chapter one by one.

Chapter 1:

- The significance and necessity for the current research has been documented and demonstrated. In particular it relies upon a series of modeling studies which reveal:

  1. An unusual surface heating and stratospheric cooling effect from modeled high clouds
  2. A strong sensitivity of current atmospheric radiative transfer models to the inputted values of Q_{ext}, ω_0, and g, and
  3. A partially discovered but largely uninvestigated sensitivity of particle scattering results to particle shape.

- It has become well-known from previous studies that the scattering properties of particles bears some dependence upon the particle shape, and that the scattering properties of particles bearing shapes similar to those of ice hydrometeors should, thus, be studied in order to arrive at a more prudent analysis of ice clouds. To the knowledge of the authors, however, no study has begun to intensively address this issue, until now. These results point to the need for a greater understanding of certain nonspherical particles towards the more accurate depiction of these clouds

in radiative transfer models. Taking the first logical step in this process, we begin examining thoroughly a second approximation from spheres, cylinders and disks.

- Towards this end we have given an overview of existing scattering theories, revealing the best choices for this study to be the Discrete Dipole Approximation (DDA) and the Anomalous Diffraction Theory (ADT).

- In addition, a simple analysis has been made of some sample FIRE II data, revealing the existence of plates and columns, the latter with aspect ratios sometimes reaching as high as 6.

- Lastly, apart from the atmospheric applications, the present work contains value in a pure form as it has many other possible applications. As a result, there is additional merit in an exhaustive analysis of scattering by cylindrical particles.

Chapter 2:

- The problem of scattering by an infinite cylinder is presented along with a discussion which emphasizes its history and clearly demonstrates the general technique which applies to any particle for which an analytical solution is currently possible.

- An illustration of all previous experimental scattering studies on finite cylinders has also been provided. The studies reveal that:

    1. The polarization results of thin fibers exhibits a certain simplicity which makes possible the remote sensing of the fiber radius and refractive index as long as the particle orientation is known to be that of perpendicular incidence.
    2. At least in terms of depolarization, at oblique angles longer fiber lengths are required for a thin fiber to act as an infinite cylinder.
    3. At perpendicular incidence infinite cylinder values can provide a reasonable approximation for extinction even for particles with aspect ratios as low as 2.
    4. The extinction per unit length of a finite cylinder as it is elongated to an infinite cylinder can go through a series of maxima and minima, oscillating about the infinite cylinder value.

5. At parallel incidence there can sometimes arise an effect in which the extinction exhibits a very strong maximum. This effect shows a dependence on cylinder radius, and, thus, may be the result of a waveguide effect.

6. The angular structure of the phase function and polarization information becomes increasingly more complex as the radius of a cylinder increases.

Chapter 3:

- The theoretical origin, formulation, and history of the Discrete Dipole Approximation has been presented. In doing so, we have mentioned its relationship to other scattering solution methods, and we have found from previous studies that:

  1. When applied to particle distributions and microwave frequencies, the use of Mie results provided a poor approximation for distributions of plates, especially at higher frequencies.

  2. For cases of high absorption the overestimation of g by the use of Mie results has been observed in studies involving individual particles and suggested from studies involving distributions of plates. For nonabsorbing cases, however, this changes to an underestimation.

  3. The scattering results of ice particle distributions show a strong sensitivity to maximum particle size as well as to the presence of internal bubbles or porous surfaces.

  4. For a given particle size, distributions of needles produce a relatively small radiative effect compared with plates and columns. This implies particle volume as being an additional variable of sensitivity.

- The procedure for determining the incidence angles and refractive indices for this study have been documented with the understanding that in this work we have laid an outline not only for the present research but also for subsequent studies. This will be discussed more in the upcoming section on future research.

- For individual particles the DDA yields the following results (these statements apply only to particles in which $a_{eff} \leq 6$):

  1. Extinction Efficiency, Q_{ext}:

     - At perpendicular incidence the behavior of finite cylinders can approach that of their infinite counterparts very quickly, sometimes with aspect ratios as low as one or less, providing confirmation of previously published results.
     - The realm of this infinite cylinder behavior shows a dependence upon r_{cyl}, occurring at lower values of β as r_{cyl} increases, again showing a partial confirmation of previous results.
     - As incidence angles become oblique the aforementioned region of infinite cylinder behavior can start to develop resonance peaks which are believed by the principle author to be analogous to the previously discovered extinction maxima and minima found to occur as cylinders are successively elongated (see listed results from chapter 2).
     - For small cylinders and disks, the extinction results behave in a way which is best described to resemble those of spheres; that is, the variable of greatest sensitivity is a_{eff}.
     - Large extinction per unit length values have been observed for large, thin disks ($r_{cyl} \sim 10$, $\beta \sim .1$). These peaks become strongest near parallel incidence, and can be explained as being a compromise between the particles behaving somewhat as cylinders and somewhat as spheres. Since the peak disappears in a plot of $\frac{Q_{ext}}{Q_{ext_{Mie}}}$ and the region approximately corresponds to an a_{eff} of about 4 where a well-known extinction peak occurs in the Mie results, such extinction amounts apparently translate to a high value of extinction per unit length.
     - In general there is a remarkable amount of agreement between cylinders and spheres in a region which is centered around $\beta = 1$ and that which also exists in a slightly larger region in cases of strong absorption.

- In general, however, if we consider a wide distribution of particles with refractive indices, sizes, and aspect ratios discussed in this work, it can be said that the method of equivalent spheres should in most cases result in an overestimation of the extinction. The main exceptions are:
  (a) Cases at or near parallel incidence where equivalent spheres underestimates the extinction for small disks ($r_{cyl} < 2$) and large cylinders ($r_{cyl} > 1.5$).
  (b) Cases at or near perpendicular incidence where equivalent spheres underestimates the extinction for large disks ($r_{cyl} > 3$) and, in weakly absorbing cases, for some small cylinders ($1 < r_{cyl} < 2$) and disks ($r_{cyl} < 2$).
  (c) Weakly absorbing cases where β is near one, where extinction is, again, underestimated by equivalent spheres applied to small cylinders ($r_{cyl} < 2$).

2. Single Scatter Albedo, ω_0:
   - Cylinder results for ω_0 show an almost exclusive dependence on a_{eff}, except for long cylinders where the dependence on length must disappear in an approach to an infinite cylinder value. These properties are found at all incidence angles in both weak and strong absorption cases.

3. Asymmetry Parameter, g:
   - As would be suggested by intuition, at parallel incidence the results of g show an almost exclusive dependence on cylinder length, and as θ is increased to perpendicular incidence the dependence slowly shifts to being almost exclusive to r_{cyl}.
   - Even at perpendicular incidence there is, however, a small dependence on cylinder length, revealing edge effects to play a role, albeit a small one.
   - For disks at perpendicular incidence values of g possess little or no dependence on length, making the Rayleigh dipole behavior for thin disks at this incidence angle visible even for aspect ratios close to 1.

- The tendency for cylinders and disks of the same r_{cyl} to act identically in the case of perpendicular incidence and such particles of the same length to act identically in the case of parallel incidence has effects in the case of ratioing the results with spheres. For most disks ($r_{cyl} < 5$) near perpendicular incidence, as an example, the cylinder results, as was stated before, are similar to those of long cylinders of the same radius, giving them a value of g which is larger than what their effective radius would suggest. Similar effects occur for small cylinders ($r_{cyl} < 1.5$) near parallel incidence with opposite effects occurring for small and large disks near parallel incidence and small cylinders ($r_{cyl} < 1.5$) near perpendicular incidence. For the more atmospherically common cases of disks at $\theta = 0$ and cylinders at $\theta = 90$ this translates to overestimations of g.
- For aspect ratios near 1 the use of equivalent spheres appears to introduce little bias (within about 10%).
- For particles in which $a_{eff} > 3$ the g values appear to be in the vicinity of those values found in the Mie results (within about 10%). With this in mind we now more quantitatively define the regions of small, intermediate, and large sized particles as particles in which $a_{eff} < 3$, $3 < a_{eff} < 6$, and $a_{eff} > 6$, respectively[1].
- As the cylinder results shift from a dependence upon length at $\theta = 0$ to r_{cyl} at $\theta = 90$ there is a value of θ at which the pattern of dependence most closely approximates a dependence on a_{eff}. For all values of m the closest θ value found to this point is $\theta = 48.1897$, and it is in this case the large particle region of agreement with spheres maximizes in size, taking effect now when $a_{eff} > 2$.

---

[1] Exceptions to this definition are found in cases in which the term 'small' or 'large' is followed by a parenthetical definition, like those which have appeared earlier in this itemization.

- These results for g, like those of ω_0, appear to show little or no sensitivity to the addition of absorption, although its dependence upon the real part of the refractive index is yet to be addressed.

- For distributions of particles the curve fitting process of the DDA results yields the following results:

  1. Single Scatter Albedo, ω_0:

     - In general if we consider a distribution of particles with refractive indices and aspect ratios discussed in this work, it can be said that the use of equivalent spheres should in most cases for small and large particles result in an overestimation of ω_0 and a consequential underestimation of absorption.
     - In most cases of weak absorption ω_0 is overestimated by spheres by about 5% when measured on a $-\log_{10}(1-\omega_0)$ scale. In the vicinity of parallel incidence this overestimation gets as high as 12%. Both of these overestimations extend to underestimations of absorption.
     - For cases of strong absorption in which aspect ratios are close to 1, the ω_0 results agree remarkably well with those of spheres. In most cases, however, a departure of the aspect ratio in either direction from 1 results in the need for correction factors.
     - In most cases of strong absorption where correction factors occur they reveal an overestimation of ω_0 which can be as high as 10-20%, as in the case of long cylinders at perpendicular incidence.

  2. Asymmetry Parameter, g:

     - It is noted that, unlike in the ω_0 results, which apply to particles of all sizes, the results for g apply only to large particles.
     - If we consider a distribution of particles with refractive indices and aspect ratios discussed in this work, it can be said that the use of equivalent spheres should in most cases for large particles result in an underestimation of the amount of forward scatter. For small particles overestimations are found.

- For aspect ratios near 1 or for incidence angles near $\theta_4 = 48.1897$ there appears to be little or no bias introduced into the large particle g data by the use of Mie results.
- Underestimations of g by the use of spheres on large particle data are found for thin disks and long cylinders at or near perpendicular and parallel incidences. These biases for cases of little or no absorption reached a level of 6-10% for the cases of near parallel incidence on long cylinders and thin disks and decreased to a level of 5-7% for the cases of near perpendicular incidence on thin disks and long cylinders. These biases become virtually nonexistent for cases of strong absorption and may even reverse themselves for cases of exceedingly strong absorption. The dependence on $Re\{m\}$ is yet to be addressed, but results from Flatau (1992) suggest that this dependence may be weak.

Chapter 4:

- The theoretical origin, formulation, and history of the Anomalous Diffraction Theory has been presented. In doing so we have especially explored and exploited its ability to simulate and, thus, reveal the existence of certain effects.
- The application of ADT to infinite and finite cylinders has been discussed, revealing that for finite cylinders the associated integrals become unsolvable by analytical means, requiring the numerical evaluation methods utilized by the model.
- Reflection and refraction effects take a minor role in the case of long cylinders at incidence angles which are perpendicular or near to perpendicular. As the cylinders are shortened into disks or the incidences become oblique, however, that starts to change. In the case of disks at perpendicular incidence extinction takes on a value greater than what would be expected by ADT due to edge effects which decrease path lengths traversed within the particle. In the case of cylinders at oblique incidences extinction is again increased and path lengths shortened but due to base refraction effects, which become excessively strong as θ approaches 0. In addition, edge effects appear to also be

at work in at least the θ_5 and θ_6 cases. For disks at some incidence angles in the vicinity of 60° and lower, effects which decrease extinction start to become important again, effects which cannot be adequately described by geometric optics. The predominance of refractive effects which shorten path lengths may provide some explanation for the single scatter albedo results from chapter 3, which found that, relative to spheres, the shape of a cylinder or disk had the effect of directing the incident radiation out of the particle's clutch and making a less efficient absorptive use of the particle's volume. Also, there is additional confirmation from the asymmetry parameter results, which suggest a relatively high amount of forward scatter in cylinders compared with spheres, since refraction and edge effects tend to scatter more towards this direction while reflection effects tend to result in backscatter.

- The closeness of spherical results to that of cylinders in which β is near 1 is reiterated by the ADT model's ability to accurately simulate the extinction of these particles in the same way it performs on spheres, only requiring the addition of a simple virtually constant correction factor.

- In a close examination of a case in which extinction is measured for disks at $\theta = 0$ slowly elongated to cylinders, we find from the placements of the extinction peaks confirmation of a fact which we could have deduced merely from how well ADT performs on these particles - reflection effects are weak in comparison to those of diffraction.

- Waveguide effects have been implicated for the extinction resonance peaks previously mentioned for cylinders especially at $\theta = 0$.

- In general for extensions to larger particles, ADT gives an underestimation of extinction, except for the following:

    1. Cylinders at or near perpendicular incidence, where extinction is well-represented by ADT

2. Disks at parallel or oblique incidence, where ADT represents the extinction well and for some thin disks at oblique incidence can even provide overestimations of extinction

- From a short comparison of the ω_0 results between the DDA and ADT it is found that in most cases ADT overestimates ω_0 in a way which would be easily resolvable through correction factors. This would result in a macroscale underestimation of absorption. The best results came from thin disks at $\theta = 0$, although for this case secondary resonances existed in the DDA results and not the ADT results, making a curve fit less appropriate, and indicating these resonances to most likely not be diffractive in nature. The worst agreement was found for long cylinders at $\theta = 0$ and thin disks at $\theta = 90$.

5.2 Summary and Extrapolation

In response to this listing it is now most appropriate to list these results in terms of five categories of particles:

1. Disks at or near perpendicular incidence:

   - For these particles Q_{ext} is overestimated for small particles ($r_{cyl} < 3$) and is underestimated for larger particles ($r_{cyl} > 3$). The exception to this is for weak absorption, where Q_{ext} is underestimated by small particles ($r_{cyl} < 2$). For the extensions to larger particles ADT model correction factors are required, as ADT underestimates the extinction, most likely due to edge effects. For large disks a peak exists in values of extinction per unit length which is most likely not related to a waveguide phenomenon, but is explainable as a kind of compromise between 'Mie-like' and 'cylinder-like' behavior.

   - Single scatter albedo results show almost exclusive dependence on a_{eff}, revealing the curve-fitting procedure to Mie results to be most appropriate for this quantity. It is found that equivalent spheres overestimates ω_0 in both weak and strong absorption. ADT also overestimates ω_0.

- Asymmetry parameter results show a strong sensitivity to r_{cyl} and a very small sensitivity to changes in length, revealing the thin disk Rayleigh dipole behavior to be visible at this incidence angle for a wide range of aspect ratios. For most particles ($r_{cyl} < 5$), g is underestimated by spheres but quickly approaches a region in which it is very close to spherical results (within about 10%). This region in general exists for particles in which $a_{eff} > 3$ except for $\theta = \theta_4$ in which it is even more prevalent ($a_{eff} > 2$). Extensions of g to large particles reveal g to be underestimated by Mie theory by about 5-7%. This is only true, however, for nonabsorbing and weakly absorbing cases. For strong absorption better agreement is observed.

2. Cylinders at or near parallel incidence

- For cases of small particles ($r_{cyl} < 1.5$) Q_{ext} is overestimated by spheres. For larger particles ($r_{cyl} > 1.5$) this switches to an underestimation. For larger particle extensions ADT underestimates the extinction in all cases. Comparisons with ADT reveal waveguide effects to be very strong.
- The ω_0 results are qualitatively the same as those for disks at perpendicular incidence, except that for long cylinders the dependence on a_{eff} begins to flatten out to a dependence only on r_{cyl}.
- Asymmetry parameter results show a strong dependence on length. This results in underestimations by spheres for small particles ($r_{cyl} < 1.5$). The approach to near-spherical behavior is done in the same fashion as before, and the extensions of g to larger particles yield qualitatively and quantitatively similar results as before.

3. Disks at or near parallel incidence

- Here the threshold between underestimation and overestimation of extinction by equivalent spheres shifts to $r_{cyl} \sim 2$, with the larger particles overestimated by equivalent spheres. The aforementioned extinction peak for large disks is

again visible. For extensions to larger particles ADT performs well in all cases except those for thin disks at oblique incidence, where ADT overestimates the extinction. Such comparisons with ADT reveal that effects beyond the realm of geometric optics to be at work in those cases.

- Comparisons of ω_0 with results from spheres reveal qualitatively the same results as for disks at perpendicular incidence. Here, however, the best agreement with ADT for this quantity is observed.
- As in the previous case, g shows a strong dependence on length and is overestimated by equivalent spheres for small particles. Despite this, however, g still approaches the region of general agreement with spheres in the same way as in previous cases and even, again, shows a significant underestimation by spheres for large particles in nonabsorbing and weakly absorbing cases. This underestimation amounts to about 6-10% and, as before, becomes less with the addition of absorption.

4. Cylinders at or near perpendicular incidence

- This is the case in which infinite cylinder extinction results can, of course, be the most useful. This is especially true for $\theta = 90$, where near infinite cylinder behavior is quite common even for aspect ratios as low as 1. For smaller particles, however, greater β values are required to reach this behavior. As we decrease θ from 90, resonance peaks become visible in this region of agreement with infinite cylinders. For larger particle extensions ADT provides good results for long cylinders at or near perpendicular incidence, but underestimates the extinction for shorter cylinders and for cylinders at more oblique incidences. Comparisons with ADT reveal all refraction and reflection effects to most likely be negligible for incidence angles greater than about 75°, but base refraction and edge effects have been implicated for incidence angles lower than this and for shorter aspect ratios. Extinction efficiency is overestimated by spheres in all cases except a weakly absorbing case in which a small valley of underestimation ($1 < r_{cyl} < 2$) appears.

- Single scatter albedo displays the same dependencies as are found for cylinders at or near parallel incidence, and is once again overestimated by spheres in both weakly and strongly absorbing cases, in the latter case providing the greatest overestimation of all particle shapes. ADT once again also overestimates ω_0.
- Like those of disks at this incidence angle, g shows a strong dependence on r_{cyl}. For this reason g is overestimated for $r_{cyl} < 1.5$. We then see the same approach by g to the intermediate-sized particles as in all previous cases, and underestimations of g are predicted, again, for large particles in all cases except strong absorption, where little bias is found.

5. Particles with aspect ratios near 1

- Extinction efficiency is well represented by equivalent spheres in all cases except weak absorption, where Q_{ext} is underestimated. ADT also treats this case much like spheres, universally underestimating the extinction and requiring a relatively simple correction.
- Dependencies of ω_0 on a_{eff} are again prevalent. For strong absorption ω_0 is well represented by equivalent spheres, although for weak absorption ω_0 is overestimated. ADT also overestimates ω_0.
- The asymmetry parameter is well represented by equivalent spheres, and extensions of the results point to little or no biases found for large particles.

In applying these summaries to distributions we make a small concentration on small particles, a matter of some controversy in the study of cirrus clouds. Since the sizes of the small particles in question ranges from about 10-30μm in diameter, this corresponds to a_{eff}'s of about 5-15μm. With all of our measurements being for wavelengths of 2π this corresponds approximately to a change of an order of magnitude for solar studies ($\sim .628\mu m$) and a twofold increase for longwave studies ($\sim 12.57\mu m$). For solar studies, thus, this puts the small particle threshold on our scale at $a_{eff} \leq 150$, and for thermal studies this threshold becomes $a_{eff} \leq 7.5$. Thus, since the small particle debate rests on the possibility that the

results of a given distribution depend powerfully on the effects provided by the smaller particles, inasmuch as our contribution to this debate can only be in the form of showing anomalous optical properties associated with sphericity and as compared to larger particles, we can only provide insight with respect to the infrared portion of the spectrum.

Thus, in all our upcoming discussions of generalized distributions for the solar cases we will be compelled to implicitly assume that we are dealing with only very small particles, and we will apply only our results for large particle extensions to conclusions for this case. For the infrared, however, our results will be more reliable, except for the extinction, where in terms of comparisons with spheres our information will also only be secure for small particles. In addition, only the strongly absorbing cases will be applied to the infrared statements, while the solar statements will be based mostly on results from the nonabsorbing and weakly absorbing cases.

We examine the following distributions:

1. Plates (disks at or near parallel incidence)

    - Q_{ext}: overestimated by small particles (infrared); overestimated by ADT (solar and infrared)
    - ω_0: overestimated (solar and infrared)
    - g: underestimated (solar); overestimated for small particles and with little bias for large particles (infrared)

2. Columns or needles (cylinders at or near perpendicular incidence)

    - Q_{ext}: overestimated by small particles (infrared); underestimated by ADT (solar and infrared)
    - ω_0: overestimated (solar and infrared)
    - g: underestimated (solar); overestimated for small particles and with little bias for large particles (infrared)

3. Particles with aspect ratios near 1

- Q_{ext}: little bias (infrared); underestimated by ADT (solar and infrared)
- ω_0: overestimated (solar); little bias (infrared)
- g: little bias (solar and infrared)

Inasmuch as cases 1 and 2 show some similarity, we are really presented with two kinds of distributions. The first contains particles with aspect ratios near 1. For this distribution results of Q_{ext}, ω_0, and g in the infrared are well represented by distributions of spheres, but extinction, and, thus, optical depth, is underestimated by ADT. No further insight into any small particle radiative anomalies (i.e., any unique radiative characteristics for small particles which may prove significant considering our current inability to make in-situ measurements of concentrations for particles which are less that about $30\mu m$ in diameter) can be gained for this distribution. The solar case is identical to that of the infrared, except that absorption is underestimated by spheres.

When we introduce columns or needles, however, this begins to change. For solar cases optical depth is underestimated by ADT, and the amount of forward scatter is also underestimated by equivalent spheres (g underestimated). Absorption is underestimated (ω_0 overestimated). For infrared cases the amount of forward scatter is now overestimated for smaller particles and has little bias for larger particles. Optical depth is overestimated for small particles. For plates all previous statements apply, except that now ADT overestimates the optical depth. *These results do not appear at first glance to provide a large enough difference between small and large particles for us to say conclusively that any considerable insight can be gained into any small particle radiative anomalies from our research, but there is, however, a difference in the g results which may give some insight one way or another.* It may underscore the importance of small particles by explaining the overestimation of g for plates mentioned throughout this work.

What can be said with some certainty from this study is that *in the infrared portion of the spectrum the use of ADT within current ice cloud modeling efforts should result in underestimations of optical depth except for plates, where at least slight overestimations should be observed, and the use of equivalent spheres should result in underestimations of absorption for infrared.*

In closing, our most important conclusions are herein listed in order of decreasing significance:

1. For aspect ratios near 1 the use of equivalent spheres appears to introduce little or no bias for the extinction efficiency, single scatter albedo, or the asymmetry parameter, except for a weakly absorbing case in which Q_{ext} can be underestimated and ω_0 possibly overestimated.

2. The use of equivalent spheres should in most cases for small and large particles result in an overestimation of ω_0 and a consequential underestimation of absorption.

3. At perpendicular incidence the behavior of finite cylinders can approach that of their infinite cylinder counterparts very quickly, but as incidence angles become oblique the results become more complex.

4. For small cylinders and disks found in the atmosphere there appears to be a strong departure from results for equivalent spheres which may have some implications with respect to small particles.

5.3 Suggestions for Further Research

The results from our present study have been valuable and plentiful, but there are numerous additions and extensions which can make these findings more useful:

1. It is obvious that for a more quantitative description of the biases introduced on ice clouds by the use of the equivalent sphere technique or an ADT model in the description of the cloud optical properties, the present data from this study will have to be applied to macroscale distributions. This will most likely involve data from FIRE II to more quantitatively assess the observed cirrus cloud distributions of particle size and aspect ratio. Some suggestions for the direction of such an analysis include:

    - a reconstruction of the surface plot used by Ou and Liou (1984) to provide a relationship between cloud solar reflectance and infrared emissivity as a function of the solar zenith angle as well as a similar reconstruction of a relationship of both these quantities to IWP.

- an investigation into confirming the results of Evans and Vivekanandan (1990) showing the sensitivities of ice layer optical properties to changes in maximum particle size and particle volume, as well as the poor performance of equivalent spheres for the depiction of distributions of plates.

2. In addition, as was stated before in chapter 3, this current study lists an outline of investigation which extends beyond itself. A current undertaking of the study expressed in #1 would have to incorporate refractive index spectra which assumed the real part of m to always be near 1.3, an incomplete depiction of reality especially for the infrared. In addition, there is also the matter of the additional values of θ listed in table 3.4, which are not investigated in this study. Since the current results appear to suggest that the results exhibit smooth variations with changes in θ , these aditional angles may prove to be superfluous. There may, however, be a few cases, as was found for infinite cylinders, where significant errors may arise if information for these additional angles is not known. These additional angles should, thus, be examined.

3. The curve fit extensions to large particles appear in most cases to be reliable, but even in the best cases they are, after all, only hypothetical. To insure their accuracy, additional studies will be necessary. In particular towards this end, there is a technique known as the T-Matrix technique discussed in Barber and Hill (1990), which may prove useful.

4. The current results are not extendible to remote sensing or Monte Carlo applications, since these require reliable phase function information. Extensions to these applications will require the initiation of the same runs with much higher dipole resolution. Again, the T-Matrix technique may also prove useful here.

5. Circular cylinders and disks still do not describe full the shapes of ice hydrometeors. It is left to subsequent study the unenviable task of assessing the effects of hexagonality, porosity, holes, and dendritic structure, effects which Evans and Vivekanandan (1990) suggested may be of considerable importance (see the third enumeration in the first

part of the itemized results of chapter 3). Flatau (1992) demonstrated the ability of DDA to provide results for particles with such fine structure.

Hopefully from these extensions of the present results we will be able to more fully assess the effects of cirrus clouds upon climate and humanity.

Bibliography

Abramowitz, M. and I. A. Stegun, 1972: *Handbook of mathematical functions with formulas, graphs, and mathematical tables.* Dover Publications, New York.

Ackerman, S. A. and G. L. Stephens, 1987: The absorption of solar radiation by cloud droplets: an application of anomalous diffraction theory. *J. Atmos. Sci*, **44**, 1574—1588.

Allan, L. E. and G. C. McCormick, 1980: Measurements of the backscatter matrix of dielectric bodies. *IEEE Transactions on Antennas and Propagation*, **AP-28**(2), 166–169.

Barber, P. W. and S. Hill, 1990: *Light Scattering by Particles: Computational Methods.* World Scientific, Teaneck, N.J., 261.

Barton, I. J., 1983: Upper level cloud climatology from an orbiting satellite. *J. Atmos. Sci.*, **40**, 435–447.

Bohren, C. F. and D. R. Huffman, 1983: *Absorption and scattering of light by small particles.* J. Wiley and Sons, New York.

Cooke, D. D. and M. Kerker, 1969: Light scattering from long thin glass cylinders at oblique incidence. *J. Opt. Soc. Am.*, **59**(1), 43–48.

Cox, S. K., 1971: Cirrus clouds and climate. *J. Atmos. Sci.*, **28**, 1513—1515.

Cross, D. A. and P. Latimer, 1970: General solutions for the extinction and absorption efficiencies of arbitrary oriented cylinders by anomalous-diffraction methods. *J. Opt. Soc. Am.*, **60**, 904—907.

Draine, B. T., 1988: The discrete-dipole approximation and its application to interstellar graphite grains. *Astrophys. J.*, **333**, 848—872.

Dungey, C. E. and C. F. Bohren, 1991: Light scattering by nonspherical particles: A refinement to the coupled-dipole method. *J. Opt. Soc. Am.*, **8**(1), 81–87.

Evans, K. F. and J. Vivekanandan, 1990: Multiparameter radar and microwave radiative transfer modeling. *IEEE Transactions on Geoscience and Remote Sensing*, **28**(4), 423—437.

Farone, W. A. and M. Kerker, 1966: Light scattering from long submicron glass cylinders at normal incidence. *J. Opt. Soc. Am.*, **56**(4), 481–487.

Farone, W. A. and C. W. Querfield, 1966: Electromagnetic scattering from raidally inhomogeneous infinite cylinders at oblique incidence. *J. Opt. Soc. Am.*, **56**(4), 476–480.

Flatau, P. J., 1992: *Scattering by irregular particles in anomalous diffraction and discrete dipole approximations.* PhD thesis, Colorado State University, Fort Collins, Colorado 80523, 147.

Flatau, P. J., G. L. Stephens, B. T. Draine, and A. Maslowska, 1989: Scattering by the hexagonal ice cystals in the discrete dipole approximation. In preparation.

Freeman, K. P. and K.-N. Liou, 1979: Climatic effects of cirrus clouds. *Advances in Geophysics*, **21**, 231—287.

Fuller, K. A., 1991: Optical resonances and two-sphere systems. *Appl. Opt.*, **30**, 4716—4731.

Fuller, K. A. and G. W. Kattawar, 1988: Consummate solution to the problem of classical electromagnetic scattering by an ensemble of spheres. I. Linear chains. *Opt. Lett.*, **13**, 90—92.

Goodman, J. J., B. T. Draine, and P. J. Flatau, 1991: Application of fast-Fourier-transform techniques to the discrete-dipole approximation. *Optics Letters*, **16**, 1198—1200.

Greenberg, J. M., N. E. Pedersen, and J. C. Pedersen, 1961: Microwave analog to the scattering of light by nonspherical particles. *Journal of Applied Physics*, **32**(2), 233–242.

Hecht, E., 1987: *Optics.* Addison-Wesley Publishing Co., 676, 2 edition.

Heymsfield, A. J., 1972: Ice crystal terminal velocities. *J. Atmos. Sci.*, **29**, 1348—1356.

Jackson, J. D., 1975: *Classical electrodynamics.* Wiley, New York, 2nd edition.

Kerker, M., 1969: *The scattering of light and other electromagnetic radiation.* Academic Press, New York and London.

Lind, A. and J. M. Greenberg, 1966: Electromagnetic scattering by obliquely ... cylinders. *J. Appl. Phys.*, **37**(8), 3195–3203.

Liou, K.-N., 1986: Influence of cirrus clouds on weather and climate processes: A global perspective. *Mon. Wea. Rev.*, **114**, 1167—1199.

Liou, K.-N. and K. L. Gebhart, 1982: Numerical experiments on the thermal equilibrium temperature in cirrus cloudy atmospheres. *J. Meteor. Soc. Japan*, **60**(1), 570–582.

Machta, L. and T. Carpenter, 1971: Trends in high cloudiness at denver and salt lake city. In *Man's Impact on Climate*, Matthews, W. H., Kellogg, W. W., and Robinson, G. D., editors, MIT Press, Cambridge, Mass., 410–415.

Mahood, R. W., 1987: The application of vector diffraction to the scalar anomalous diffraction approximation of van de Hulst. Master's thesis, The Pennsylvania State University, Department of Meteorology.

Manabe, S. and R. F. Strickler, 1964: Thermal equilibrium of the atmosphere with a convective adjustment. *J. Atmos. Sci.*, **21**, 361—385.

Manabe, S. and R. T. Wetherald, 1967: Thermal equilibrium of the atmosphere with a given distribution of relative humidity. *J. Atmos. Sci.*, **24**, 241—259.

Maxwell, J. C., 1892: *A Treatise on Electricity and Magnetism*, volume 2. Oxford Clarendon Press, 500.

Ou, S. S. and K.-N. Liou, 1984: A two dimensional radiation-turbulence climate model. I: Sensitivity to cirrus radiative properties. *J. Atmos. Sci.*, **41**, 2289—2309.

Pozar, D. M., 1990: *Microwave Engineering.* Addison-Wesley Publishing Co., 154–163.

Press, W. H., B. P. Flannery, S. A. Teukolsky, and W. Vetterling, 1992: *Numerical recipes, the art of scientific computing.* Cambridge University Press, Cambridge.

Prudnikov, A., Y. Brychkov, and O. Marichev, 1988: *Special Functions*, volume 2 of *Integrals and Series.* Gordon and Breach Science Publishers.

Purcell, E. M. and C. R. Pennypacker, 1973: Scattering and absorption of light by non-spherical dielectric grains. *Astrophys. J.*, **186**, 705—714.

Randall, D. A., J. A. Coakley, C. W. Fairall, R. A. Kropfli, and D. H. Lenschow, 1984: Outlook for research on subtropical marine stratiform clouds. *Bull Am. Met. Soc*, **65**(12), 1290–1301.

Rayleigh, J. W. S., 1881: On the electromagnetic theory of light. *Philosophical Magazine*, **12**, 81–101.

Rayleigh, J. W. S., 1918: On the dispersal of light by a dielectric cylinder. *Philosophical Magazine*, **36**, 365–376.

Rayleigh, J. W. S., 1945: *The Theory of Sound*, volume 2. Dover Publications, 504.

Southworth, G. C., 1961: *Principles and Applications of Waveguide Transmission.* D. van Nostrand Company, Inc., 689.

Stephens, G. L., 1980: Radiative properties of cirrus clouds in the infrared region. *J. Atmos. Sci.*, **37**, 435—446.

Stephens, G. L., 1984a: The parameterization of radiation for numerical weather prediction and climate models. *Mon. Wea. Rev.*, **112**, 826—867.

Stephens, G. L., 1984b: Scattering of plane waves by soft obstacles: Anomalous diffraction theory for circular cylinders. *Appl. Optics*, **23**, 954—959.

Stephens, G. L., S.-C. Tsay, P. W. Stackhouse, and P. J. Flatau, 1990: The relevance of the microphysical and radiative properties of cirrus clouds to climate and climate feedback. *J. Atmos. Sci.*, **47**, 1742–1753.

Stephens, G. L. and P. J. Webster, 1981: Clouds and climate: sensitivity of simple systems. *J. Atmos. Sci.*, **38**, 235—247.

van de Hulst, H. C., 1957: *Light Scattering by Small Particles.* Dover Publications.

Wait, J. R., 1955: Scattering of a plane wave from a circular dielectric cylinder at oblique incidence. *Canadian Journal of Physics*, **33**, 189–195.

Weast, R. C., M. J. Astle, and W. H. Beyer, 1986: *CRC Handbook of Chemistry and Physics.* CRC Press, Inc., 66 edition.

Wylie, D. P., W. P. Menzel, H. M. Woolf, and K. I. Strabala, 1994: Four years of global cirrus cloud statistics using hirs. Journal of Climate in press.

Yamashita, A., 1973: On the trigonal growth of ice crystals. *J. Meteor. Soc. Japan*, **51**(5), 307–317.

Appendix A

THE ENTIRETY OF THE DDA EXTINCTION EFFICIENCY RESULTS

This appendix shows the full extent of the extinction efficiency results From the usage of the DDA model. For a full explanation of the model, the format of the plots, or the values of the four refractive indices or the seven incidence angles the reader is referred to sections 3.1 and 3.2 of chapter 3. The results are displayed in three forms:

$$Q_{ext} \qquad \frac{Q_{ext}}{Q_{ext_{Mie}}} \qquad \frac{Q_{ext1}}{Q_{ext_{inf}}}$$

the second ratioing the results with results from equivalent spheres and the latter with results from an infinite cylinder of the same radius.

For the Q_{ext} results the labelled contours are .8, 1.6, 2.4, 3.2 and 4.0. The contour interval is .2. For the $\frac{Q_{ext}}{Q_{ext_{Mie}}}$ results the labelled contours are .4, .8, 1.2, 1.6, 2.0, and 2.4. The contour interval is .1. Lastly, for the $\frac{Q_{ext}}{Q_{ext_{inf}}}$ results the labelled contours are .4, .8, 1.2, 1.6, 2.0, 2.4, and 2.8. The contour interval is .1, and the contours extend from a minimum value of .2 to a maximum value of 3.0, and since there are cases in which the data exceeds these extremes, one must approach the plots with some caution. The m_1, θ_2 case is a good example, where the peak in the upper left does not plateau, but exceeds 3.0.

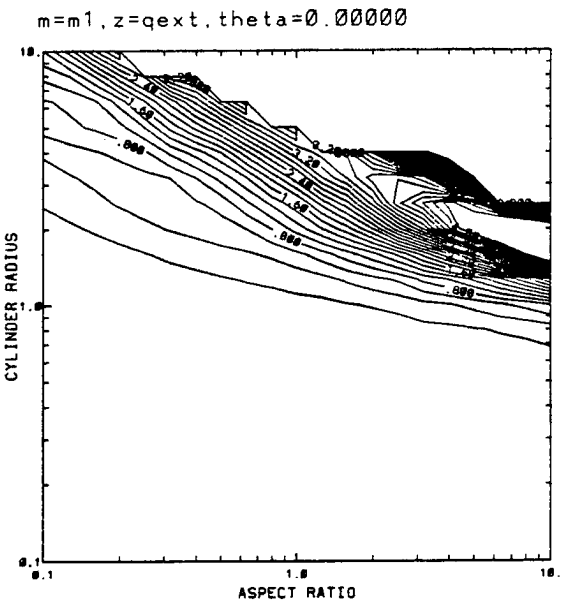

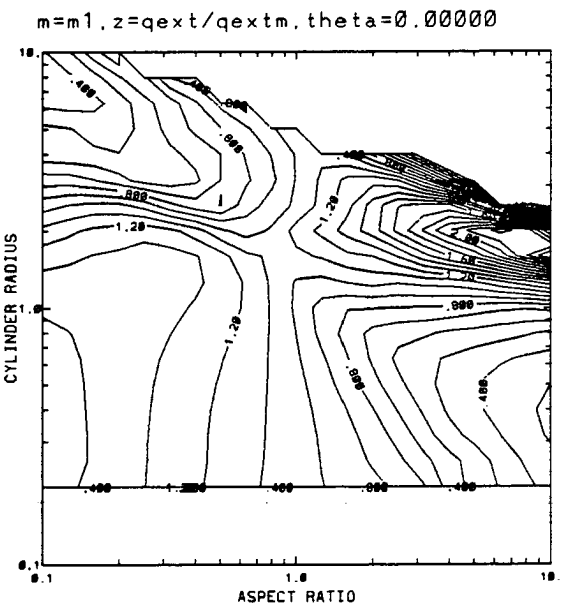

Figure A.1: Results for $m = m_1$ and $\theta = \theta_1$. (The last of the three plots is inapplicable.)

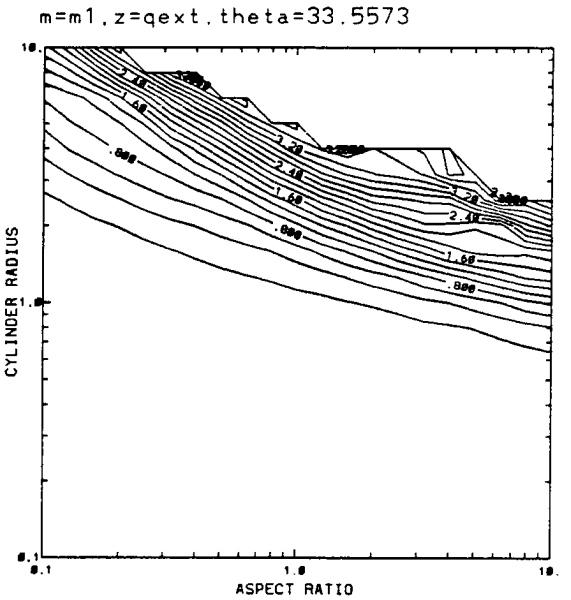

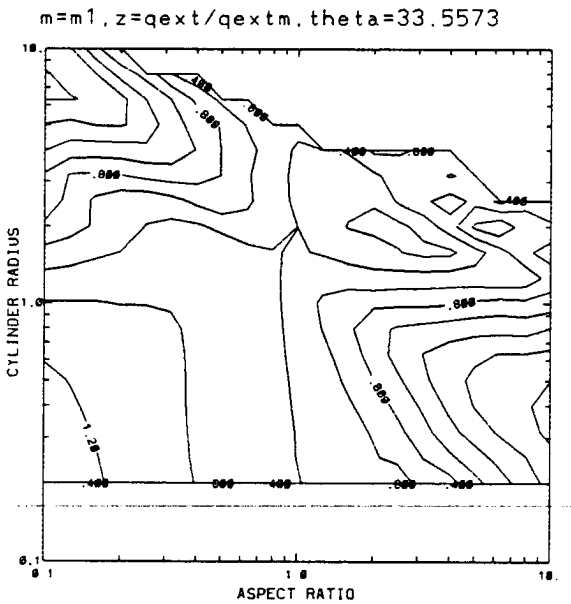

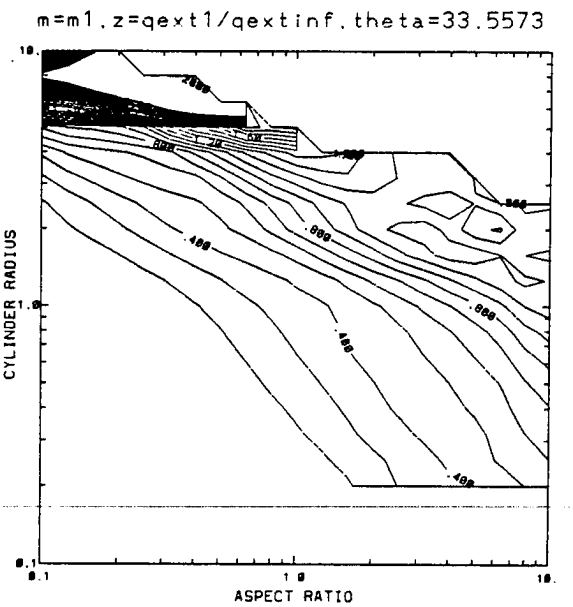

Figure A.2: Results for $m = m_1$ and $\theta = \theta_2$.

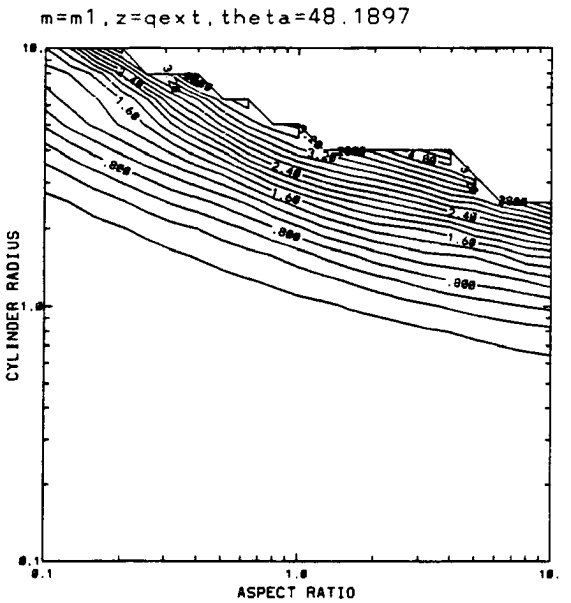

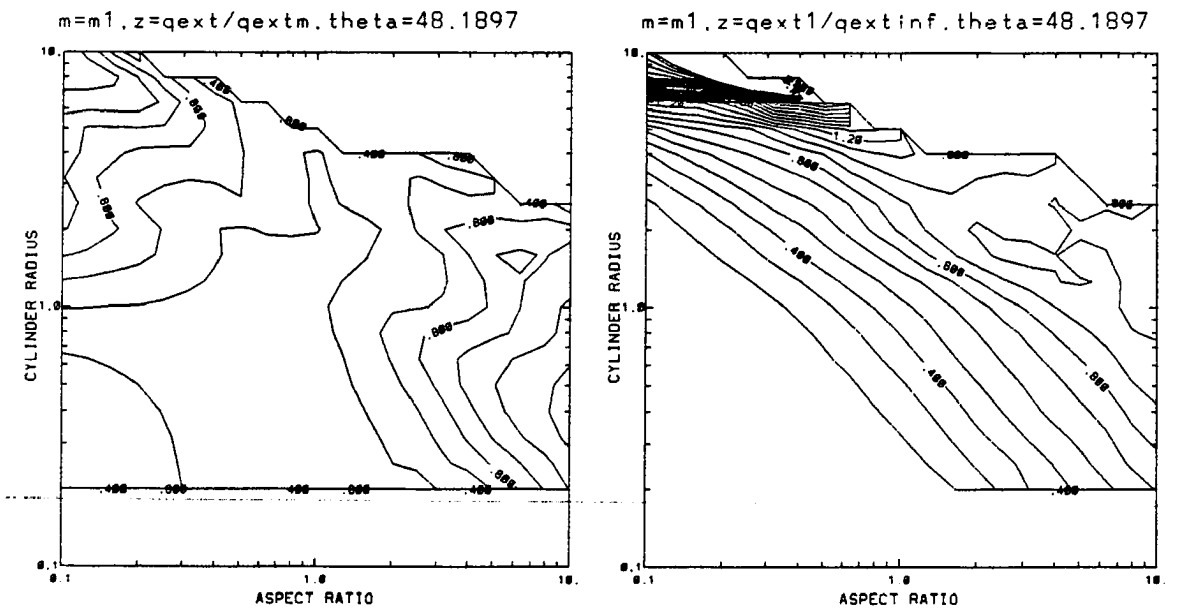

Figure A.3: Results for $m = m_1$ and $\theta = \theta_3$.

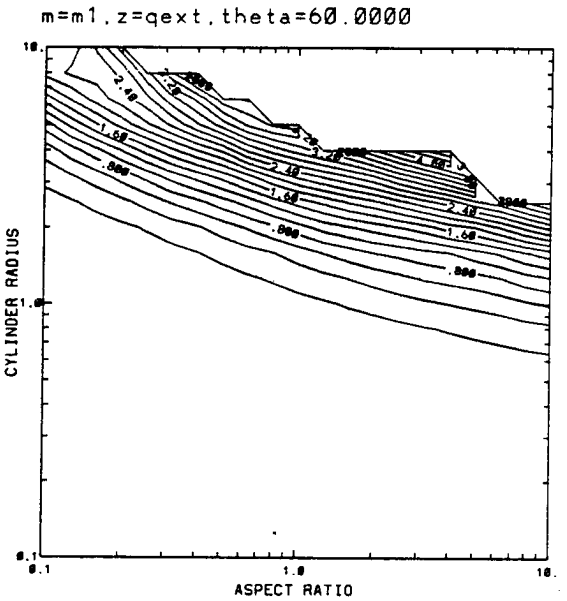

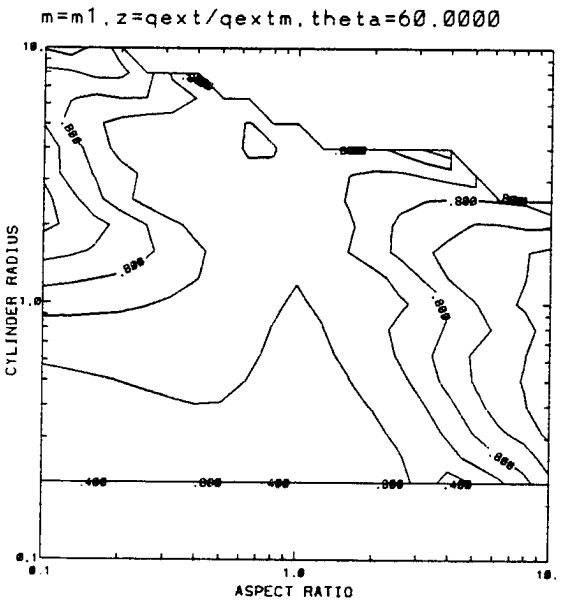

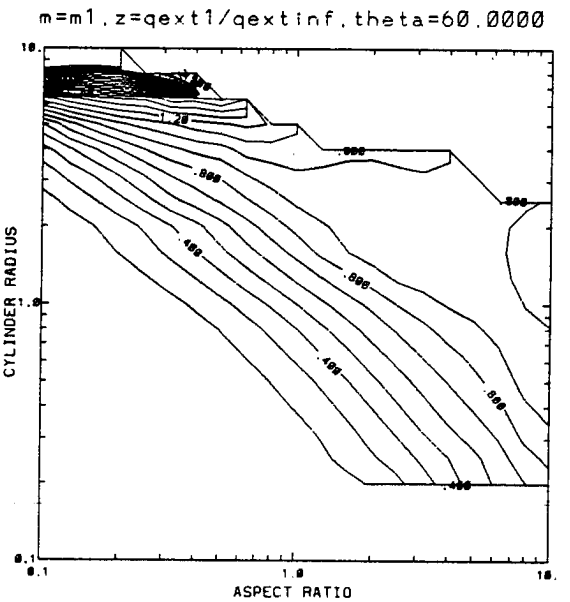

Figure A.4: Results for $m = m_1$ and $\theta = \theta_4$.

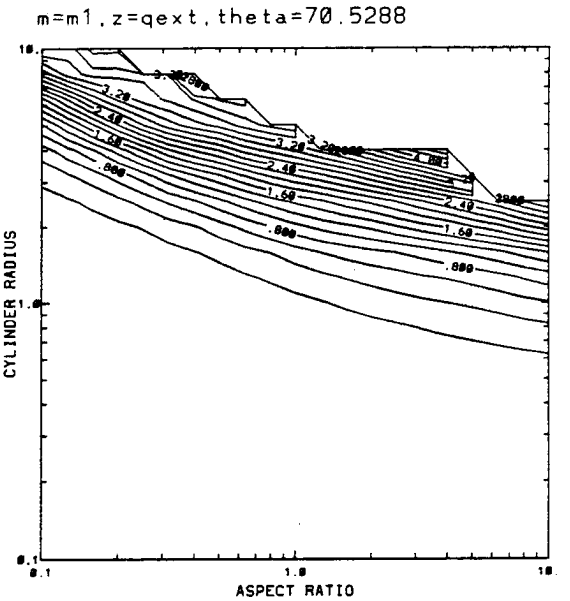

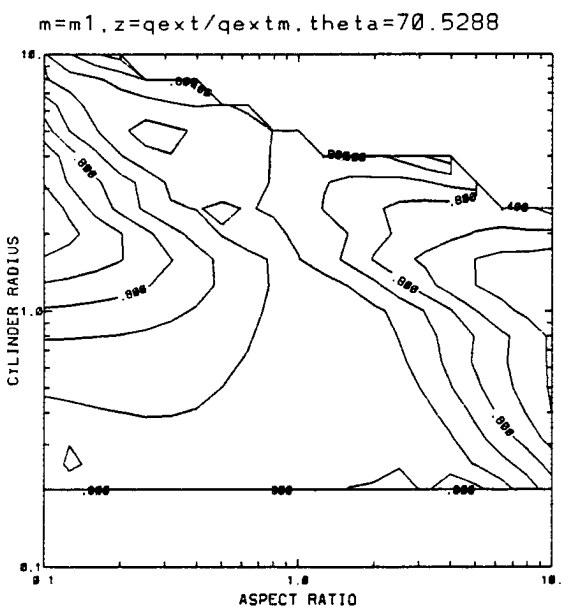

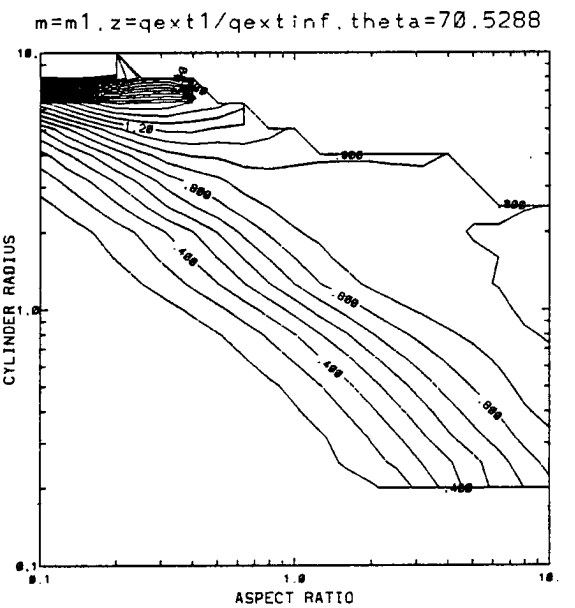

Figure A.5: Results for $m = m_1$ and $\theta = \theta_5$.

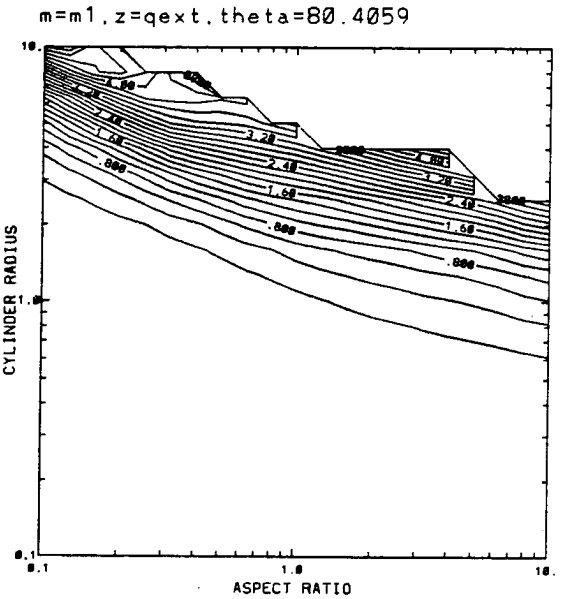

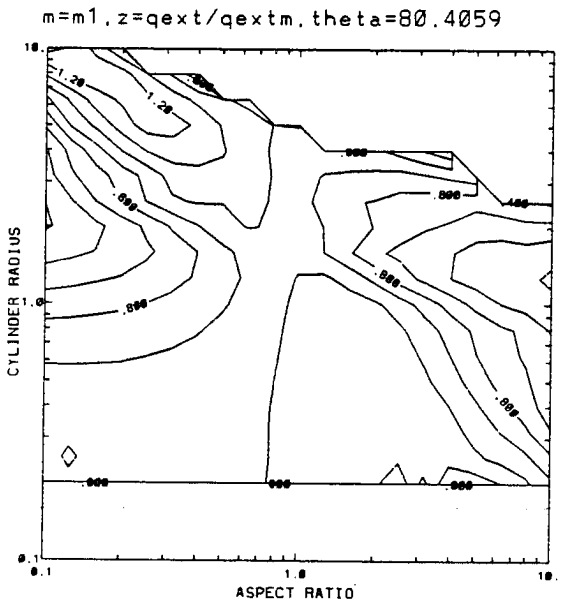

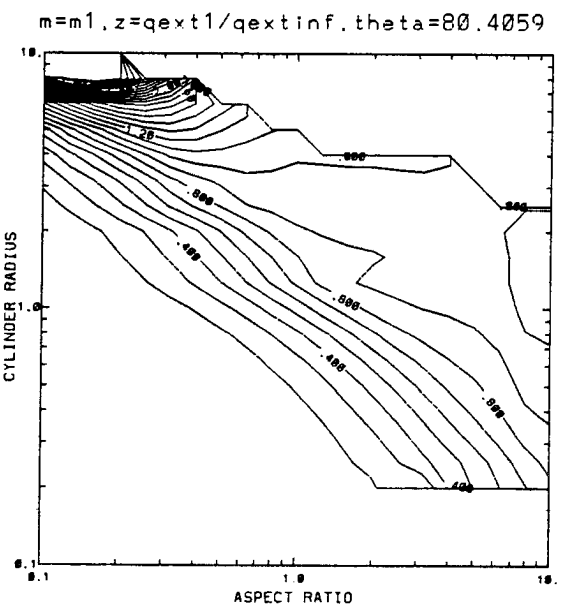

Figure A.6: Results for $m = m_1$ and $\theta = \theta_6$.

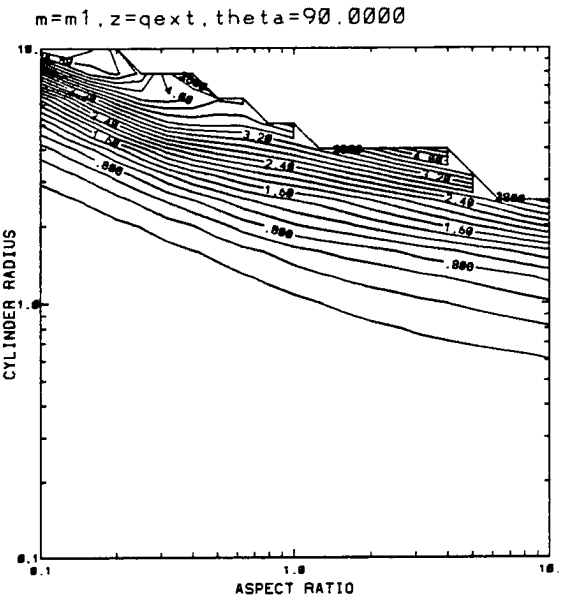

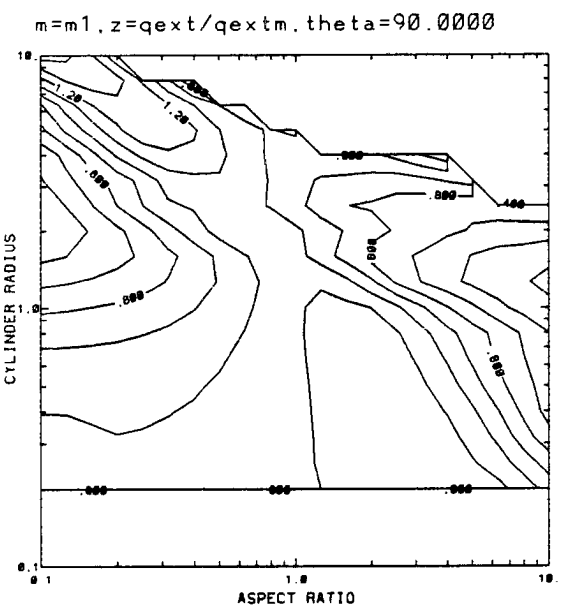

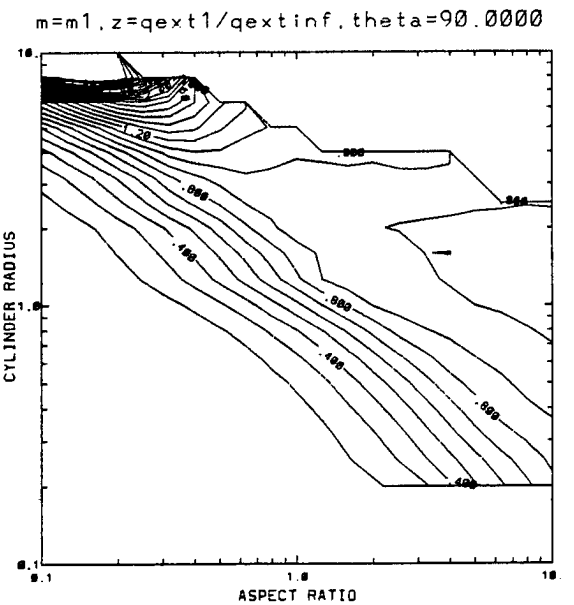

Figure A.7: Results for $m = m_1$ and $\theta = \theta_7$.

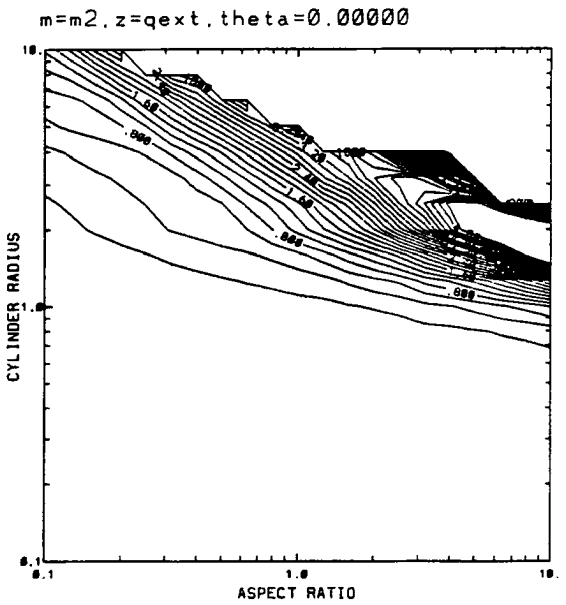

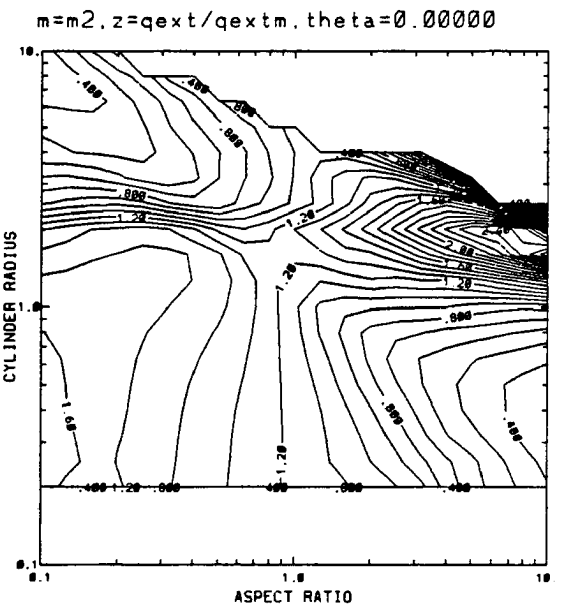

Figure A.8: Results for $m = m_2$ and $\theta = \theta_1$. (The last of the three plots is inapplicable.)

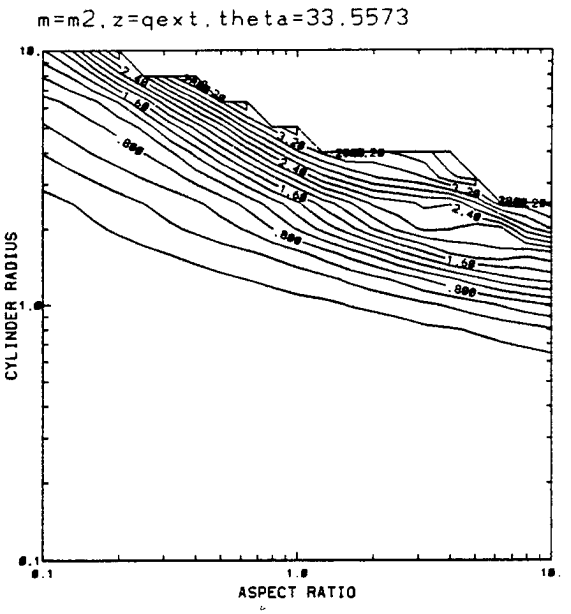

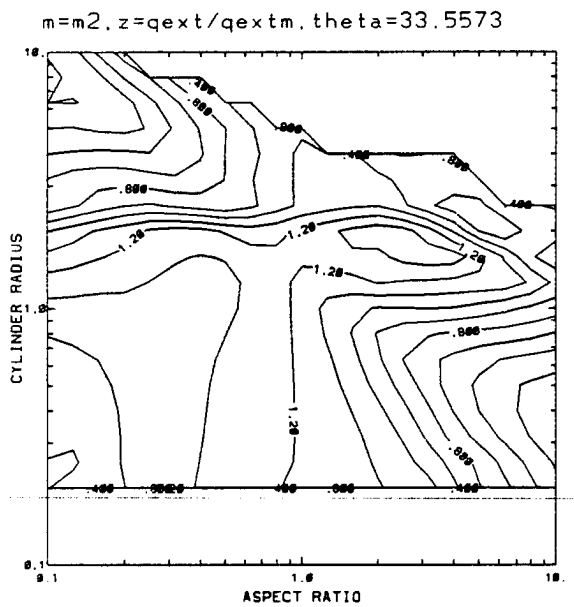

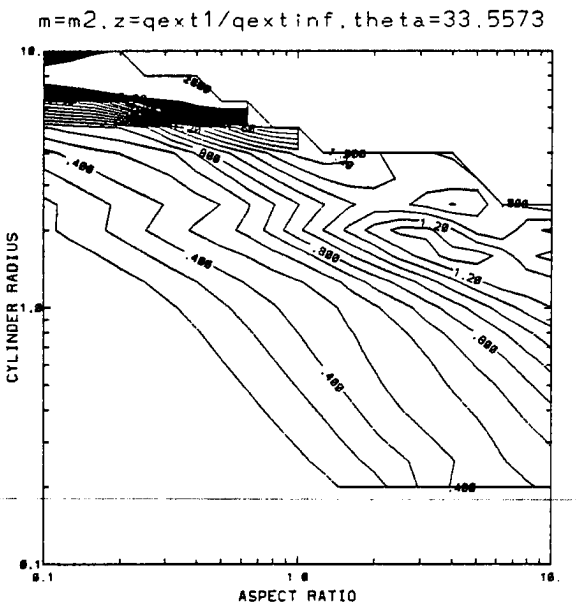

Figure A.9: Results for $m = m_2$ and $\theta = \theta_2$.

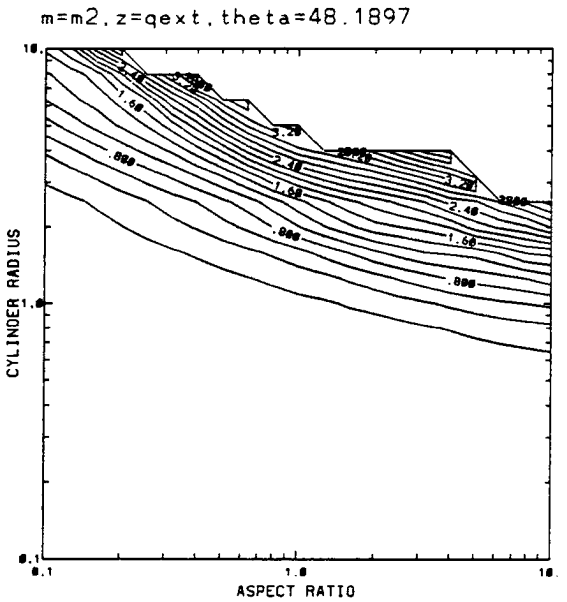

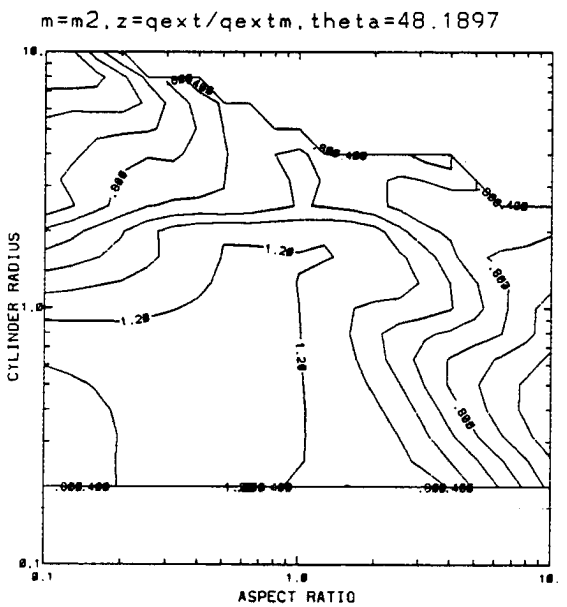

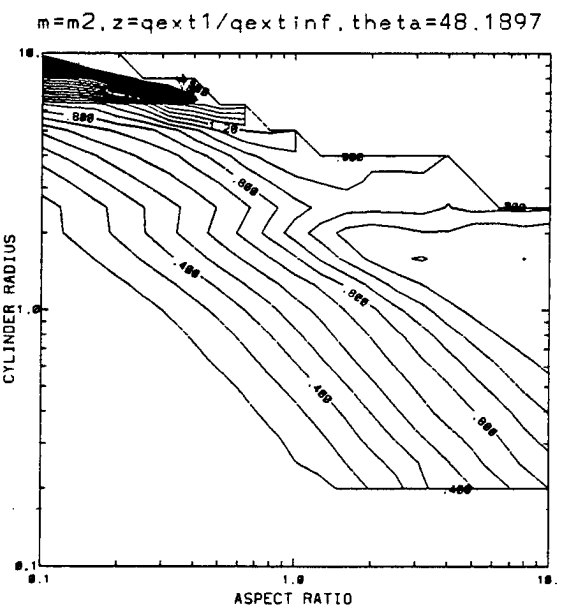

Figure A.10: Results for $m = m_2$ and $\theta = \theta_3$.

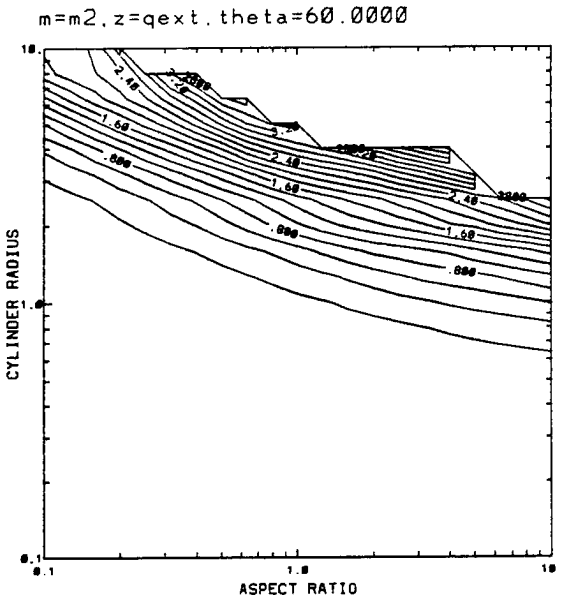

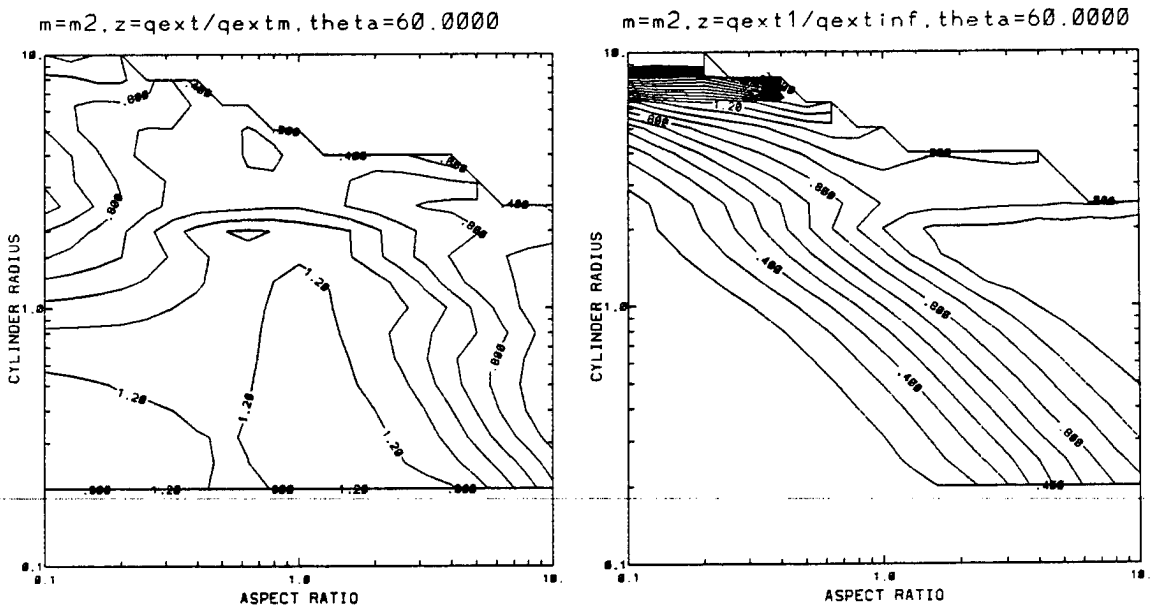

Figure A.11: Results for $m = m_2$ and $\theta = \theta_4$.

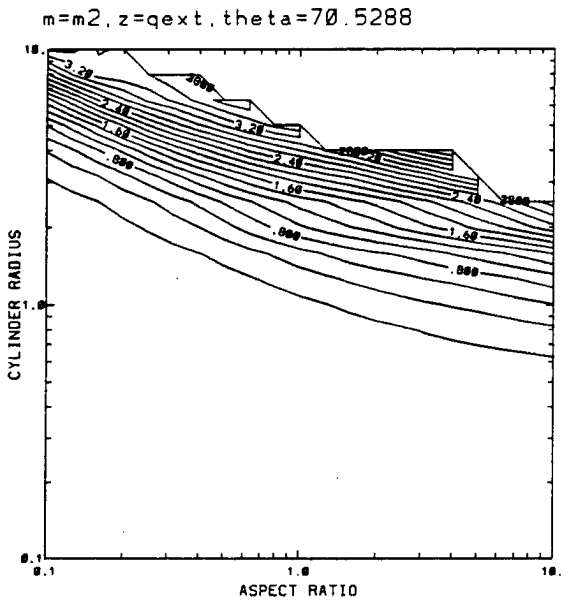

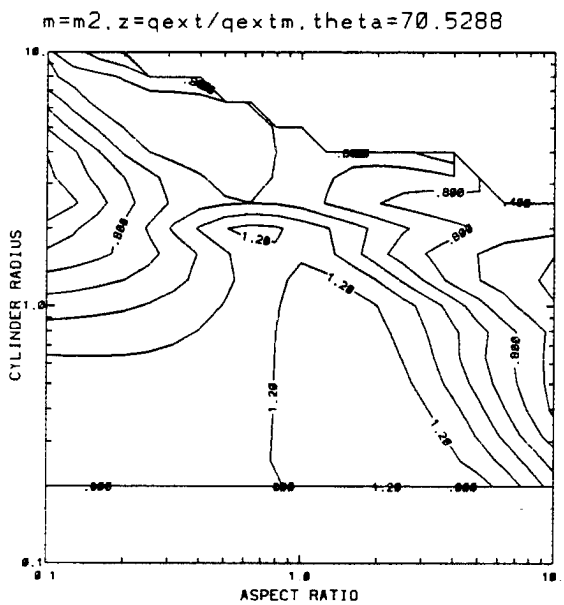

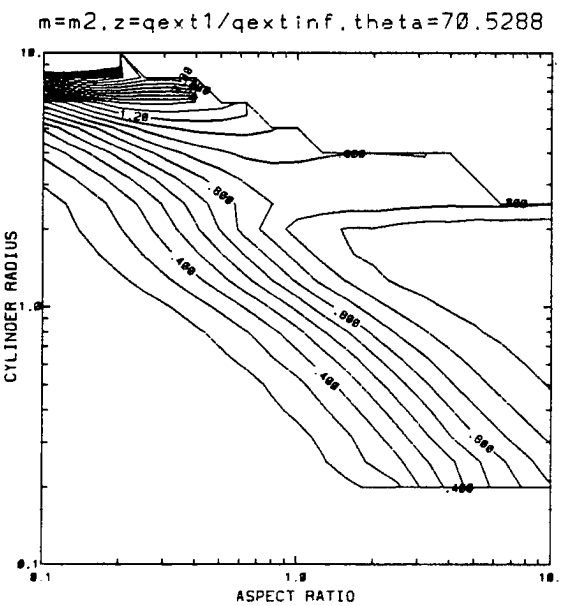

Figure A.12: Results for $m = m_2$ and $\theta = \theta_5$.

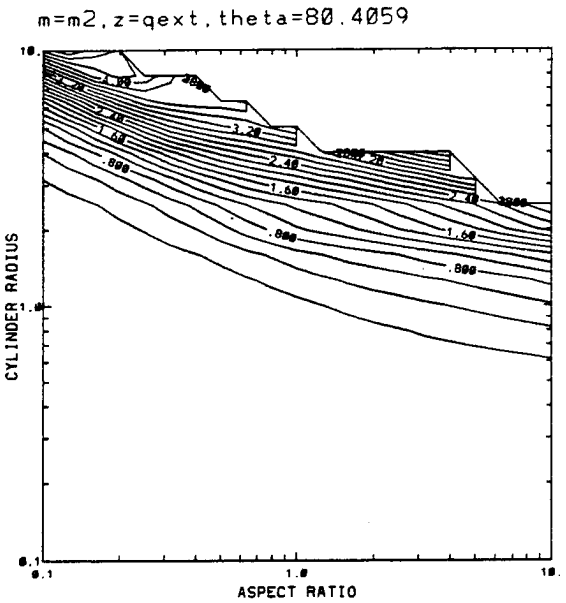

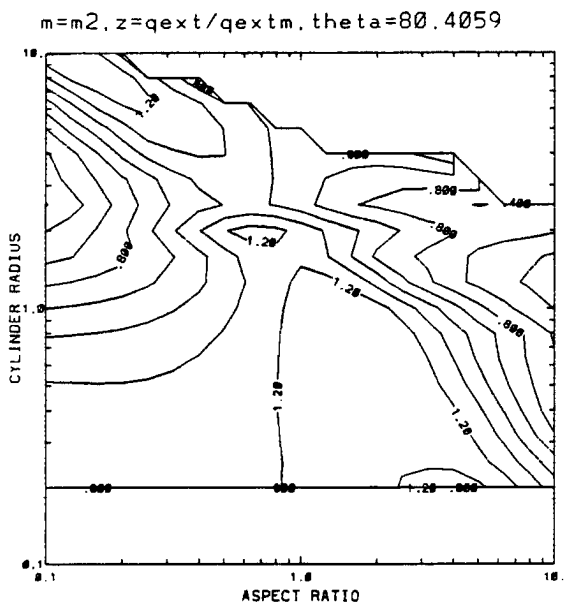

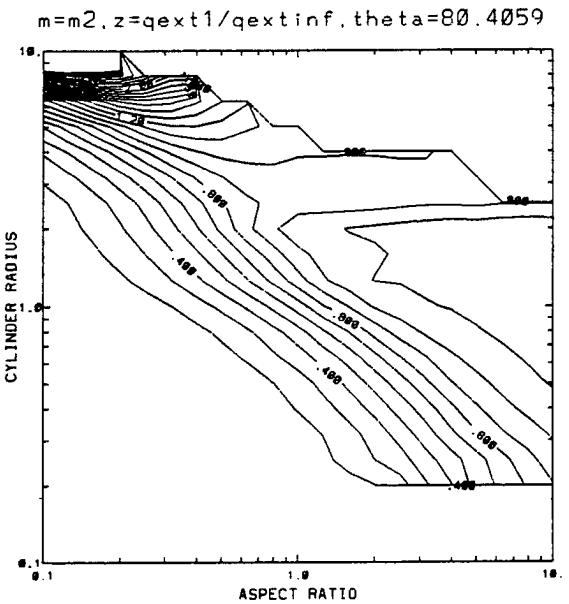

Figure A.13: Results for $m = m_2$ and $\theta = \theta_6$.

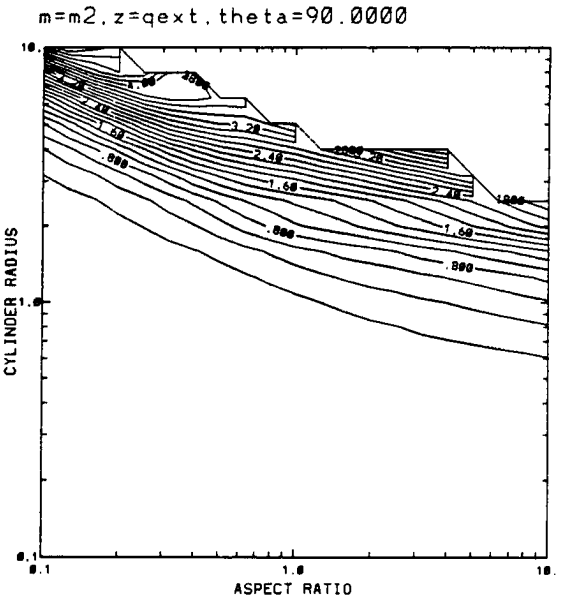

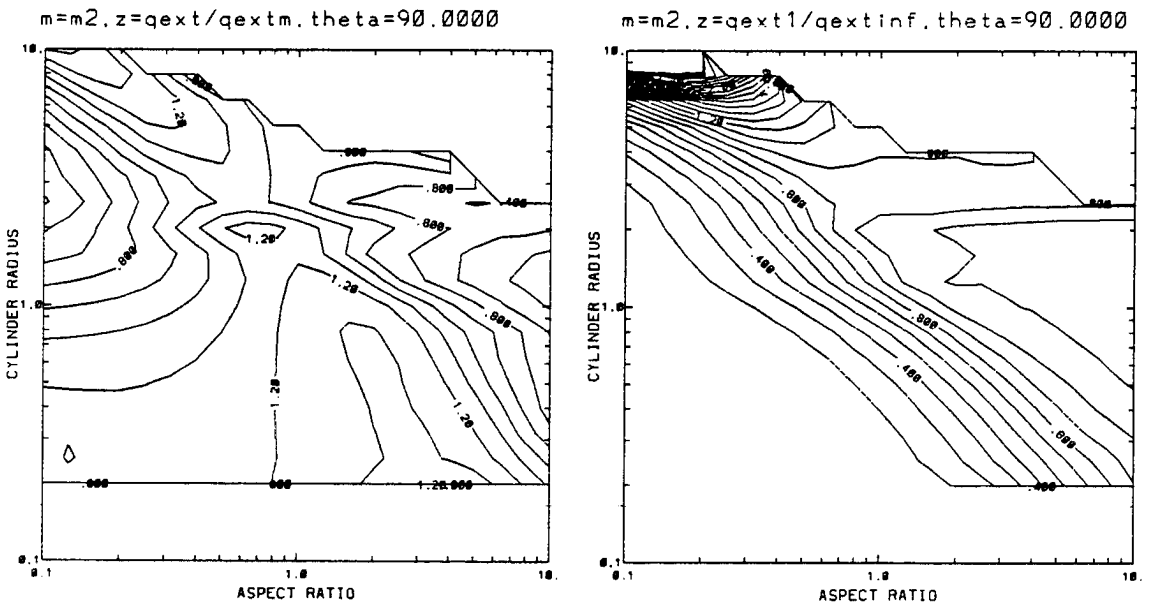

Figure A.14: Results for $m = m_2$ and $\theta = \theta_7$.

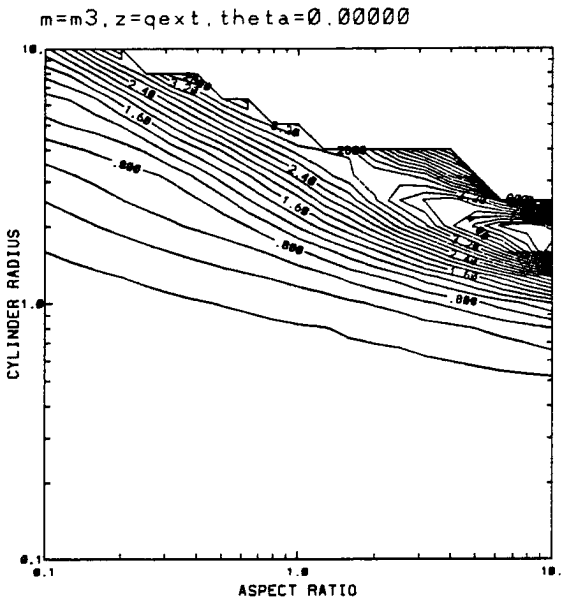

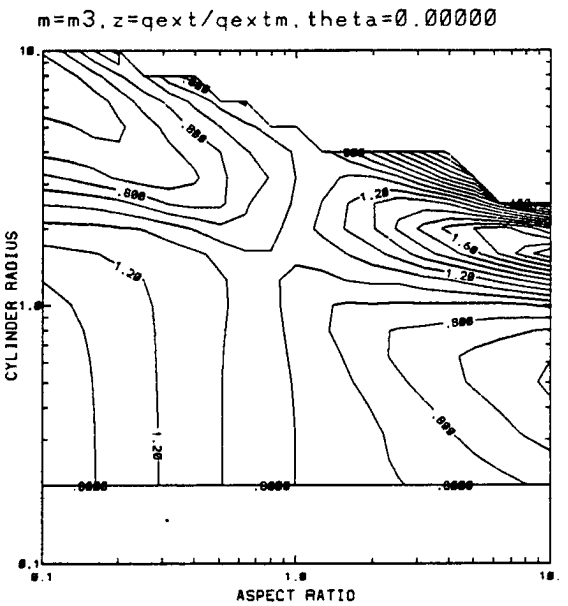

Figure A.15: Results for $m = m_3$ and $\theta = \theta_1$. (The last of the three plots is inapplicable.)

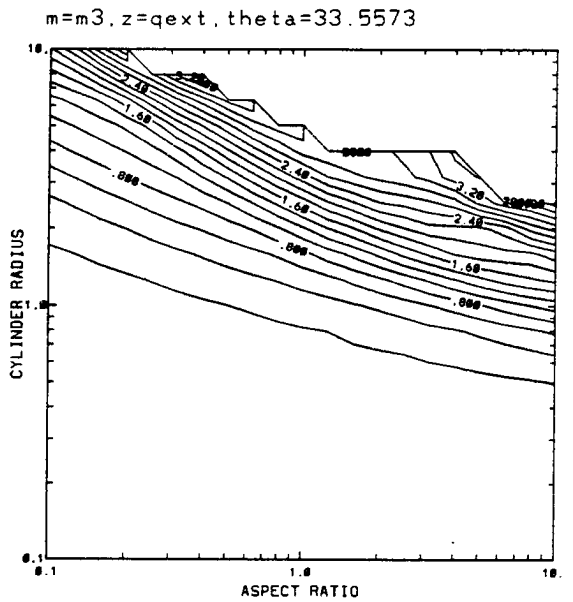

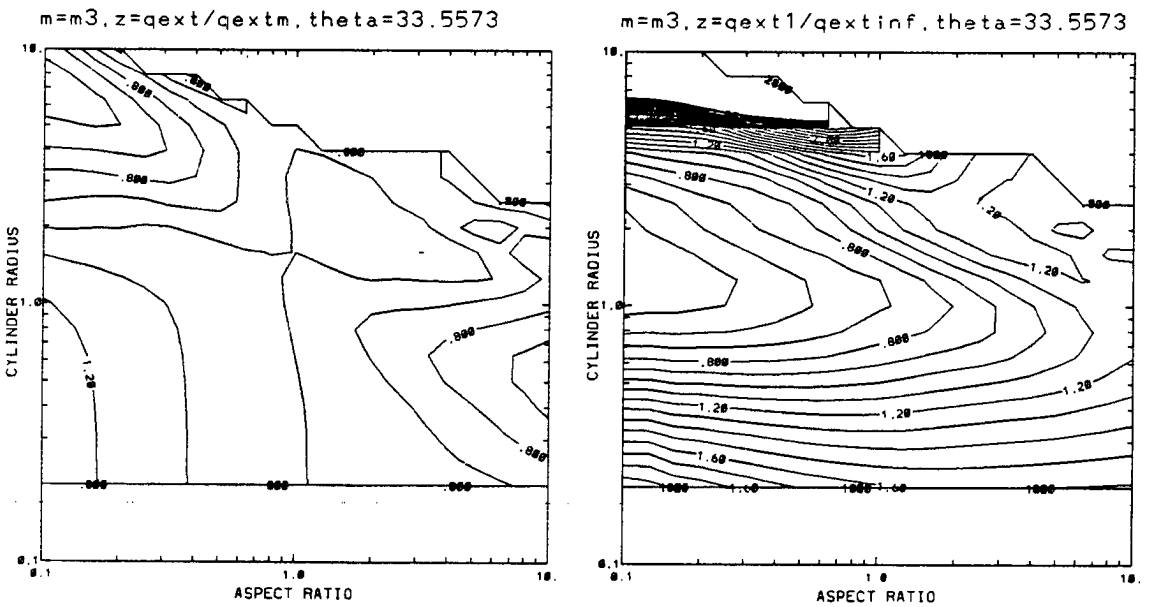

Figure A.16: Results for $m = m_3$ and $\theta = \theta_2$.

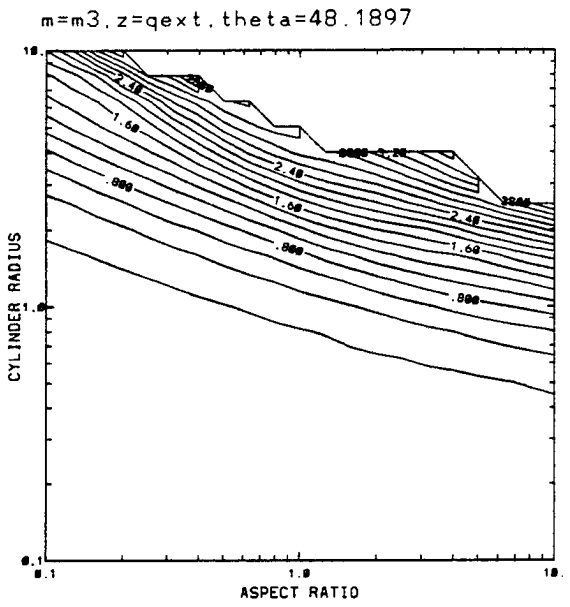

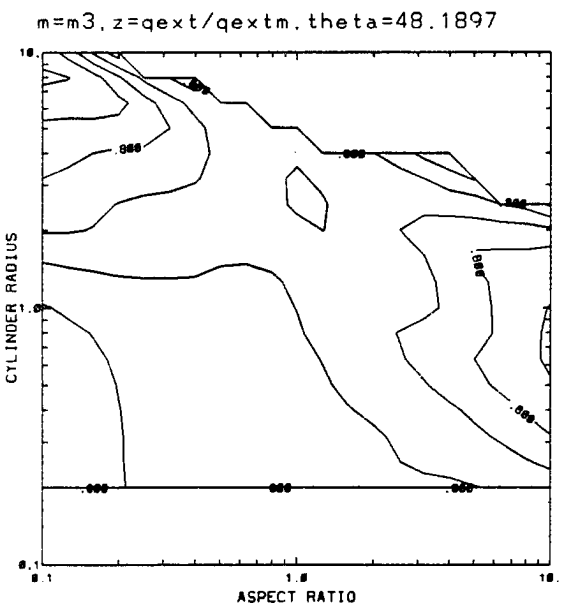

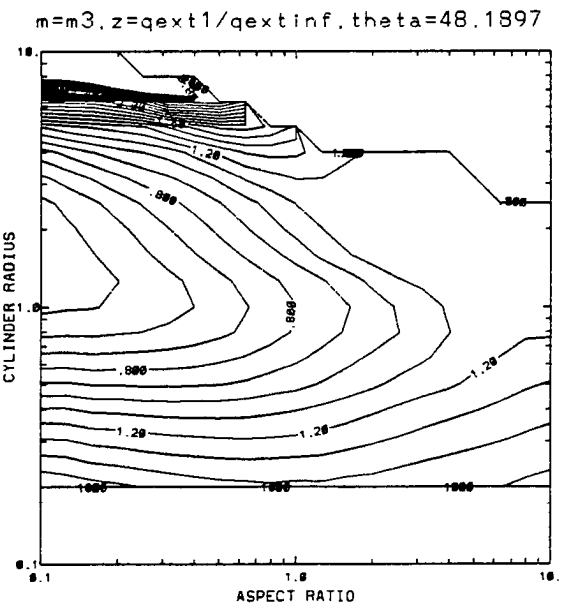

Figure A.17: Results for $m = m_3$ and $\theta = \theta_3$.

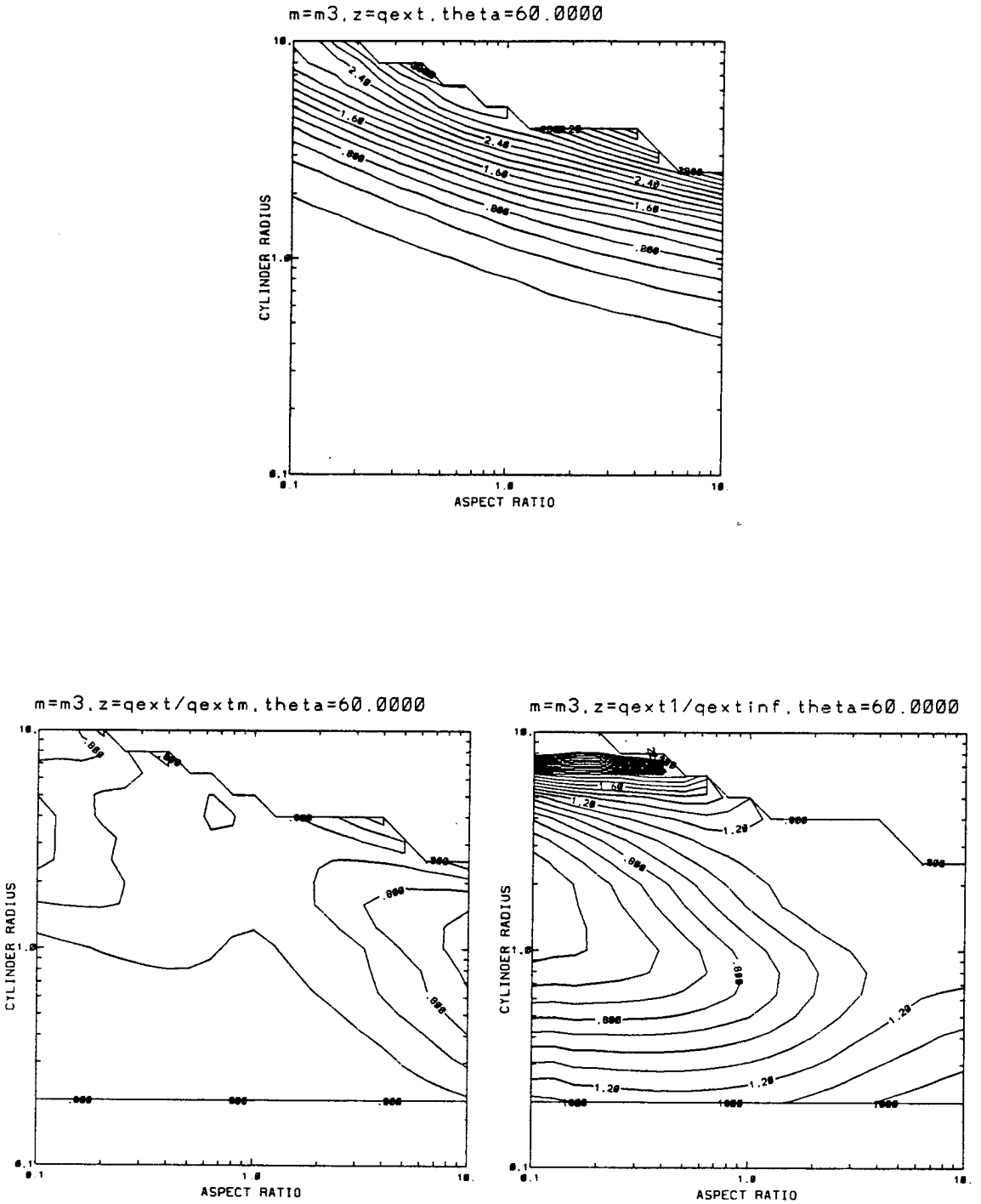

Figure A.18: Results for $m = m_3$ and $\theta = \theta_4$.

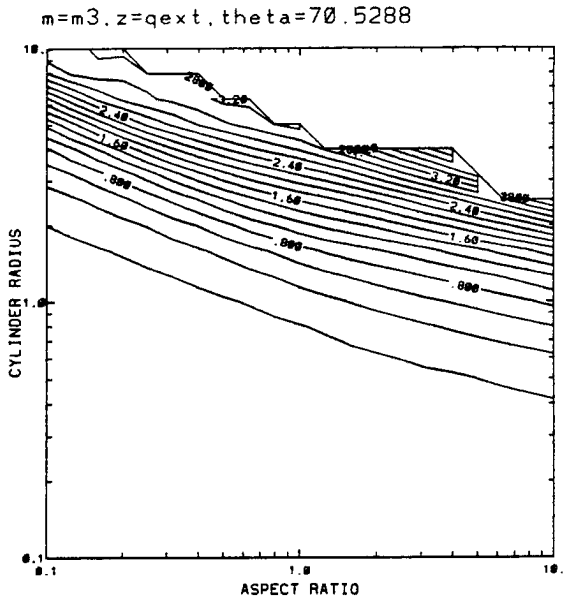

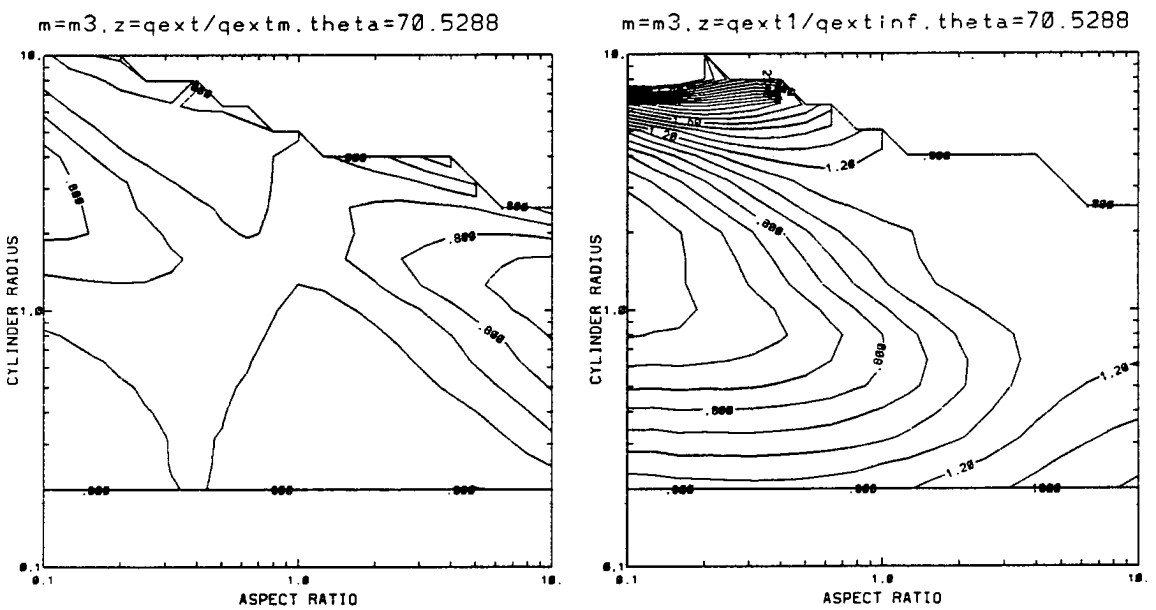

Figure A.19: Results for $m = m_3$ and $\theta = \theta_5$.

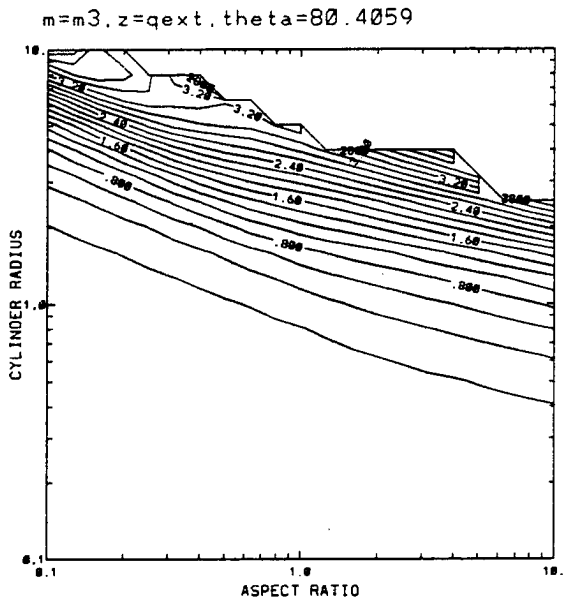

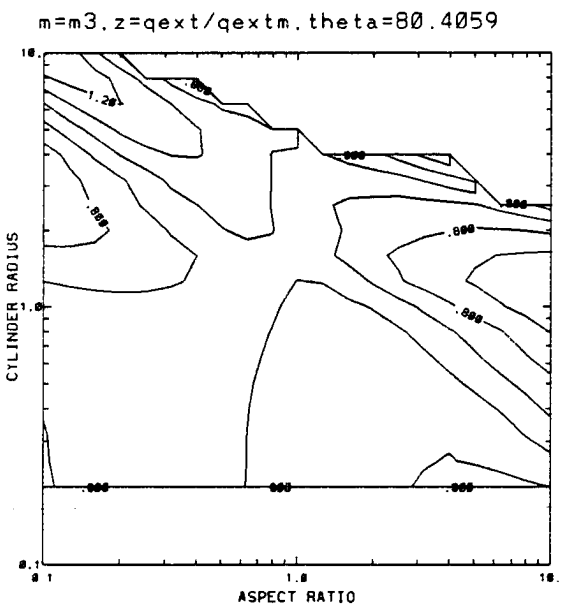

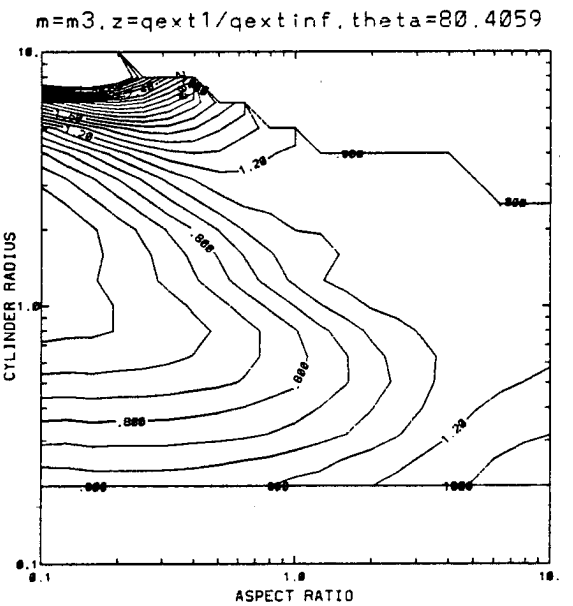

Figure A.20: Results for $m = m_3$ and $\theta = \theta_6$.

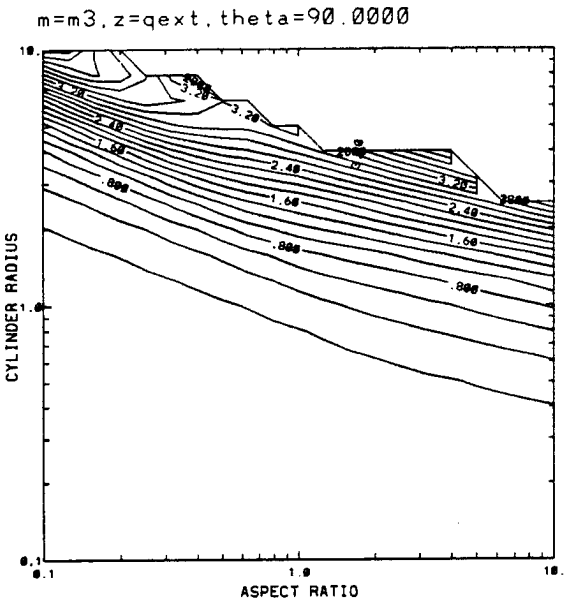

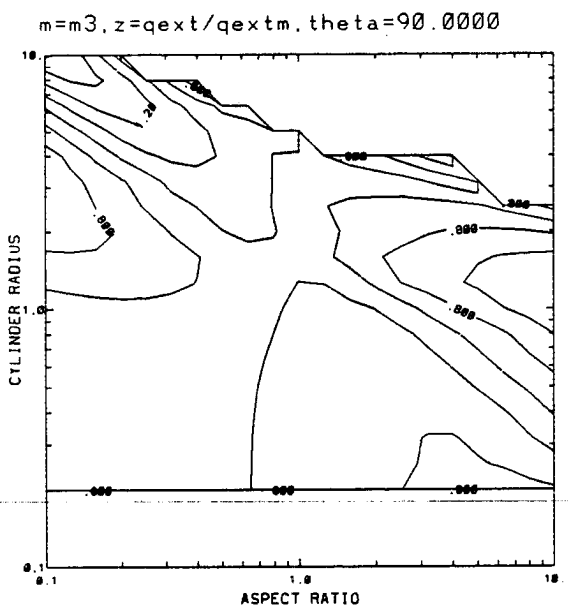

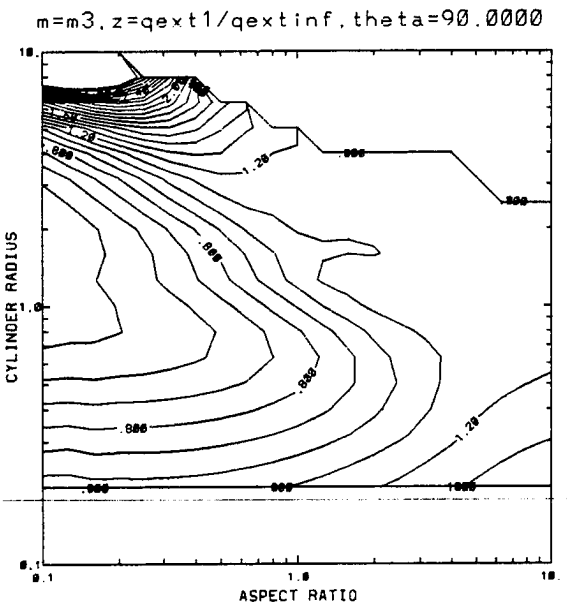

Figure A.21: Results for $m = m_3$ and $\theta = \theta_7$.

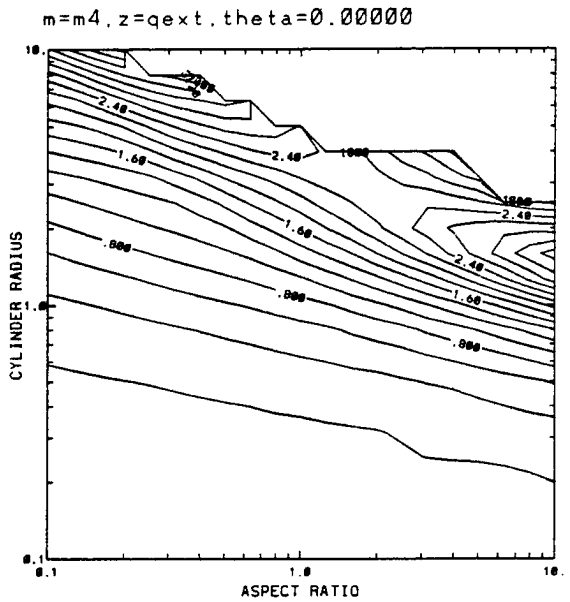

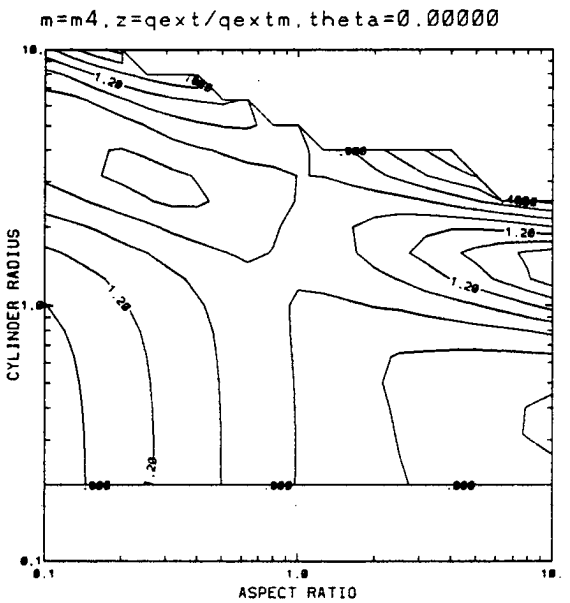

Figure A.22: Results for $m = m_4$ and $\theta = \theta_1$. (The last the three plots is inapplicable.)

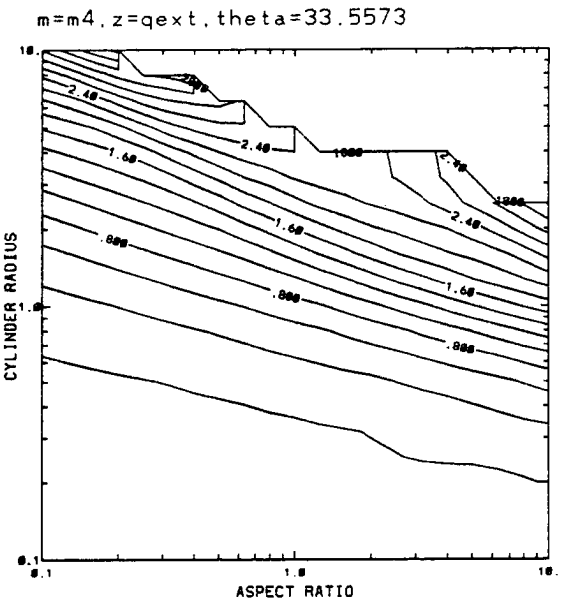

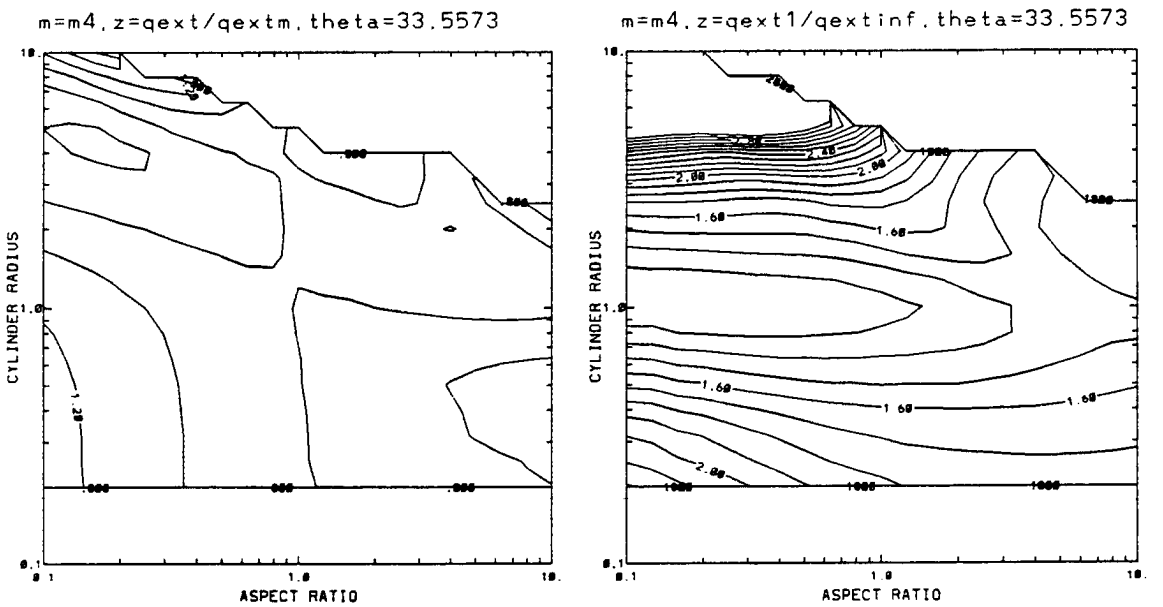

Figure A.23: Results for $m = m_4$ and $\theta = \theta_2$.

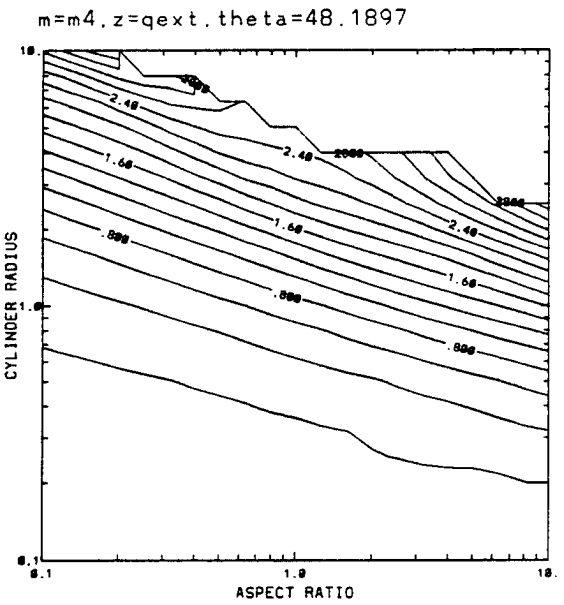
m=m4, z=qext, theta=48.1897
CYLINDER RADIUS
ASPECT RATIO
2.48
1.68
.880
2.48
1.68
.880
2.48
1.68
.880

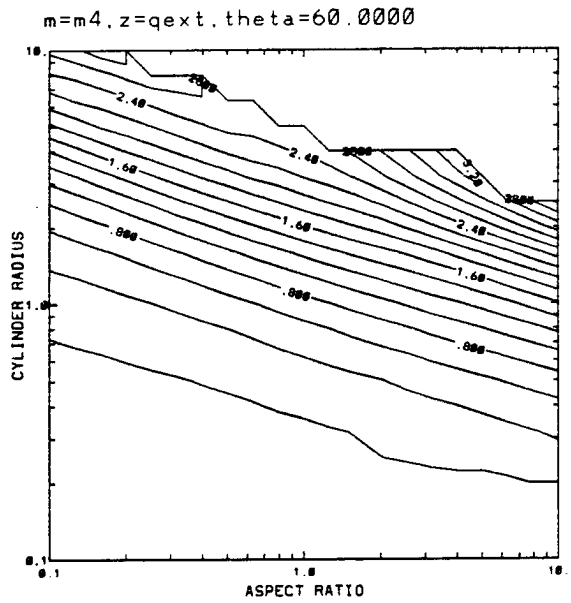

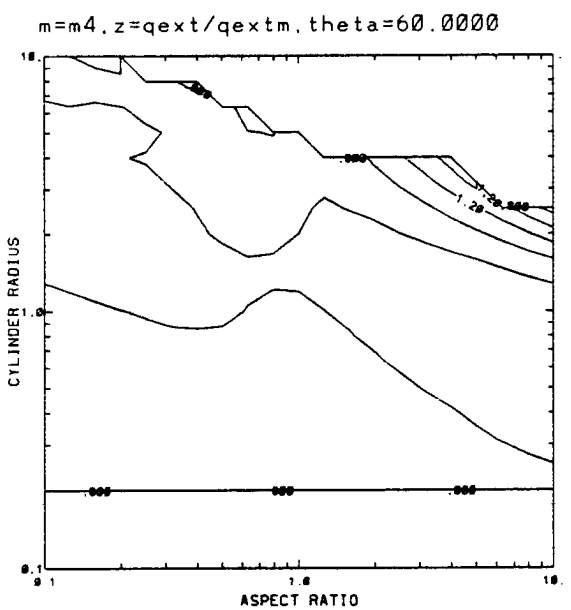

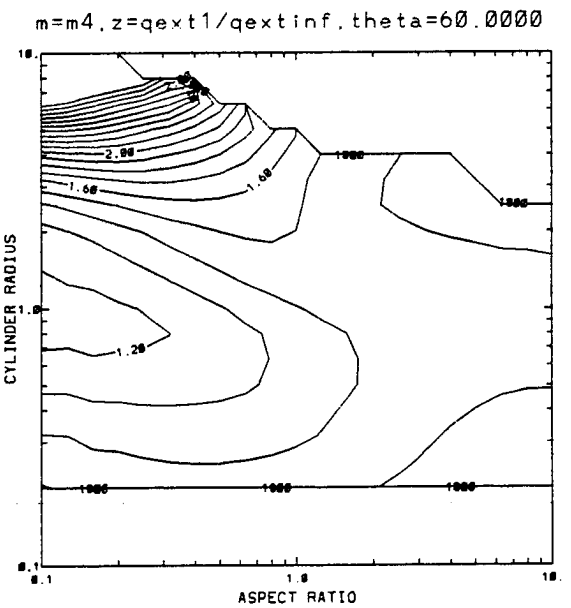

Figure A.25: Results for $m = m_4$ and $\theta = \theta_4$.

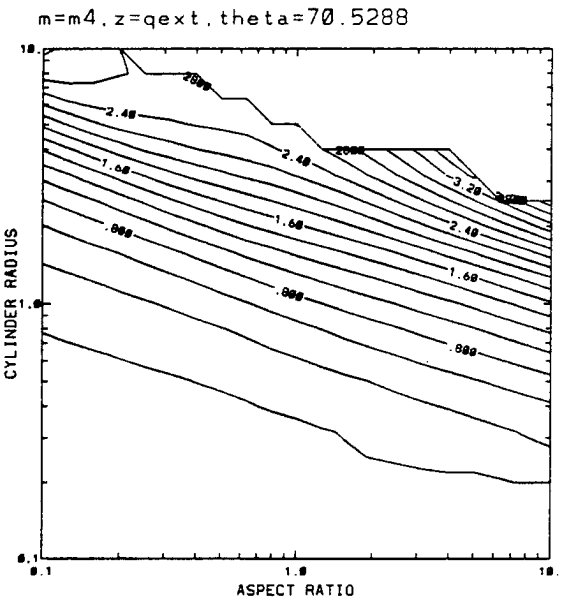

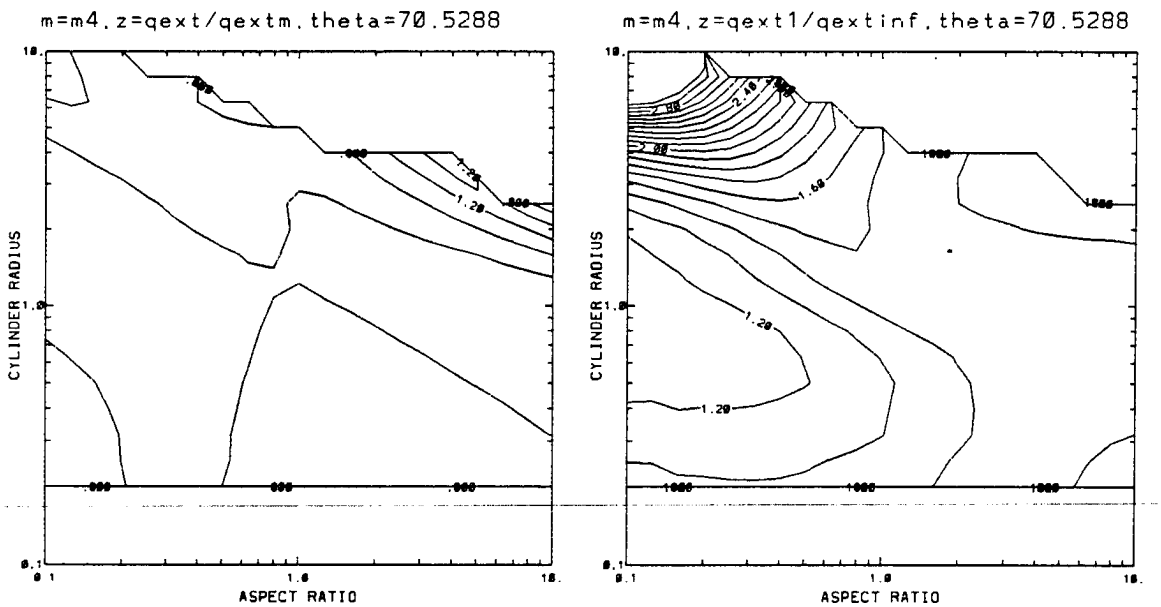

Figure A.26: Results for $m = m_4$ and $\theta = \theta_5$.

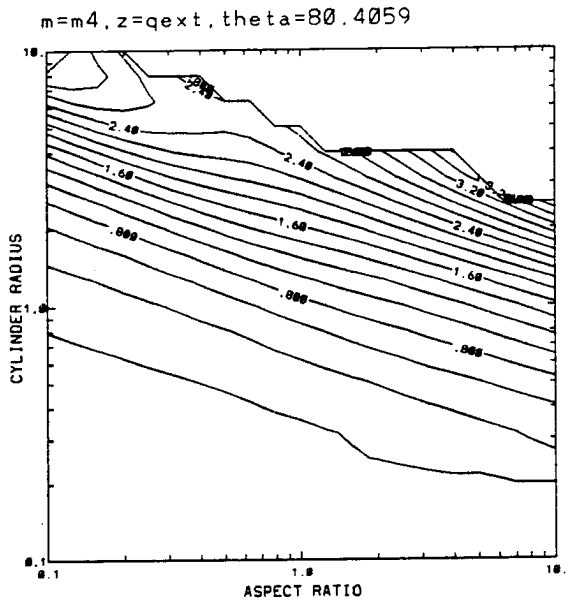

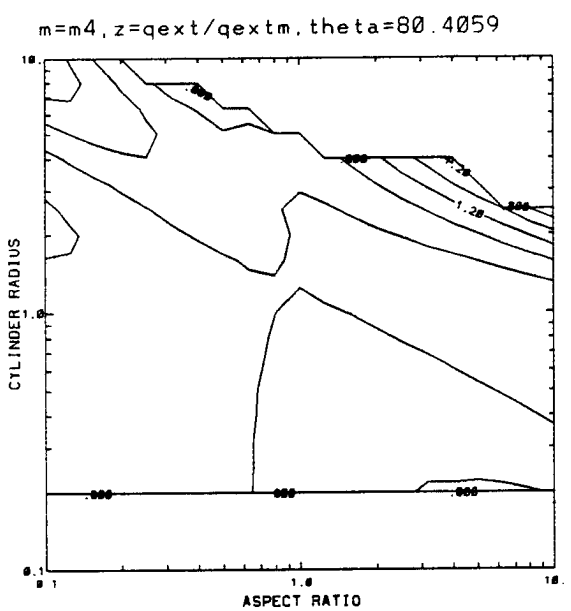

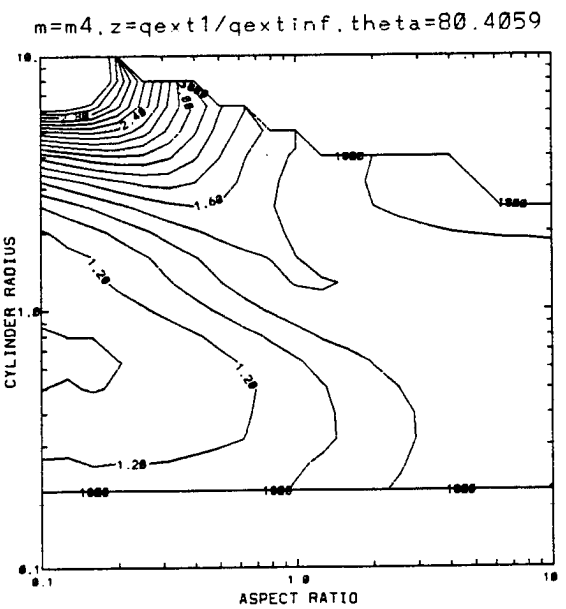

Figure A.27: Results for $m = m_4$ and $\theta = \theta_6$.

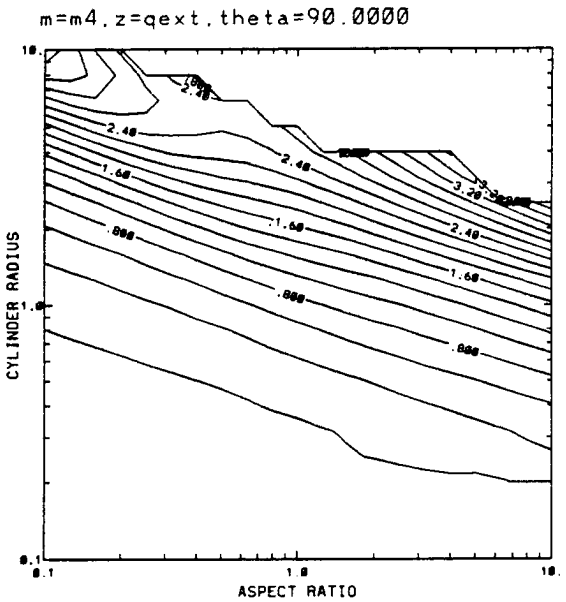

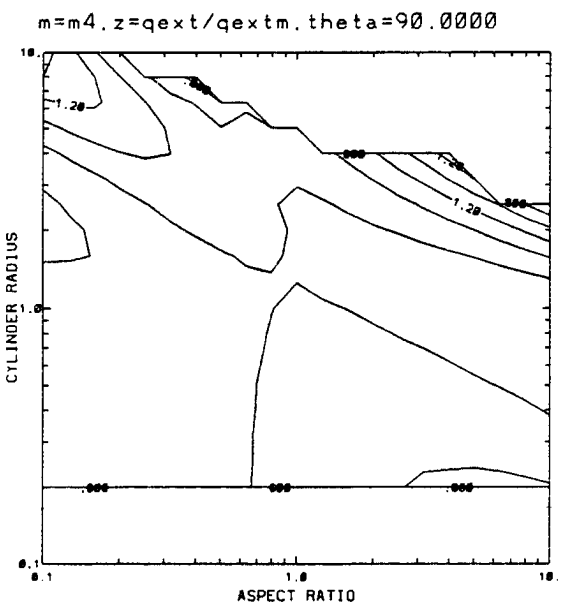

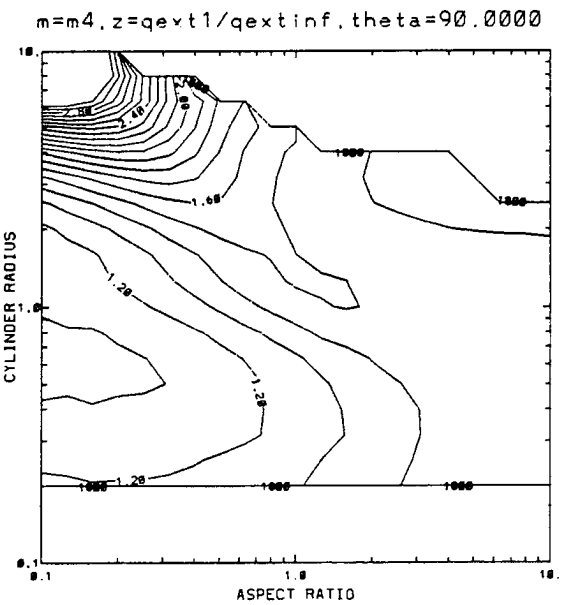

Figure A.28: Results for $m = m_4$ and $\theta = \theta_7$.

Appendix B

THE ENTIRETY OF THE DDA SINGLE SCATTER ALBEDO RESULTS

This appendix shows the full extent of the ω_0 results from the usage of the DDA model. For a full explanation of the model, the format of the plots, or the values of the four refractive indices or the seven incidence angles the reader is referred to sections 3.1 and 3.2 of chapter 3.

For the plots associated with m_2 the contours go from values of .9 to .91 to .92, .93, ..., .98, .99, .991, .992, .993, ..., .998, .999, .9991, and so on. The labelled contours are .9, .99, .999, and .9999. The .9999 contours are labelled '1.00' on the plots since the contour labelling system of the plotting package cannot exceed three significant figures. For the plots associated with m_3 and m_4 the labelled contours are .2, .4, .6, .8, and 1.0. The contour interval is .05.

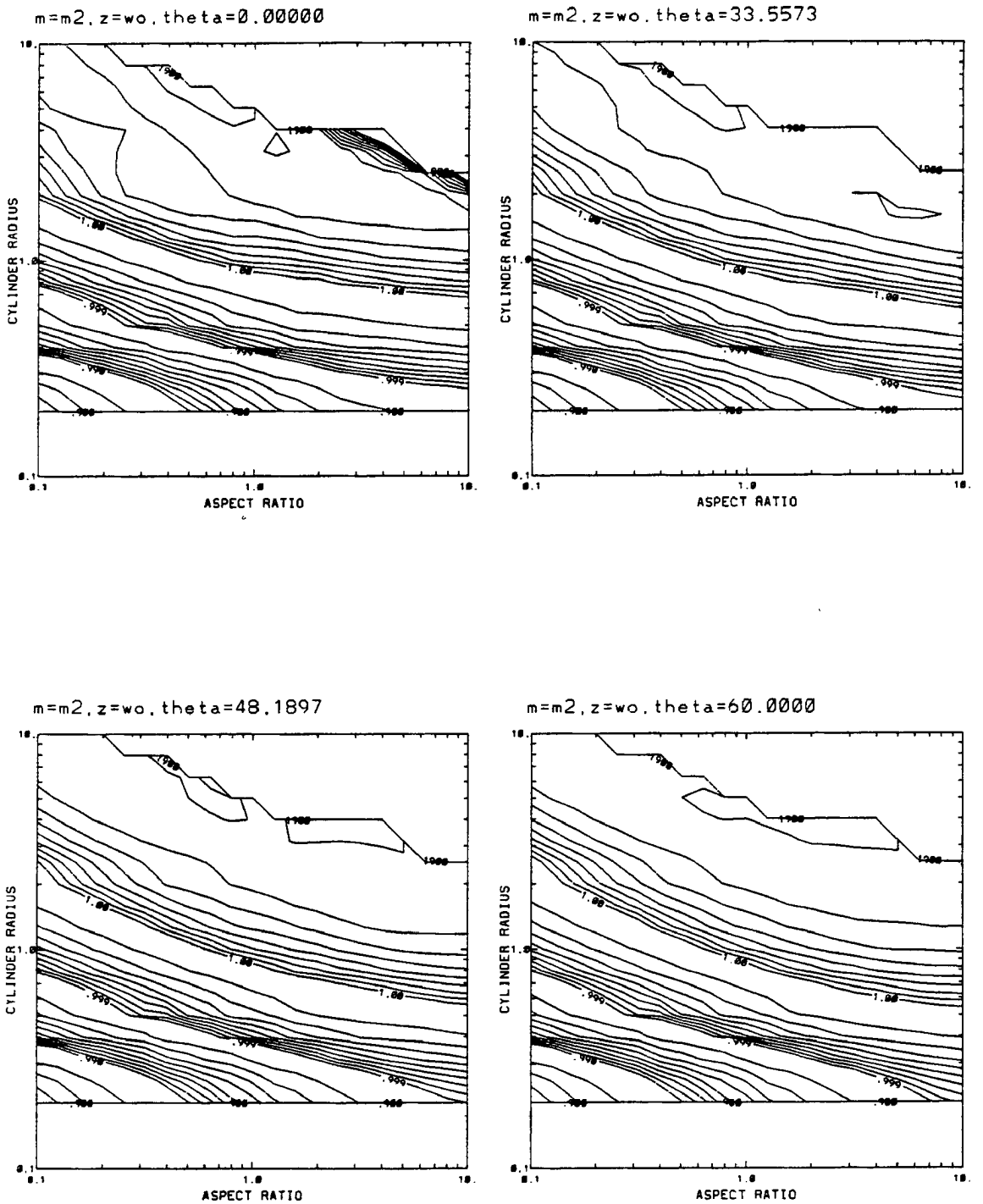

Figure B.1: Results for $m = m_2$ and $\theta = \theta_1, \theta_2, \theta_3, \theta_4$.

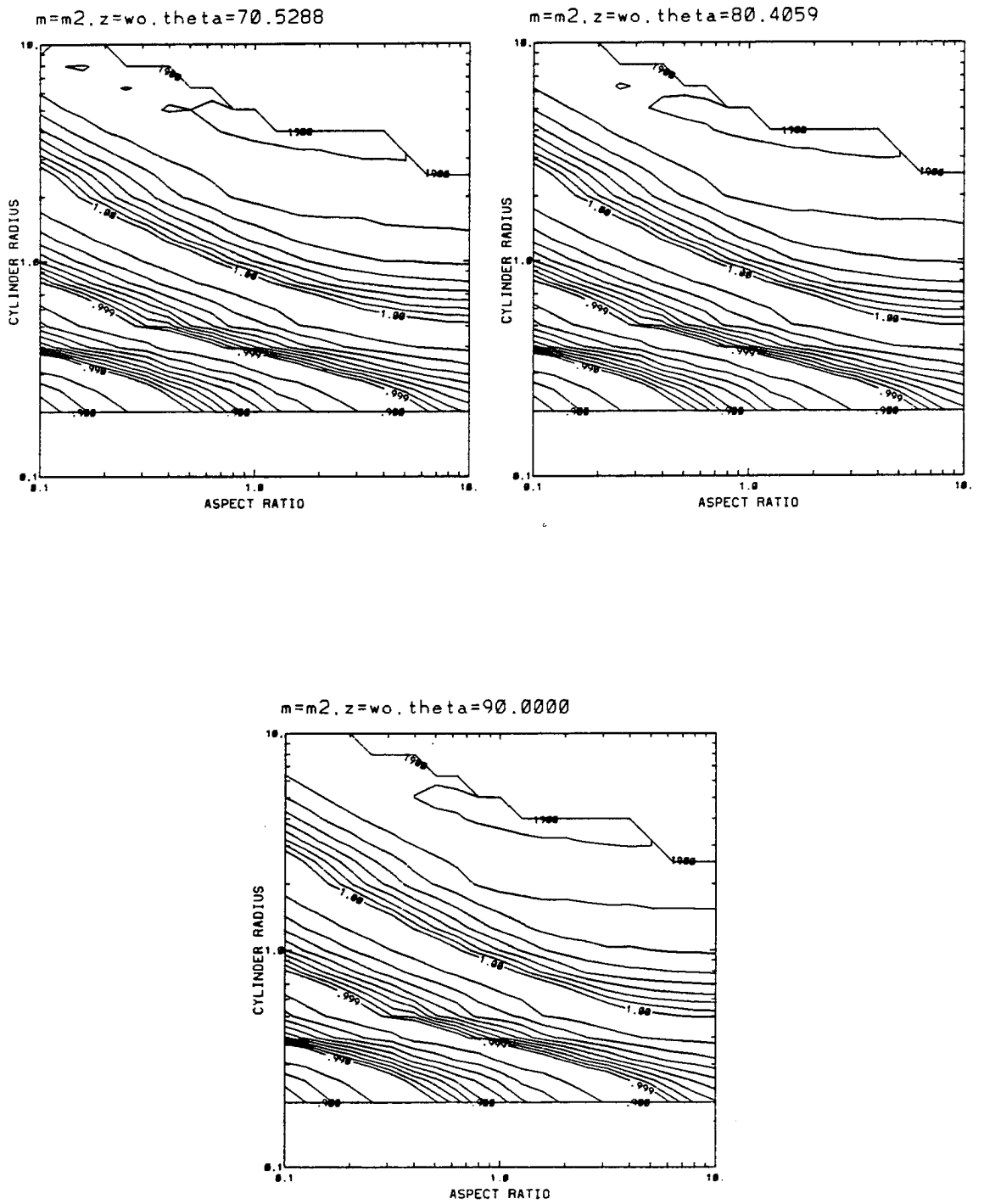

Figure B.2: Results for $m = m_2$ and $\theta = \theta_5, \theta_6, \theta_7$.

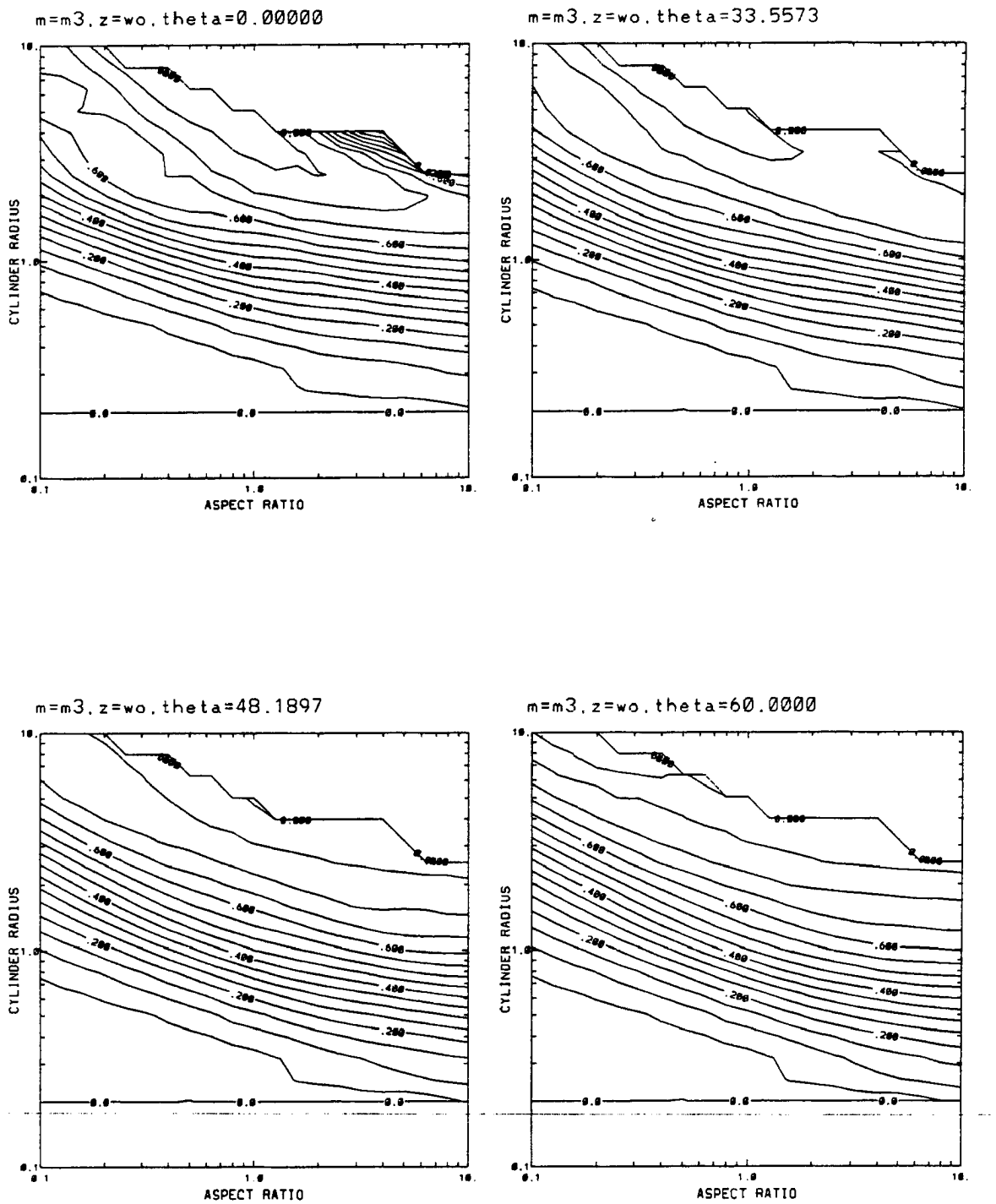

Figure B.3: Results for $m = m_3$ and $\theta = \theta_1, \theta_2, \theta_3, \theta_4$.

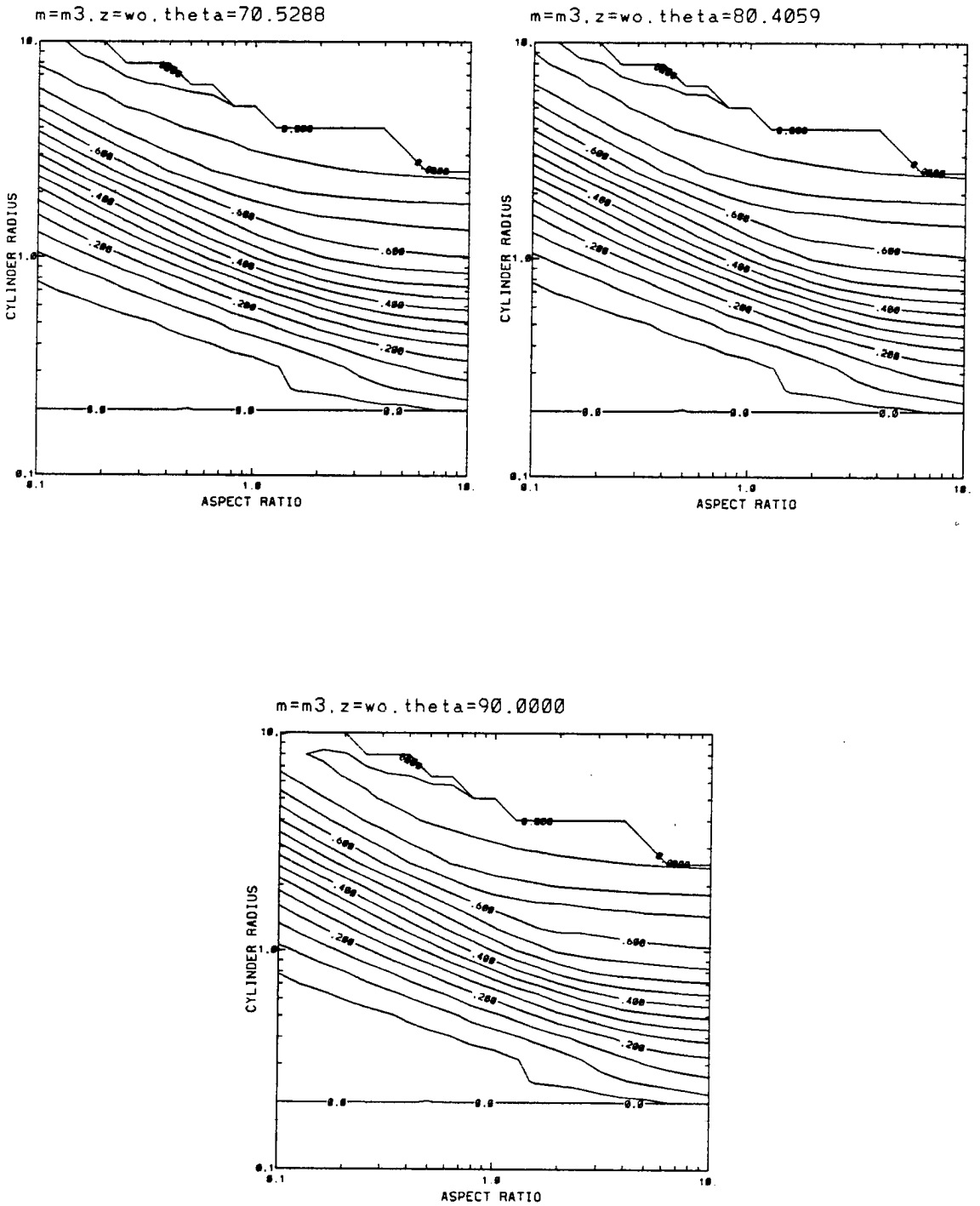

Figure B.4: Results for $m = m_3$ and $\theta = \theta_5, \theta_6, \theta_7$.

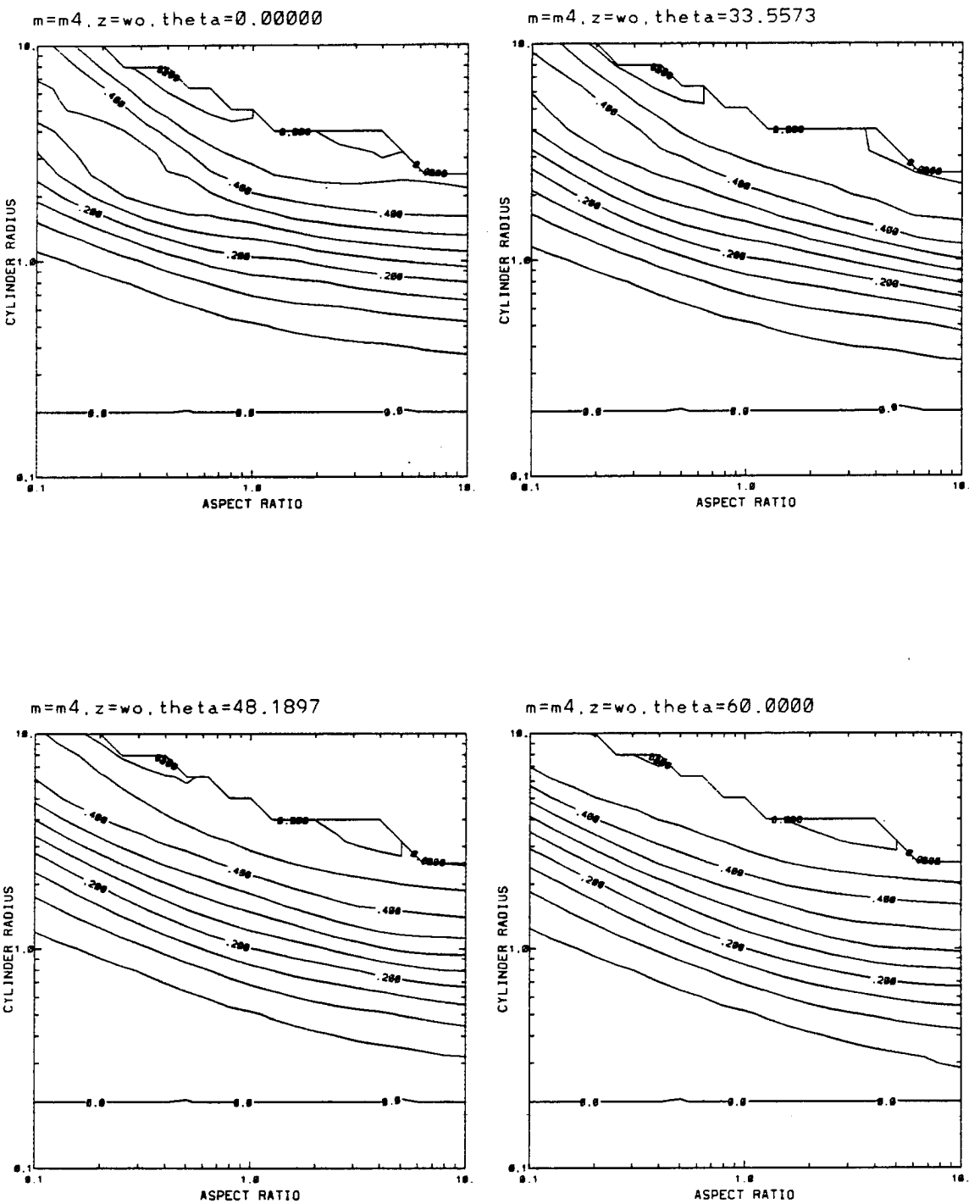

Figure B.5: Results for $m = m_4$ and $\theta = \theta_1, \theta_2, \theta_3, \theta_4$.

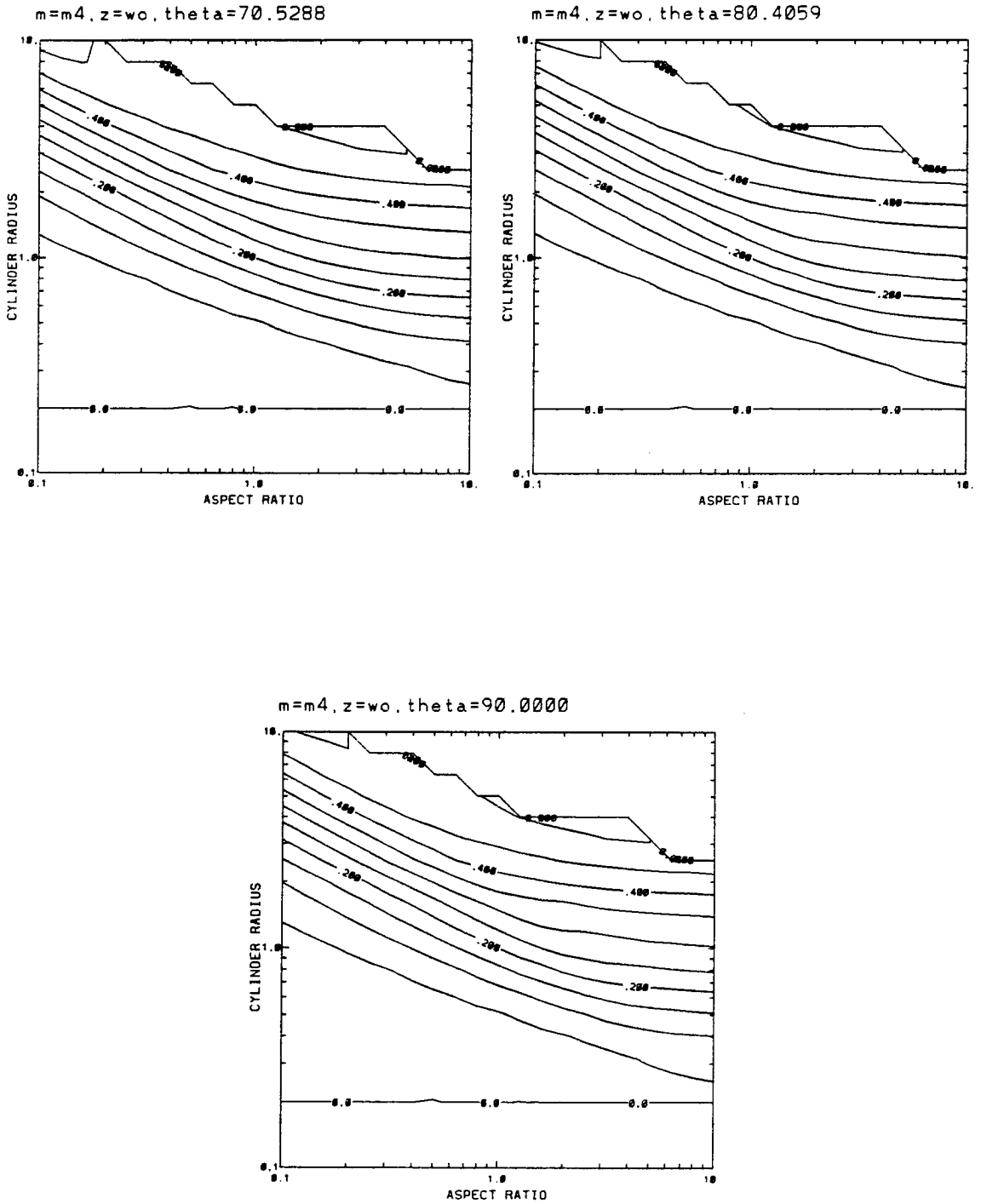

Figure B.6: Results for $m = m_4$ and $\theta = \theta_5, \theta_6, \theta_7$.

Appendix C

THE ENTIRETY OF THE DDA ASYMMETRY PARAMETER RESULTS

This appendix shows the full extent of the asymmetry parameter results from the usage of the DDA model. For a full explanation of the model, the format of the plots, or the values of the four refractive indices or the seven incidence angles the reader is referred to sections 3.1 and 3.2 of chapter 3. The results are displayed in two forms:

$$g \quad \frac{g}{g_{Mie}}$$

the latter ratioing the results with results from equivalent spheres.

For plots of g the contour labels reach values of .2, .4, .6, .8, and 1. The contour interval is .05. For plots of $\frac{g}{g_{Mie}}$ the labels are .4, .8, 1.2, 1.6, 2.0, 2.4, and 2.8. The contour interval is .1, and the contours extend from a minimum value of .2 to a maximum value of 3.0, and since there are cases in which the data exceeds these bounds, one must observe these figures with care. An example of this is the first such figure on the following page. The peak in the lower right portion of the plot is not a plateau, but a peak which contains values which exceed 3.0.

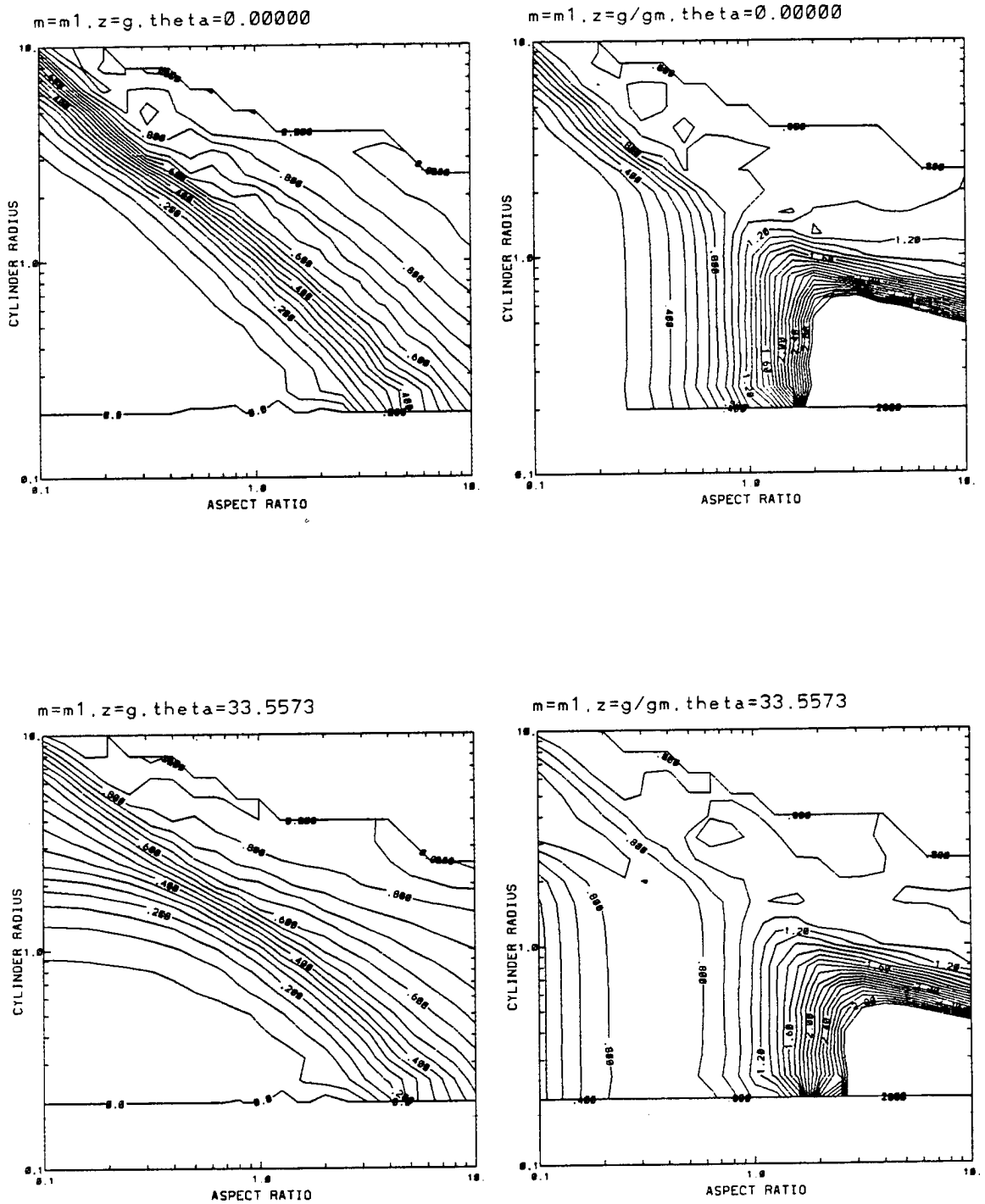

Figure C.1: Results for $m = m_1$ and $\theta = \theta_1, \theta_2$.

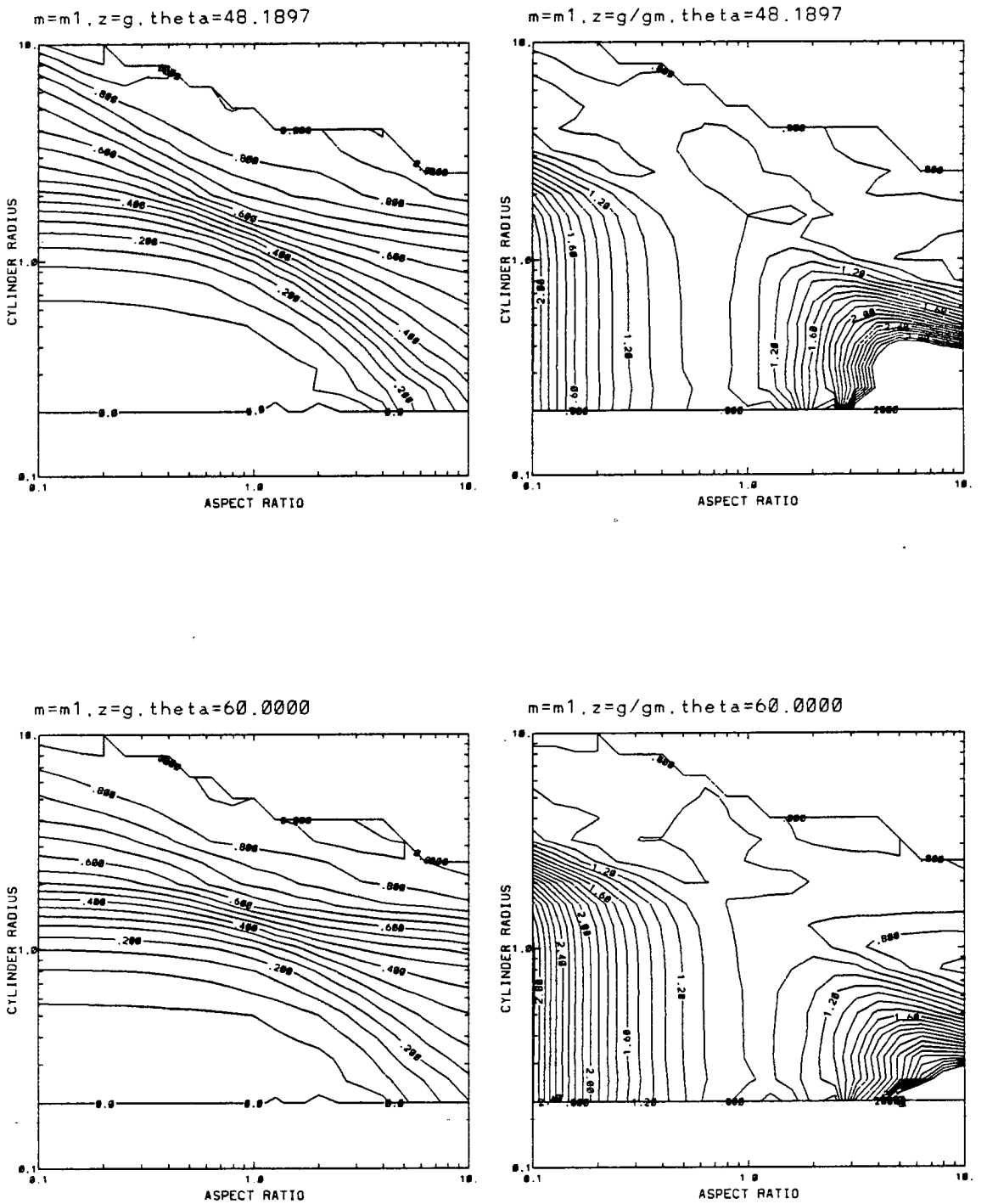

Figure C.2: Results for $m = m_1$ and $\theta = \theta_3, \theta_4$.

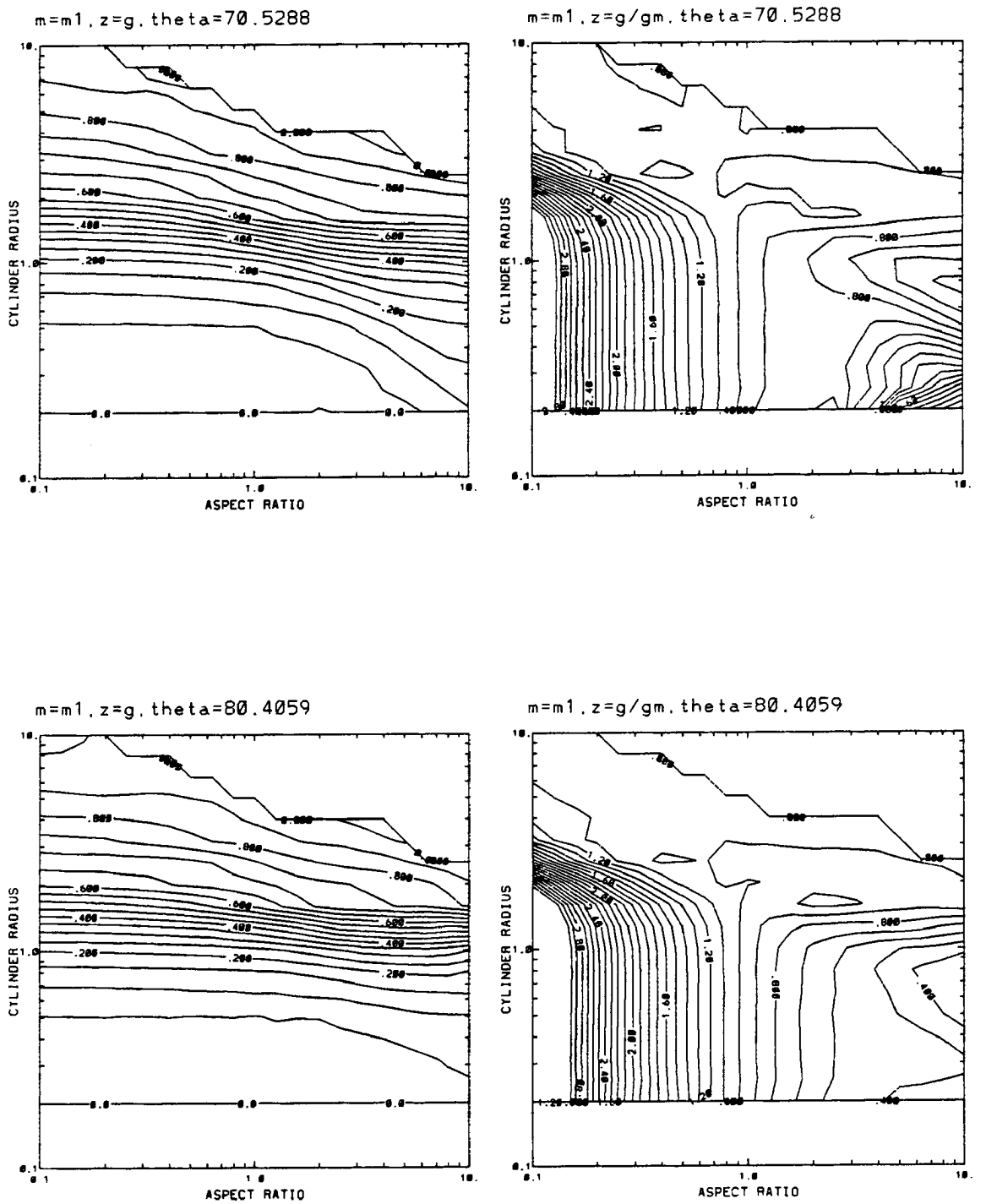

Figure C.3: Results for $m = m_1$ and $\theta = \theta_5, \theta_6$.

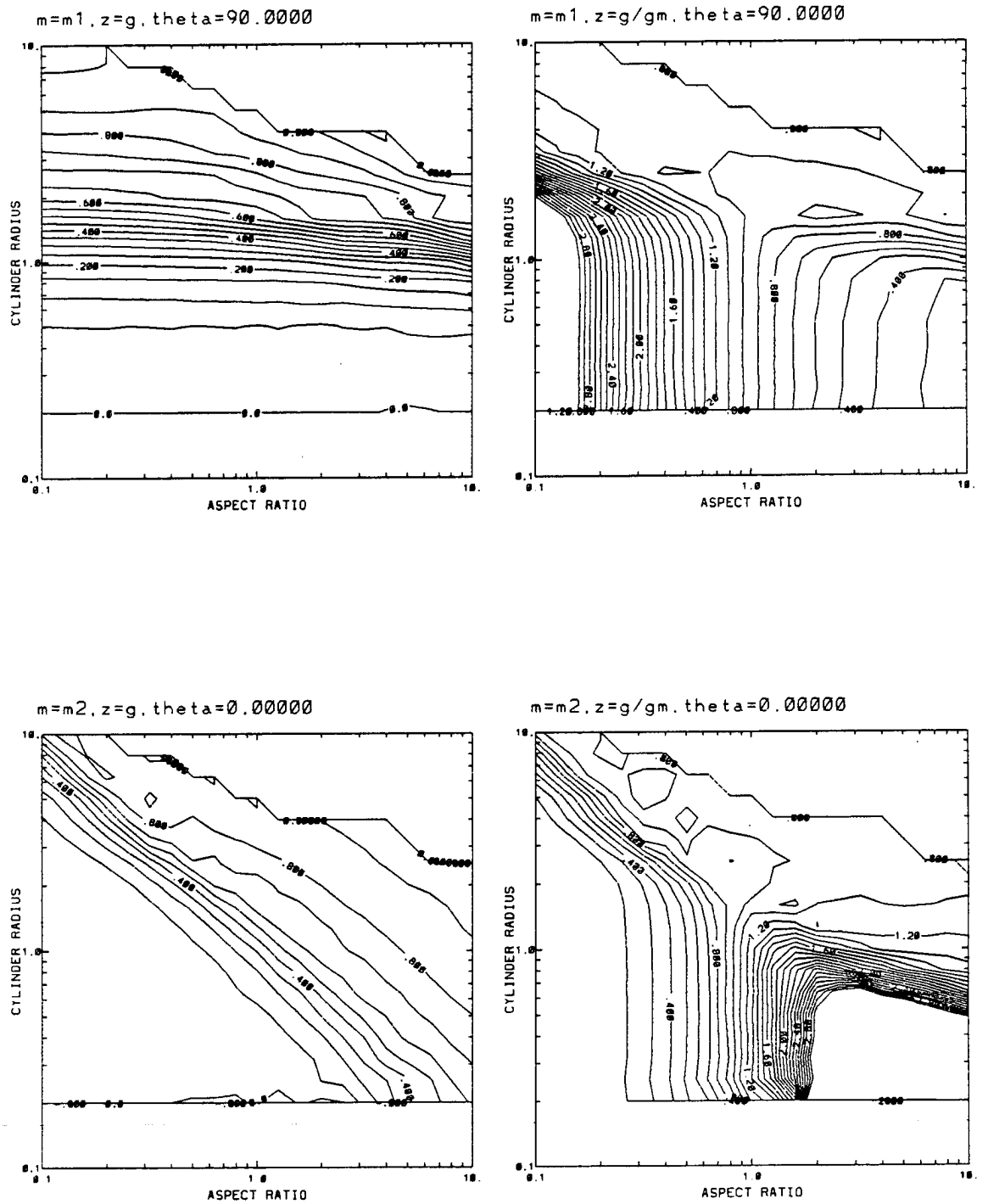

Figure C.4: Results for $m = m_1$ and $\theta = \theta_7$; $m = m_2$ and $\theta = \theta_1$.

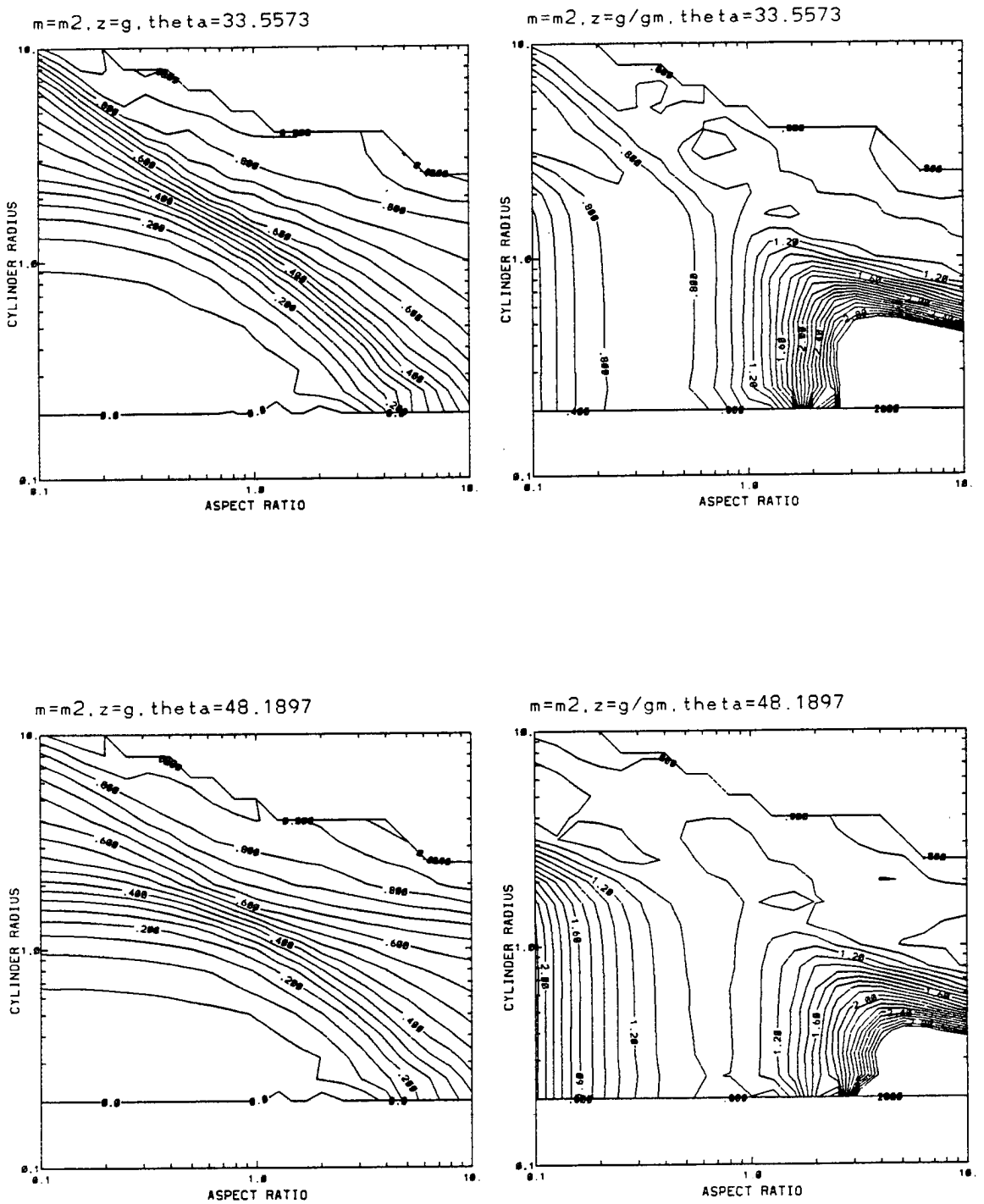

Figure C.5: Results for $m = m_2$ and $\theta = \theta_2, \theta_3$.

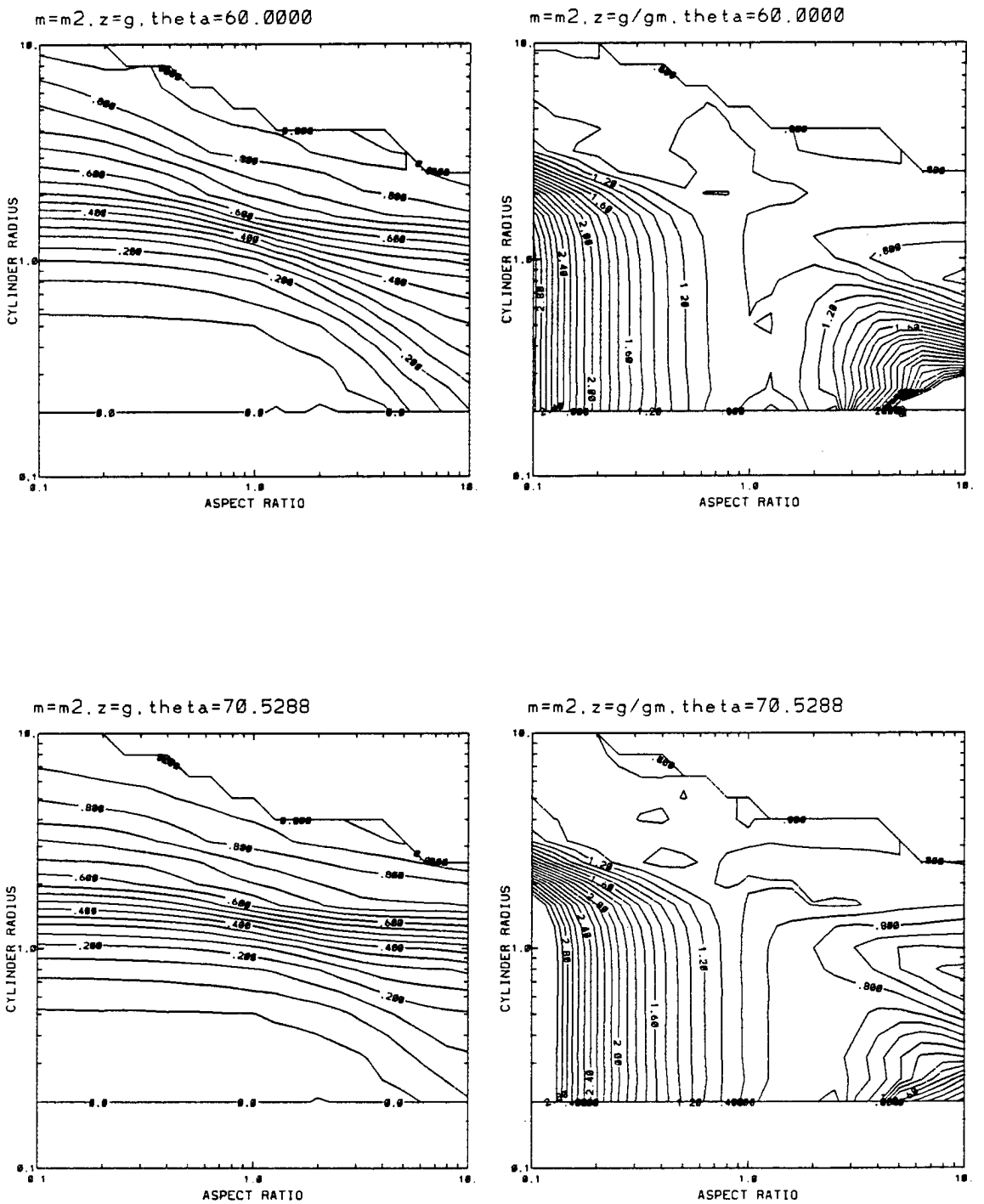

Figure C.6: Results for $m = m_2$ and $\theta = \theta_4, \theta_5$.

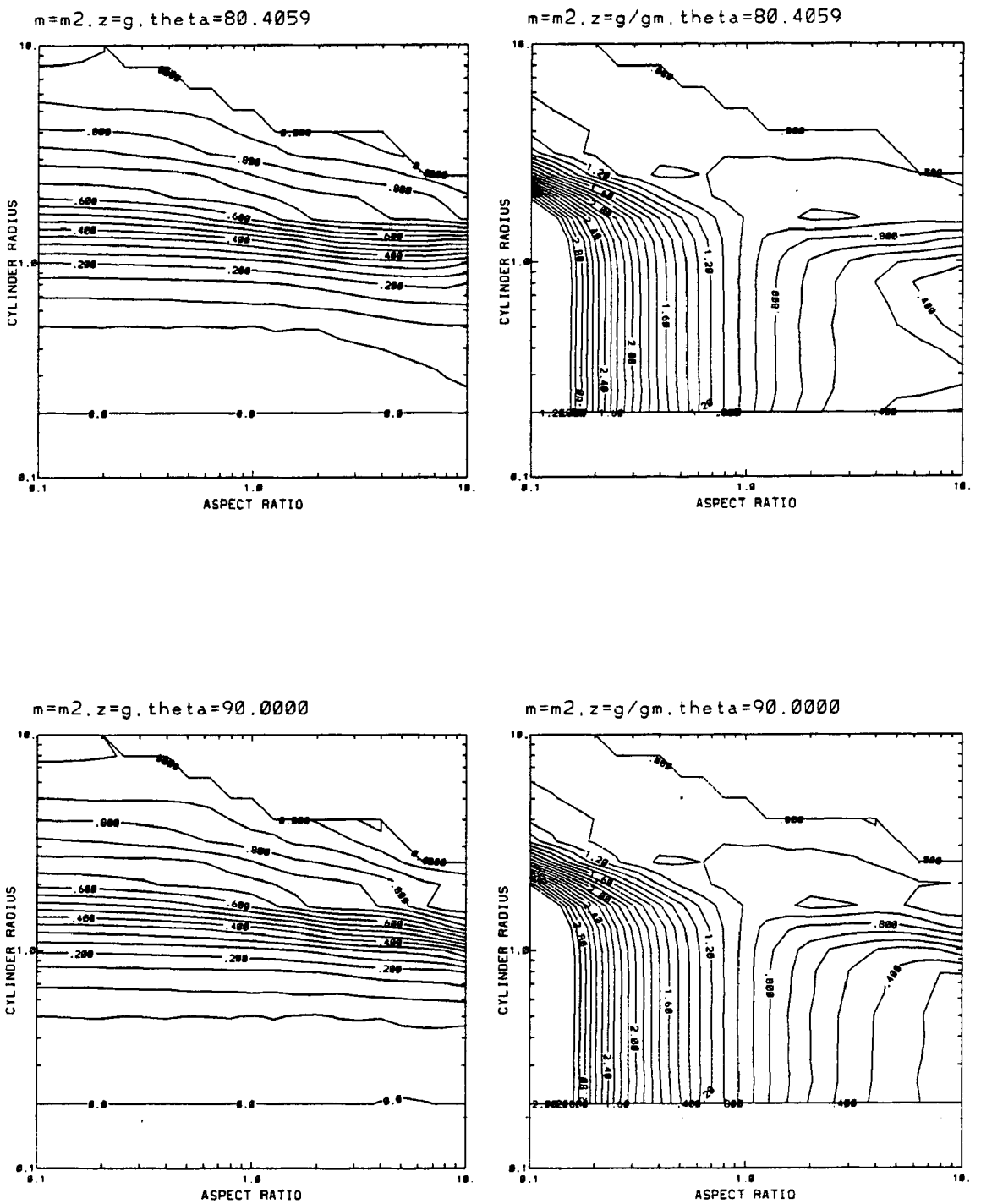

Figure C.7: Results for $m = m_2$ and $\theta = \theta_6, \theta_7$.

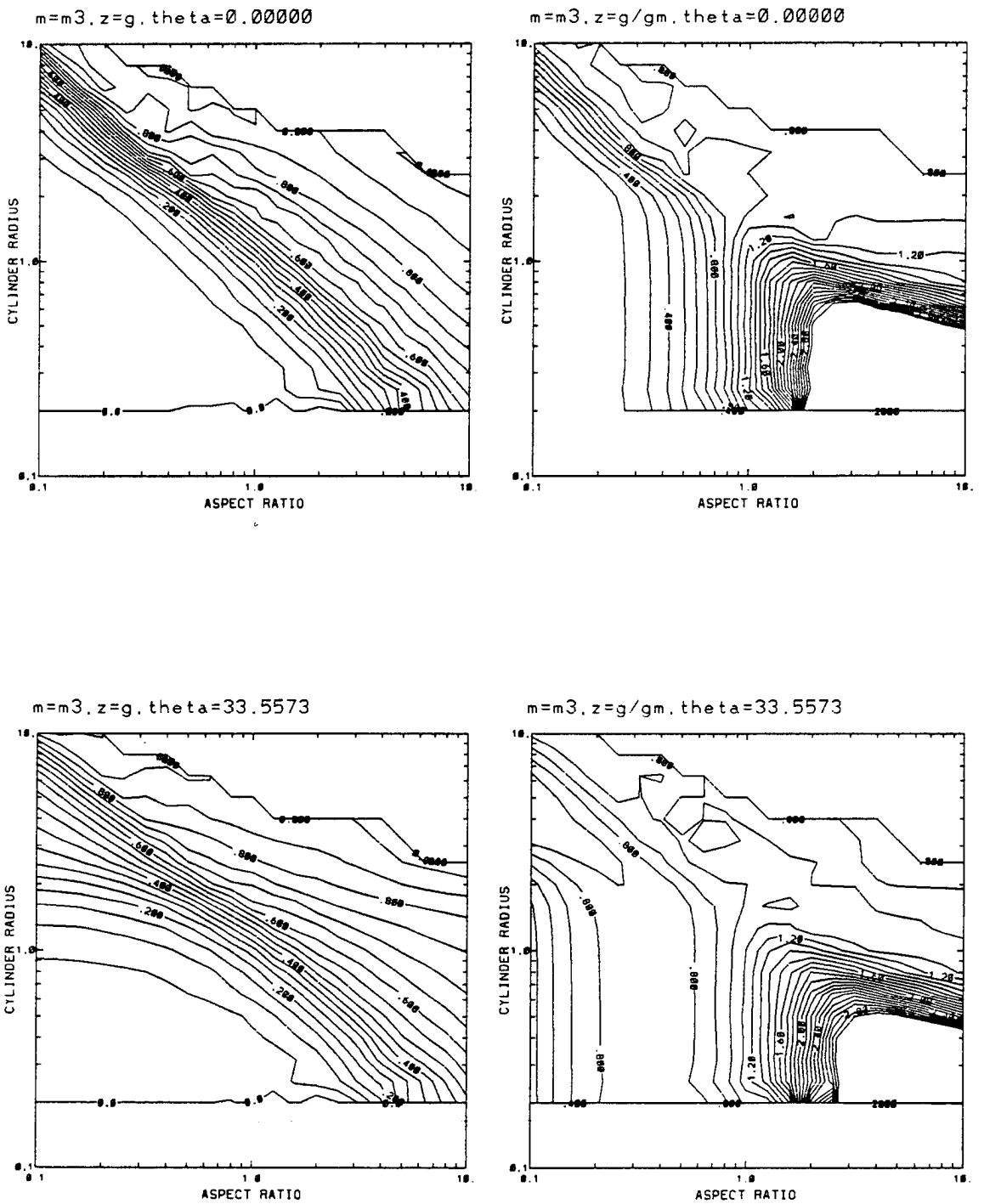

Figure C.8: Results for $m = m_3$ and $\theta = \theta_1, \theta_2$.

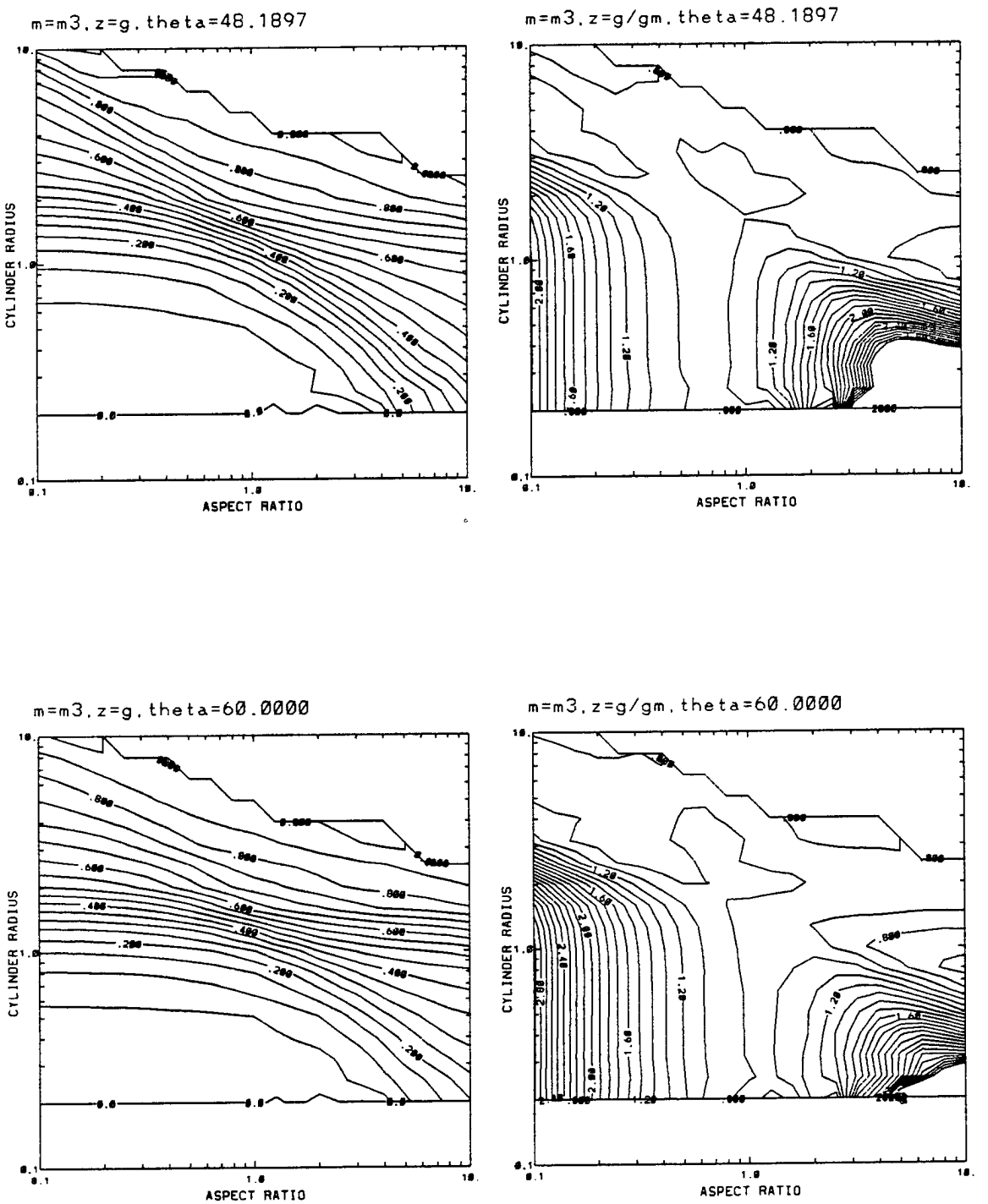

Figure C.9: Results for $m = m_3$ and $\theta = \theta_3, \theta_4$.

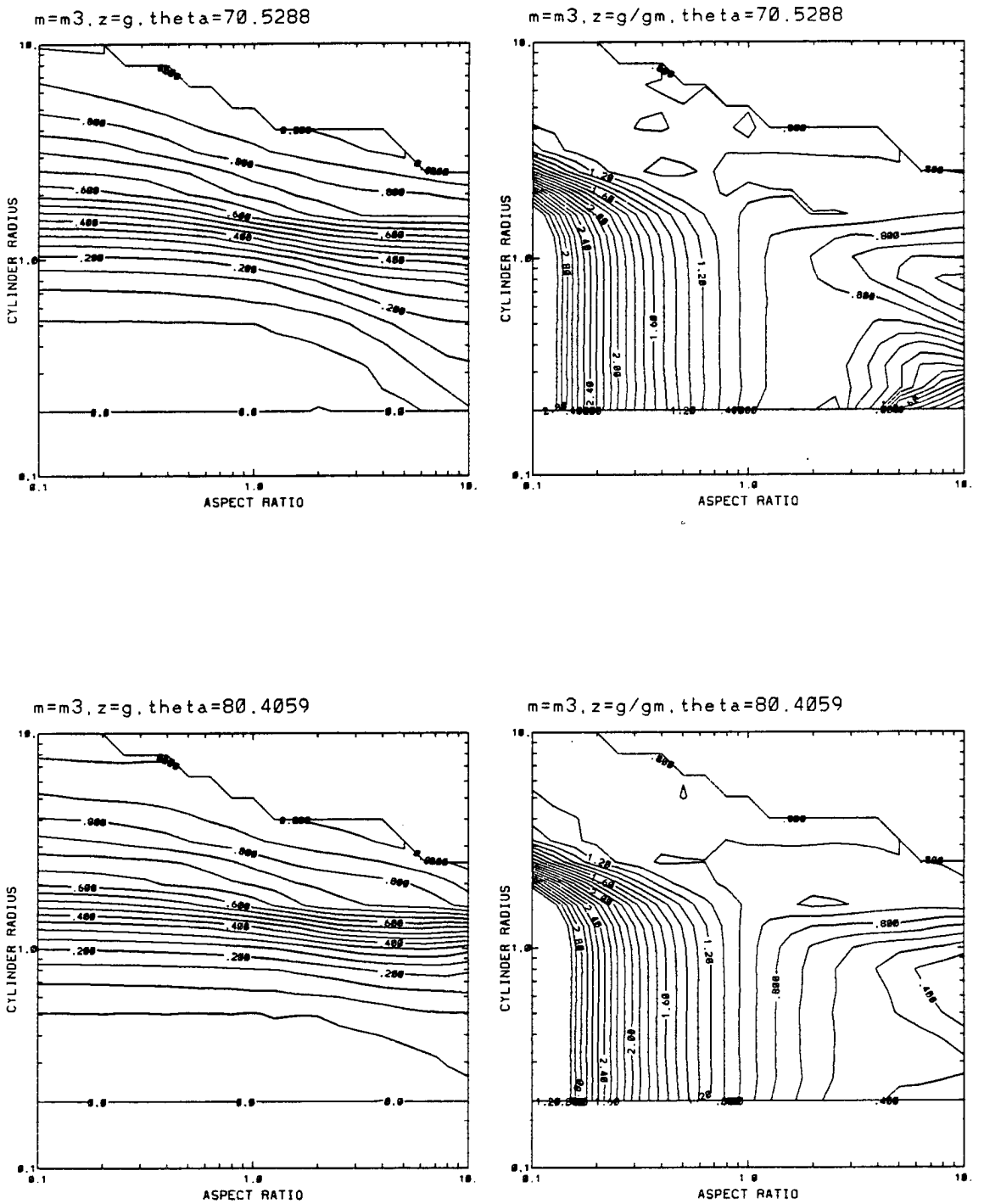

Figure C.10: Results for $m = m_3$ and $\theta = \theta_5, \theta_6$.

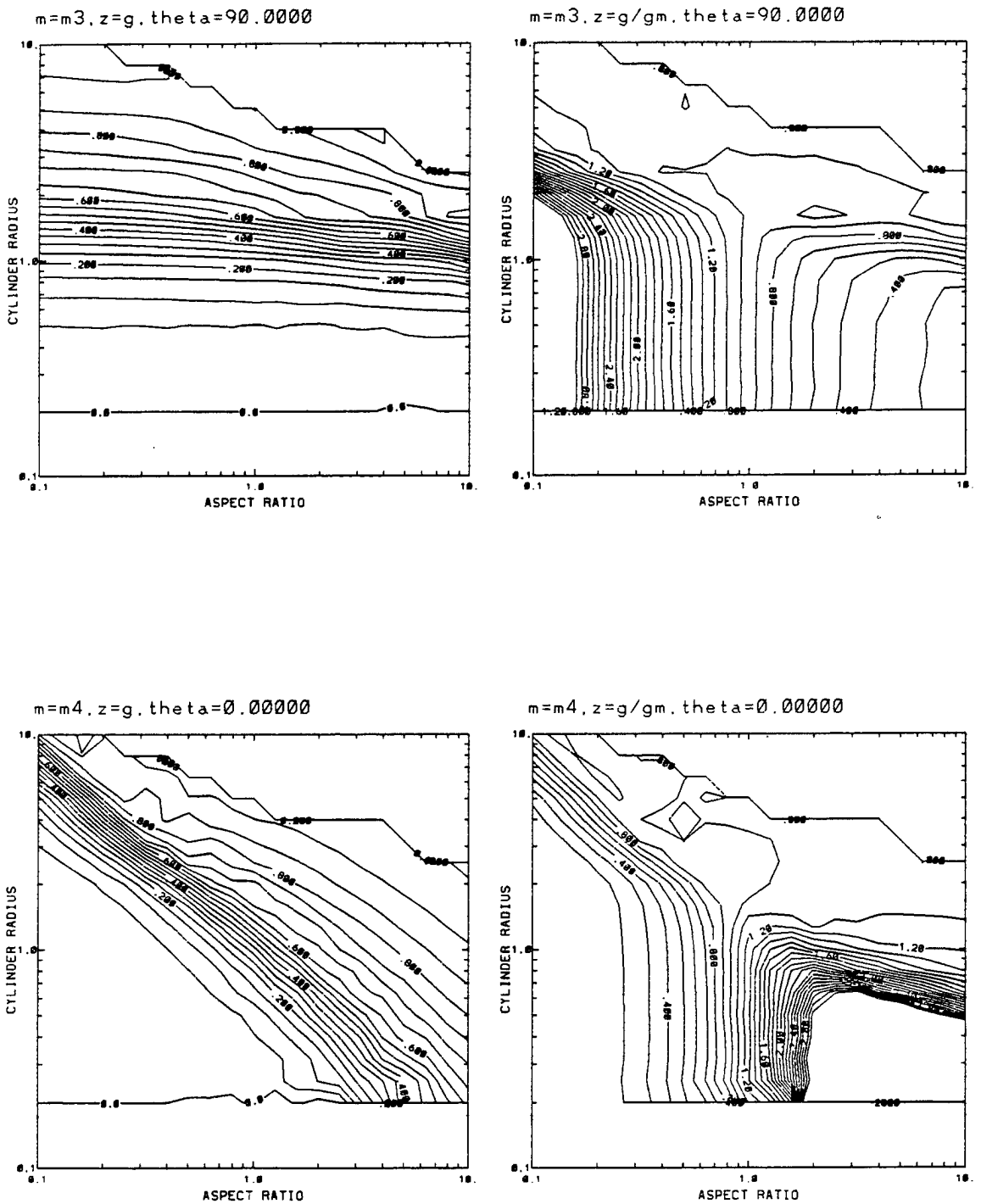

Figure C.11: Results for $m = m_3$ and $\theta = \theta_7$; $m = m_4$ and $\theta = \theta_1$.

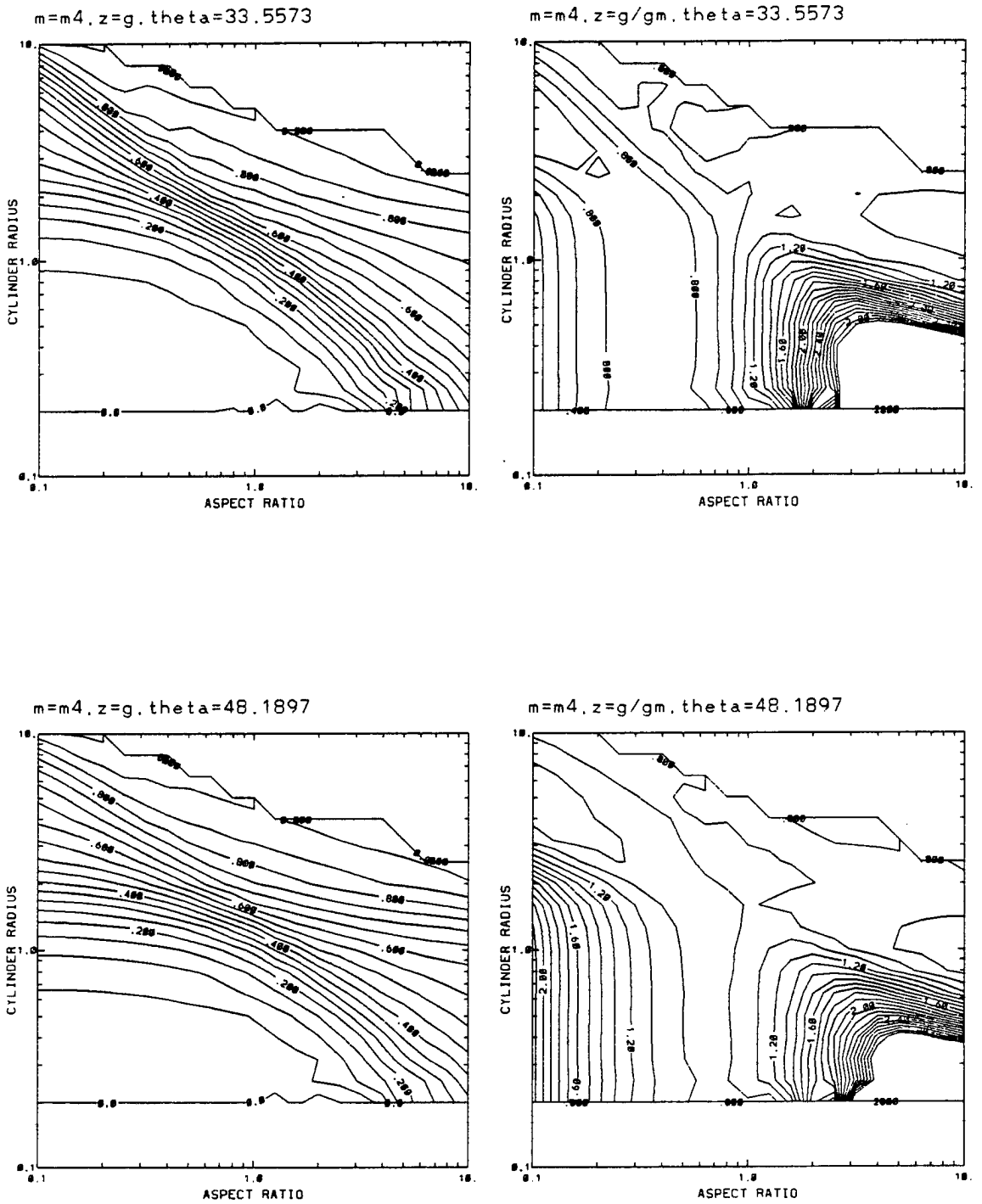

Figure C.12: Results for $m = m_4$ and $\theta = \theta_2, \theta_3$.

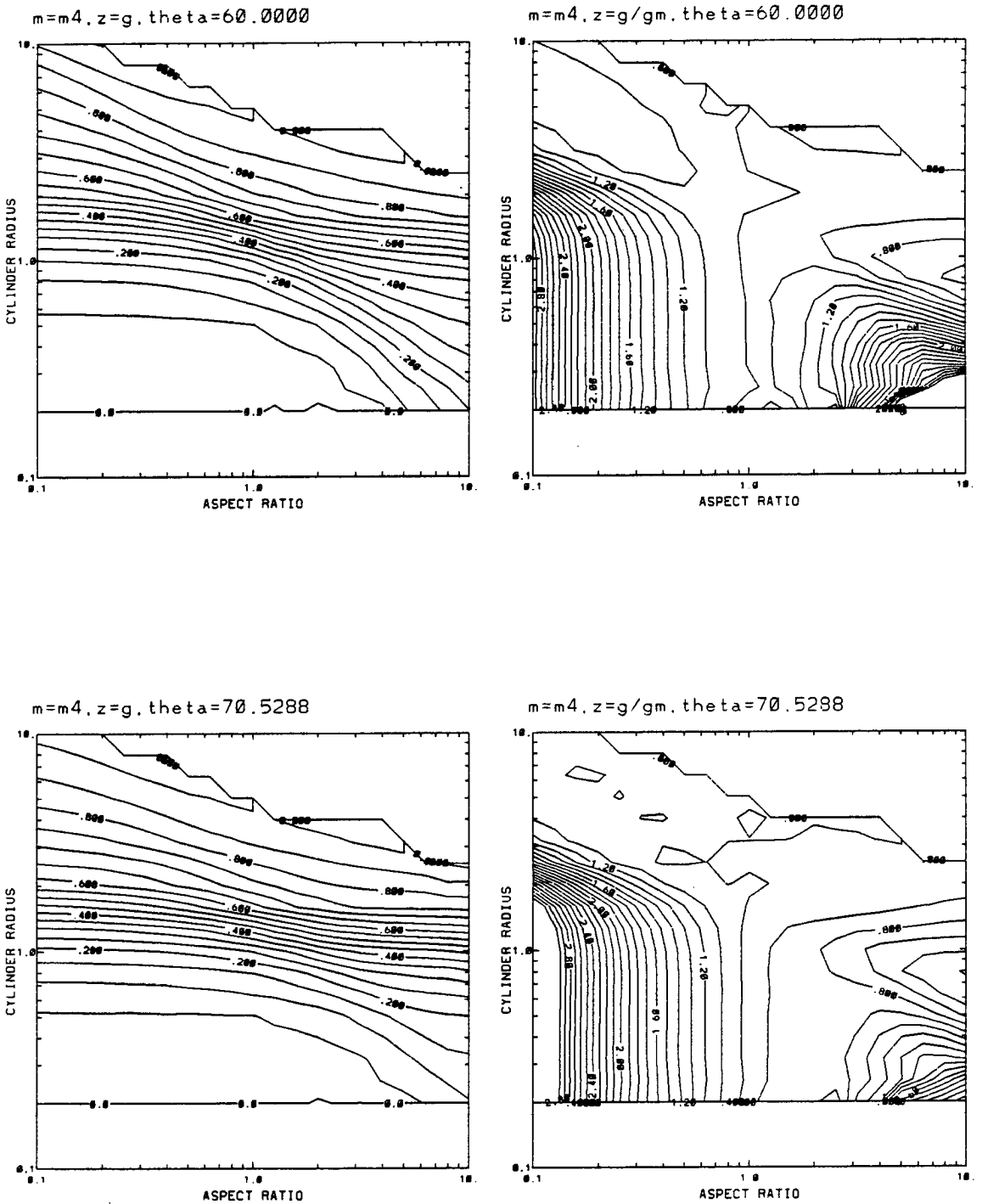

Figure C.13: Results for $m = m_4$ and $\theta = \theta_4, \theta_5$.

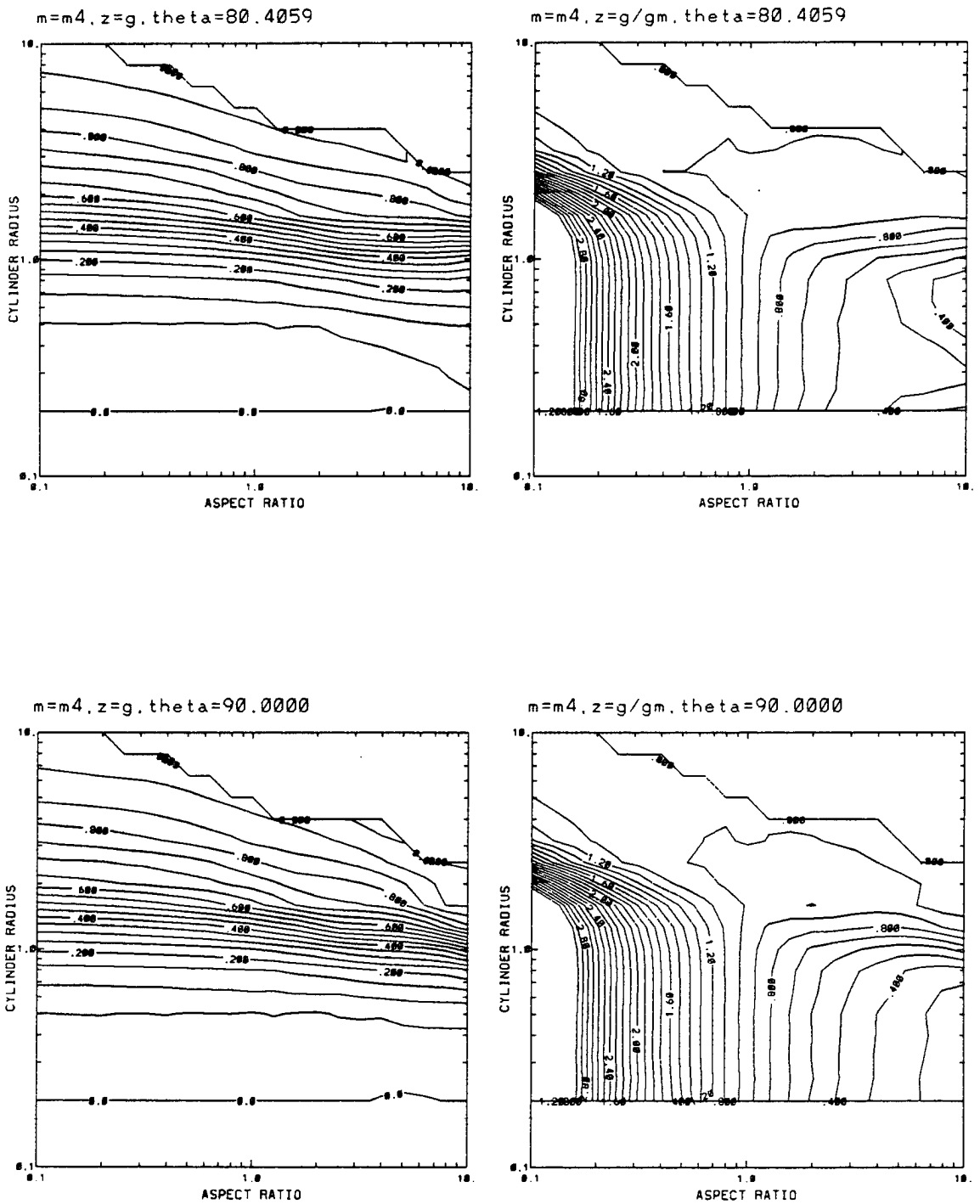

Figure C.14: Results for $m = m_4$ and $\theta = \theta_6, \theta_7$.

Appendix D

CURVE FIT PARAMETERS FOR THE SINGLE SCATTER ALBEDO DERIVED FROM THE DDA DATA

This appendix shows the *ad nauseum* results for the numerical coefficients derived for the extension of the DDA ω_0 results to larger particles through the empirical fitting of a Mie curve to the cylinder data. The coefficients are according to equation 3.10 in chapter 3, and are applied as a function of a_{eff}. These coefficients are found through an iterative method in which the Mie results are successively stretched in two independent dimensions and their linearly interpolated values are compared with the less plentiful DDA results by calculating a χ^2 difference between the two curves:

$$\chi^2 = \sum_i \frac{(X_{i_{Mie}} - X_{i_{DDA}})^2}{X_{i_{DDA}}}$$

Once a case is found which minimizes χ^2, an r^2 value is then calculated according to the equation:

$$r^2 = 1 - \frac{\chi^2}{N\sigma^2}$$

where σ^2 is the variance of the DDA data and N is the number of DDA points. (This is taken from page 658 of Press et. al. (1992).).

Before proceeding it should be pointed out that although the a and b values are given to the nearest thousandth, they are probably only accurate to within a few hundredths. This should be immediately evident to even a casual observer of the data. Still, the data is presented with this superfluous precision, since this degree of accuracy is most likely related to the finite amount of data as well as to the slight inaccuracies of the DDA results and not to inaccuracies in the curve fitting process. Also, for information showing each of the seven values of θ and the 21 values of β tables 3.3 and 3.4 in chapter 3 should be consulted.

Table D.1: Results for $m_2 = 1.3 + .000003i$. These results showed little or no dependence on aspect ratio β.

θ	a	b	r^2
1	.968	.878	.991
2	.985	.933	.997
3	.988	.948	.998
4	.988	.953	.998
5	.987	.958	.988
6	.985	.953	.997
7	.985	.955	.997

Table D.2: Results for $m_3 = 1.32 + .05i$.

θ	β	a	b	r^2	θ	β	a	b	r^2
1	1	1.065	0.848	0.997	2	1	0.990	0.882	0.996
	2	1.071	0.858	0.996		2	0.995	0.893	0.997
	3	1.069	0.873	0.993		3	0.997	0.905	0.997
	4	1.068	0.892	0.987		4	1.001	0.920	0.996
	5	1.056	0.918	0.977		5	0.999	0.940	0.993
	6	1.064	0.928	0.973		6	1.004	0.951	0.993
	7	1.048	0.958	0.965		7	1.003	0.974	0.990
	8	1.046	0.977	0.969		8	1.008	0.988	0.993
	9	1.024	1.004	0.987		9	1.004	1.005	0.996
	10	1.007	1.007	0.997		10	1.004	1.001	0.999
	11	0.976	1.002	0.998		11	0.993	0.993	1.000
	12	0.945	0.981	0.987		12	0.972	0.982	0.994
	13	0.958	0.933	0.932		13	0.952	0.974	0.985
	14	0.963	0.876	0.766		14	0.891	0.986	0.980
	15	0.883	0.884	0.802		15	0.838	1.003	0.979
	16	0.809	0.909	0.889		16	0.796	1.018	0.978
	17	0.801	0.887	0.864		17	0.771	1.020	0.977
	18	0.739	0.921	0.935		18	0.749	1.024	0.977
	19	0.727	0.904	0.917		19	0.730	1.025	0.979
	20	0.715	0.894	0.915		20	0.714	1.025	0.981
	21	0.667	0.930	0.970		21	0.694	1.033	0.983
3	1	0.924	0.923	0.987	4	1	0.869	0.962	0.977
	2	0.932	0.930	0.989		2	0.879	0.964	0.980
	3	0.937	0.938	0.990		3	0.888	0.966	0.983
	4	0.947	0.947	0.992		4	0.905	0.966	0.986
	5	0.951	0.960	0.993		5	0.919	0.967	0.988
	6	0.961	0.967	0.995		6	0.930	0.972	0.990
	7	0.964	0.985	0.995		7	0.946	0.978	0.994
	8	0.979	0.992	0.998		8	0.963	0.985	0.997
	9	0.993	0.997	1.000		9	0.985	0.990	0.999
	10	1.001	0.995	1.000		10	0.996	0.992	1.000
	11	1.000	0.992	1.000		11	0.999	0.995	1.000
	12	0.982	0.992	0.999		12	0.989	0.997	0.999
	13	0.955	0.997	0.997		13	0.969	1.001	0.997
	14	0.908	1.003	0.993		14	0.934	0.996	0.992
	15	0.872	1.001	0.990		15	0.911	0.983	0.990
	16	0.847	0.994	0.988		16	0.889	0.970	0.990
	17	0.819	0.994	0.988		17	0.860	0.968	0.987
	18	0.800	0.987	0.988		18	0.849	0.953	0.987
	19	0.780	0.984	0.988		19	0.828	0.950	0.985
	20	0.760	0.983	0.988		20	0.806	0.949	0.983
	21	0.747	0.975	0.988		21	0.798	0.935	0.984

Table D.3: Results for $m_3 = 1.32 + .05i$ continued.

θ	β	a	b	r^2	θ	β	a	b	r^2
5	1	0.850	0.958	0.971	6	1	0.849	0.939	0.969
	2	0.858	0.963	0.975		2	0.854	0.947	0.973
	3	0.865	0.967	0.978		3	0.861	0.953	0.976
	4	0.882	0.967	0.982		4	0.875	0.957	0.980
	5	0.897	0.967	0.985		5	0.887	0.961	0.983
	6	0.911	0.971	0.987		6	0.901	0.966	0.985
	7	0.934	0.970	0.990		7	0.924	0.966	0.988
	8	0.955	0.976	0.994		8	0.946	0.973	0.992
	9	0.978	0.985	0.998		9	0.973	0.984	0.997
	10	0.990	0.992	1.000		10	0.985	0.993	0.999
	11	0.998	0.998	1.000		11	0.996	1.001	1.000
	12	0.996	0.998	0.998		12	1.001	0.998	0.996
	13	0.982	0.999	0.994		13	0.991	0.996	0.989
	14	0.957	0.988	0.987		14	0.972	0.982	0.982
	15	0.939	0.971	0.985		15	0.955	0.965	0.980
	16	0.924	0.954	0.987		16	0.949	0.944	0.982
	17	0.898	0.950	0.982		17	0.923	0.940	0.977
	18	0.892	0.931	0.985		18	0.917	0.920	0.983
	19	0.867	0.929	0.982		19	0.893	0.918	0.978
	20	0.845	0.928	0.978		20	0.869	0.917	0.974
	21	0.841	0.911	0.982		21	0.870	0.898	0.980

Table D.4: Results for $m_3 = 1.32 + .05i$ continued.

θ	β	a	b	r^2
7	1	0.848	0.931	0.969
	2	0.855	0.939	0.972
	3	0.861	0.946	0.976
	4	0.874	0.952	0.979
	5	0.885	0.957	0.983
	6	0.897	0.964	0.985
	7	0.920	0.965	0.988
	8	0.943	0.973	0.991
	9	0.970	0.984	0.996
	10	0.982	0.994	0.999
	11	0.997	1.001	1.000
	12	1.003	0.997	0.996
	13	0.994	0.995	0.988
	14	0.976	0.981	0.979
	15	0.960	0.963	0.978
	16	0.959	0.940	0.980
	17	0.929	0.938	0.975
	18	0.927	0.916	0.981
	19	0.901	0.915	0.977
	20	0.877	0.914	0.973
	21	0.880	0.894	0.979

Table D.5: Results for $m_4 = 1.3 + .2i$.

θ	β	a	b	r^2	θ	β	a	b	r^2
1	1	1.131	0.732	0.993	2	1	1.019	0.793	0.993
	2	1.136	0.746	0.987		2	1.023	0.809	0.993
	3	1.135	0.766	0.977		3	1.022	0.829	0.992
	4	1.128	0.795	0.957		4	1.024	0.853	0.987
	5	1.110	0.834	0.930		5	1.014	0.887	0.979
	6	1.110	0.856	0.915		6	1.020	0.905	0.978
	7	1.084	0.906	0.894		7	1.006	0.948	0.969
	8	1.073	0.943	0.911		8	1.012	0.970	0.976
	9	1.036	0.992	0.967		9	1.008	0.996	0.990
	10	1.008	1.005	0.993		10	1.007	0.994	0.998
	11	0.970	1.007	0.996		11	0.995	0.984	0.999
	12	0.933	0.987	0.978		12	0.967	0.979	0.989
	13	0.916	0.958	0.958		13	0.937	0.982	0.981
	14	0.860	0.945	0.947		14	0.871	1.014	0.974
	15	0.799	0.956	0.955		15	0.819	1.044	0.970
	16	0.746	0.976	0.967		16	0.778	1.068	0.967
	17	0.713	0.976	0.971		17	0.752	1.076	0.968
	18	0.678	0.991	0.975		18	0.726	1.091	0.966
	19	0.655	0.989	0.978		19	0.703	1.105	0.969
	20	0.637	0.987	0.977		20	0.694	1.092	0.971
	21	0.620	0.986	0.972		21	0.672	1.108	0.974
3	1	0.919	0.881	0.980	4	1	0.832	0.977	0.959
	2	0.925	0.893	0.983		2	0.842	0.980	0.967
	3	0.930	0.907	0.985		3	0.854	0.982	0.972
	4	0.936	0.923	0.988		4	0.871	0.981	0.977
	5	0.940	0.944	0.987		5	0.886	0.984	0.982
	6	0.950	0.955	0.990		6	0.902	0.985	0.985
	7	0.951	0.982	0.989		7	0.919	0.991	0.989
	8	0.968	0.989	0.993		8	0.946	0.989	0.994
	9	0.993	0.989	0.999		9	0.981	0.983	0.999
	10	1.006	0.984	1.000		10	0.997	0.982	1.000
	11	1.003	0.980	0.999		11	1.002	0.985	1.000
	12	0.978	0.988	0.998		12	0.985	0.992	0.999
	13	0.944	1.002	0.995		13	0.959	1.000	0.996
	14	0.893	1.016	0.990		14	0.918	0.996	0.986
	15	0.857	1.016	0.986		15	0.888	0.982	0.983
	16	0.830	1.010	0.985		16	0.869	0.962	0.982
	17	0.801	1.010	0.986		17	0.839	0.959	0.978
	18	0.785	0.998	0.986		18	0.832	0.934	0.980
	19	0.761	0.999	0.986		19	0.809	0.930	0.976
	20	0.743	0.994	0.987		20	0.785	0.931	0.975
	21	0.734	0.980	0.986		21	0.787	0.903	0.980

Table D.6: Results for $m_4 = 1.3 + .2i$ continued.

θ	β	a	b	r^2	θ	β	a	b	r^2
5	1	0.798	0.995	0.945	6	1	0.799	0.961	0.942
	2	0.806	1.002	0.954		2	0.806	0.972	0.949
	3	0.815	1.006	0.962		3	0.812	0.983	0.957
	4	0.833	1.004	0.969		4	0.825	0.989	0.965
	5	0.851	1.000	0.976		5	0.839	0.993	0.972
	6	0.872	0.996	0.978		6	0.859	0.993	0.975
	7	0.899	0.990	0.984		7	0.885	0.989	0.982
	8	0.930	0.985	0.989		8	0.919	0.984	0.985
	9	0.969	0.982	0.996		9	0.960	0.984	0.994
	10	0.987	0.985	0.999		10	0.979	0.990	0.998
	11	0.997	0.992	0.999		11	0.995	0.996	0.999
	12	0.991	0.992	0.995		12	0.996	0.990	0.991
	13	0.972	0.993	0.987		13	0.980	0.987	0.978
	14	0.939	0.978	0.973		14	0.952	0.968	0.960
	15	0.915	0.957	0.966		15	0.931	0.943	0.952
	16	0.903	0.929	0.968		16	0.926	0.910	0.953
	17	0.871	0.926	0.960		17	0.892	0.908	0.944
	18	0.871	0.894	0.968		18	0.897	0.873	0.955
	19	0.849	0.887	0.960		19	0.877	0.863	0.946
	20	0.826	0.885	0.955		20	0.852	0.862	0.941
	21	0.831	0.858	0.970		21	0.861	0.833	0.962

Table D.7: Results for $m_4 = 1.3 + .2i$ continued.

θ	β	a	b	r^2
7	1	0.804	0.942	0.942
	2	0.810	0.955	0.948
	3	0.813	0.969	0.958
	4	0.825	0.978	0.964
	5	0.838	0.986	0.971
	6	0.854	0.990	0.975
	7	0.880	0.989	0.981
	8	0.914	0.986	0.985
	9	0.957	0.985	0.992
	10	0.976	0.992	0.998
	11	0.995	0.997	0.999
	12	0.999	0.989	0.989
	13	0.983	0.985	0.973
	14	0.956	0.965	0.954
	15	0.939	0.938	0.946
	16	0.934	0.904	0.947
	17	0.900	0.902	0.937
	18	0.906	0.866	0.950
	19	0.886	0.856	0.940
	20	0.864	0.853	0.934
	21	0.872	0.825	0.958

Appendix E

CURVE FIT PARAMETERS FOR THE ASYMMETRY PARAMETER

This appendix shows the *ad nauseum* results for the numerical coefficients derived for the extension of the DDA g data to larger particles through the fitting of Mie curves to the cylinder data. The coefficients are according to equation 3.10 in chapter 3, and are applied as a function of a_{eff}. These coefficients are found through an iterative method in which the Mie results are successively stretched in two independent dimensions and their linearly interpolated values are compared with the less plentiful DDA results by calculating a χ^2 difference between the two curves:

$$\chi^2 = \sum_i \frac{(X_{i_{Mie}} - X_{i_{DDA}})^2}{X_{i_{DDA}}} \tag{E.1}$$

Once a case is found which minimizes this value, an r^2 value is then calculated according to the equation:

$$r^2 = 1 - \frac{\chi^2}{N\sigma^2}$$

where σ^2 is the variance of the DDA data, and N is the number of DDA points. (This is taken from page 658 of Press et. al. (1992).)

Although this is the generalized technique, most of the coefficients were not arrived at this easily. In many cases the DDA data which exists more plentifully for smaller particles (which in the calculation of a χ^2 value receive a relatively large amount of weight - see equation E.1) resulted in curve fittings which appeared by the principal author to provide unrealistic extensions for the larger particles. To correct this, in many cases the small particle DDA data was deleted from the curve fitting process, leaving only the DDA data for the largest particles to still be used for this fitting process. It is believed that this is justifiable, since *we are not seeking here to provide a generalized Mie fit to the entirety of the*

scattering results or to even try to arrive at a reasonable duplication of the smaller particle data; we already have that from the DDA results. What is desired is an extension of this to larger particles. Towards this end it is intuitively reasonable to assume that the data for the largest particles should be the most reliable for the task of 'leading the curve fit down the proper path'.

In these cases in which the data is truncated a number is shown in the remarks column which reveals the number of points which remained for the coefficient analysis. This number was not allowed to become smaller than 4, although in many cases reliable results were not possible without reducing the number of points to this minimum.

In revealing the qualitative nature of the cases in which the conditions for this curve fitting were less than ideal, it is first most appropriate to list a case which does appear to be ideal. Figure E.1 shows a case in which the DDA results, listed in the key under the name 'DDSCAT', are fitted to analogous Mie data. The figure shows a common case for aspect ratios close to 1. (An aspect ratio of 1 corresponds to $\beta = \beta_{11}$.) From the figure the legitimacy of this analysis becomes evident, and in a valuable way, since things change rapidly as aspect ratios depart from 1 in either direction.

Two common examples of this departure are shown in figures E.2 and E.3. These scenarios occur for long cylinders and thin disks at oblique incidences. As was stated before, the chosen remedy for this is to only make use of the latter few points in the curve fitting process. These same figures also show the results of this technique for our two illustrated examples, revealing a much more realistic and apparently reliable extension to large particles.

Figure E.4 shows a case which occurs for the two least likely atmospheric scenarios, thin disks at perpendicular incidence and long cylinders at parallel incidence. In this case, again, the need for the technique of adjusting the curve fit exclusively to the latter particles is visible, and is shown in the same figure.

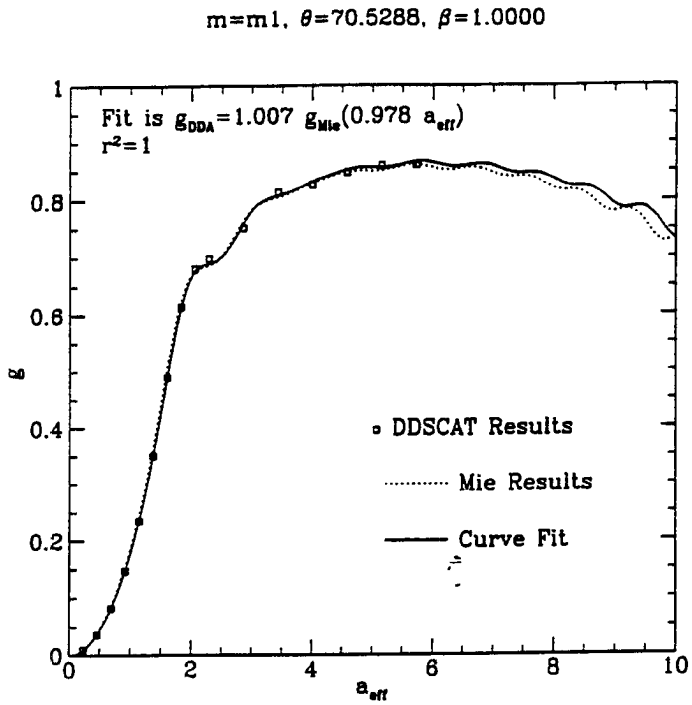

Figure E.1: . Curve fit results for the m_1, θ_5, β_{11} case.

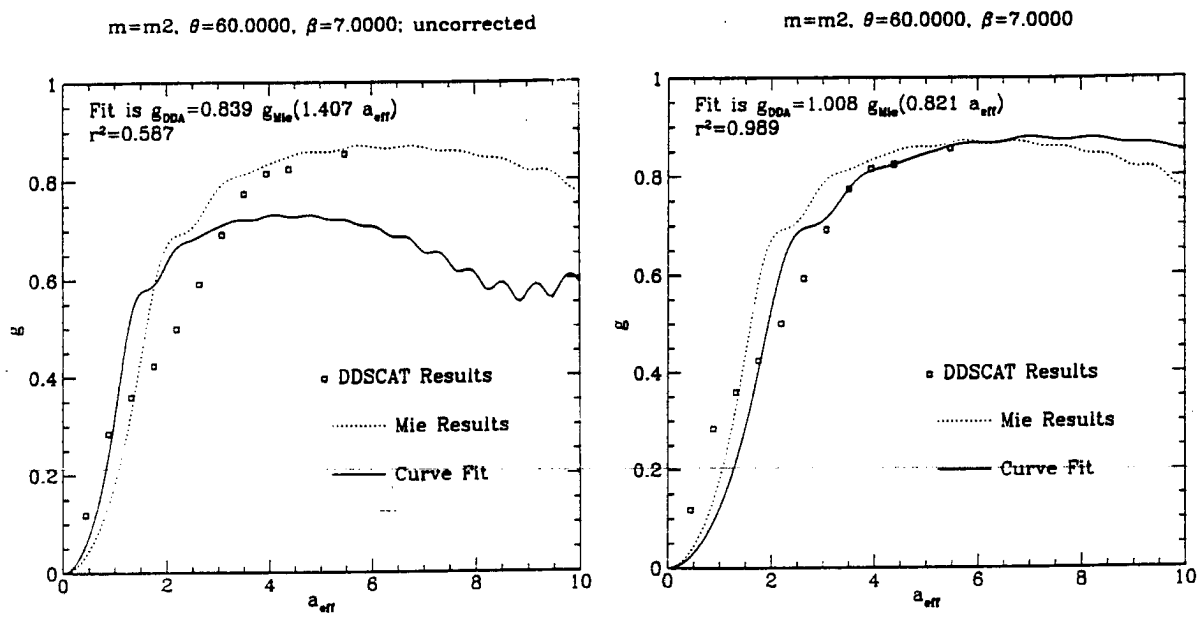

Figure E.2: . Initial and corrected curve fit results for the m_2, θ_4, β_{18} case.

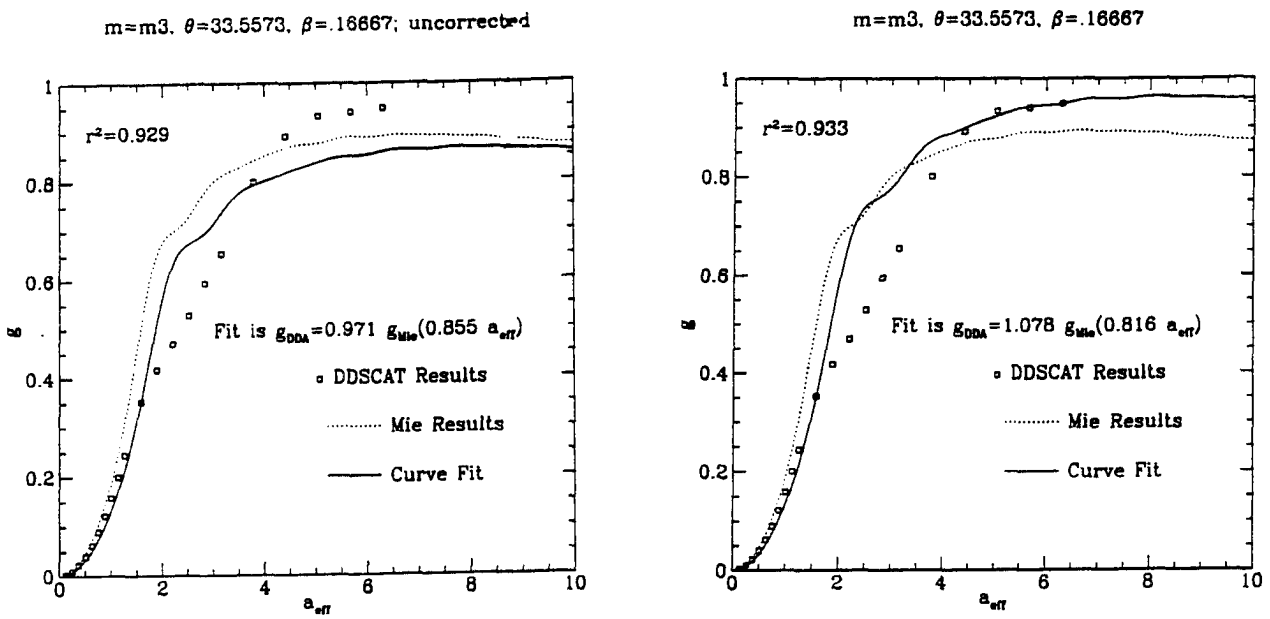

Figure E.3: . Initial and corrected curve fit results for the m_3, θ_2, β_5 case.

Lastly, figure E.5 shows a situation which was common for thin disks at parallel incidence as well as long cylinders at perpendicular incidence. Sadly for this analysis we find the two relatively common atmospheric cases receiving results which are the most uncertain. Since g cannot be greater than 1, in the given case the fitting curve is led to an impossible conclusion. In this case what must be occurring for large particles is a sudden and sharp deflection of the cylinder results into and along the vicinity of the Mie results. Perhaps an important comfort here, however, is the realization that this proves that there are some instances in which the data for smaller particles can be relatively unreliable for the extension to larger particles according to a fitted Mie curve, thus providing further legitimization of our technique of excluding the smaller particle data from the curve fit. In most of these cases an attempt was made to correct the problem through this small particle exclusion technique, which worked in some instances. In the instances in which it was futile, however, the values of a, b, and r^2 are presented in the tables along with a remark of '> 1 FP'. This occurrence was more common for cases of strong absorption, since the Mie curve for this case shows an almost monotonic increase towards a very high value of g; it was simply easier in this case for this illustrated anomaly to occur.

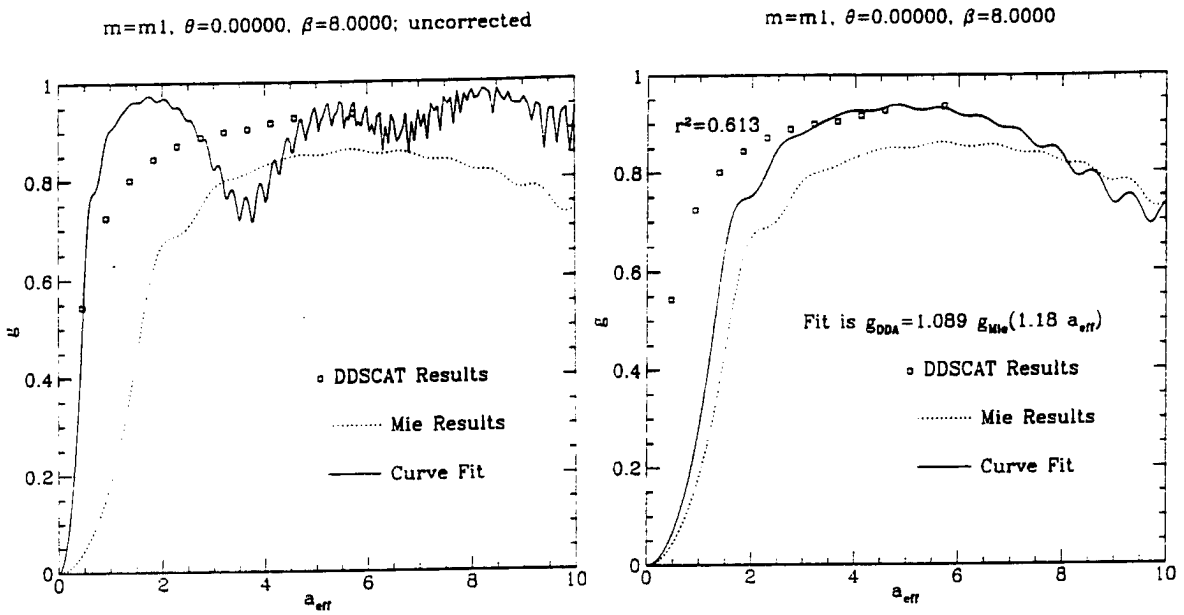

Figure E.4: . Initial and corrected curve fit results for the m_1, θ_1, β_{19} case.

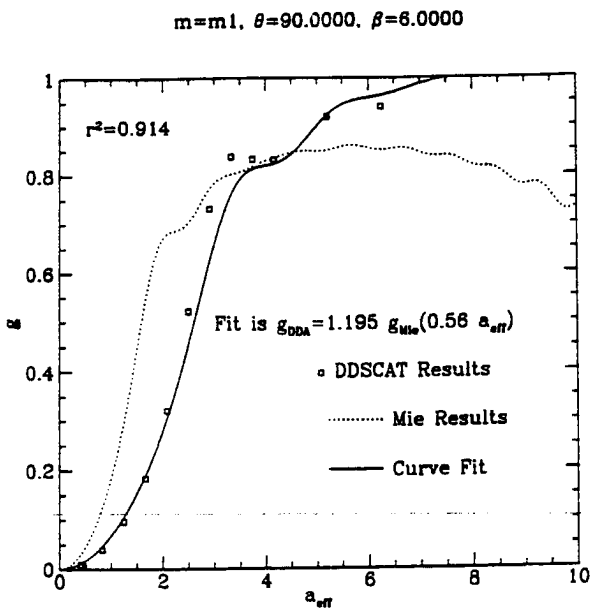

Figure E.5: . Curve fit results for the m_1, θ_7, β_{17} case.

In addition, there were also cases in which the curve fit was giving results which were clearly misleading or uncertain. In these cases the numerical results were presented with a remark of 'FP' (FIT POOR) or 'FU' (FIT UNCERTAIN), respectively. These messages should not be confused with the r^2 goodness-of-fit information, which covers the degree of agreement for particle sizes in which DDA information was available.

Finally, two important points should be mentioned before proceeding. One is that, since this data is to only provide extensions to larger particles, it should be emphatically noted that *these coefficients are only valid for particles which have effective radii larger than about 6.* Secondly, although the a and b values are given to the nearest thousandth, they are probably only accurate to within a few hundredths. This should be immediately evident to even a casual observer of the data. Still, the data is presented with this superfluous precision, since this degree of accuracy is most likely related to the finite amount of data as well as to the slight inaccuracies of the DDA results and not to inaccuracies in the curve fitting process.

Table E.1: Results for $m_1 = 1.32 + 0i$.

θ	β	a	b	r^2	**Remarks**	θ	β	a	b	r^2	**Remarks**
1	1	0.610	0.852	0.257	4,FP	2	1	0.614	1.009	0.632	4,FU
	2	0.597	0.995	0.433	4,FP		2	0.598	1.065	0.703	4,FU
	3	0.589	1.110	0.628	4,FP		3	0.585	1.122	0.814	4,FU
	4	0.838	1.068	0.522	4		4	0.584	1.161	0.964	4,> 1FP
	5	0.762	1.022	0.478	6		5	0.789	1.095	0.904	4
	6	0.785	1.018	0.561	6		6	0.988	1.057	0.902	4
	7	1.025	1.016	0.250	6		7	0.851	1.052	0.882	6
	8	0.911	1.032	0.375	6		8	0.823	1.041	0.993	
	9	0.721	1.084	0.925	6		9	0.872	1.025	0.998	
	10	0.821	1.054	0.887	6		10	0.927	1.016	0.999	
	11	0.973	1.021	0.888	6		11	1.042	0.995	0.999	
	12	1.075	1.010	0.905	6		12	1.137	0.979	0.983	6
	13	1.069	1.018	0.914	6		13	1.218	0.961	0.972	6
	14	1.157	1.041	0.703	6		14	1.043	0.979	0.890	6
	15	1.050	1.071	0.931	6		15	0.955	1.018	0.912	6
	16	1.096	1.082	0.943	6		16	0.813	1.054	0.973	4
	17	1.281	1.063	0.803	6		17	0.927	1.031	0.900	6
	18	1.223	1.076	0.767	6		18	0.813	1.050	0.955	4
	19	1.180	1.089	0.613	6		19	0.771	1.060	0.962	4
	20	1.143	1.096	0.215	6		20	0.735	1.069	0.970	4
	21	1.349	1.088	0.690	6		21	0.843	1.025	0.932	4

Table E.2: Results for m_1 continued.

θ	β	a	b	r^2	**Remarks**	θ	β	a	b	r^2	**Remarks**
3	1	0.615	1.088	0.955	4	4	1	1.038	0.989	0.912	6
	2	0.596	1.112	0.958	4		2	1.007	0.993	0.914	6
	3	0.578	1.139	0.968	4		3	0.972	0.999	0.915	6
	4	0.566	1.162	0.993	4,FP		4	0.934	1.006	0.907	6
	5	0.589	1.152	0.985	4		5	0.895	1.013	0.908	6
	6	0.666	1.102	0.986	4		6	0.937	0.997	0.983	6
	7	0.785	1.043	0.977	6		7	0.927	0.993	0.973	6
	8	0.907	0.998	0.951	6		8	1.071	0.977	0.960	6
	9	1.042	0.983	0.955	6		9	1.066	0.983	0.998	
	10	1.023	0.995	0.993	6		10	1.019	1.001	0.999	
	11	1.044	0.991	0.982	6		11	0.987	1.004	0.999	
	12	1.092	0.969	0.994			12	0.980	1.002	0.997	
	13	1.007	0.987	0.959	6		13	0.951	1.017	0.897	6
	14	0.907	1.025	0.933	6		14	0.897	1.034	0.883	6
	15	0.886	1.030	0.979	6		15	0.880	1.029	0.893	6
	16	0.842	1.034	0.979	6		16	0.848	1.018	0.918	6
	17	0.794	1.044	0.985	6		17	0.800	1.028	0.928	6
	18	0.751	1.057	0.986	4		18	1.005	0.978	0.861	4
	19	0.715	1.071	0.976	4		19	0.786	1.020	0.988	4
	20	0.700	1.076	0.983	4		20	0.925	0.992	0.894	4
	21	0.689	1.076	0.979	4		21	0.721	1.037	0.993	4

Table E.3: Results for m_1 continued.

θ	β	a	b	r^2	**Remarks**	θ	β	a	b	r^2	**Remarks**
5	1	1.099	1.032	0.965	6	6	1	1.121	1.063	0.956	6
	2	1.070	1.032	0.968	6		2	1.088	1.063	0.950	6
	3	1.041	1.031	0.977	6		3	1.053	1.062	0.950	6
	4	1.015	1.028	0.977	6		4	1.022	1.059	0.946	6
	5	1.058	1.016	0.977	6		5	1.046	1.048	0.964	6
	6	1.111	1.005	0.977	6		6	1.091	1.036	0.990	6
	7	1.097	1.000	0.991	6		7	1.067	1.029	0.972	6
	8	1.083	0.995	0.942	6		8	1.051	1.015	0.941	6
	9	1.062	0.997	0.975	6		9	1.060	1.000	0.957	6
	10	1.017	1.005	0.996	6		10	1.012	1.004	0.978	6
	11	0.978	1.007	1.000			11	0.970	1.011	1.000	
	12	0.913	1.028	0.999			12	0.880	1.040	0.998	
	13	0.877	1.037	0.998			13	0.829	1.053	0.996	
	14	0.831	1.042	0.984			14	0.755	1.068	0.997	
	15	0.809	1.028	0.954			15	0.697	1.082	0.998	
	16	0.847	1.004	0.860	6		16	0.652	1.096	0.997	
	17	0.613	1.100	0.975	6		17	0.613	1.111	0.994	
	18	0.796	0.992	0.866	4		18	0.825	1.006	0.898	4
	19	0.573	1.100	0.982	6		19	0.784	1.024	0.924	4
	20	0.550	1.107	0.985	6		20	0.759	1.039	0.954	4
	21	0.725	0.982	0.984	4		21	0.991	0.964	0.431	4,FU

Table E.4: Results for m_1 continued.

θ	β	a	b	r^2	**Remarks**
7	1	1.127	1.074	0.948	6
	2	1.090	1.074	0.940	6
	3	1.055	1.073	0.938	6
	4	1.021	1.070	0.933	6
	5	1.043	1.060	0.953	6
	6	1.085	1.047	0.987	6
	7	1.031	1.042	0.983	6
	8	0.953	1.034	0.942	6
	9	1.062	1.000	0.952	6
	10	1.009	1.004	0.967	6
	11	0.970	1.012	0.999	
	12	0.874	1.041	0.997	
	13	0.817	1.061	0.993	
	14	0.733	1.089	0.992	
	15	0.669	1.117	0.993	
	16	0.869	1.043	0.839	6
	17	0.560	1.195	0.914	4,> 1FP
	18	0.863	1.077	0.644	4
	19	0.847	1.089	0.223	4
	20	0.852	1.073	0.671	6
	21	1.452	1.031	0.749	4,FP

Table E.5: Results for $m_2 = 1.3 + .000003i$.

θ	β	a	b	r^2	**Remarks**	θ	β	a	b	r^2	**Remarks**
1	1	0.616	0.830	0.237	4,FP	2	1	0.621	0.996	0.630	4,FU
	2	0.603	0.973	0.415	4,FP		2	0.605	1.051	0.697	4,FU
	3	0.593	1.094	0.608	4,FU		3	0.592	1.107	0.800	4,FU
	4	0.843	1.058	0.517	4		4	0.589	1.150	0.950	4,> 1FP
	5	0.981	1.019	0.450	5		5	0.798	1.085	0.881	4
	6	1.045	0.987	0.293	5		6	0.997	1.048	0.882	4
	7	1.039	1.003	0.360	6		7	0.842	1.049	0.889	6
	8	0.929	1.028	0.338	6		8	0.828	1.037	0.993	
	9	0.756	1.079	0.988			9	0.879	1.022	0.998	
	10	0.885	1.033	0.995			10	0.934	1.015	0.999	
	11	0.969	1.019	0.899	6		11	1.051	0.991	0.999	
	12	1.002	1.016	0.826	4		12	1.123	0.980	0.992	6
	13	1.011	1.027	0.962	6		13	1.213	0.958	0.948	6
	14	1.001	1.056	0.953	6		14	1.055	0.974	0.953	6
	15	1.059	1.064	0.959	6		15	0.972	1.009	0.930	6
	16	1.104	1.074	0.927	6		16	0.823	1.046	0.978	4
	17	1.102	1.071	0.875	6		17	0.786	1.053	0.971	4
	18	1.252	1.064	0.767	6		18	0.823	1.042	0.955	4
	19	1.187	1.081	0.681	6		19	0.780	1.052	0.966	4
	20	1.133	1.092	0.568	6		20	0.746	1.059	0.973	4
	21	1.386	1.075	0.651	6		21	0.856	1.016	0.935	4

Table E.6: Results for m_2 continued.

θ	β	a	b	r^2	Remarks	θ	β	a	b	r^2	Remarks
3	1	0.622	1.078	0.949	4	4	1	1.052	0.979	0.919	6
	2	0.604	1.101	0.951	4		2	1.020	0.984	0.921	6
	3	0.586	1.127	0.962	4		3	0.984	0.990	0.924	6
	4	0.572	1.151	0.986	4,> 1FP		4	0.943	0.998	0.921	6
	5	0.582	1.142	0.983	6,> 1FP		5	0.905	1.005	0.926	6
	6	0.620	1.115	0.978	6		6	0.942	0.992	0.986	6
	7	0.787	1.039	0.986	6		7	0.935	0.990	0.991	6
	8	0.920	0.996	0.966	6		8	1.077	0.976	0.957	6
	9	0.989	0.991	0.999			9	1.086	0.987	0.997	6
	10	0.985	1.003	0.999			10	1.028	0.998	1.000	
	11	1.015	0.999	0.999			11	0.996	1.002	1.000	
	12	1.098	0.967	0.994			12	0.987	0.999	0.997	
	13	0.912	0.994	0.996	4		13	0.876	1.026	0.970	4
	14	0.756	1.043	0.997	4		14	0.703	1.063	0.980	4
	15	0.886	1.023	0.944	4		15	0.780	1.045	0.924	4
	16	0.837	1.032	0.968	4		16	0.816	1.024	0.891	4
	17	0.782	1.043	0.995	4		17	0.777	1.032	0.881	4
	18	0.752	1.053	0.990	4		18	0.821	1.008	0.989	4
	19	0.720	1.065	0.985	4		19	0.798	1.011	0.987	4
	20	0.706	1.069	0.988	4		20	0.939	0.982	0.907	4
	21	0.697	1.067	0.976	4		21	0.730	1.028	0.990	4

Table E.7: Results for m_2 continued.

θ	β	a	b	r^2	**Remarks**	θ	β	a	b	r^2	**Remarks**
5	1	1.120	1.021	0.973	6	6	1	1.144	1.052	0.966	6
	2	1.088	1.022	0.974	6		2	1.110	1.052	0.961	6
	3	1.056	1.022	0.979	6		3	1.076	1.051	0.957	6
	4	1.029	1.020	0.981	6		4	1.086	1.044	0.956	6
	5	1.058	1.010	0.982	6		5	1.054	1.041	0.962	6
	6	1.107	0.999	0.980	6		6	1.109	1.027	0.986	6
	7	1.109	0.995	0.997	6		7	1.075	1.023	0.989	6
	8	1.084	0.993	0.950	6		8	0.972	1.023	0.954	6
	9	1.066	0.995	0.976	6		9	0.965	1.013	0.961	6
	10	1.020	1.003	0.997	6		10	1.015	1.002	0.987	6
	11	0.985	1.005	1.000			11	0.979	1.007	1.000	
	12	0.921	1.023	0.999			12	0.889	1.034	0.998	
	13	0.885	1.031	0.998			13	0.838	1.046	0.996	
	14	0.838	1.035	0.985			14	0.763	1.060	0.997	
	15	0.756	1.040	0.953	4		15	0.706	1.072	0.998	
	16	0.576	1.122	0.959	4		16	0.660	1.086	0.997	
	17	0.544	1.127	0.993	4		17	0.620	1.102	0.994	
	18	0.806	0.983	0.876	4		18	0.839	0.996	0.902	4
	19	0.764	0.993	0.871	4		19	0.797	1.014	0.926	4
	20	0.740	0.997	0.848	4		20	0.771	1.029	0.954	4
	21	0.735	0.973	0.980	4		21	0.729	1.033	0.811	4

Table E.8: Results for m_2 continued.

θ	β	a	b	r^2	**Remarks**
7	1	1.153	1.062	0.960	6
	2	1.118	1.062	0.953	6
	3	1.084	1.061	0.949	6
	4	1.092	1.054	0.948	6
	5	1.052	1.052	0.953	6
	6	1.102	1.038	0.984	6
	7	1.047	1.035	0.992	6
	8	0.957	1.032	0.965	6
	9	0.966	1.013	0.957	6
	10	1.015	1.001	0.980	6
	11	0.978	1.008	0.999	
	12	0.880	1.037	0.997	
	13	0.823	1.056	0.992	
	14	0.739	1.082	0.991	
	15	0.674	1.111	0.993	
	16	0.600	1.158	0.985	4,> 1FP
	17	0.565	1.187	0.931	4,> 1FP
	18	0.878	1.066	0.630	4
	19	1.160	1.037	0.182	4
	20	1.123	1.042	0.184	4
	21	0.850	1.060	0.676	5

Table E.9: Results for $m_3 = 1.32 + .05i$.

θ	β	a	b	r^2	**Remarks**	θ	β	a	b	r^2	**Remarks**
1	1	0.596	0.866	0.290	4,FP	2	1	0.601	1.018	0.644	4,FP
	2	0.585	1.001	0.462	4,FU		2	0.588	1.072	0.720	4,> 1FP
	3	0.580	1.107	0.657	4,> 1FP		3	0.578	1.124	0.833	4,> 1FP
	4	0.605	1.138	0.811	4,> 1FP		4	0.583	1.155	0.975	4,> 1FP
	5	1.087	1.004	0.387	5		5	0.816	1.078	0.933	4,> 1FP
	6	1.125	0.978	0.335	5,FU		6	0.989	1.044	0.892	4,> 1FP
	7	1.013	1.006	0.397	6		7	0.851	1.049	0.906	6,> 1FP
	8	0.996	1.011	0.481	6		8	0.825	1.044	0.995	> 1FP
	9	0.757	1.080	0.988	> 1FP		9	0.873	1.028	0.998	
	10	0.883	1.031	0.996	> 1FP		10	0.929	1.016	0.999	
	11	0.968	1.017	0.947	6		11	1.045	0.989	0.999	
	12	1.068	1.004	0.963	6		12	1.105	0.982	0.999	6
	13	1.103	1.004	0.988	6		13	1.064	0.979	0.985	6
	14	1.139	1.025	0.935	6		14	0.974	1.001	0.983	6
	15	1.075	1.053	0.977	6,> 1FP		15	0.928	1.021	0.970	6
	16	1.103	1.062	0.978	6,> 1FP		16	0.953	1.015	0.948	6
	17	1.099	1.065	0.951	6,> 1FP		17	0.904	1.024	0.946	6
	18	1.213	1.059	0.889	6,> 1FP		18	1.014	0.995	0.885	6
	19	1.170	1.071	0.837	6,> 1FP		19	0.970	1.001	0.886	6
	20	1.243	1.068	0.790	6,> 1FP		20	0.932	1.006	0.880	6
	21	1.490	1.053	0.875	6,> 1FP		21	0.805	1.026	0.935	4

Table E.10: Results for m_3 continued.

θ	β	a	b	r^2	**Remarks**	θ	β	a	b	r^2	**Remarks**
3	1	0.601	1.091	0.935	4,> 1FP	4	1	0.782	1.026	0.971	4
	2	0.640	1.074	0.934	6,> 1FP		2	0.985	0.984	0.908	6
	3	0.614	1.104	0.950	6,> 1FP		3	0.944	0.995	0.898	6
	4	0.593	1.132	0.972	6,> 1FP		4	0.897	1.009	0.892	6
	5	0.581	1.147	0.987	6,> 1FP		5	0.857	1.022	0.907	6
	6	0.626	1.119	0.982	6,> 1FP		6	0.885	1.013	0.960	6
	7	0.769	1.055	0.993	6,> 1FP		7	0.871	1.014	0.991	6
	8	0.889	1.015	0.980	6		8	0.928	1.003	0.991	6
	9	0.980	0.996	0.999			9	1.066	0.982	0.998	
	10	1.016	0.994	0.998	6		10	1.022	0.996	1.000	
	11	1.038	0.989	0.994	6		11	0.989	1.003	0.999	6
	12	1.075	0.981	0.994	6		12	0.981	1.002	0.998	
	13	0.980	0.999	0.976	6		13	0.955	1.012	0.955	6
	14	0.909	1.022	0.972	6		14	0.911	1.022	0.937	6
	15	0.874	1.026	0.990	6		15	0.873	1.022	0.944	6
	16	0.833	1.027	0.985	6		16	0.833	1.013	0.943	6
	17	0.785	1.036	0.988	6,> 1FP		17	0.792	1.020	0.946	6
	18	0.692	1.069	0.975	6,> 1FP		18	0.630	1.092	0.933	6,> 1FP
	19	0.711	1.061	0.981	4,> 1FP		19	0.605	1.098	0.934	6,> 1FP
	20	0.694	1.066	0.973	4,> 1FP		20	0.587	1.102	0.935	6,> 1FP
	21	0.678	1.068	0.972	4,> 1FP		21	0.626	1.063	0.939	6,> 1FP

Table E.11: Results for m_3 continued.

θ	β	a	b	r^2	**Remarks**	θ	β	a	b	r^2	**Remarks**
5	1	1.115	1.008	0.976	6	6	1	1.171	1.033	0.972	6,> 1FP
	2	1.082	1.010	0.977	6		2	1.142	1.033	0.971	6,> 1FP
	3	1.051	1.011	0.979	6		3	1.110	1.033	0.973	6,> 1FP
	4	1.025	1.011	0.979	6		4	1.073	1.033	0.976	6,> 1FP
	5	1.010	1.010	0.977	6		5	1.046	1.031	0.972	6,> 1FP
	6	1.025	1.004	0.990	6		6	1.081	1.021	0.996	6
	7	1.009	1.004	0.997	6		7	1.032	1.020	0.992	6
	8	1.022	0.999	0.983	6		8	1.031	1.010	0.981	6
	9	1.042	0.996	0.988	6		9	1.031	0.999	0.980	6
	10	1.057	0.989	0.999			10	1.003	1.003	0.989	6
	11	0.978	1.006	1.000			11	0.973	1.008	1.000	
	12	0.917	1.025	0.999			12	0.862	1.035	0.980	6,> 1FP
	13	0.884	1.030	0.998			13	0.880	1.025	0.977	6
	14	0.839	1.031	0.986			14	0.825	1.032	0.934	6,> 1FP
	15	0.821	1.013	0.959			15	0.739	1.058	0.892	6,> 1FP
	16	0.659	1.083	0.954	6,> 1FP		16	0.834	1.003	0.900	6
	17	0.621	1.088	0.978	6,> 1FP		17	0.613	1.105	0.960	6,> 1FP
	18	0.602	1.085	0.990	6,> 1FP		18	0.807	1.007	0.949	4
	19	0.577	1.090	0.988	6,> 1FP		19	0.769	1.024	0.972	4
	20	0.553	1.098	0.990	6,> 1FP		20	0.746	1.038	0.985	4,> 1FP
	21	0.565	1.069	0.969	6,> 1FP		21	0.705	1.044	0.823	4,> 1FP

Table E.12: Results for m_3 continued.

θ	β	a	b	r^2	**Remarks**
7	1	1.188	1.042	0.969	6,> 1FP
	2	1.156	1.042	0.968	6,> 1FP
	3	1.114	1.043	0.969	6,> 1FP
	4	1.081	1.042	0.972	6,> 1FP
	5	1.045	1.041	0.969	6,> 1FP
	6	1.082	1.030	0.995	6,> 1FP
	7	1.019	1.030	0.990	6,> 1FP
	8	1.030	1.015	0.980	6
	9	1.033	0.999	0.977	6
	10	0.996	1.004	0.982	6
	11	0.971	1.010	1.000	
	12	0.876	1.032	0.987	6,> 1FP
	13	0.780	1.056	0.988	6,> 1FP
	14	0.740	1.080	0.992	> 1FP
	15	0.697	1.097	0.971	6,> 1FP
	16	0.836	1.043	0.890	6,> 1FP
	17	0.856	1.055	0.921	6,> 1FP
	18	0.869	1.066	0.885	5,> 1FP
	19	0.878	1.073	0.658	5,> 1FP
	20	1.095	1.041	0.428	5,> 1FP
	21	0.833	1.065	0.702	5,> 1FP

Table E.13: Results for $m_4 = 1.3 + .2i$.

θ	β	a	b	r^2	**Remarks**	θ	β	a	b	r^2	**Remarks**
1	1	0.342	1.337	1.000	4,> 1FP	2	1	0.417	1.250	0.974	4,> 1FP
	2	0.365	1.330	0.999	4,> 1FP		2	0.420	1.266	0.986	4,> 1FP
	3	0.396	1.300	0.997	4,> 1FP		3	0.430	1.267	0.996	4,> 1FP
	4	0.601	1.091	0.858	4,> 1FP		4	0.562	1.137	0.977	4,> 1FP
	5	0.751	1.023	0.596	5		5	0.695	1.080	0.988	4,> 1FP
	6	0.780	1.012	0.633	5		6	0.916	1.028	0.979	4
	7	1.041	0.978	0.691	6		7	0.850	1.035	0.956	6
	8	0.988	0.992	0.672	6		8	0.839	1.033	0.997	
	9	0.973	0.997	0.931	8		9	0.882	1.026	0.999	
	10	0.898	1.017	0.997			10	0.935	1.015	0.999	
	11	0.957	1.009	0.993	6		11	1.014	0.998	0.998	6
	12	1.045	1.000	0.992	6		12	1.051	0.995	0.999	6
	13	1.070	1.003	0.998	6		13	1.003	1.003	0.997	6
	14	1.184	1.004	1.000	6		14	0.953	1.013	0.998	6
	15	1.272	1.007	0.997	6		15	0.920	1.019	0.997	6
	16	1.343	1.010	0.999	6		16	0.849	1.031	0.997	4
	17	1.397	1.012	0.998	6		17	0.808	1.038	0.996	4,> 1FP
	18	1.500	1.011	0.996	6		18	0.778	1.044	0.997	4,> 1FP
	19	1.553	1.013	0.997	6		19	0.796	1.034	0.983	4
	20	1.611	1.014	0.997	6		20	0.715	1.057	0.998	4,> 1FP
	21	1.712	1.013	0.997	6		21	0.746	1.041	0.980	4,> 1FP

Table E.14: Results for m_4 continued.

θ	β	a	b	r^2	**Remarks**	θ	β	a	b	r^2	**Remarks**
3	1	0.492	1.184	0.985	4,> 1FP	4	1	0.937	0.984	0.930	6
	2	0.481	1.203	0.994	4,> 1FP		2	0.889	0.998	0.929	6
	3	0.476	1.215	0.993	4,> 1FP		3	0.832	1.017	0.936	6
	4	0.579	1.128	0.996	4,> 1FP		4	0.792	1.033	0.948	6
	5	0.640	1.099	0.990	4,> 1FP		5	0.777	1.042	0.965	6,> 1FP
	6	0.702	1.076	0.990	4,> 1FP		6	0.825	1.032	0.983	6
	7	0.860	1.035	0.992	4		7	0.835	1.032	0.997	6
	8	0.900	1.022	0.994	6		8	0.909	1.018	1.000	6
	9	0.981	1.002	0.999			9	1.012	1.002	0.998	6
	10	0.981	1.005	1.000			10	1.025	0.996	1.000	
	11	1.011	1.000	1.000			11	0.992	1.005	1.000	
	12	1.026	0.996	0.997	6		12	0.988	1.000	0.999	
	13	0.974	1.006	0.992	6		13	0.959	1.006	0.985	6
	14	0.923	1.014	0.993	6		14	0.909	1.012	0.980	6
	15	0.865	1.020	0.984	4		15	0.843	1.019	0.981	6
	16	0.838	1.021	0.996	4		16	0.768	1.027	0.969	6
	17	0.795	1.028	0.997	4		17	0.742	1.027	0.967	6
	18	0.735	1.044	0.991	4,> 1FP		18	0.649	1.065	0.973	6,> 1FP
	19	0.706	1.044	0.981	4,> 1FP		19	0.729	1.014	0.971	4
	20	0.702	1.050	0.972	4,> 1FP		20	0.746	1.006	0.998	4
	21	0.546	1.156	0.988	4,> 1FP		21	0.688	1.021	0.980	4

Table E.15: Results for m_4 continued.

θ	β	a	b	r^2	**Remarks**	θ	β	a	b	r^2	**Remarks**
5	1	1.149	0.988	0.979	6	6	1	1.241	1.007	0.987	6
	2	1.109	0.992	0.978	6		2	1.213	1.007	0.987	6
	3	1.065	0.997	0.977	6		3	1.175	1.008	0.989	6
	4	1.012	1.004	0.976	6		4	1.135	1.009	0.989	6
	5	0.962	1.012	0.976	6		5	1.090	1.011	0.988	6
	6	0.977	1.009	0.988	6		6	1.086	1.007	0.995	6
	7	0.931	1.017	0.994	6		7	1.028	1.010	0.994	6
	8	0.946	1.014	0.999	6		8	0.996	1.009	0.998	6
	9	0.988	1.006	0.999	6		9	0.971	1.008	0.999	6
	10	1.018	1.000	1.000	6		10	0.991	1.004	0.998	6
	11	0.984	1.005	1.000			11	0.981	1.004	1.000	
	12	0.968	1.004	0.987	6		12	0.953	1.006	0.993	6
	13	0.902	1.016	0.999			13	0.896	1.011	0.994	6
	14	0.865	1.009	0.990			14	0.843	1.013	0.975	6
	15	0.826	1.012	0.979	6		15	0.810	1.015	0.961	6
	16	0.700	1.046	0.979	6,> 1FP		16	0.720	1.033	0.980	4
	17	0.653	1.055	0.989	6,> 1FP		17	0.696	1.041	0.981	4,> 1FP
	18	0.621	1.059	0.997	6,> 1FP		18	0.728	1.024	0.993	4
	19	0.578	1.081	0.998	4,> 1FP		19	0.568	1.114	0.950	4,> 1FP
	20	0.555	1.089	0.999	4,> 1FP		20	0.545	1.130	0.926	4,> 1FP
	21	0.545	1.080	0.988	4,> 1FP		21	0.501	1.197	0.982	4,> 1FP

Table E.16: Results for m_4 continued.

θ	β	a	b	r^2	**Remarks**
7	1	1.272	1.014	0.987	6
	2	1.240	1.014	0.988	6
	3	1.196	1.015	0.990	6
	4	1.157	1.015	0.991	6
	5	1.125	1.014	0.991	6
	6	1.127	1.008	0.996	6
	7	1.066	1.009	0.995	6
	8	1.020	1.007	0.997	6
	9	0.963	1.009	0.999	6
	10	0.978	1.006	0.996	6
	11	0.980	1.004	1.000	
	12	0.947	1.007	0.995	6
	13	0.797	1.037	0.993	5
	14	0.757	1.053	0.983	6,> 1FP
	15	0.729	1.066	0.983	6,> 1FP
	16	0.688	1.095	0.975	6,> 1FP
	17	0.801	1.056	0.955	6,> 1FP
	18	0.854	1.054	0.950	5,> 1FP
	19	0.892	1.059	0.922	4,> 1FP
	20	1.020	1.040	0.877	4,> 1FP
	21	2.009	0.968	0.530	4,FU

Appendix F

ADT CORRECTION FACTORS FOR THE EXTINCTION EFFICIENCY

This appendix shows the *ad nauseum* results for the numerical coefficients derived for the correction of ADT data to the more correct DDA data. The coefficients are according to equation 4.12 in chapter 4, and are applied as a function of ρ much like the results presented in figure 4.14 of chapter 4, shown again as figure F.1, but are applied to a series of aspect ratios as well as refractive indices and incidence angles. In addition, similar comparisons are given between infinite cylinder results and ADT results applied to cylinders with aspect ratios of 1000. These coefficients are found through an iterative method in which the ADT results are successively stretched in two dimensions and their linearly interpolated values are compared with the less plentiful DDA results by calculating a χ^2 difference between the two curves:

$$\chi^2 = \sum_i \frac{(X_{i_{ADT}} - X_{i_{DDA}})^2}{X_{i_{DDA}}} \tag{F.1}$$

Upon arriving at a fit which minimizes χ^2, r^2 values are then calculated according to the equation:

$$r^2 = 1 - \frac{\chi^2}{N\sigma^2}$$

where σ^2 is the variance of the DDA data, and N is the number of DDA points. (This is taken from page 658 of Press et. al. (1992).)

Although this is the generalized technique, most of the coefficients were not arrived at this easily. In many cases the DDA data which exists more plentifully for the smaller particles (which in the calculation of a χ^2 value receive a relatively large amount of weight - see equation F.1) resulted in corrected ADT results which appeared by the author to provide unrealistic extensions to the larger particles. To correct this, in many cases the smaller particle DDA data was deleted from the curve fitting process, leaving only the

DDA data for the largest particles to still be used for the fitting process. It is believed that this is justifiable for the following reasons:

1. It is known that ADT is less reliable for these smaller particles.

2. The analyses which are used in chapter 4 to describe the behavior in response to ADT's performance make use of arguments which have their roots in geometric optics. These arguments are, of course, most valid for larger particles.

3. An important point should be made concerning the objective of this analysis. *We are not seeking here to provide a generalized ADT fit to the entirety of the scattering results or to even try to get a reasonable duplication of the small particle data; we already have that from the DDA results. What is desired is an extension of this to larger particles.* Towards this end, the data for the largest particles should be the most relevant.

In these cases a number is shown in the remarks column which reveals the number of points which remained for the coefficient analysis. This number was not allowed to become smaller than 4, although in many cases reliable results were not possible without reducing the number of points to this minimum.

Another form in which ambiguity arose in this analysis is again illustrated in figure F.1, which raises a question concerning the cases like those in figure F.4, where the DDA data is plotted under the key name 'DDSCAT'. On the left plot of this figure the DDA results clearly show a peak around $\rho = 6$, but examining the infinite cylinder results in figure F.1 reveals that there are two classes of peaks to which this DDA peak can belong. There are what is termed here as 'primary' peaks, which are also present in the ADT results in this figure, and imbedded in these are 'secondary' peaks. Two other examples of secondary resonances are shown in the DDA results in figures F.2 and F.3. The question arises as to whether the DDA peak in figure F.4 is primary or secondary. If a primary peak is present, it calls for a truncation of the DDA points to fit the ADT curve to this peak. If, however, only secondary peaks are present, like the one shown at around $\rho = 1$ in figure F.2, then the fit is chosen as if it were to smooth out these fluctuations. Sometimes in cases

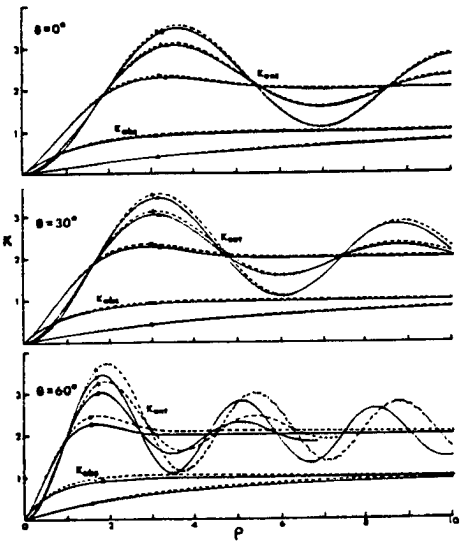

Figure F.1: . Infinite cylinder results shown from a consummate solution technique (dotted lines showing two separate polarizations) and from ADT (solid line). Here $n = 1.5$, and the cases of $n' = 0$, $n' = .05$, and $n' = .25$ are shown by circular, triangular, and square data points, respectively. Also, for this figure the values of θ, unlike those in our analysis, are measured relative to a normal from the cylinder axis.

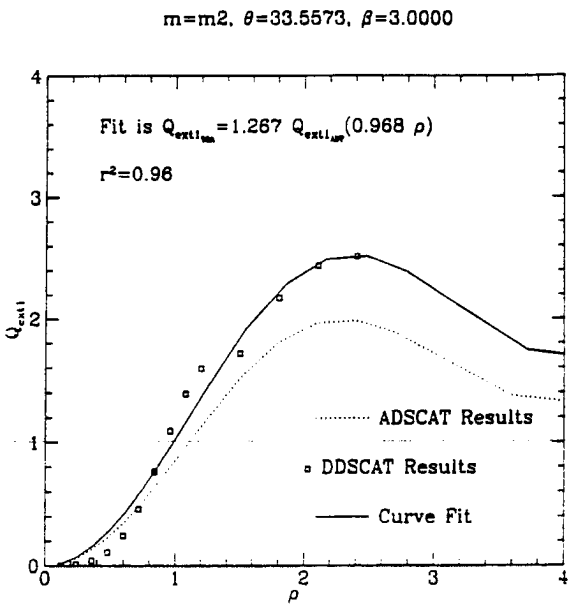

Figure F.2: . Curve fit results for the m_2, θ_2, β_{14} case.

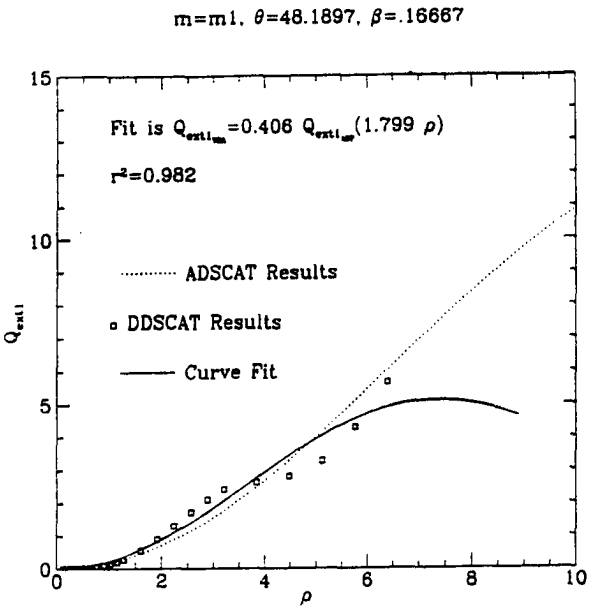

Figure F.3: . Curve fit results for the m_1, θ_3, β_5 case.

with thin disks this sometimes even meant foregoing the curve fit altogether (figure F.3), realizing through inspection of the curves that the DDA results were most likely showing secondary fluctuations around an apparent otherwise primary curve which was being well simulated by the ADT results. In such cases the curve fitting coefficients were presented but with an asterisk, indicating that, although the results are here presented, they should most likely be replaced with $a = 1, b = 1$. This primary/secondary determination often required information from curve fits of adjacent values of β and θ. An example of this is given by comparing the plots in figure F.4 with figure F.5. (Note that these three plots are of cases which are identical in every way with the exception of a slight change in β.) An examination of the latter two figures reveals the aforementioned peak in question to be most likely of a primary nature.

Still, in some cases the coefficient results were uncertain at best, cases which contained peaks in the DDA data which departed heavily from the ADT results - so that the aforementioned '1,1' replacement was not appropriate - and to which the ADT results would not fit well, even after the maximum degree of truncation. In these cases the best possible coefficient results were obtained and presented with the disclaimer 'FP' (FIT POOR)

listed in the 'Remarks' column. This message was given to indicate an instance where the corrected ADT curve was clearly giving misleading values for particles larger than those for which DDA results were available. This message should, thus, not be confused with the r^2 goodness-of-fit information, which covers the amount of agreement for the ADT information for particle sizes in which DDA information was available.

In addition, there were also cases in which the DDA points were only covering the starting portion of the first primary peak and, thus, were almost purely linear. In such cases the resulting a and b values were given with the disclaimer 'FU' (FIT UNCERTAIN) in the 'Remarks' column, to indicate the possibility that the results are misleading due to the small scope of the DDA data compared to the size of the curve which it covers.

Lastly, there are two important points which should be mentioned. The first is that since the curve fit results are mere extensions to larger particles, *the results should only be used for particles with effective radii larger than about 6.* Secondly, one should mention that although the a and b values are given to the nearest thousandth, they are probably only accurate to within a few hundredths. This should be immediately evident to even a casual observer of this coefficient data. Still, the data is presented with this superfluous precision, since this degree of accuracy is most likely related to the finite amount of data as well as to the slight inaccuracies of the DDA and ADT results and not to inaccuracies in the curve fitting process.

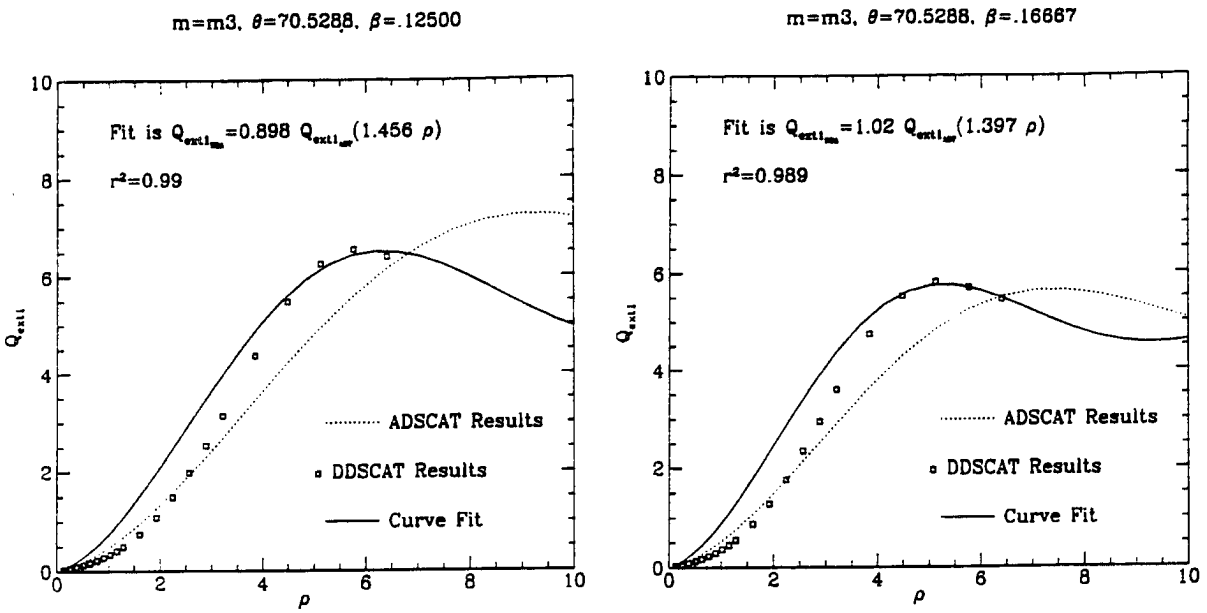

Figure F.4: . Curve fit results for the cases of m_3, θ_5, β_3 and m_3, θ_5, β_5.

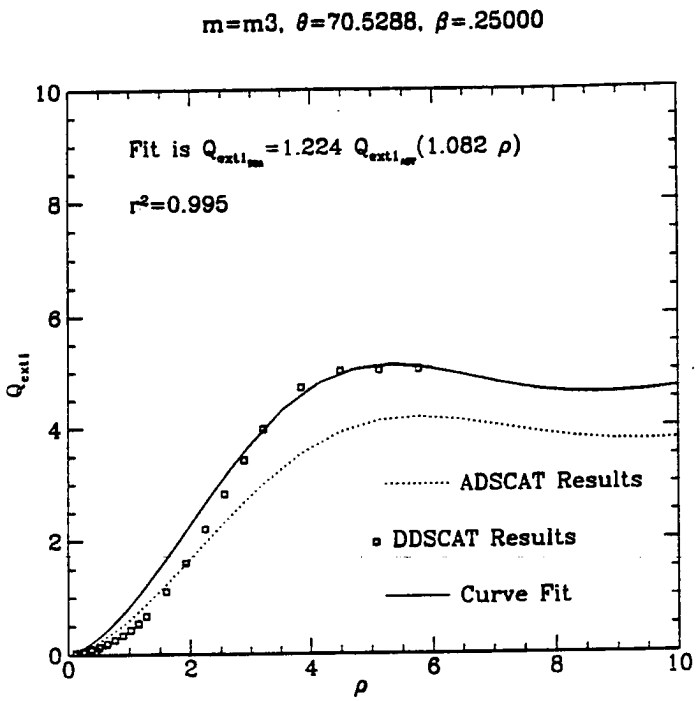

Figure F.5: . Curve fit results for the m_3, θ_5, β_7 case.

Table F.1: Results for $m_1 = 1.32 + 0i$.

θ	β	a	b	r^2	**Remarks**	θ	β	a	b	r^2	**Remarks**
1	1	1.111*	.968*	.755	6	2	1	2.789	.174	1.000	4
	2	2.999*	.148*	.982	4		2	2.436	.210	1.000	4
	3	1.111*	.807*	.991	4		3	1.824	.328	1.000	4
	4	.874*	1.285*	.996	4		4	1.042	.872	1.000	4
	5	.857	1.354	.999	4		5	.857*	1.270*	.999	4
	6	1.010	.996	.996	6		6	.667*	2.032*	.998	4
	7	1.165	.761	1.000	6		7	.998	.980	.999	6
	8	1.068	.906	.998	6		8	1.048	.941	1.000	6
	9	.852	1.272	.997			9	.542	2.109	1.000	
	10	.741	1.567	.996			10	.942	1.225	1.000	
	11	.668	1.799	.989			11	.963	1.346	1.000	4
	12	.842	1.601	.993	4		12	.983	1.397	.990	4
	13	.818	2.096	.998	4		13	.975	1.322	.994	6
	14	.737	3.638	.990	4		14	.839	1.387	.966	
	15	.510	2.948	.797	FP		15	.834	1.381	.956	
	16	.415	3.868	.792	FP		16	.758	1.585	.953	
	17	.401	4.435	.770	FP		17	.801	1.408	.945	
	18	.300	6.006	.800	FP		18	.751	1.609	.938	
	19	.405	9.441	.926	4, FP		19	.771	1.514	.944	
	20	.395	12.866	.935	4, FP		20	.751	1.594	.954	
	21	.222	10.714	.882	FP		21	.626	2.234	.940	FU
	∞	N/A	N/A	N/A			∞	.818	1.271	.983	

Table F.2: Results for m_1 continued.

θ	β	a	b	r^2	**Remarks**	θ	β	a	b	r^2	**Remarks**
3	1	3.054*	.174*	.981		4	1	2.705*	.308*	.994	4
	2	2.858*	.194*	.981			2	2.614*	.332*	.994	4
	3	2.531*	.235*	.980			3	2.465*	.365*	.991	4
	4	2.199*	.294*	.980			4	2.164*	.408*	.994	6
	5	1.799*	.406*	.982			5	1.865*	.488*	.964	6
	6	1.596*	.492*	.983			6	1.680*	.574*	.987	6
	7	1.234*	.747*	.991			7	1.309*	.798*	.976	6
	8	1.085	.932	.993			8	1.108	1.048	.996	6
	9	1.015	1.118	1.000	6		9	.951	1.315	.998	6
	10	.940	1.311	.998	6		10	.982	1.326	.998	4
	11	.925	1.372	.997	6		11	.988	1.252	1.000	4
	12	.961	1.252	.999	6		12	.935	1.253	1.000	4
	13	.939	1.244	1.000	6		13	.911	1.272	.999	4
	14	.889	1.291	1.000	6		14	.909	1.260	1.000	4
	15	.841	1.373	.998	6		15	.849	1.384	1.000	4
	16	.780	1.556	.998	6		16	.779	1.589	.999	4
	17	.898	1.230	.998	6		17	.780	1.563	.999	4
	18	.823	1.457	.999	6		18	.876	1.334	.994	4
	19	.914	1.201	.999	6		19	.949	1.150	.996	4
	20	.835	1.418	.997	6		20	.876	1.331	.995	4
	21	.877	1.305	.994	4, FU		21	.716	1.928	.994	4, FU
	∞	.909	1.186	.995			∞	.959	1.136	.997	

Table F.3: Results for m_1 continued.

θ	β	a	b	r^2	**Remarks**	θ	β	a	b	r^2	**Remarks**
5	1	1.250	.971	.997	4, FP	6	1	.357	6.537	.999	4, FP
	2	1.359	.883	.995	4, FP		2	.463	4.104	.998	4, FP
	3	1.443	.860	.990	4		3	.611	2.703	.997	4, FP
	4	1.448	.902	.979	4		4	.732	2.233	.993	4, FP
	5	1.418	.978	.980	4		5	.826	2.060	.976	4, FP
	6	1.263	1.069	.985	4		6	.756	2.086	.986	4, FP
	7	1.105	1.202	.995	6		7	.909	1.838	.967	4
	8	.994	1.364	.997	6		8	.926	1.663	.989	4
	9	.912	1.432	.997	6		9	.902	1.441	.996	6
	10	.899	1.410	.998	6		10	.891	1.380	.999	6
	11	.908	1.318	.999	6		11	.853	1.395	1.000	6
	12	.871	1.357	1.000	6		12	.827	1.442	1.000	6
	13	.896	1.290	1.000	6		13	.862	1.350	1.000	6
	14	.891	1.293	1.000	6		14	.855	1.367	1.000	6
	15	.886	1.305	1.000	4		15	.855	1.371	1.000	4
	16	.888	1.297	.998	4		16	.788	1.581	1.000	4, FP
	17	.916	1.230	.999	4		17	.783	1.600	.999	4, FP
	18	.998	1.072	.992	4		18	1.043	.984	.991	4
	19	1.022	1.022	.992	4		19	1.043	.984	.991	4
	20	1.008	1.053	.992	4		20	1.073	.939	.991	4
	21	.858	1.396	.979	4, FU		21	.858	1.396	.974	4, FU
	∞	.984	1.115	.998			∞	.993	1.108	.998	

Table F.4: Results for m_1 continued.

θ	β	a	b	r^2	**Remarks**
7	1	.228	9.187	.997	4, FU
	2	.236	9.005	.999	4, FU
	3	.333	5.248	.998	4, FU
	4	.456	3.479	.996	4, FU
	5	.557	2.830	.991	4, FP
	6	.596	2.567	.993	4, FP
	7	.737	2.130	.977	4
	8	.828	1.793	.992	4
	9	.876	1.436	.995	6
	10	.872	1.359	.999	6
	11	.819	1.432	1.000	6
	12	.845	1.375	.999	6
	13	.884	1.290	.999	6
	14	.906	1.252	.999	6
	15	.946	1.171	.998	4
	16	1.014	1.048	.997	4
	17	1.025	1.033	.998	4
	18	1.060	.960	.992	4
	19	.980	1.073	.990	
	20	1.001	1.042	.990	
	21	1.001	1.041	.982	FU
	∞	.997	1.088	.998	

Table F.5: Results for $m_2 = 1.3 + .000003i$.

θ	β	a	b	r^2	**Remarks**	θ	β	a	b	r^2	**Remarks**
1	1	3.806*	.104*	.978	4	2	1	2.893	.162	1.000	4
	2	2.999*	.144*	.982	4		2	2.543	.194	1.000	4
	3	1.665*	.380*	.990	4		3	1.924	.298	1.000	4
	4	1.277*	.875*	.996	4		4	1.142	.739	1.000	4
	5	1.000*	1.014*	.995	6		5	.857*	1.274*	.999	4
	6	1.000*	1.005*	.997	6		6	1.000	.980	.995	6
	7	.950*	1.071*	.999	6		7	.999	.980	.998	4
	8	.858*	1.285*	.999	6		8	.952	1.072	1.000	6
	9	.819*	1.353*	1.000	6		9	.533	2.154	.996	
	10	.733	1.610	.999	6		10	.937	1.226	1.000	6
	11	.738	1.582	.989			11	.938	1.363	1.000	4
	12	.817	1.573	.996	6		12	.967	1.395	.994	4
	13	.788	1.915	.967	6		13	1.016	1.298	.994	6
	14	.732	3.305	.985	4		14	.968	1.267	.960	
	15	.596	3.581	.881	6		15	1.002	1.190	.948	
	16	.541	5.234	.947	4		16	.959	1.239	.942	
	17	.468	5.493	.844	6		17	1.002	1.126	.945	
	18	.339	5.839	.794	FP		18	.955	1.199	.933	
	19	.334	6.262	.752	FP		19	1.001*	1.101*	.940	
	20	.334	6.873	.709	FP		20	1.002*	1.100*	.944	
	21	.251	8.222	.657	FP		21	.894*	1.388*	.986	6, FU
	∞	N/A	N/A	N/A			∞	.827	1.266	.983	

Table F.6: Results for m_2 continued.

θ	β	a	b	r^2	**Remarks**	θ	β	a	b	r^2	**Remarks**
3	1	3.124*	.163*	.983		4	1	2.712*	.296*	.995	4
	2	2.953*	.179*	.984			2	2.646*	.316*	.994	4
	3	2.611*	.215*	.984			3	2.344*	.346*	.986	6
	4	2.299*	.264*	.985			4	2.189*	.386*	.989	6
	5	1.818*	.382*	.986			5	1.930*	.456*	.988	6
	6	1.657*	.448*	.988			6	1.691*	.543*	.996	6
	7	1.229*	.732*	.994			7	1.319*	.761*	.991	6
	8	1.075	.925	.996			8	1.072	1.046	.999	6
	9	1.012	1.113	1.000	6		9	.971	1.293	.999	4
	10	.983	1.250	1.000	4		10	.956	1.346	.999	4
	11	.974	1.311	1.000	4		11	.981	1.251	1.000	4
	12	1.015	1.184	.998	6		12	.933	1.248	.991	
	13	.935	1.240	.999	4		13	.954	1.204	.993	
	14	.883	1.303	1.000	4		14	.997	1.117	.994	
	15	.999	1.112	.986			15	1.002	1.105	.990	
	16	1.002	1.101	.979			16	1.017*	1.076*	.987	
	17	1.017	1.069	.979			17	1.047*	1.020*	.987	
	18	1.001	1.109	.973			18	1.001*	1.123*	.979	
	19	1.002	1.094	.972			19	1.002*	1.114*	.980	
	20	1.002	1.102	.972			20	1.002*	1.120*	.981	
	21	1.001	1.119	.959	FU		21	1.001*	1.144*	.974	FU
	∞	.910	1.185	.996			∞	.964	1.127	.997	

Table F.7: Results for m_2 continued.

θ	β	a	b	r^2	**Remarks**	θ	β	a	b	r^2	**Remarks**
5	1	1.139	1.109	.998	4, FP	6	1	.357	6.624	.998	4, FU
	2	1.252	.965	.997	4, FP		2	.398	5.395	.998	4, FU
	3	1.362	.885	.994	4, FP		3	.514	3.484	.998	4, FU
	4	1.419	.885	.987	4, FP		4	.652	2.499	.996	4, FP
	5	1.406	.944	.977	4		5	.775	2.102	.992	4
	6	1.250	1.043	.991	4		6	.728	2.145	.994	4
	7	1.142	1.174	.998	4		7	.873	1.810	.985	4
	8	.988	1.349	.999	4		8	.858	1.666	.992	4
	9	.926	1.422	.999	4		9	.921	1.428	.999	4
	10	.928	1.374	.999	4		10	.910	1.355	1.000	4
	11	.944	1.266	.999	4		11	.886	1.333	1.000	4
	12	.910	1.280	.993			12	.870	1.351	.994	
	13	.947	1.205	.995			13	.938	1.209	.996	
	14	1.001	1.106	.995			14	1.002	1.099	.995	
	15	1.025	1.063	.993			15	1.048	1.019	.993	
	16	1.072	.985	.988			16	1.145*	.880*	.989	
	17	1.081	.974	.989			17	1.146*	.881*	.990	
	18	1.002	1.129	.981			18	1.153*	.871*	.982	
	19	1.028	1.073	.981			19	1.166*	.853*	.982	
	20	1.022	1.091	.982			20	1.168*	.855*	.982	
	21	1.001	1.164	.981	FU		21	1.001*	1.167*	.983	FU
	∞	.981	1.114	.998			∞	.990	1.106	.999	

Table F.8: Results for m_2 continued.

θ	β	a	b	r^2	**Remarks**
7	1	.228	9.235	.996	4, FU
	2	.229	9.650	.998	4, FU
	3	.285	6.853	.999	4, FU
	4	.409	4.013	.998	4, FP
	5	.537	2.915	.996	4
	6	.567	2.679	.996	4
	7	.714	2.117	.988	4
	8	.788	1.784	.990	4
	9	.850	1.454	.996	6
	10	.866	1.361	.999	6
	11	.808	1.461	1.000	6
	12	.861	1.343	.994	
	13	.928	1.209	.996	
	14	1.000	1.090	.995	
	15	1.047*	1.015*	.993	
	16	1.145*	.877*	.989	
	17	1.154*	.869*	.990	
	18	1.168*	.854*	.982	
	19	1.169*	.856*	.982	
	20	1.169*	.859*	.982	
	21	1.001*	1.174*	.983	FU
	∞	.994	1.086	.999	

Table F.9: Results for $m_3 = 1.32 + .05i$.

θ	β	a	b	r^2	**Remarks**	θ	β	a	b	r^2	**Remarks**
1	1	.500*	3.114*	.991		2	1	.900	1.168	.986	4
	2	.501*	3.050*	.991			2	2.071	.343	1.000	4
	3	.888*	1.195*	.998	4		3	1.517	.521	1.000	4
	4	.874*	1.234*	.999	4		4	.857	1.206	1.000	4
	5	.833*	1.333*	.999	6		5	.833*	1.273*	.999	6
	6	.800*	1.410*	.999	6		6	.764*	1.452*	.999	4
	7	.996*	1.009*	1.000	6		7	1.010	.986	1.000	4
	8	1.031*	.987*	.997			8	1.033	.989	.998	
	9	.863	1.240	1.000	6		9	.527	2.122	.997	
	10	.780	1.408	.997			10	.962	1.198	1.000	6
	11	.813	1.425	1.000	6		11	.956	1.312	.997	6
	12	.796	1.639	.991	6		12	.967	1.349	.991	6
	13	.771	1.969	.954	6		13	1.001	1.299	.994	6
	14	.673	2.722	.923	6		14	.948	1.310	.996	6
	15	.572	3.482	.893	6		15	.939	1.282	.987	6
	16	.481	4.208	.808	6		16	.921	1.275	.974	6
	17	.374	4.350	.719	FP		17	.882	1.297	.967	6
	18	.334	5.158	.704	FP		18	.860	1.321	.970	6
	19	.334	5.717	.642	FP		19	.869	1.292	.984	6
	20	.334	6.453	.563	FP		20	.846*	1.333*	.992	6
	21	.334	7.366	.459	FP		21	.837*	1.332*	.996	4, FU
	∞	N/A	N/A	N/A			∞	.835	1.269	.982	

Table F.10: Results for m_3 continued.

θ	β	a	b	r^2	**Remarks**	θ	β	a	b	r^2	**Remarks**
3	1	2.896*	.252*	.998		4	1	1.872*	.463*	.993	
	2	2.582*	.290*	.997			2	1.849*	.471*	.993	
	3	2.300*	.337*	.996			3	1.764*	.501*	.992	
	4	1.946*	.419*	.995			4	1.655*	.547*	.993	
	5	1.594*	.548*	.994			5	1.464*	.643*	.993	
	6	1.444*	.628*	.995			6	1.300*	.754*	.992	
	7	1.152*	.855*	.997			7	1.065	.983	.993	
	8	1.028	1.010	.997			8	1.049	1.107	.999	6
	9	1.020	1.129	1.000	6		9	.999	1.243	.998	6
	10	.995	1.224	.998	6		10	.978	1.286	.996	6
	11	.992	1.260	.997	6		11	.982	1.237	.999	6
	12	.986	1.220	.999	6		12	.939	1.240	1.000	6
	13	.951	1.229	1.000	6		13	.920	1.245	1.000	6
	14	.896	1.268	.999	6		14	.893	1.266	.999	6
	15	.837	1.349	.999	6		15	.852	1.334	.999	6
	16	.804	1.422	.999	6		16	.840	1.363	1.000	4
	17	.897	1.245	.999	4		17	.865	1.305	.999	4
	18	.722	1.660	.999	4		18	.751	1.594	.998	4
	19	.779	1.480	.999	4		19	.751	1.588	.999	4
	20	.680	1.797	.999	4		20	.751	1.591	.999	4
	21	.801	1.415	.998	6, FU		21	.716	1.699	.996	4, FU
	∞	.860	1.174	.995			∞	.960	1.138	.998	

Table F.11: Results for m_3 continued.

θ	β	a	b	r^2	**Remarks**	θ	β	a	b	r^2	**Remarks**
5	1	1.374	.884	.997	4, FP	6	1	.505	3.116	.999	4, FU
	2	1.444	.870	.995	4, FP		2	.616	2.456	.998	4, FP
	3	1.456	.898	.990	4		3	.667	2.270	.995	4, FP
	4	1.453	.947	.982	4		4	.778	2.028	.988	4, FP
	5	1.397	1.020	.989	4		5	.921	1.899	.952	4
	6	1.269	1.101	.993	4		6	.869	1.858	.979	4
	7	1.082	1.224	.995	6		7	.992	1.732	.951	4
	8	1.035	1.324	1.000	4		8	.892	1.580	.985	6
	9	1.002	1.333	.996	4		9	.932	1.409	.996	6
	10	.999	1.287	.997	4		10	.915	1.347	.999	6
	11	.939	1.265	.999	6		11	.884	1.322	1.000	6
	12	.901	1.281	1.000	6		12	.874	1.313	1.000	6
	13	.913	1.248	1.000	6		13	.902	1.259	1.000	6
	14	.898	1.261	1.000	6		14	.897	1.260	1.000	6
	15	.885	1.283	1.000	4		15	.893	1.267	1.000	4
	16	.852	1.348	1.000	4		16	.847	1.359	1.000	4
	17	.859	1.330	1.000	4		17	.862	1.323	1.000	4
	18	.751	1.611	.998	4		18	.751	1.606	.999	4
	19	.751	1.605	.998	4		19	.751	1.603	.999	4
	20	.751	1.609	.998	4		20	.751	1.608	.998	4
	21	.858	1.308	.989	4, FU		21	.858	1.308	.987	4, FU
	∞	.982	1.120	.999			∞	.992	1.112	.999	

Table F.12: Results for m_3 continued.

θ	β	a	b	r^2	**Remarks**
7	1	.228	7.540	.999	4, FU
	2	.314	4.970	.998	4, FP
	3	.409	3.697	.997	4, FP
	4	.507	3.037	.994	4, FP
	5	.612	2.662	.974	4
	6	.628	2.418	.989	4
	7	.766	2.088	.970	4
	8	.837	1.758	.981	4
	9	.907	1.459	.999	4
	10	.878	1.370	1.000	6
	11	.868	1.335	1.000	4
	12	.907	1.260	1.000	4
	13	.895	1.259	1.000	6
	14	.885	1.272	1.000	6
	15	.834	1.373	.999	6
	16	.847	1.356	1.000	4
	17	.858	1.334	1.000	4
	18	.751	1.615	.999	4
	19	.751	1.617	.999	4
	20	.751	1.618	.999	4
	21	.858	1.312	.987	4, FU
	∞	.995	1.093	.999	

Table F.13: Results for $m_4 = 1.3 + .2i$.

θ	β	a	b	r^2	Remarks	θ	β	a	b	r^2	Remarks
1	1	1.306*	.768*	1.000	4	2	1	1.324	.731	1.000	4
	2	.911*	1.103*	1.000	4		2	1.099	.883	1.000	4
	3	1.067*	.950*	.999	6		3	.905	1.071	1.000	4
	4	.813	1.249	1.000	6		4	.819	1.188	1.000	4
	5	.849	1.196	1.000	6		5	.837	1.170	1.000	6
	6	.864	1.180	1.000	6		6	.834	1.182	1.000	6
	7	.931	1.111	1.000	6		7	.871	1.147	1.000	6
	8	.917	1.148	1.000	6		8	.918	1.127	1.000	6
	9	.891	1.219	.999			9	.593	1.898	1.000	6
	10	.824	1.335	.999			10	1.028	1.155	1.000	6
	11	.817	1.468	1.000	6		11	.923	1.262	.991	
	12	.808	1.740	.998	6		12	.933	1.289	.983	
	13	.821	2.065	.976	6		13	.964	1.268	.979	
	14	.524	2.652	.886	FP		14	.921	1.307	.977	
	15	.501	3.195	.825	FP		15	.890	1.328	.979	
	16	.501	3.777	.732	FP		16	.858	1.353	.979	
	17	.467	4.908	.701	4, FP		17	.851	1.350	.982	
	18	.334	4.940	.442	FP		18	.816	1.391	.981	
	19	.334	5.404	.341	FP		19	.809	1.395	.981	
	20	.334	5.902	.234	FP		20	.881	1.325	.996	6
	21	.334	6.462	.136	FP		21	.942	1.263	.999	6, FU
	∞	N/A	N/A	N/A			∞	.915	1.248	.978	

Table F.14: Results for m_4 continued.

θ	β	a	b	r^2	**Remarks**	θ	β	a	b	r^2	**Remarks**
3	1	1.943*	.539*	.999		4	1	1.542*	.688*	.998	
	2	1.777*	.589*	.999			2	1.481*	.720*	.998	
	3	1.598*	.655*	.999			3	1.397*	.767*	.998	
	4	1.404*	.744*	.999			4	1.299*	.829*	.998	
	5	1.241*	.843*	.999			5	1.186*	.912*	.998	
	6	1.183*	.893*	.999			6	1.095	.995	.997	
	7	.940	1.075	1.000	6		7	.998	1.099	.997	
	8	1.013	1.072	.999			8	.947	1.181	.996	
	9	.969	1.159	.997			9	.923	1.239	.994	
	10	.935	1.220	.995			10	.911	1.261	.993	
	11	.944	1.228	.992			11	.936	1.227	.994	
	12	.953	1.218	.992			12	.933	1.217	.996	
	13	.953	1.209	.993			13	.936	1.203	.997	
	14	.973	1.196	.999	6		14	.980	1.170	1.000	6
	15	.933	1.220	.999	6		15	.950	1.188	1.000	6
	16	.903	1.245	.999	6		16	.911	1.221	1.000	6
	17	.908	1.237	1.000	6		17	.911	1.217	.999	6
	18	.877	1.270	1.000	6		18	.866	1.217	1.000	6
	19	.880	1.263	1.000	6		19	.867	1.264	1.000	6
	20	.883	1.259	1.000	6		20	.865	1.267	1.000	6
	21	.900	1.236	1.000	6, FU		21	.804	1.357	1.000	6, FU
	∞	.960	1.168	.995			∞	.984	1.136	.998	

Table F.15: Results for m_4 continued.

θ	β	a	b	r^2	Remarks	θ	β	a	b	r^2	Remarks
5	1	.845	1.283	.996		6	1	.500	2.304	.994	
	2	.857	1.268	.996			2	.501	2.296	.994	
	3	.876	1.249	.995			3	.498	2.294	.994	
	4	.916	1.216	.994			4	.504	2.251	.992	
	5	.908	1.238	.994			5	.572	2.011	.990	
	6	.846	1.331	.993			6	.586	1.968	.989	
	7	.849	1.345	.992			7	.678	1.727	.987	
	8	.833	1.379	.991			8	.725	1.608	.987	
	9	.871	1.329	.991			9	.802	1.443	.990	
	10	.875	1.312	.993			10	.836	1.373	.993	
	11	.906	1.257	.995			11	.862	1.310	.996	
	12	.908	1.237	.997			12	.882	1.265	.998	
	13	.920	1.212	.998			13	.905	1.228	.999	
	14	.913	1.209	.999			14	.907	1.215	.999	
	15	.892	1.230	.999			15	.890	1.231	.999	
	16	.867	1.260	.999			16	.867	1.259	.999	
	17	.871	1.253	.999			17	.871	1.250	1.000	
	18	.820	1.326	.999			18	.817	1.327	1.000	
	19	.827	1.311	.999			19	.823	1.314	1.000	
	20	.831	1.305	.999			20	.827	1.310	1.000	
	21	.709	1.531	1.000	FU		21	.686	1.585	1.000	FU
	∞	.998	1.120	.999			∞	1.000	1.115	.999	

Table F.16: Results for m_4 continued.

θ	β	a	b	r^2	**Remarks**
7	1	.333	3.604	.987	
	2	.334	3.550	.988	
	3	.332	3.501	.988	
	4	.365	3.170	.988	
	5	.501	2.468	.988	
	6	.500	2.383	.989	
	7	.559	2.103	.986	
	8	.646	1.819	.986	
	9	.743	1.559	.990	
	10	.784	1.458	.993	
	11	.830	1.358	.997	
	12	.856	1.299	.998	
	13	.884	1.253	.999	
	14	.897	1.228	.999	
	15	.885	1.239	.999	
	16	.859	1.272	.999	
	17	.868	1.258	1.000	
	18	.816	1.335	1.000	
	19	.824	1.320	1.000	
	20	.829	1.312	1.000	
	21	.712	1.530	1.000	FU
	∞	1.001	1.096	1.000	